

AD-A159 242

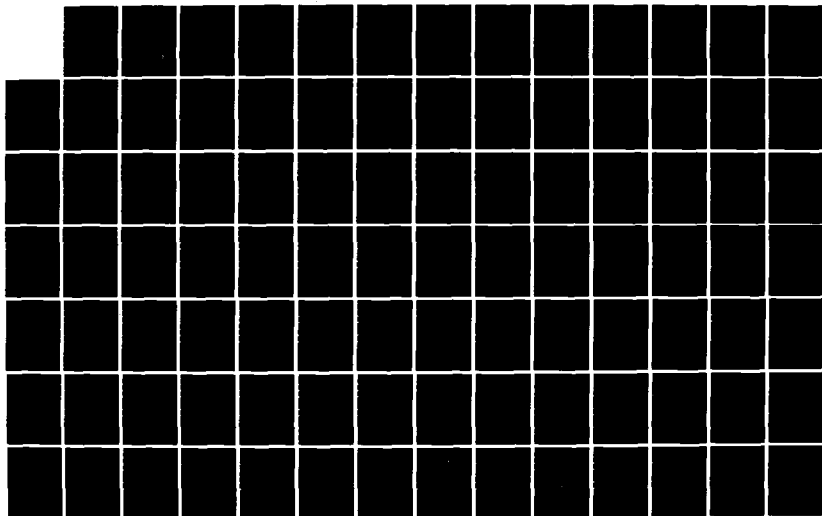
COLLISIONAL DYNAMICS OF THE $B^3P(0^+)$ STATE OF IODINE
MONOFLUORIDE(U) AIR FORCE INST OF TECH WRIGHT-PATTERSON
AFB OH SCHOOL OF ENGINEERING P J WOLF MAR 85
AFIT/DS/PH/85-1

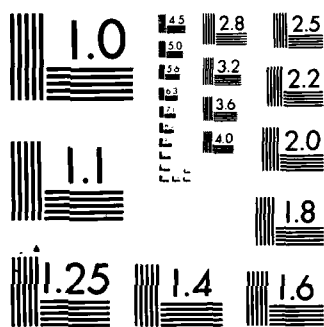
1/3

UNCLASSIFIED

F/G 7/4

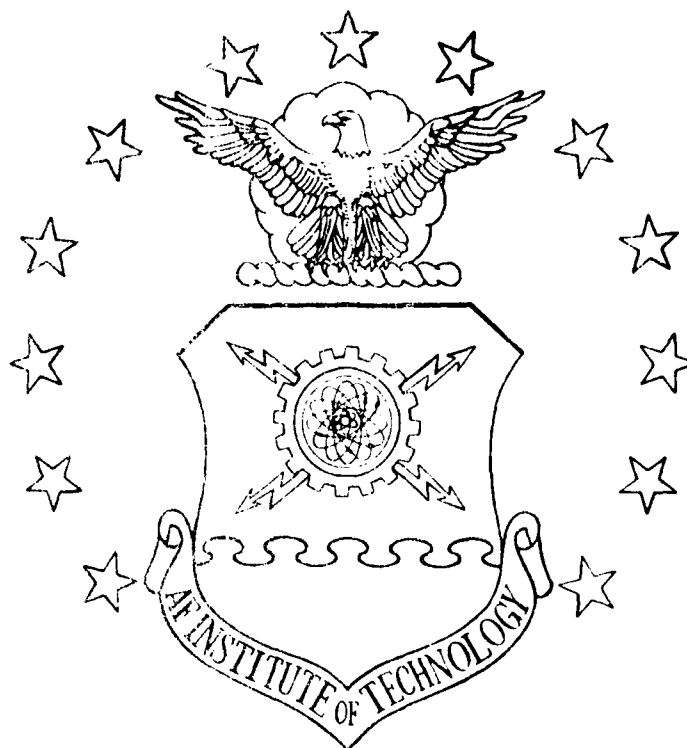
NL





MICROCOPY RESOLUTION TEST CHART
NATIONAL BUREAU OF STANDARDS 1963-A

AD-A159 242



COLLISIONAL DYNAMICS OF THE $B^3\Pi(0^+)$ STATE
OF IODINE MONOFLUORIDE $^{127}\text{I}^{19}\text{F}$

DISSERTATION

AFIT/DS/PH/85-1

Paul J. Wolf
Capt USAF

This document has been approved
for public release and sale, its
distribution is unlimited.

DEPARTMENT OF THE AIR FORCE
AIR UNIVERSITY (ATC)

AIR FORCE INSTITUTE OF TECHNOLOGY

Wright-Patterson Air Force Base, Ohio

DTIC
EL

SEP 18 1985

A

DTIC FILE COPY

85 09 17 036

COLLISIONAL DYNAMICS OF THE $B^3\Pi(0^+)$ STATE
OF IODINE MONOFLUORIDE I

DISSERTATION

AFIT/DS/PH/85-1

Paul J. Wolf
Capt USAF

①
DTIC
SEP 18 1985
S
A

Approved for public release; distribution unlimited

ACKNOWLEDGEMENTS

The author gratefully acknowledges the support and interest of the Air Force Weapons Laboratory and the financial support of the Air Force Office of Scientific Research for allowing him to perform his dissertation work in pursuit of a Ph.D degree.

Special thanks go to Dr. Steven J. Davis for proposing this investigation, and for his encouragement, support, and timely advice throughout much of this research effort. The author is deeply indebted to Dr. Davis for providing him with valuable, practical insights in conducting experimental research and the numerous, stimulating discussions with Dr. Davis have greatly contributed to the author's knowledge of the field. The author also greatly appreciates the aid given by Dr. Ernest A. Dorko. He has continually provided moral support and the author has benefited from several discussions with him especially in the late stages of the research.

The author also extends his gratitude to Dr. Robert Shea, Mr. Leonard Hanko, and especially, Mr. Sam Herrera. Dr. Shea provided the needed computational support, without which much of the detailed modeling and data analysis could not have been performed. Mr. Hanko greatly aided in the gathering of important data in the later stages of this work. His humor also made the long hours of data gathering more bearable. Finally, Mr. Herrera's patience and consciousness in reducing copious amounts of data is greatly appreciated. His efforts helped to successfully conclude this research effort.

The author would also like to thank Ms Mary Hanks and Mrs Gloria Alvarez for preparing the initial drafts of this text. Above all, the author is most indebted to his wife, Kathy, and daughter, Angela for their lasting patience and love throughout the author's graduate career.

Contents

	<u>Page</u>
Acknowledgements	iii
List of Figures	viii
List of Tables	xii
Abstract	xiv
I. Introduction	
A. Background.	1
B. Energy Transfer and Resonance Fluorescence.	6
C. Purpose of Study.	7
D. Text Organization	9
II. Kinetic Analysis	
A. Introduction	11
B. Development of the Master Rate Equation	11
C. Steady-State Analysis	18
1. Electronic Quenching	19
2. Vibrational Relaxation	21
3. Rotational Relaxation	25
D. Time Dependent Analysis	26
1. Electronic Quenching	26
2. Vibrational Relaxation.	27
III. Experimental	
A. Introduction	33
B. Time Resolved Studies	33
1. IF Production	33
2. Flow System Design	34
3. Excitation Source	37
4. Laser Excitation Spectra	40
5. Electronic Quenching Measurements	42
6. Vibrational Relaxation Studies	44
C. Steady-State Experiments	47
1. IF Production	47
2. Fluorescence Cell Design	50

Contents

	<u>Page</u>
3. Excitation Source	51
4. Fluorescence Detection and Data Processing	52
IV. Results	
A. Electronic Quenching	56
1. Quenching by the Noble Gases, N ₂ , I ₂ , and F ₂	56
2. Quenching by O ₂	66
3. Quenching by H ₂ O	72
B. Vibrational Relaxation: Time-Resolved Results	76
C. Vibrational Transfer: CW Results	83
D. Multiple Quantum Vibrational Transfer	92
E. Rotational Relaxation	104
1. Rate Constants.	104
2. Band Contours: Rotational Memory	109
3. Band Contours: Multiquantum Transfer	110
V. Discussion	
A. Electronic Quenching	114
B. Vibrational Energy Transfer	120
1. Cross Sections.	120
2. Cross Section Trends.	132
3. Multiple Quantum Vibrational Transfer	139
4. Comparisons With Other Studies	143
C. Rotational Energy Transfer	145
D. General Observations Concerning Steady-State and Time-Resolved Experiments	151
VI. Conclusions	
A. Summary	153
B. Further Studies	155

Contents

	<u>Page</u>
References	157
Appendix A: Radiative and Spectroscopic Properties of the IF(B \rightarrow X) System	161
Appendix B: Elementary Vibrational Transfer Models	163
1. Collision Geometry.	163
2. Adiabatic Approximation	163
3. Landau- Teller Model.	166
4. SSH Theory.	168
Appendix C: Steady-State Backtransfer Corrections.	170
Appendix D: Qualitative Features of Temporally Resolved Vibrational Relaxation Data.	173
Appendix E: Montroll and Shuler Solution to Time Resolved Vibrational Relaxation.	177
Appendix F: Number Density Estimates for the Time Resolved Experiments	180
Appendix G: Laser Excitation Spectra Results	185
Appendix H: Calibration of the Fluorescence Detection System	191
Appendix I: Spectral Band Area Calculations in the CW Experiments	194
1. Vibrational Transfer Experiments.	194
2. Rotational Transfer Experiments	194
Appendix J: Error Analysis	197
1. CW Error Estimates.	197
2. Time Resolved Error Estimates	199
Appendix K: Multiquantum Vibrational Transfer.	200
Appendix L: Steady-State Vibrational Transfer Modeling	204
Vita	206

List of Figures

<u>Figure</u>	<u>Page</u>
1-1 Potential energy curves for the $B^3\Pi(0^+)$ and $X^1\Sigma(0^+)$ states of IF.	3
2-1 Spectrally resolved laser induced fluorescence showing the appearance of satellite lines due to collision induced vibrational energy transfer	22
2-2 Energy level diagram showing the various rate processes occurring in the vicinity of the initially populated level, v.	28
3-1 Schematic diagram of the low pressure flow system explicitly showing the gas delivery network.	35
3-2 Cross-sectional view of the fluorescence cell	39
3-3 Block diagram of the apparatus for recording laser excitation spectra.	41
3-4 Block diagram of the apparatus used in the electronic quenching experiments.	43
3-5 Block diagram of the apparatus used in the time resolved energy transfer studies.	46
3-6 Cross-sectional view of the differentially pumped flow system.	48
3-7 Block diagram of the apparatus used in the cw energy transfer studies.	54
4-1 IF(B) total fluorescence decay curve and the corresponding logarithmic plot in the presence of 0.161 Torr of He	57
4-2 Stern-Volmer plot for quenching of IF(B) by F_2	58
4-3 Stern-Volmer plot for quenching of IF(B) by He.	59
4-4 CW electronic quenching data for He	61
4-5 Relative IF(B \rightarrow X) fluorescence intensity and Stern-Volmer plot for IF(B) decay as a function of Ar bath gas pressure.	63

List of Figures

<u>Figure</u>		<u>Page</u>
4-6	Total IF(B) fluorescence decay curves in the presence of O ₂	67
4-7	Stern-Volmer plots for determining IF(B) depletion rate constants by O ₂	69
4-8	Total IF(B) fluorescence decays with H ₂ O.	73
4-9	Temporally and spectrally resolved IF(B) fluorescence emission from v'= 4 and v'= 3 with H ₂ O.	74
4-10	Time evolutions of v'= 2, 3, and 4 subsequent to excitation of v'= 3 with 0.65 Torr of He.	77
4-11	Comparison of data and fit using the Montroll-Shuler model with 1.7 Torr of He	79
4-12	Stern-Volmer plot for extracting vibrational relaxation rate constants	82
4-13	Spectrally resolved IF(B) fluorescence emission showing the development of vibrational satellite bands by energy transfer with He.	86
4-14	Relative, steady-state IF(B) vibrational population distributions as a function of He pressure.	89
4-15	Vibrational relaxation data for He.	91
4-16	Stern-Volmer plot for determining the multiquantum vibrational transfer rate constant, k(3,1).	95
4-17	Temporal history of the collisionally populated states, v'= 3 and v'= 2 subsequent to excitation of v'= 4 with He bath gas.	99
4-18	Comparison of data and fit using the Montroll-Shuler solution for decay of a $\Delta v = -2$ transfer band	103
4-19	IF(B;v'= 3) fluorescence emission showing rotational population redistribution from J'= 22 with He bath gas.	105
4-20	IF(B;v'= 3) rotational relaxation data with various collision partners.	108

List of Figures

<u>Figure</u>	<u>Page</u>
4-21 Comparison of the $v'=3$ rotational distributions with He and Xe	112
5-1 Steady-state model predictions of the IF(B) relative populations in $v'=2, 3$, and 4 using rate constants measured in the time resolved experiments	122
5-2 Stern-Volmer plot for determining the total removal rate constant from $v'=3$ using the synthetic data of Fig. 5-1.	124
5-3 Computer simulated fluorescence decay curves using rate constants measured in the cw experiments.	126
5-4 Stern-Volmer plot for determining the rate constant, $k(3,2)$, from the data of Fig. 5-3b.	130
5-5 Plot of the vibrational transfer efficiencies vs. the square root of the collision reduced mass	133
5-6 Vibrational relaxation probabilities for IF(B; $v'=3$) with the noble gases plotted logarithmically against reduced mass to the $1/3$ power	136
5-7 Vibrational level scaling of the $\Delta v = -1$ energy transfer cross sections.	138
5-8 Predicted population distributions due to multiquantum vibrational transfer.	141
5-9 Plot of rotational transfer efficiencies vs. the square root of the collision reduced mass.	146
5-10 Plot of the rotational transfer cross sections vs the polarizability parameter, $(\alpha \mu^2)^{1/3}$, for the noble gases	150
B-1 Collision geometry for an atom-diatom encounter	164
D-1 Comparison of spectrally unresolved and spectrally resolved temporal decays in IF(B)	174
D-2 Time history of $v' = 2$ in IF(B) subsequent to $v' = 3$ excitation.	176
G-1 Laser excitation spectrum recorded at 0.5 nm resolution showing the IF(B \rightarrow X) vibrational structure	186

List of Figures

<u>Figure</u>		<u>Page</u>
G-2	Rotationally resolved excitation spectrum of the (4,0) band recorded at 0.4 cm^{-1} resolution.	187
G-3	Laser excitation spectrum of the (5,0) band	190
H-1	A comparison of the experimental and theoretical black-body spectra.	192
H-2	A plot of the relative blackbody response (experimental to theoretical) as a function of wavelength.	193
K-1	Schematic energy level diagram comparing single and multiple quantum transitions.	201

exchange of vibrational and rotational energy. Finally, the important conclusions of these studies are summarized in Chapter VI.

Throughout the text, references are made to elementary vibrational energy transfer theories. For the convenience of the reader, a brief discussion of these theories is presented in Appendix B. This discussion is developed strictly for background information so the reader may refer to them when the theories are referenced in succeeding sections.

energy transfer rate coefficients in a chemically reactive flow system.

D. Text Organization

Chapter II develops the kinetic equations which are used to extract energy transfer rate constants from the experimental data. The kinetic analysis begins with a description of the relevant collisional and radiative properties of IF(B) molecules in a heat bath. The master rate equation describing these processes is then analyzed using both steady-state and time-dependent methods.

Chapter III is devoted to a detailed description of the experimental arrangements that were used in both the cw and time resolved studies. The descriptions of these experiments include the design of the flow system, the method for producing IF, and a presentation on the details of the various experiments that were performed.

The results of the energy transfer experiments are detailed in Chapter IV. This chapter is divided into three sections which are devoted to the results of each major study. First, the results of the electronic quenching experiments are discussed. The results of the vibrational and rotational energy transfer experiments are presented in the last two sections.

In Chapter V, a discussion of the results of each energy transfer process examined in this study are presented. The most important aspect of this chapter are the observations that are made about the trends in the energy transfer cross sections. These trends, in turn, reveal certain characteristics of the collision processes that are important in the

CW and time resolved LIF techniques were used to probe the B state manifold to obtain information on internal state dynamics. This study also developed temporally and spectrally resolved LIF for studying state resolved energy transfer in an electronically excited state of a diatomic molecule.

Both quenching and quantum resolved vibrational energy transfer were examined as a function of both collision partner and initially excited vibrational level, v_i' . The removal of rotational energy from an initially populated J' level was also examined as a function of collision partner. The study of both vibrational and rotational transfer vs. collision partner was performed to determine if physical properties (i.e., mass, polarizability) of the bath gas influenced the rate of energy transfer. The vibrational transfer investigations vs. v_i' attempted to determine an appropriate scaling law for vibrational transfer (how the transfer rates depend on v_i'). The results were then qualitatively compared to elementary theoretical models, thereby, obtaining information on the conditions, such as adiabaticity, for the collision process. The final objective of this study was to evaluate the two LIF techniques to determine the method which provided a more complete physical insight to the collision process.

The detailed energy transfer studies for molecules other than IF mentioned previously were conveniently performed with gases that can be isolated in sealed chambers. IF, however, is kinetically unstable and rapidly disproportionates into I_2 and IF_5 when confined in a static cell. Thus, this study is the first in which cw LIF was utilized in determining

detailed studies exist for I_2 in which electronic, vibrational, and rotational energy transfer was examined as a function of both initially excited level and collision partner. In these studies, population of specific ro-vibrational levels was achieved through cw excitation using both incoherent and laser sources. The energy transfer rate constants were obtained by spectrally resolving the fluorescence and analyzing the relative populations of individual quantum states as a function of the collision partner density using the steady-state approximation.

Energy transfer measurements in other halogen and interhalogen molecules are less extensive. The most detailed studies reported the effects of electronic quenching in the B states of Br_2 , $BrCl$, BrF , and Cl_2 by various collision partners.²⁶ Electronic quenching was also examined as a function of vibrational level in several of these molecules. However, little or no data exist for vibrational or rotational energy transfer. Limited spectrally resolved cw studies were performed in $Br_2(B)$ while energy transfer in $Cl_2(B)$, $BrF(B)$, and $BrCl(B)$ was investigated by examining spectrally unresolved fluorescence decay waveforms with various bandpass filters using pulsed excitation. These time resolved studies did not specifically monitor the population evolutions in the collisionally populated levels. Therefore, no state resolved data are available.

C. Purpose of Study

Since previous studies of $IF(B)$ energy transfer were at best qualitative, this study attempted a systematic investigation of electronic, vibrational, and rotational energy transfer in the $B^3\Pi(0^+)$ state of IF .

B. Energy Transfer and Resonance Fluorescence

Resonance fluorescence of molecules excited by monochromatic radiation is a well established method for determining energy transfer rate constants in electronically excited molecular states. The first investigation of collision induced changes in a resonance fluorescence series was made by Franck and Wood in 1911 using electronically excited iodine.¹⁹ Since then, advances in electronic instrumentation and optical excitation sources have made laser induced fluorescence (LIF) a very powerful technique for examining molecular inelastic collision processes.²⁰

Collision induced energy transfer has been examined using LIF for a variety of electronically excited molecules. For example, cw excitation studies have yielded extremely detailed data on the variations of vibrational and rotational energy transfer rate constants with initial (v' , J') levels for the $B^1\pi_u$ states of the alkali metal dimers, Na_2 ²¹ and Li_2 .²² Studies of this type have been carried out on other molecules such as NO $A^2\Sigma^+$,²³ HD $B^1\Sigma_u$,²⁴ and S_2 $B^3\Sigma_u$.²⁵ Time resolved laser induced fluorescence has also been used to study collision-induced energy transfer. In the past, this method has been generally limited to the study of vibrational relaxation in the electronic ground states of molecules.^{2c} The availability of narrow, tunable pulsed lasers operating at visible frequencies has recently made molecular electronic states accessible for time resolved energy transfer studies.

Several collisional energy transfer studies were also reported in the $B^3\pi(0_u^+)$ states of the halogen and interhalogen diatomics.²⁶ The most

population over many vibrational and rotational energy levels. These rovibrational levels must be thermalized to achieve the highest possible single line gain for an active chemical laser system.¹⁵ Thermalization can only be achieved through collisions with a suitable bath gas. Moreover, electronic quenching due to these bath gases, as well as the possibility of collision-induced predissociation, must also be examined. These processes represent a loss in the total excited state number density and would, therefore, reduce the overall laser efficiency. Thus, an examination of the energy transfer pathways in collisions between IF(B) and various bath gases is critical for determining the suitable conditions for chemical laser demonstration.

Much of the qualitative information on IF(B) energy transfer came from the IF optically pumped lasing demonstrations.^{16,17} The quenching effects of O₂, N₂, and He were examined by monitoring the IF laser performance as a function of bath gas pressure. The IF laser showed no discernable degradation with high pressures ($P > 10$ Torr) of He or N₂ which signified small quenching effects. However, the laser became very unstable for small O₂ partial pressures (5 Torr). The O₂ quenching rate was estimated as being at least 40 times faster than that for helium.¹⁷ Furthermore, IF lasing was observed from collisionally pumped states in IF + He mixtures which indicated that He efficiently thermalized the IF(B) vibrational manifold. A preliminary V-T rate constant for transfer from $v' = 3$ to $v' = 2$ was reported as $1.2 \times 10^{-11} \text{ cm}^3 \text{ molecule}^{-1} \text{ s}^{-1}$.¹⁷

experiments, Trickl and Wanner¹³ and Trautman et al.¹⁴ reported improved spectroscopic constants for both the X and B states of IF. The use of Trickl and Wanner's¹³ Dunham coefficients enables one to calculate the B→X spectral line positions to within 0.03 cm⁻¹, and excellent agreement is obtained with Durie's experimentally determined values. The lowest order Dunham coefficients and the IF(B) radiative lifetimes are collected in Appendix A.

The various chemical, spectroscopic, and radiative studies listed above have several important implications for the possible development of an IF(B→X) visible chemical laser.¹⁵ First, the numerous I₂ + F₂ chemiluminescence investigations indicate that the B state of IF is accessible by chemical excitation. Furthermore, as shown in Figure 1-1, the B state equilibrium internuclear separation is shifted with respect to the X state by 0.021 nm. Since this shift is so great, the Franck-Condon principle implies that the most probable B→X transition terminates at the high vibrational levels (v" > 3) in the X state. If the ground state manifold is thermalized, these high v" levels are essentially empty. Therefore, a population inversion can be established between these two electronic states without having the total B state population greater than that for the X state. Finally, the relatively large transition moment (.101 D²) between the B and X states facilitates the coupling of a large number of vibrational levels.¹² The importance of the latter two properties were realized when lasing was demonstrated on the B→X system via optical pumping.¹⁶⁻¹⁸

Unlike optical pumping, however, chemical excitation distributes the

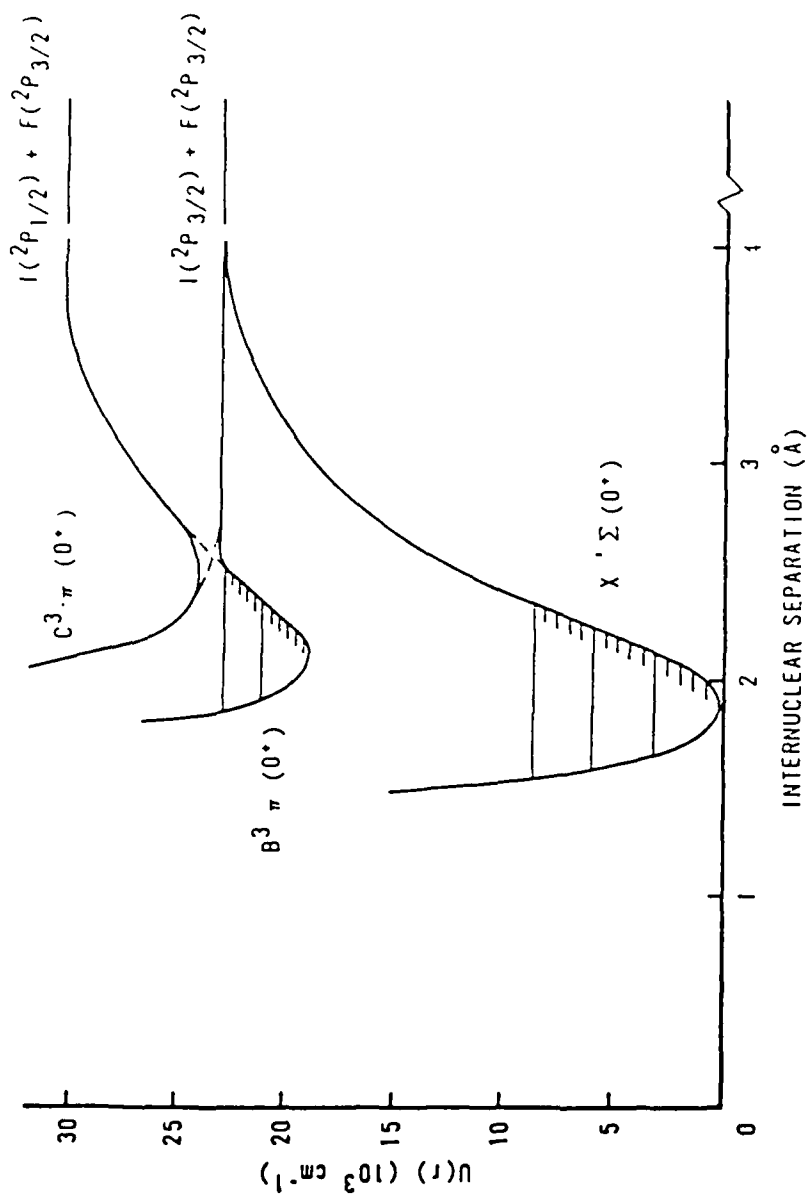


Figure 1-1. Potential energy curves for the B and X states of IF based on Clyne and McDermid's RKR potential calculations (Ref 9). An avoided crossing between the B and C state diabatic surfaces causes the B state to predissociate to two ground state atoms.

emission and determined the variation in the $B \rightarrow X$ relative electronic transition moment with r -centroid. This study also reported both Franck-Condon factors for the $B \rightarrow X$ transition and emission from the previously unobserved $IF\ A^3\Pi(1) \rightarrow X^1\Sigma(0^+)$ system. Using spectral parameters derived from Coxon's⁸ reinterpretation of Durie's data, Clyne and McDermid recalculated the Franck-Condon factors, and obtained the first RKR potential curve turning points for the B and X states of IF .⁹ Figure 1-1 shows the potential curves using the RKR values determined by Clyne and McDermid. The electronic state labeled $C^3\Pi(0^+)$ in Figure 1-1 is, diabatically, a repulsive surface. There exists a strong interaction between the B state and the (0^+) surface which forces avoided crossing.¹⁰ Consequently, the B state predissociates to two ground state atoms via a potential energy maximum. This effect makes the B state more or less unstable by limiting the number of stable vibrational levels. (The predissociative nature of $IF(B)$ was initially observed by Clyne and McDermid.¹¹)

In a subsequent study, Clyne and McDermid measured the radiative lifetimes of all the stable $IF(B)$ vibrational levels at pressures where the collision frequency was much less than the radiative rate.¹² The collision-free lifetimes, τ_R , varied monotonically with v' from $(8.8 \pm .89)\ \mu s$ for $v' = 9$ to $(6.96 \pm .47)\ \mu s$ for $v' = 0$. In addition, the onset of predissociation was observed in $v' = 8$, $J' \geq 52$ and $v' = 9$, $J' \geq 6$ as a shortening of the lifetime. These predissociated levels all had comparable lifetimes near $1\ \mu s$. (The vibrational levels above $v' = 9$ are all predissociated.)

In recent high resolution laser induced fluorescence spectroscopy

I. INTRODUCTION

A. Background

Detailed collisional energy transfer measurements between individual quantum levels in electronically excited states of small molecules are providing a wealth of information for a better understanding of collision dynamics on a microscopic level. Energy transfer collisions form an important class of elementary processes and as such are of great theoretical interest.¹ The availability of accurate cross section data for well-defined quantum state changes plays a vital role in shaping theoretical formulations of collision processes.^{1,2} A knowledge of such cross sections, for example, can be used to map out important features of the intermolecular potential governing the collision.^{1,3}

The collisional exchange of energy also has practical importance in fields like chemical reaction kinetics, atmospheric phenomena, and laser physics. In the latter field, the $B^3\Pi(0^+) \rightarrow X^1\Sigma(0^+)$ transition in iodine monofluoride (IF) has received considerable interest as a potential candidate for an electronic transition chemical laser operating at visible frequencies.

The IF($B \rightarrow X$) transition was first observed by Durie in emission from an iodine fluorine flame.^{4,5} In these studies, Durie assigned both the rotational and vibrational spectrum and determined the first spectroscopic constants. Clyne, et al.⁶ observed additional vibrational bands in the $B \rightarrow X$ system from the recombination of $F(2P_{3/2})$ and $I(2P_{3/2})$ ground state atoms in the presence of $O_2(^1\Delta_g)$. Birks, et al.,⁷ in a low pressure $I_2 + F_2$ experiment, also observed IF($B \rightarrow X$) chemiluminescence

discussed. The most efficient quencher was I_2 with an estimated rate constant of $2.8 \times 10^{-10} \text{ cm}^3 \text{ molecule}^{-1} \text{ s}^{-1}$.

Vibrational energy transfer was 10^2 to 10^3 times more efficient than electronic quenching. The vibrational transfer rate constants from $v'=3$ to $v'=2$ varied from $(5.9 \pm 0.6) \times 10^{-12} \text{ cm}^3 \text{ molecule}^{-1} \text{ s}^{-1}$ for He to $(5.8 \pm 2.3) \times 10^{-13} \text{ cm}^3 \text{ molecule}^{-1} \text{ s}^{-1}$ for Xe. The relative V-T cross sections for the noble gases showed a smooth dependence on the collision reduced mass. The $v'=3$ to $v'=2$ vibrational transfer coefficients for N_2 , O_2 , and F_2 were $(2.8 \pm 0.6) \times 10^{-12}$, $(5.9 \pm 2.4) \times 10^{-12}$ and $(5.8 \pm 0.5) \times 10^{-12} \text{ cm}^3 \text{ molecule}^{-1} \text{ s}^{-1}$, respectively. However, these rate constants showed no dependence on collision reduced mass signifying that a V-T process may not be the dominant mechanism. The IF(B) vibrational transfer cross sections for the noble gases, N_2 and O_2 scaled linearly with vibrational quantum number. The rate constants for $\Delta v = -2$ vibrational transfer were estimated as less than 15 percent of the total removal rate constants for each bath gas.

Rotational energy transfer was the most efficient kinetic process in IF(B). Total rotational removal rate constants were obtained in IF(B) + noble gas and N_2 collisions subsequent to the initial excitation of $(v',J') = (3,22)$. The estimated efficiencies for rotational energy transfer were typically 100 times greater than those for vibrational transfer. The rate constants ranged from $(9.7 \pm 1.3) \times 10^{-11}$ to $(1.1 \pm .1) \times 10^{-10} \text{ cm}^3 \text{ molecule}^{-1} \text{ s}^{-1}$ for He and Xe, respectively. The relative rotational transfer efficiencies also displayed a smooth dependence on the collision reduced mass.

Abstract

The collision dynamics in the IF $B^3\Pi(0^+)$ state were examined in a chemically reactive flow system using both time resolved and steady-state laser induced fluorescence. Rate constants for quenching and vibrational and rotational energy transfer were determined by analyzing IF($B \rightarrow X$) fluorescence emission in the presence of various foreign gases.

IF(B) deactivation rate constants were determined as a function of vibrational quantum number for the following collision partners: He, Ne, Ar, Kr, Xe, N_2 , F_2 , I_2 , O_2 , and H_2O . Quenching by the noble gases and N_2 was extremely slow with all rate constants less than $1 \times 10^{-14} \text{ cm}^3 \text{ molecule}^{-1} \text{ s}^{-1}$ for $3 \leq v' \leq 8$. The quenching rate constants for F_2 showed a weak dependence on vibrational quantum number, ranging from $(3.4 \pm 0.5) \times 10^{-12}$ to $(5.2 \pm 0.4) \times 10^{-12} \text{ cm}^3 \text{ molecule}^{-1} \text{ s}^{-1}$ for $v' = 3$ and $v' = 7$, respectively. Double exponential IF(B) fluorescence decays were observed with both O_2 and H_2O indicating two depletion processes occurring over the lifetime of IF(B). The quenching rate constants, extracted from the decays at long times, were $(1.4 \pm 0.2) \times 10^{-12} \text{ cm}^3 \text{ molecule}^{-1} \text{ s}^{-1}$ for O_2 and $(7.6 \pm 1.6) \times 10^{-12} \text{ cm}^3 \text{ molecule}^{-1} \text{ s}^{-1}$ for H_2O . At early times, the respective deactivation rate constants for O_2 and H_2O were $(8.3 \pm 1.4) \times 10^{-12} \text{ cm}^3 \text{ molecule}^{-1} \text{ s}^{-1}$ and $(2.4 \pm 0.7) \times 10^{-10} \text{ cm}^3 \text{ molecule}^{-1} \text{ s}^{-1}$. A possible quenching mechanism by O_2 is

List of Tables

<u>Table</u>		<u>Page</u>
A-2	IF(B) spectroscopic constants	162
F-1	IF(B) + M collision frequencies	183
G-1	Air Wavelengths of band heads and Franck-Condon Factors of the IF(B \rightarrow X) system seen in laser induced fluorescence.	188

List of Tables

<u>Table</u>	<u>Page</u>
2-1 Notation used in kinetic analyses	12
3-1 Wavelength ranges for various dyes used in pumping IF(B) vibrational states from IF(B; $v''=0$)	38
4-1 IF(B) quenching rate constants by F ₂	60
4-2 Total vibrational removal rate constants and the corresponding cross sections obtained in the pulsed experiments.	84
4-3 State-to-state vibrational transfer rate constants and the corresponding cross sections obtained in the pulsed experiments.	85
4-4 CW vibrational transfer rate constants and corresponding cross sections.	93
4-5 Estimated multiple quantum vibrational transfer rate constants	96
4-6 Vibrational relaxation rate constant ratios for the initial excitation of $v'=3$ in the cw experiments . .	98
4-7 Total rotational relaxation rate constants and corresponding cross sections.	107
4-8 Estimated J changes per collision for various colli- sion partners	111
5-1 Summary of electronic quenching cross sections, gas kinetic cross sections, and quenching probabilities . . .	115
5-2 IF(B) deactivation cross sections and relative efficiencies for O ₂ and H ₂ O	116
5-3 Comparison of B state quenching cross sections.	118
5-4 Ratios of $k(3,2)$ to $k(3,4)$ rate constants from the cw experiments.	131
5-5 Relative energy transfer cross sections determined in the $v'=3$ excitation studies.	145
A-1 IF(B) collision free lifetimes and electric dipole moments	162

II. KINETIC ANALYSIS

A. Introduction

Kinetic analyses of collision induced energy transfer in IF $B^3\pi(0^+)$ are presented in this chapter. The master rate equation is developed describing the various kinetic processes in the B state of IF. Solutions to this equation are obtained by applying both steady-state and time-dependent analyses which yield expressions that are used to extract energy transfer rate constants from experimental data. Definitions and notation used in these kinetic analyses are collected in Table 2-1.

B. Development of the Master Rate Equation

In these experiments, one considers a system of gas phase IF molecules capable of existing in a large number of accessible energy levels. A non-equilibrium IF distribution is created by selectively populating a specific ro-vibrational energy level in the $B^3\pi(0^+)$ state using laser excitation. These excited molecules are dilutely dispersed in an inert gas (bath) with which they can exchange energy. Let IF^+ represent IF molecules in ro-vibrational levels in any electronic state lying below $IF(B)$ in energy and Y , foreign gas atoms/molecules. The kinetic processes which can occur in these experiments are shown below.

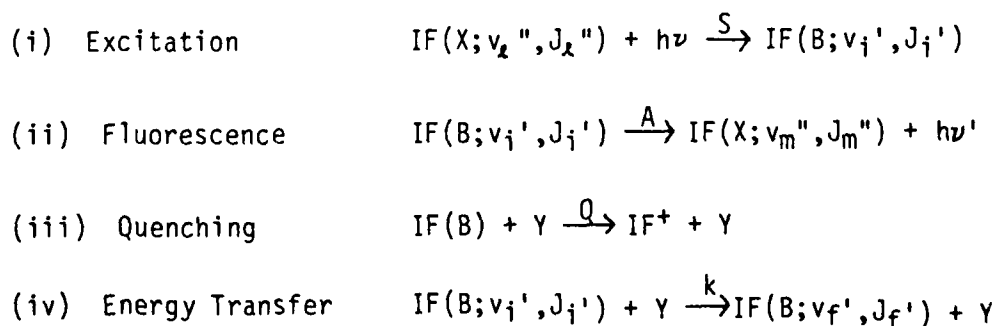


TABLE 2-1. Notation used in kinetic analyses.

NOTATION	QUANTITY(PAGE)*	COMMENT	UNITS
A	Fluorescence decay rate constant (15)	$A = 1/\tau_R$	s^{-1}
I, I ₀ , I _m	Total fluorescence intensity (20)		arbitrary
k	Energy transfer rate constant (17)		$cm^3 s^{-1}$
k _B	Energy transfer rate constant by background gases (23)		$cm^3 s^{-1}$
k _B '	(23)	$k_B' = k_B \tau_R$	cm^3
k _{ifm}	General state-to-state rate constant for the mth collision partner (17)		$cm^3 s^{-1}$
k _{ifm} '	(18)	$k_{ifm}' = k_{ifm} \tau_R$	cm^3
k _r	Total rotational transfer rate constant from J to all J + ΔJ (25)	$k_r = \sum_J k(v_i, J_i; v_i, J)$	$cm^3 s^{-1}$
k _r '	(25)	$k_r' = k_r \tau_R$	cm^3
k _v	Total vibrational transfer rate constant from v to all v + Δv (21)	$k_v = \sum_{v, J} k(v_i, J_i; v, J)$	$cm^3 s^{-1}$
k _v '	(23)	$k_v' = k_v \tau_R$	cm^3
k(v _i , v _f)	State-to-state vibrational transfer rate constant (24)	$k(v_i, v_f) = \sum_J k(v_i, J_i; v_f, J)$	$cm^3 s^{-1}$
k(v _i , v _f)'	(24)	$k(v_i, v_f)' = k(v_i, v_f) \tau_R$	cm^3
M	Bath gas concentration (14)		cm^{-3}

* Page where symbol is first defined.

NOTATION	QUANTITY (PAGE)	COMMENT	UNITS
N_B	Total background gas concentration (14)		cm^{-3}
N_O	Total IF(X) concentration (19)		cm^{-3}
N	Total IF(B) concentration (19)	$N = \sum_{v,J} N(v,J)$	cm^{-3}
$N(J)$	IF(B) concentration in rotational state J (25)		cm^{-3}
$N(v)$	IF(B) concentration in vibrational state v (23)	$N(v) = \sum_J N(v,J)$	cm^{-3}
N_i	IF(B) concentration in ro-vibrational state (v,J) (14)	$N_i = N(v,J)$	cm^{-3}
Q_B	Electronic quenching rate constant by background gases (20)		$\text{cm}^3 \text{ s}^{-1}$
Q_B'	(20)	$Q_B' = Q_B \tau_R$	cm^3
Q_m	Electronic quenching rate constant by species M (16)		$\text{cm}^3 \text{ s}^{-1}$
Q_m'	(18)	$Q_m' = Q_m \tau_R$	cm^3
R_m	Sum of quenching and energy transfer rate constants by species m (23)	$R_m = Q_m + k_v$	$\text{cm}^3 \text{ s}^{-1}$
R_m'	(23)	$R_m = R_m \tau_R$	cm^3
S	First order excitation rate constant (15)		s^{-1}
S'	(18)	$S' = S \tau_R$	
Y_m	Concentration of mth collision partner (15)		cm^{-3}
τ_R	Radiative (collision-free) lifetime (16)	$\tau_R = 1/A$	s^{-1}
Γ	Sum of first order radiative and quenching rate constants (27)	$\Gamma = A + Q_m M$	s^{-1}

Experiments which examine processes (iii) and (iv) are performed by adding an inert bath gas. (The definition of bath gas usually includes species responsible for "self-quenching" and "self-relaxation" which, in these experiments, is IF(X).) However, since IF(X) must be chemically produced, an incomplete reaction may establish a mixture of unreacted species. These residual gases may have an appreciable kinetic effect and must, therefore, be considered in the analysis. Furthermore, it is assumed that the IF(B) concentration is sufficiently small so that interactions between these molecules are negligible. So, we will generally define the foreign gas to include the bath gas (inert species added to the system, whose concentration is denoted by M) and "background" gases (residual reactants plus IF(X), whose concentrations are denoted as N_B).

Using the notation defined in Table 2-1, the master rate equation describing the rate of change of IF(B;v',J') population, N_i, is given in Eq.(2-1).²⁷

$$\begin{aligned} \frac{dN_i}{dt} = & \overset{(1)}{S_{li}N_l} - \overset{(2)}{\sum_l A_{il}N_i} - \overset{(3)}{\sum_m Q_{im}N_iY_m} - \overset{(4)}{\sum_{fm} k_{ifm} N_iY_m} + \\ & \overset{(5)}{\sum_{fm} k_{fim} N_fY_m} \end{aligned} \quad (2-1)$$

The sums over m in Eq.(2-1) include contributions from different foreign gases present in the system; specifically, the bath gas, M, and background gases, N_B. The concentration symbol used in Eq.(2-1) is the general one, Y_m.

Each kinetic process along with the corresponding elements of Eq.(2-1)

will now be described.

(1) Process (i), the pump process, corresponds to the initial preparation of a specific (v', J') level in IF(B) via monochromatic, optical excitation and contributes term (1) in Eq.(2-1). Term (1) is first order in the number density of the ground state, IF(X), molecules, and $S_{\ell i}$ is the proportionality constant (excitation rate constant) where $\ell = (v'', J'')$ and $i = (v', J')$.

The preparation of a pure quantum state requires that the exciting frequency, ν , has a linewidth that does not overlap more than one rotational absorption line. Fulfilling this requirement, the excitation rate constant takes on the simple form²⁷

$$S_{\ell i} \propto \delta(E' - E'' - h\nu) |\langle i | \bar{V} | \ell \rangle|^2 \quad (2-2)$$

where \bar{V} is the electric dipole moment operator connecting the rovibrational levels i and ℓ . Thus, all $S_{\ell i}$ are zero except one, for a narrow exciting frequency (i.e. a small bandwidth).

(2) Process (ii) describes purely radiative emission from IF(B) to IF(X). This process contributes term (2) to Eq.(2-1). This term is first order with respect to N_i ; and A_i , the proportionality constant, is the total, first order radiative decay rate constant from quantum state i . (A_i is defined as the Einstein A coefficient and is equal to the inverse of the radiative lifetime, τ_r .) Remember, radiative decay from the B state populates a number of ground state vibrational levels.* So,

* The B state reradiation also produces a nonequilibrium vibrational distribution in IF(X). But, since it was assumed that the IF(B) concentration is very small, this represents a negligible perturbation to

the sum over ℓ must extend over the quantum levels of the ground electronic state.

(3) Process (iii) represents a collisional interaction which depletes $IF(B)$ population through non-radiative decay (electronic quenching). This process contributes term (iii) to Eq.(2-1). This term is second order with respect to Y_m and N_i . Q_{im} is, therefore, the proportionality constant and is defined as the electronic quenching rate constant by the m^{th} collision partner. Since electronic quenching involves a loss in total electronic energy, $IF(B)$ can decay via two, kinetically equivalent mechanisms: predissociation, where $IF(B)$ decays to two ground state atoms, $I(^2P_{3/2})$ and $F(^2P_{3/2})$; and "true" electronic quenching, where $IF(B)$ decays to quantum levels in either the $X^1\Sigma(0^+)$, $A^3\Pi(1)$, or $A'^3\Pi(2)$ electronic states with the energy difference being absorbed by the bath gas. Since these two mechanisms are kinetically equivalent, one must be careful in interpreting the quenching mechanism. However, these energy transfer studies were performed by exciting quantum levels that lay well below the predissociation limit, making collision induced predissociation highly improbable.

(4) The fourth term in Eq.(2-1), which corresponds to process (iv), accounts for the collisional redistribution of population from the initially prepared state, i , to other quantum levels, f . Various mechanisms may be responsible for energy transfer between $IF(B)$ and Y (i.e.,

the overall distribution among the $IF(X)$ levels. Thus, no information on vibrational relaxation in $IF(X)$ can be directly obtained in these experiments.

V-V, V-T, R-T, etc.) with k , the rate constant, representing the rapidity of the process. For this discussion, however, no distinction is made as to the mechanism for energy transfer.

In general, k is an $n \times n$ matrix with the main diagonal elements being the sum of the second order, state-to-state rate constants, k_{if} , from i to f .^{*} These main diagonal elements are formally defined as the total removal rate constants. Single quantum transitions are defined for $f = i \pm 1$, while multiple quantum state transitions are defined for $f = i \pm n$ ($n = 2, 3, 4, \dots$). For vibrational energy transfer in IF(B), the k matrix may contain 72 non-zero elements. These elements give the rate constants for both collisional excitation and de-excitation for each stable IF(B) vibrational level. For rotational energy transfer, however, the dimensionality of the k matrix can be extremely large depending on the number of rotational levels admitted in the transfer process.

(5) The fifth term in Eq.(2-1), which also corresponds to process (iv), describes the collisional population of state i from state f . These rate constants correspond to the off diagonal terms in the general k matrix. For sufficiently low foreign gas pressures, the effects of secondary transfer due to multiple collisions which repopulate the state i (backtransfer) may be neglected. Under these conditions, the sum over f reduces to a single term if f is the initially prepared state. Thus, k_{fi} is

^{*} The matrix k is equal to the transition matrix formally defined in quantum scattering theory. This matrix is proportional to the scattering matrix, S , and for initial excitation of one quantum state, the energy transfer experiments yield one column of the molecular S -matrix.

defined as the second order, state-to-state rate constant for populating i from state f . However, there is no contribution from this term in Eq. (2-1) if i is the initially prepared state. At pressures where multiple collisions occur, k_{fi} describes the population of state i from all other levels f (back-transfer collisions).

C. Steady-State Analysis

In a steady-state analysis, it is assumed that the $IF(B)$ concentration is small and does not change in time. Using the steady-state assumption, $dN_i/dt=0$ for all i . Thus, setting the time derivative equal to zero in Eq.(2-1) and solving for N_i , one obtains

$$N_i = \frac{S_{ji} N_j + \sum_{fm} k_{fim} N_f Y_m}{A_i + \sum_m Q_{im} Y_m + \sum_{fm} k_{ifm} Y_m} \quad (2-3a)$$

In the study of collisional energy transfer, the radiative lifetime, τ_R , defines the observational time scale for all the kinetic events. We can rewrite Eq.(2-3a) to emphasize this property by dividing the numerator and denominator by $1/\tau_R$ where $1/\tau_R = \sum_i A_{ij}$. The result is Eq. (2-3b).

$$N_i = \frac{S_{ji}' N_j + \sum_{fm} k_{fim}' N_f Y_m}{1 + \sum_m (Q_{im}' + \sum_f k_{ifm}') Y_m} \quad (2-3b)$$

where $S_{ji}' = S_{ji} \tau_R$, etc. Equation (2-3b) can be used to obtain the relevant expressions for determining the electronic quenching and vibrational and rotational energy transfer rate constants. One final note is needed before proceeding with the derivations. In all these experiments, $IF(B)$ levels were populated by optically pumping from $v''=0$ in $IF(X)$. Thus, we

shall set $N = N_0$ to represent ground state IF(X) molecules.

1. Electronic Quenching

Electronic quenching is examined in steady-state experiments by monitoring the total IF(B) population (or, equivalently, total fluorescence) as a function of the foreign gas concentration. (Since spectrally resolved data are not obtained in quenching experiments, we can eliminate terms (4) and (5) from Eq.(2-1). However, vibrational relaxation occurs when electronically excited molecules collide with the bath gas. Therefore, the quenching rate constants are to be considered as averaged values for the set of states which have appreciable population.) The appropriate form of Eq.(2-3b) for describing electronic quenching is

$$N = \frac{S_{01} N_0}{1 + \sum_m Q_{1m}' Y_m} \quad (2-4a)$$

where $N = \sum_i N_i$, $Q_m' = \sum_i Q_{im}'$, and $S_{01} = \sum_i S_{0i}'$ with $i = 1$ corresponding to the initially prepared state. Implicit in Eq.(2-4a) is the sum of $\sum_l A_{1l}$ over l . The lifetimes of the vibrational levels that contribute to the total fluorescence differ by no more than ten percent.¹² Therefore, we assume that τ_R is a constant.

Experimentally, quenching effects are most easily observed by monitoring the total, spectrally unresolved fluorescence intensity. Defining the fluorescence intensity, I , as the number of emissions per cm^3 per s ($I = N/\tau_R$), Eq.(2-4a) is rewritten as

$$I = \frac{C S_{01} N_0}{1 + \sum_m Q_m' Y_m} \quad (2-4b)$$

where C is the proportionality constant relating I to the number density, N .¹⁰

In the absence of a bath gas, electronic quenching can only occur via collisions between $IF(B)$ and background gases. From Eq.(2-4b), the expression describing this process is

$$I_0 = \frac{C S_0 I N_0}{1 + Q_B' N_B} \quad (2-5)$$

where I_0 is the total fluorescence intensity in the absence of an added bath gas, and $Q_B' N_B$ is the sum of the first order quenching rates by the background gases. The latter rate was not measured since accurate background species concentrations could not be obtained in these experiments. However, Eq.(2-5) will aid in the development of subsequent steady-state kinetic expressions.

The addition of a bath gas may enhance electronic quenching caused by the background gases. Thus, Eq.(2-4b) becomes

$$I_m = \frac{C S_0 I N_0}{1 + Q_m' M + Q_B' N_B} \quad (2-6a)$$

where I_m is the total fluorescence intensity with an added bath gas, and M is the bath gas number density. Using Eq.(2-5) to express $S_0 I N_0$ in terms of I_0 , Eq.(2-6a) is rewritten as

$$(I_0/I_m) - 1 = Q_m' M / (1 + Q_B' N_B) \quad (2-6b)$$

The electronic quenching rate constant is obtained from the slope of the

plot of the relative intensities vs the bath gas number density assuming a constant N_B .*

2. Vibrational Relaxation

Figure 2-1 shows a generic representation of a spectrally resolved, cw fluorescence experiment. (The energy levels shown in Fig. 2-1 may represent either vibrational or rotational states. We will only consider vibrational levels for this discussion.) In this figure, the vibrational level, v_i , is initially prepared with a cw excitation source. A subsequent collision with a bath gas redistributes the population from this "parent" level to other vibrational levels, $v_i \pm 1$. The spectrally resolved fluorescence spectrum shows the appearance of collisionally populated "satellite" bands due to the vibrational redistribution. Vibrational energy transfer is quantitatively analyzed by monitoring the population evolutions of the parent and satellite bands while changing the bath gas concentration. The expression for obtaining the total transfer rate constant, k_v , is developed first, followed by the derivation of the expression for determining the state-to-state rate coefficients, $k(v_i, v_f)$.

Assuming single collision conditions (i.e., the radiative rate equals the collision frequency), the second term in the numerator of Eq.(2-3b) can be eliminated. This approximation allows vibrational relaxation to

* For $M=0$, the y-intercept of Eq.(2-6b) is zero. Thus, no information on quenching by the background gases can be obtained in steady-state experiments unless separate experiments are performed to determine the quenching effects of these gases. An estimate of the quantity $Q_B N_B$ was obtained from the time resolved quenching experiments.

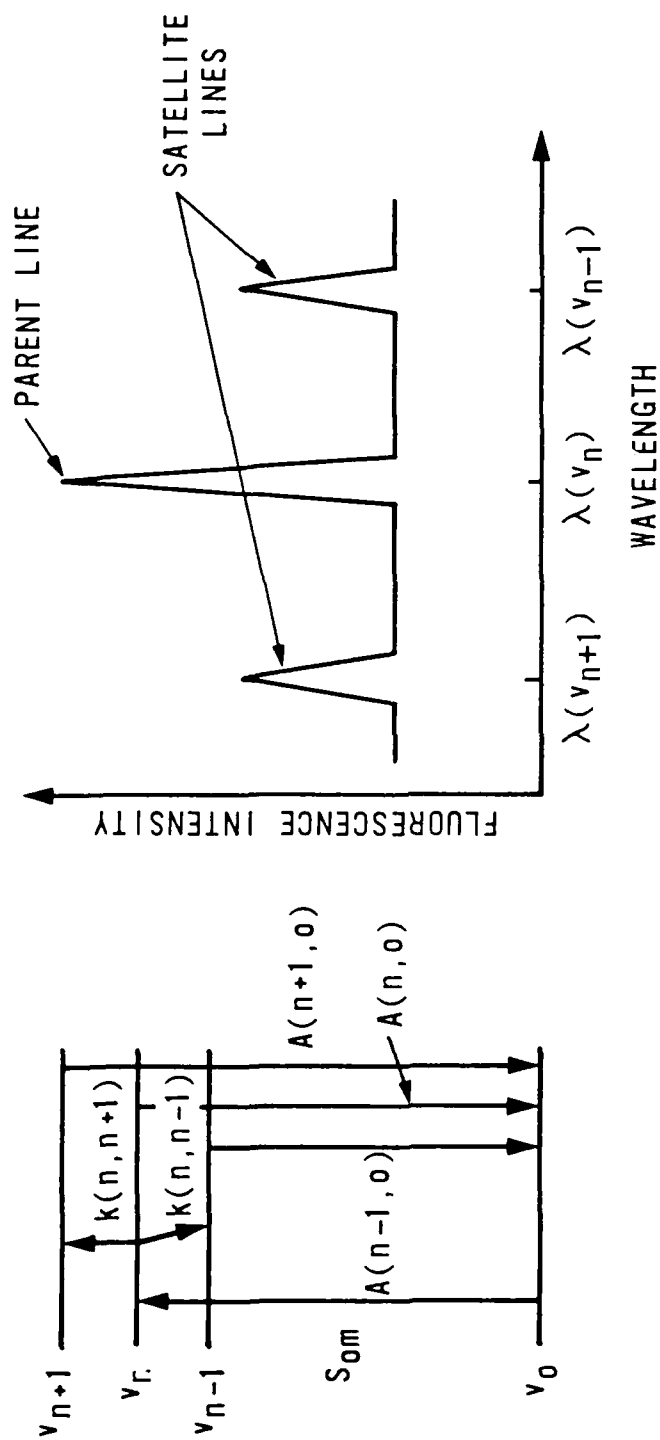


Figure 2-1. Spectrally resolved cw laser fluorescence emission showing the appearance of satellite lines due to collision induced vibrational energy transfer.

proceed only from the initially prepared state, v_i , to other vibrational levels, v_f , where repopulation of the initial level is excluded. The population removal from v_i to all other states in a collision with a single species, M , is described by Eq.(2-7a).

$$N(v_i) = \frac{S_{0i}'N_0}{1 + (Q_m' + k_v')M + R_B'N_B} \quad (2-7a)$$

where $k_v' = \sum_f k_{if}'$, $N_i = N(v_i)$, and $R_B' = (Q_B' + k_B')$. (Vibrational relaxation by the background gases must now be explicitly included, where k_B is the vibrational energy transfer rate constant since this process also contributes to the depletion of v_i .) Eliminating the pump term, $S_{0i}'N_0$, using Eq.(2-4a), the expression for determining the total transfer rate coefficient, k_v' , is given in Eq.(2-7b).

$$[N/N(v_i) - 1] = k_v'M/[1 + Q_m'M + R_B'N_B] \quad (2-7b)$$

In order to determine the state-to-state rate coefficients, $k(v_i, v_f)$, the relationship between the initially populated level, v_i , and the collisionally populated vibrational state, v_f , which is populated by collisions from v_i must be considered. Redefining terms in Eq.(2-3b), we now let i represent the collisionally populated state and f the initial level (i.e., let $N_i = N(v_f)$, $N_f = N(v_i)$, and $k_{fi} = k(v_i, v_f)$). Since we are assuming single collision conditions, the sum over f in the second term of the numerator in Eq.(2-3b) reduces to a single term. Also, the first term in the numerator of Eq. (2-3b) can be eliminated since the state v_f is not directly pumped by the laser. Thus, the steady-state population evolution of the collisionally populated state, v_f , is given by Eq.(2-8a).

$$N(v_f) = \frac{k(v_i, v_f)' N(v_i)M}{1 + R_B' N_B + (Q_m' + k_v')M} \quad (2-8a)$$

where k_v' is now the total removal rate coefficient from v_f . Rearranging Eq.(2-4a), the expression for obtaining the state-to-state vibrational transfer rate constant is

$$N(v_f)/N(v_i) = k(v_i, v_f)' M/[1 + R_B' N_B + (Q_m' + k_v')M] \quad (2-8b)$$

Equation (2-8b) can be used to determine both single and multiquantum state-to state vibrational transfer rate constants. The collisionally populated vibrational level, v_f , is generally defined as $v_f = v_i \pm n$ ($n = 1, 2, 3, \dots$).

Equations (2-7b) and (2-8b) give the prescription for determining the total vibrational removal rate constant and the state-to-state rate coefficients, respectively. These rate constants are obtained from the slope of the plots of the relative vibrational state populations vs bath gas number density where, for example, $k_v = k_v'/\tau_R$. However, the relative band intensities are the experimentally measured quantities. The band intensities must be converted to vibrational state populations for extracting the rate constants. This procedure is discussed in Chapter IV.

In practice, it is quite difficult to maintain single collision conditions when studying vibrational relaxation. For sufficiently high bath gas pressures, one must consider back-transfer in which secondary collisions repopulate the initially excited level from all other levels populated by the first collision. The method for obtaining these back-transfer corrections is detailed in Appendix C.

TABLE 3-1. Wavelength ranges for various dyes used in pumping IF(B) vibrational states from IF(X; $v''=0$).

DYE	WAVELENGTH REGION (nm)	PUMP TRANSITIONS
Coumarin 500	480-510	$v''=0$ to $v'=3$ and 4
Coumarin 480	460-510	$v''=0$ to $v'=3-6$
Coumarin 460	440-490	$v''=0$ to $v'=6-9$

the wavelength of the dye laser to a suitable absorption line of the B \rightarrow X system with the appropriate dyes listed in Table 3-1. The dye laser produced pulses approximately 7 ns in duration (FWHM) with typical energies of 0.4 to 2.0 mJ/pulse at a 10 Hz repetition rate. The linewidth of the dye laser was 0.4 cm^{-1} as measured with a Fabry-Perot spectrum analyzer.

Two arms integral to the fluorescence cell defined the laser axis as shown in Fig.3-2. These arms were 23 cm long and welded in the center and perpendicular to the plane of the cross. Each arm contained a Brewster angled window and a set of five internal light baffles made of brass. These baffles, which were conical and had a central hole 0.5 cm in diameter, minimized scattered laser light from reaching the interior of the cell. The dye laser output was steered into the baffled fluorescence cell with three internally reflecting prisms. The three mm diameter dye laser beam was focused to approximately one mm in diameter onto the center of the cell with a one meter focal length lens. The partially reflecting surfaces of the prisms and the lens resulted in a 35 percent loss in beam intensity with an additional 3 percent loss at the Brewster angled windows.

require high temperature bakeout.

After following the standard outgassing and helium leak testing procedures, the ultimate pressure in the isolated cell was 5×10^{-4} Torr with a 3×10^{-4} Torr hr^{-1} leak rate. The pressures in the cell were sampled in two locations to determine the uniformity of the gas distribution. The pressures were measured with MKS 310 monel capacitance manometers (10^{-3} - 10 Torr and 10^{-5} - 1 Torr heads).

Usable $\text{IF}(\text{B} \rightarrow \text{X})$ fluorescence signals were only obtained by choking the gas flow with a gate valve. (This was a consequence of the inefficient $\text{IF}(\text{X})$ production scheme.) Under base pressure conditions (i.e., no added bath gas), the average number densities of the various species in the cell were estimated as follows: $[\text{IF}(\text{B})] = 1.0 \times 10^{12}$ molecules cm^{-3} , $[\text{IF}(\text{X})] = 3.3 \times 10^{13}$ molecules cm^{-3} , $[\text{F}_2] = 4.0 \times 10^{14}$ molecules cm^{-3} , $[\text{I}_2] = 3.1 \times 10^{13}$ molecules cm^{-3} , and $[\text{He}] = 6.0 \times 10^{15}$ atoms cm^{-3} . The details of these calculations are shown in Appendix F.

3. Excitation Source

Tunable radiation from a Quanta Ray Nd:YAG pumped dye laser selectively populated ro-vibrational levels in the B state of IF. The 1064 nm radiation from the Q-switched Nd:YAG laser (DCR-1A) was frequency tripled to 355 nm using KD^*P crystals (HG-1 Harmonic Generator). The fundamental and first harmonic (532 nm) beams were subsequently separated with prisms (PHS-1 Harmonic Separator), allowing only the third harmonic to enter the dye laser head (PDL-1). Dye laser output was achieved by side pumping both the oscillator and the amplifier with the 355 nm radiation. Various ro-vibrational levels in $\text{IF}(\text{B})$ were accessed by tuning

capacitance manometer and ranged from 14 to 25 Torr.

Fluorine was injected into the cell through a 1.3 cm diameter nozzle. The F_2/He flow rates were controlled with a metering valve and monitored with a Matheson 8116 linear mass flow meter. Flow rates from 0.9 to 1.9 SCCM were utilized in the present work. An excess of F_2 was maintained so that the iodine partial pressure determined the upper limit of the $IF(X)$ concentration.

The bath gas ($IF(B)$ collision partner) was metered into the cell through a pyrex rake, 9 cm long and 1.3 cm in diameter. The rake had thirty 1 mm holes spaced equally along its length and was positioned so the bath gas entered the cell transverse to the flow direction. Research grade He, Ne, Ar, Kr, Xe, N_2 , F_2 , and O_2 were used as the bath gases in the energy transfer studies.

The gas flow exited the system through a liquid nitrogen cryotrap to prevent I_2 , IF , and IF_5 contamination in the vacuum pumps. The flow system was evacuated by a 5.1 cm diameter, 150 l-s^{-1} diffusion pump, backed by a two-stage rotary pump (Welch 1402). (The diffusion pump provided a constant gas flow at low pressures since the pumping speed of the rotary vacuum pump was nonlinear below a total pressure of about 0.10 Torr.) The bath gas and helium carrier gas lines were isolated from the fluorescence cell and iodine reservoir, respectively, when not in use and separately evacuated with a forepump.

The entire interior of the fluorescence cell was coated with 3M-101-C10 Nextel velvet black paint. This paint provided an extremely flat black finish which reduced scattered laser light and did not

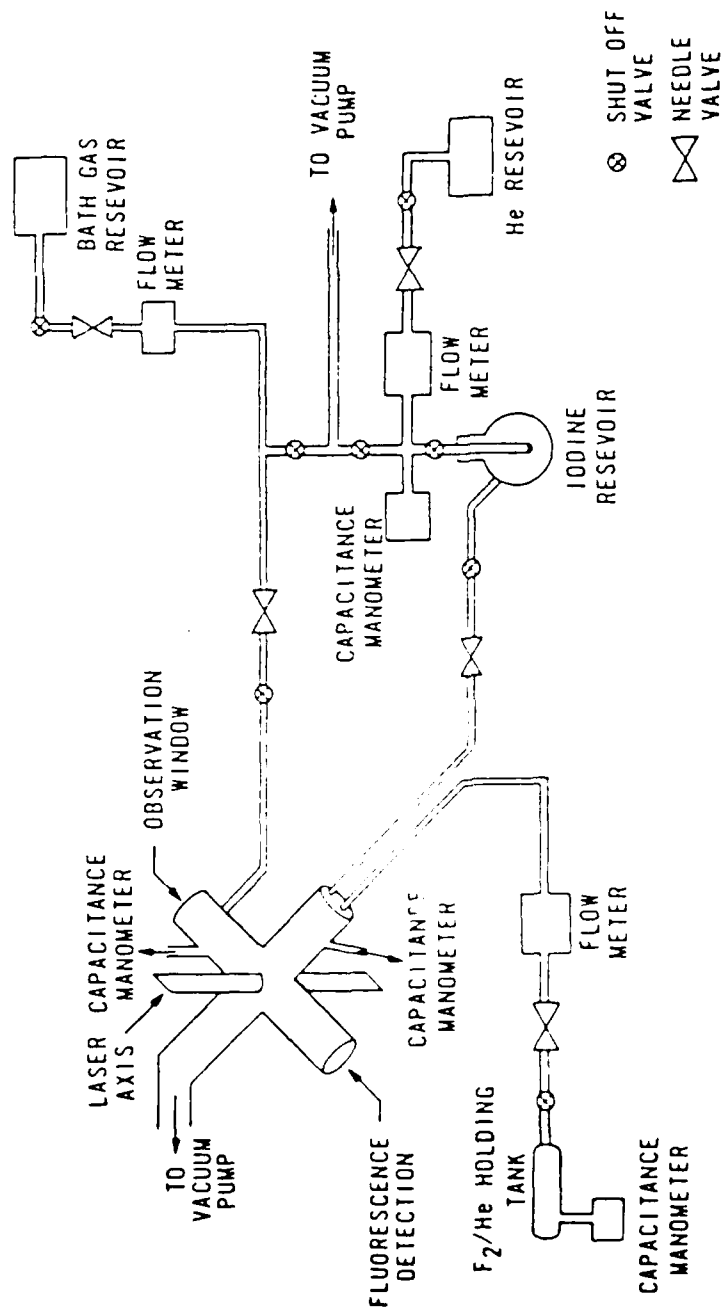


Figure 3-1. Schematic diagram of the low pressure flow system explicitly showing the gas delivery network.

IF rapidly forms IF₅ on the walls of the containment vessel via a heterogeneous reaction mechanism.³⁵ A flow system is, therefore, necessary to minimize IF₅ formation and maintain a sufficient IF concentration. IF₅ formation cannot be completely arrested because, even in a fast flow system, IF lasts for only a few msec.³⁵

2. Flow System Design

Figure 3-1 shows a schematic diagram of the flow system. The flow system was constructed with stainless steel and pyrex glass materials to accommodate the desired pressures through diffusion pumping. The fluorescence cell, which was an integral part of the flow system, provided the region where all kinetic processes were observed. The cell was constructed from a stainless steel cross, 10.2 cm in diameter and 25.4 cm in length (arm-to-arm).

The reactants were mixed approximately 8 cm from the center of the cell. Iodine was introduced by passing metered amounts of helium carrier gas (99.998% pure) over a reservoir of room temperature I₂ crystals. (The I₂ crystals were distilled before use to eliminate impurities.) The I₂/He flow was subsequently controlled with a metering valve placed at the entrance of the fluorescence cell and injected into the cell through a rake nozzle. The tee-shaped nozzle consisted of a 1.3 cm diameter pyrex tube and a 0.6 cm diameter rake. The rake was 2.5 cm long and contained four 1 mm diameter holes spaced equally along its length. The mass flow rate of the helium carrier gas typically ranged between 0.8 and 1.2 SCCM as measured with a Matheson 610 rotometer. Helium pressures in the iodine reservoir were monitored with an MKS 310

III. EXPERIMENTAL

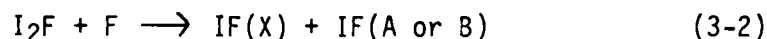
A. Introduction

Energy transfer in IF(B) was examined using LIF in a chemically reactive flow system. The experimental system is divided into four basic elements: (a) a flow system for IF production, (b) an excitation source, (c) a fluorescence detection system, and (d) a data processing system. The details of these elements along with the chemical reactions which were used to produce IF are discussed in this chapter.

B. Time Resolved Studies

1. IF Production

Ground state, $X^1\Sigma(0^+)$, IF molecules were produced via a bimolecular reaction of dilute fluorine (10% in He) and iodine. The accepted mechanism for this reaction is described below.^{32,33}



where k_1 is $(1.9 \pm 0.2) \times 10^{-15} \text{ cm}^3 \text{ molecule}^{-1} \text{ s}^{-1}$ at room temperature.³⁴ (This slow rate constant indicates that only about 5 in 10^4 $I_2 - F_2$ encounters have sufficient energy to react.³⁴) A subsequent encounter between the fluorine atom and I_2F results in IF formation. This reaction is exoergic by $64 \text{ kcal mole}^{-1}$ which is sufficient to populate the A or B state of IF. Although the $I_2 + F_2$ reaction is very inefficient, it does provide a convenient method for producing ground state IF molecules.

from n to $n-1$. Since the ratio of ω_{ex_e} in $IF(B)$ is less than 0.01, the low lying levels of $IF(B)$ will be harmonic to a good approximation. The restriction implied by Eq.(E-2a) is more difficult to assess. It is questionable whether this assumption is valid, a priori, since vibrational relaxation in many molecular systems do not follow this rule. However, this study attempted to show whether such a vibrational scaling relationship exists in $IF(B)$.

Since the analytic solution is strictly applicable to an oscillator with an infinite number of energy levels, it cannot model the fact that $IF(B)$ predissociates at $v'=9$. The levels pumped in this experiment, however, are well below $v'=9$; and it is unlikely that many molecules will collisionally ladder climb to the point where they predissociate.

If the lifetimes of the various vibrational levels in $IF(B)$ were identical, then the analytic solution could be multiplied by a factor $e^{-t/\tau}$ to account for radiative decay and electronic quenching (see Appendix E). Unfortunately, the lifetimes vary over a range from $6.7 \mu s$ to $8.6 \mu s$.¹² Therefore, we attempted to account for the variation in the lifetimes by using a value averaged over the lifetime of the level pumped and the level monitored.

Equation (E-5) was used to fit the data such as those shown in Figs. D-1b and D-2. This model gives the first order vibrational relaxation rates which were subsequently plotted vs the bath gas concentration to determine the rate constants. Several tests were made on the Montroll-Shuler model to determine its applicability to $IF(B)$. These tests are discussed in Chapter IV.

An alternate approach developed by Montroll and Shuler^{30,31} was used to determine the vibrational transfer rate constants. Briefly, Montroll and Shuler analytically solved the rate expression describing the vibrational population evolution of a system of harmonic oscillators immersed in an inert heat bath. (See Appendix E for a more complete discussion.) Assuming an initial δ -function distribution and that the rate constants are scaled according to Landau and Teller^{2d}, the solution to this problem was determined as

$$X_n(t) = \frac{(1 - e^{-\theta}) e^{m\theta}}{(e^{-\tau} - e^{-\theta})} \left(\frac{e^{-\tau} - 1}{e^{-\tau} - e^{-\theta}} \right)^{m+n} F(-n, -m, 1; U^2) \quad (E-5)$$

where $\theta = h\nu/kT$, ν is the fundamental frequency of the oscillator, $X_n(t)$ is the population in vibrational state n at time t , $U = \text{SINH}(\theta/2)/\text{SINH}(\tau/2)$, $\tau = Kt(1 - e^{-\theta})$, F is the hypergeometric function, and K is the vibrational transfer rate constant. Since several simplifying assumptions were made in order to obtain a closed form solution, these assumptions must be studied to determine the error they introduce into the analysis.

The most important assumptions are that the energy levels are strictly harmonic and that the various rates are interrelated as given by Eqs.(E-2) which are reproduced below.

$$K(n, n-1) = k(n, n-1)M = nk(1, 0)M \quad (E-2a)$$

$$K(n-1, n) = ne^{-\theta} k(1, 0)M \quad (E-2b)$$

where $k(1, 0)$ is the second order vibrational transfer rate constant from $n = 1$ to $n = 0$, and $K(n, n-1)$ is the first order vibrational transfer rate

Equations (2-12) are then solved using the standard techniques yielding

$$N(v)_t = N(v)_{t=0} e^{-\alpha t} \quad (2-13a)$$

$$N(v+1)_t = \frac{\beta}{\gamma - \alpha} (e^{-\alpha t} - e^{-\gamma t}) \quad (2-13b)$$

where $\alpha = k_v M + I'(v)$, $\beta = k(v, v+1) M N(v)_{t=0}$, and $\gamma = k_{v+1} M + I'(v+1)$.

It is quite apparent that a closed form solution to this problem would be extremely difficult to interpret. The interpretation problem occurs because all the vibrational levels are coupled due to both sequential upward and downward relaxation. The time dependence of the population of a vibrational level depends on the rate at which the nearest neighbor levels are populated and depleted. Thus, the individual rate constants appearing in Eqs.(2-13) cannot be uniquely determined in this simple analysis. (The qualitative features of spectrally resolved, time resolved vibrational relaxation are discussed in Appendix D using simplifying assumptions in the above analysis.)

As seen in Appendix D, the straightforward approach to analyzing the vibrational relaxation data will not be amenable to an analytic solution unless some simplifying assumptions are made. However, one could treat the problem numerically by assuming a set of rate constants and then integrating the rate equations on a computer. A systematic variation of the rates to yield the best fit will yield the desired numbers. Programs capable of treating the problem in this fashion do exist. Unfortunately, this type of analysis suffers from several defects, not the least of which is the excessive computer time required.²⁹ Thus, this fitting procedure will not be used in the analysis of the time resolved data.

levels. (For this discussion, we are only considering V-T collisions.)

As a first approach to analyzing this problem, consider the situation where the vibrational spacing, ΔG_v , is greater than 200 cm^{-1} ($\Delta G_v > kT$ at $T = 300 \text{ K}$). Under these conditions, Ehrenfest's adiabatic principle (see Appendix B) implies that nearest neighbor transitions are most probable (i.e., the probability of multiquantum vibrational transfer is negligible). The rate equations describing the time development of these vibrational levels are given below.

$$\begin{aligned} dN(v)/dt = & -k_v M N(v) + k(v+1, v) M N(v+1) \\ & + k(v-1, v) M N(v-1) - \bar{\Gamma}(v) N(v) \end{aligned} \quad (2-12a)$$

$$\begin{aligned} dN(v+1)/dt = & -k_{v+1} M N(v+1) + k(v, v+1) M N(v) \\ & + k(v+2, v+1) M N(v+2) - \bar{\Gamma}(v+1) N(v+1) \end{aligned} \quad (2-12b)$$

where $k_v = k(v, v+1) + k(v, v-1)$, $k_{v+1} = k(v+1, v) + k(v+1, v+2)$, and $\bar{\Gamma}(v)$ is the sum of the first order radiative and quenching rate coefficients. The problem can be further simplified if all the upward rates are negligible. This situation occurs when $\Delta G_v \gg kT$ as in the case of HF where $\Delta G_v \sim 4138 \text{ cm}^{-1}$.²⁸ In HF, detailed balance shows that the ratio of the upward rate constant to the downward rate constant is $\sim 2 \times 10^{-9}$ at $T = 300 \text{ K}$. Therefore, the upward rates are truly negligible. But, in the case of IF(B), the upward rates are ~ 20 percent of the downward rates where $\Delta G_v \sim 300 \text{ cm}^{-1}$. Therefore, the upward rates must be included in the analysis.

At low bath gas densities, where multiple collisions are negligible, one may assume that the collisional population of $N(v \pm 2)$ is small.

QUANTUM STATE

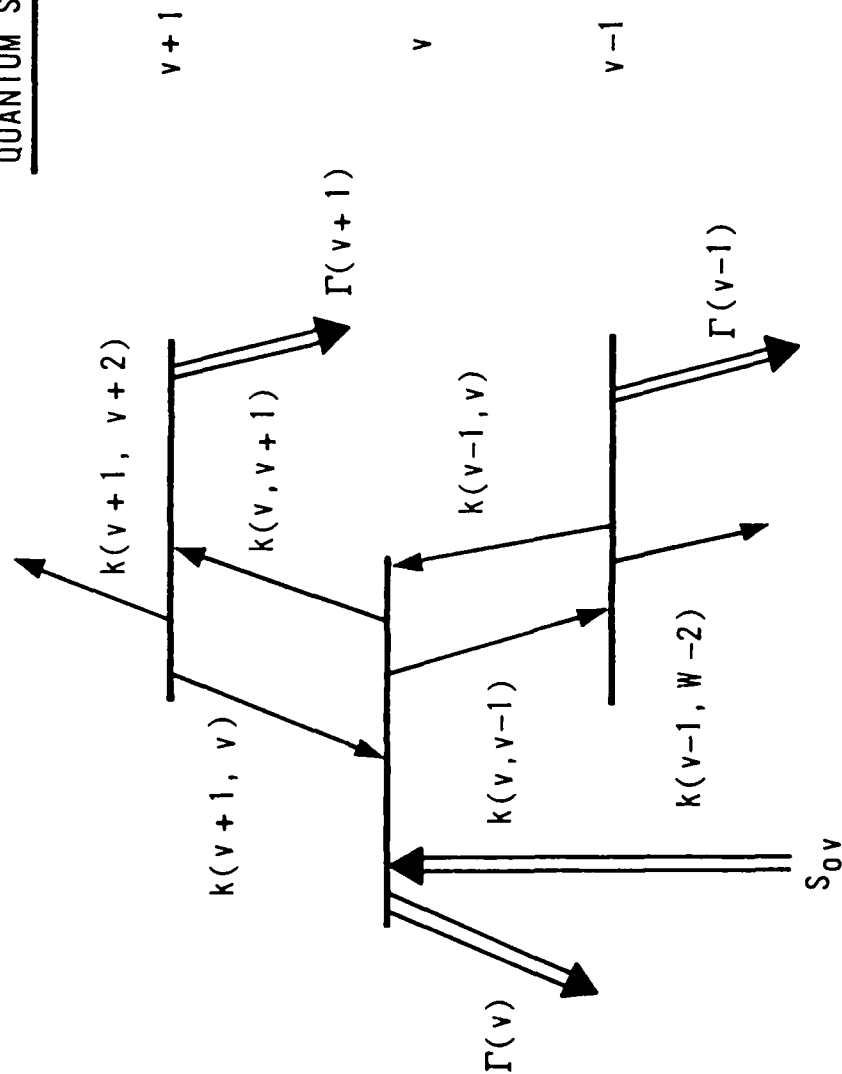


Figure 2-2. Energy level diagram showing the various rate processes occurring in the vicinity of the initially populated vibrational level, v .

The electronic quenching rate constant is obtained by first determining the decay rate, Γ , at a given bath gas pressure. Experimentally, Γ is obtained by directly integrating Eq.(2-11a) yielding

$$\ln (I/I_{t=0}) = -\Gamma t \quad (2-11b)$$

where I is the spectrally unresolved fluorescence intensity, which is proportional to the excited state number density.¹⁰ The electronic quenching rate constant, Q_m , is subsequently obtained from the slope of the plot of Γ vs M :

$$\Gamma = (\tau_R)^{-1} + Q_m M \quad (2-11c)$$

where $(\tau_R)^{-1} = \sum_i A_{i\ell}$. This procedure is referred to as a Stern-Volmer analysis.

2. Vibrational Relaxation

Vibrational relaxation is examined by spectrally resolving the fluorescence and monitoring the population evolution of vibrational levels in real time. The most straightforward method of analyzing the data is to write down a series of rate equations which includes all the relevant kinetic processes describing the evolution of the vibrational manifold. For simplicity, however, consider the three level system shown in Fig.2-2 in which a highly non-equilibrium distribution is produced in the v^{th} vibrational level via pulsed excitation. At time $t = 0$, when the excitation pulse has shut off, all the optically excited molecules reside in this vibrational level. These molecules are then subject to collisions with a foreign gas which induce transitions from v to other vibrational

in this study. Back-transfer corrections to Eq. (2-9b) are derived in Appendix C.

D. Time-Dependent Analysis

In time resolved experiments, the kinetic and radiative processes are observed subsequent to initial excitation of a specific quantum level. Therefore, the pump term in Eq.(2-1) is eliminated if the initial excitation pulse width (temporal FWHM) is sufficiently narrow so it can be approximated as a δ -function. This condition is fulfilled in these experiments, and the master rate equation is re-written as

$$\frac{dN_i}{dt} = -\left(\sum_{\ell} A_{i\ell} + \sum_m Q_{im} Y_m + \sum_{fm} k_{ifm} Y_m\right)N_i + \sum_{fm} k_{fim} N_i Y_m \quad (2-10)$$

Equation (2-10) can be directly integrated to yield expressions to extract energy transfer rate constants from the experimental data.

1. Electronic Quenching

Electronic quenching is examined by monitoring the decay of total fluorescence in real time. Quenching is characterized by a shortening of the radiative lifetime of the molecule, signifying a population loss through non-radiative decay. Therefore,

$$\frac{dN_i}{dt} = -\sum_{\ell} A_{i\ell} N_i - Q_{im} N_i M = -\Gamma N_i \quad (2-11a)$$

where quenching by a single species, M, is being considered and Γ is the total, first order fluorescence decay rate constant.

3. Rotational Relaxation

The emission spectra obtained in the vibrational transfer experiments also reveal information on rotational energy transfer only if sufficient resolution exists so that emission from the initially prepared rotational level, J_i , is observable. If this condition exists, the total population removal from J_i is examined by monitoring its population vs bath gas number density. The total rotational removal rate constant within an initially excited vibrational level, v_i , is obtained by applying the steady-state approximation to J_i . Therefore, we obtain from Eq.(2-3b) by assuming single collision conditions, the expression below.

$$N(J) = S_{0i}' N_0 / [(1 + Q_m' + k_v' + k_r')M + R_B' N_B] \quad (2-9a)$$

where $k_{if}' = \sum_f [(k_{if})_v' + (k_{if})_r'] = k_v' + k_r'$ from Eq.(2-3b). The effects of vibrational relaxation were included in Eq.(2-9a) since this process also represents a loss in population from J_i . Combining Eqs.(2-9a) and (2-7a), the total rotational removal rate constant, k_r , is obtained via Eq.(2-9b).

$$[N(v_i)/N(J) - 1] = k_r' M / [1 + (k_v' + Q_m')M + R_B' N_B] \quad (2-9b)$$

After converting the experimentally determined relative band intensities to relative populations (to be described later), the total rotational removal rate constant, k_r , is obtained from the slope of the plot of $N(v_i)/N(J_i)$ vs M , where $k_r = k_r' / \tau_R$. Expressions describing state-to-state rotational transfer can also be obtained. This derivation is not included since state-to-state rotational transfer data were not obtained

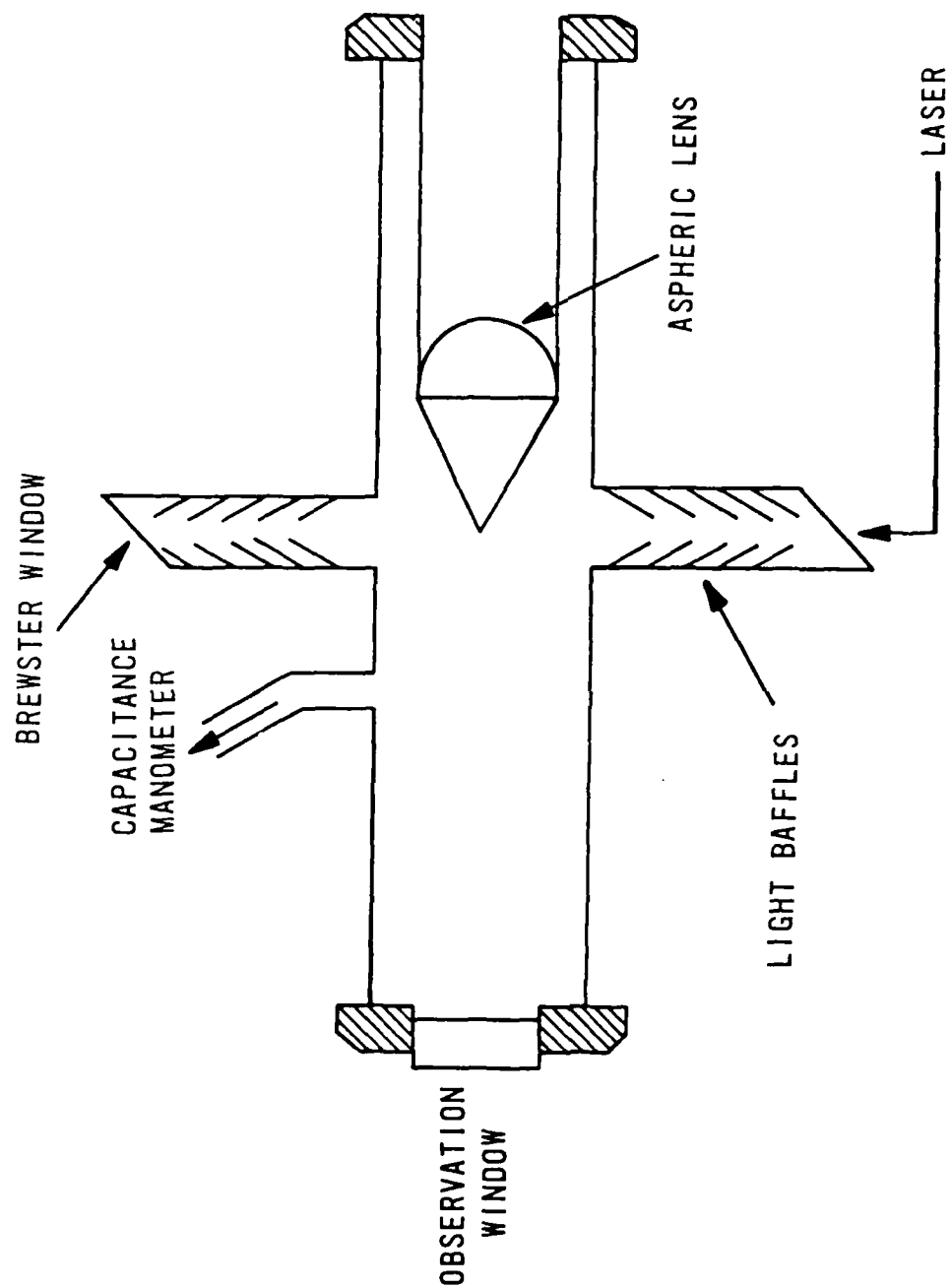


Figure 3-2. Cross sectional view of the fluorescence cell showing the two fluorescence viewing ports with the light collection optics and the laser axes. The gas flow is directed perpendicular to the plane of the page.

4. Laser Excitation Spectra

Laser excitation spectra were recorded to identify the initially prepared quantum states. These spectra were obtained by scanning the wavelength of the dye laser across absorption lines for a given $B \rightarrow X$ transition. The total fluorescence intensity, which tracked the absorption spectrum, was monitored as a function of laser wavelength. A block diagram of the apparatus is shown in Fig.3-3. High resolution spectra were obtained using the Quanta-Ray dye laser. The FWHM linewidth of this laser (0.4 cm^{-1}) was sufficiently narrow so that individual $IF(B)$ rotational levels could be excited. Low resolution spectra were also obtained using a Molelectron, SP-10, N_2 pumped dye laser. The linewidth of the dye laser was 0.5 nm (FWHM) which resulted in rotationally unresolved, vibrational excitation spectra.

Total $B \rightarrow X$ emission was detected by observing the fluorescence through the observation window of the cell. The fluorescence was focused onto the cathode of an RCA C31034A photomultiplier tube (PMT) with a 5 cm focal length lens. The output of the PMT was then amplified (HP 462A pre-amp) and fed into a 50Ω signal input of a PAR 164 Gated Integrator on a boxcar averager (PAR 162). The fluorescence signals were passed through a $0.5 \mu\text{s}$ gate and integrated for $10 \mu\text{s}$. A record of the excitation spectra was subsequently obtained by driving the Y input of a strip-chart recorder (HP-71008M) with the output of the boxcar averager. The results and analyses of the excitation spectra are discussed in Appendix G.

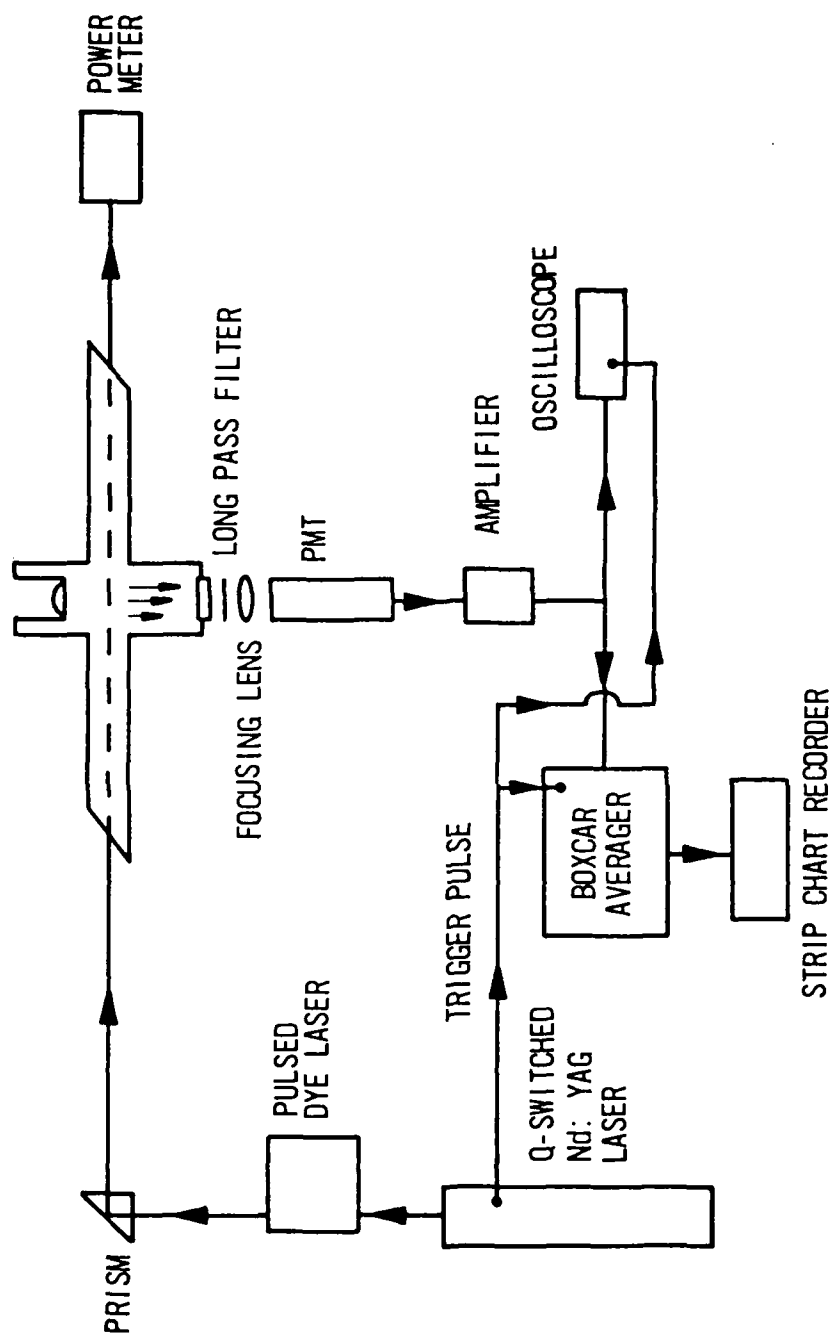


Figure 3-3. Block diagram of the apparatus used for recording laser excitation spectra.

5. Electronic Quenching Measurements

Electronic quenching was examined by monitoring the decay of total IF(B) fluorescence as a function of bath gas pressure for various initially excited levels. The spectrally unresolved fluorescence was collimated by an aspheric lens (23 mm focal length) and focused onto the cathode of an RCA C31034A PMT with a 5 cm focal length lens. The aspheric lens was sealed in the chamber so the focal plane was located approximately at the center of the cell. Long pass filters were inserted between the focusing lens and the PMT to prevent detection of scattered laser light. (These filters typically transmitted 90 percent at 50 nm above the wavelength "cut on." The extinction ratio at wavelengths below the "cut on" was $\sim 10^5$.) The amplified raw signals from the PMT were then processed with the system shown in Fig.3-4.

Individual fluorescence decay curves were digitized by a fast transient recorder (Biomation 6500). The Biomation partitioned the information into 1024 channels with a 10 ns/channel resolution. The recorded decay curves were averaged over many laser shots using a hard wired data processor (Nicolet NIC-80). Typically, 700 to 2000 laser shots were required to achieve acceptable signal-to-noise ratios. The signal averaged decay curves were stored on a floppy disk (NIC 299 diskette storage unit) for use in subsequent data analysis. A record of these decay waveforms along with the logarithms were also recorded on an X-Y plotter (HP 7004B).

The Biomation was operated in a pretrigger mode to record information for determining decay curve baselines. The trigger source was

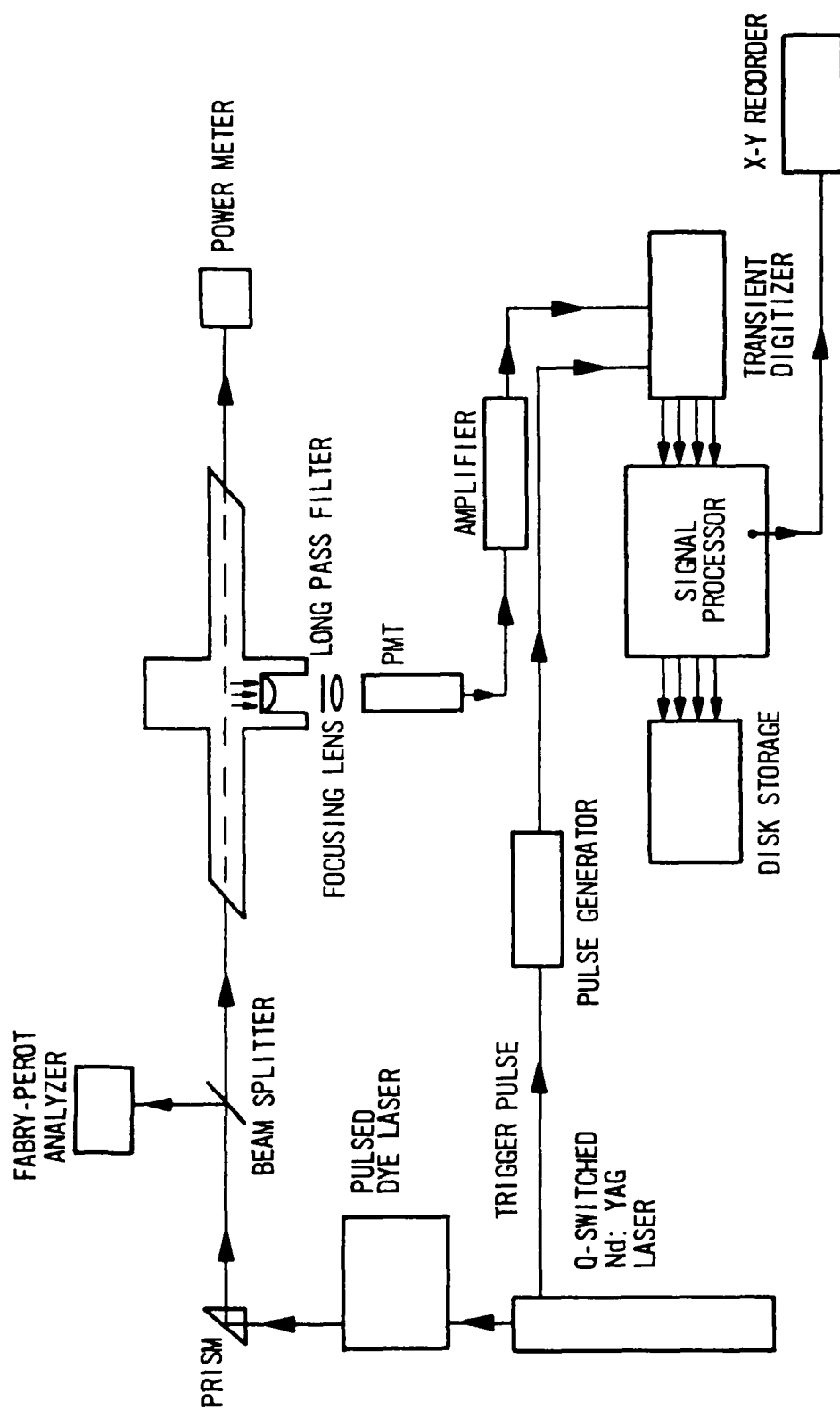


Figure 3-4. Block diagram of the apparatus used in the electronic quenching experiments.

Spectral resolution was achieved in the following way. Total IF(B) fluorescence was captured by an aspheric lens ($f/0.5$) and focused onto the slits of a 0.3 m scanning monochromator (McPherson 218) with a 30 cm focal length lens. Figure 3-5 shows a diagram of the apparatus. The aspheric lens was positioned so the focal plane (23 mm) was located at the approximate center of the fluorescence cell (Fig. 3-3). The fluorescence was dispersed with a grating blazed at 600 nm (1200 grooves/mm) and detected with an end on GaAs PMT (RCA C31034A-02). The PMT was housed in a chamber which was directly attached to the exit port of the monochromator. The chamber contained a 1.3 cm focal length lens to image the dispersed fluorescence onto the photocathode.

The amplified PMT output was signal averaged with the Biomation-Nicolet system described previously. Acceptable signal-to-noise ratios were obtained by averaging the signals for 1000-3000 laser shots. The monochromator slits were 6 mm in height and 700 μm in width which gave a 2.0 nm (FWHM) instrumental resolution. This resolution was adequate for observing the temporal history of individual vibrational states without band overlap.

Time resolved vibrational relaxation was studied as a function of both collision partner and initially excited vibrational level. The collisional dynamics following laser excitation of $v' = 3$ and $v' = 6$ were investigated with the noble gases, F_2 , and N_2 . Scaling of the vibrational energy transfer rates coefficients on the initially excited vibrational level was examined using helium as the bath gas for the levels $3 \leq v' \leq 8$.

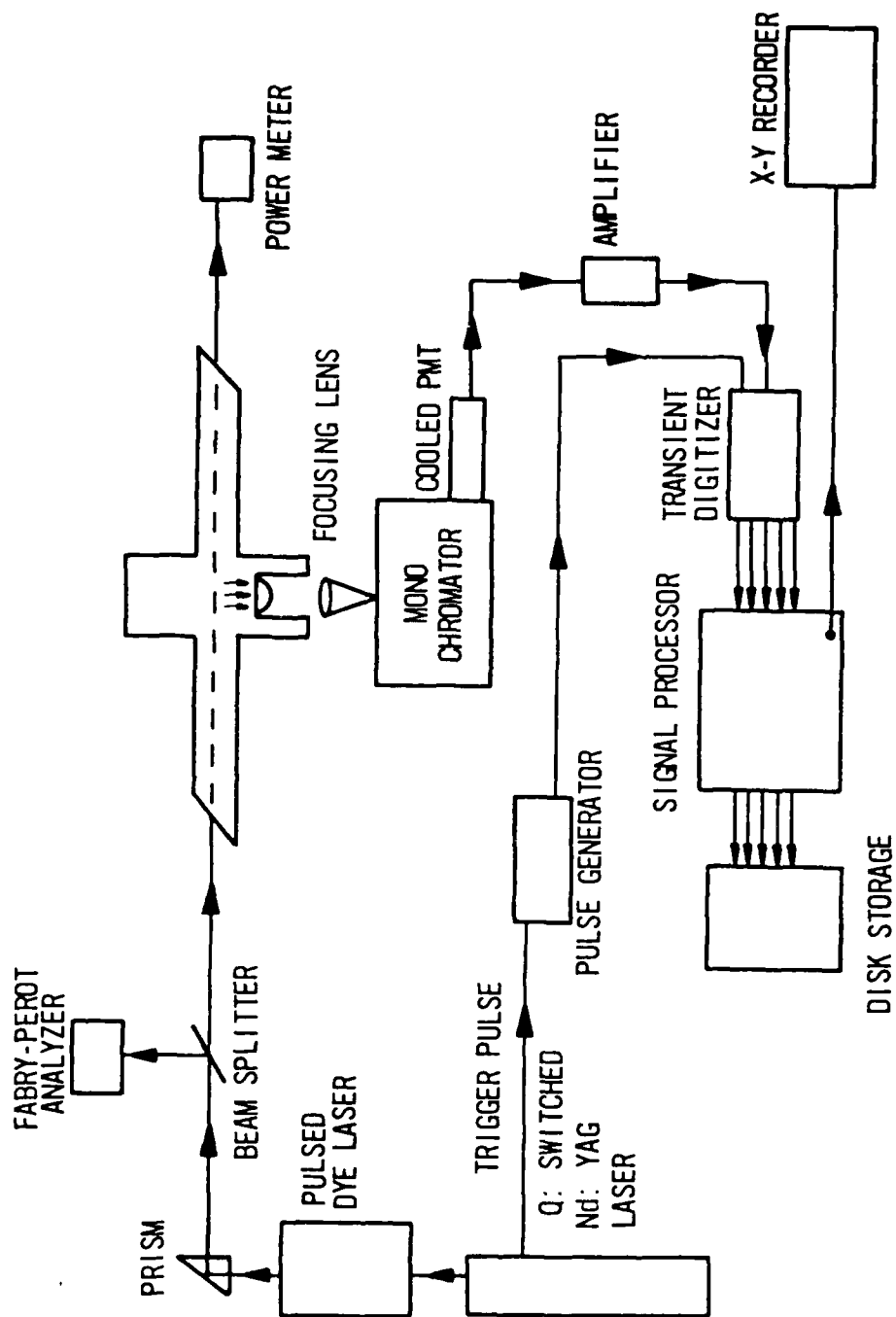


Figure 3-5. Block diagram of the apparatus used in the time resolved vibrational energy transfer experiments.

C. Steady-State Experiments

Improvements in both the flow system design and the IF production scheme were made to examine IF(B) energy transfer at base pressures which approximated collision-free conditions. This improved version attempted to eliminate a premature redistribution of the initial population in a given ro-vibrational state resulting from collisions between IF(B) molecules and residual gases (I₂, F₂, and He carrier gas)*.

1. IF Production

Ground state IF(X) molecules were produced in a reaction involving F(2P) atoms and molecular iodine:



This reaction proceeds at a gas kinetic rate with a coefficient of $(4.1 \pm 1.1) \times 10^{-10} \text{ cm}^3 \text{ molecule}^{-1}$.³⁵ Fluorine, F(2P), atoms (Boltzmann distribution at 300 K: ²P_{3/2}, 93 percent; ²P_{1/2}, 7 percent) were generated by passing metered amounts of F₂ (98 percent pure) through a microwave discharge (2.45 GHz, 70 W). The F₂ flow rate was monitored with a Matheson linear mass flowmeter and typically ranged from 20 to 37 SCCM.

The fluorine atoms were pumped from the 12 mm (O.D.) discharge tube into a thick-walled pyrex flow tube, 2.5 cm in diameter, as shown in Fig.3-6. The fluorine flow was subsequently channeled toward the fluorescence cell through a secondary tube, 1.3 cm in diameter, which

* See Appendix F

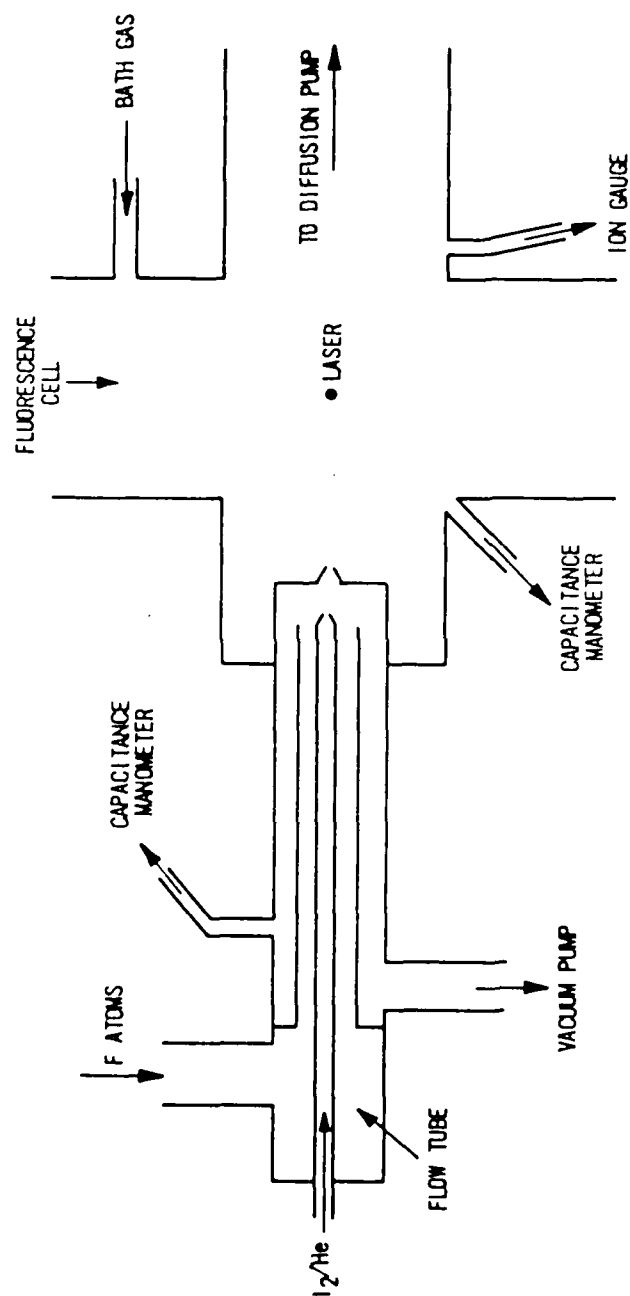


Figure 3-6. Cross sectional view of the differentially pumped flow system. The reactants are mixed in the flow tube at the left. The gas flow is forced toward the pinhole where low IF densities escape into the fluorescence cell.

was concentric with the flow tube. The flow tube was evacuated with a 150 CFM forepump, and the pressures were measured with an MKS monel capacitance manometer.

Molecular iodine was injected by passing a metered amount of helium carrier gas over a reservoir of room temperature I_2 crystals. The helium flows ranged from 14 to 28 SCCM which resulted in helium pressures in the iodine reservoir of 10 to 25 Torr, as measured with a Wallace and Tiernan pressure gauge. The I_2 /He flow entered the flow tube through an adjustable nozzle (0.64 cm in diameter with a 0.2 cm diameter orifice) that was placed through the secondary tube.

The optimum nozzle placement was obtained by adjusting the nozzle at various distances from a pinhole which separated the flow tube and the fluorescence cell. The maximum IF fluorescence signal, under non-optimum flow conditions, was observed when the nozzle was placed approximately six to seven mm from the pinhole. The F_2 flow was subsequently adjusted until the IF fluorescence reached a maximum. The probe laser was then tuned to an I_2 transition and, at the flow where the IF fluorescence was a maximum, minimal I_2 fluorescence was observed. The optimum reagent flows used in these experiments resulted in flow tube pressures between 0.1 and 0.2 Torr.

Under typical operating conditions, the F atom concentration was estimated as 2.2×10^{15} atoms cm^{-3} (assuming no wall losses and a 75 percent dissociation efficiency through microwave discharging.³⁶) The remaining gases in the flow tube were estimated as follows:

$[He] = 2.8 \times 10^{15}$ atoms cm^{-3} , $[I_2] = 7.5 \times 10^{13}$ molecules cm^{-3} , and

$[F_2] = 7.9 \times 10^{14}$ molecules cm^{-3} . Since excess F atom concentrations were used throughout these studies, the upper limit of the IF(X) number density was determined by the amount of I_2 present in the flow tube. Assuming that all the I_2 has reacted, the maximum IF(X) number density was estimated as 7.5×10^{13} molecules cm^{-3} .

2. Fluorescence Cell Design

The fluorescence cell was constructed from a 5.1 cm diameter, stainless steel cross and contained entrance and exit ports for the gas flow and two ports for fluorescence detection. The flow tube was inserted through one arm of the cross and positioned approximately four cm from the center of the cell. The flow tube and the fluorescence cell were interfaced with a pinhole through which IF molecules escaped into the fluorescence cell. The pinhole was conical in shape and had a 0.5 mm diameter hole which was drilled through a 0.32 cm thick stainless steel disk. The bath gas was metered into the cell in an arm perpendicular to the flow direction. The bath gases included research grade He, Ne, Ar, Kr, Xe, N_2 , and O_2 .

The gas flow exited the cell through a liquid nitrogen cryotrap to prevent I_2 , IF, and IF_5 contamination in the vacuum pumps. The cell was evacuated with a 5.1 cm diameter, 150 l-s^{-1} diffusion pump, backed by a two stage rotary pump (Welch 1402). The entire cell interior was coated with 3M-101-C10 Nextel Velvet black paint to reduce scattered laser light.

The cell pressures were sampled near the center of the cross as shown in Fig.3-6. After following the normal outgassing and helium leak

testing procedures, the ultimate cell pressure was 5×10^{-5} Torr as measured with a Varian ionization gauge. During the experiment, the cell pressures were monitored with a 10^{-5} to 1.0 Torr, monel capacitance manometer (MKS 310) and typically ranged between 2.5×10^{-3} and 5.0×10^{-3} Torr with no bath gas. The lower limit of the $\text{IF}(\text{X})$ number density in the cell was estimated as 4.0×10^{12} molecules cm^{-3} assuming that the ratio of the partial pressures of He to I_2 was the same as in the flow tube. The estimated residual background gases included 6×10^{13} atoms cm^{-3} of He and 6×10^{13} molecules cm^{-3} unreacted fluorine. In practice, I_2 ($\text{B} \rightarrow \text{X}$) fluorescence was observed when the laser was tuned to an appropriate I_2 transition. (The spectral purity of the dye laser described below allowed us to easily discriminate between $\text{I}_2(\text{B} \rightarrow \text{X})$ and $\text{IF}(\text{B} \rightarrow \text{X})$ emission.) The residual I_2 was present because of non-stoichiometric flow conditions.

3. Excitation Source

Single ro-vibrational states in $\text{IF}(\text{B})$ were populated with a single frequency, passively stabilized ring dye laser (Coherent CR-699) driven by a krypton ion laser (Coherent CR-3000K). The spectral purity of the dye laser was measured as less than 100 MHz (FWHM) with a Tropel 240 confocal interferometer. The dye laser wavelengths were determined to within 0.01 cm^{-1} with a Burleigh WM-20 wavemeter. The excitation lines were obtained by pumping Exciton coumarin 480 dye ($460 \text{ nm} \leq \lambda \leq 510 \text{ nm}$) and Exciton coumarin 515 dye ($477 \text{ nm} \leq \lambda \leq 548 \text{ nm}$). The excitation wavelengths were 496.03 nm and 517.07 nm which respectively populated the $(\nu', J') = (3, 19)$ and $(1, 22)$ ro-vibrational states in $\text{IF}(\text{B})$. Typical single frequency output from the ring laser was 100 mW and 40

mW for C480 and C515, respectively.

Electronic quenching and vibrational energy transfer were also studied using the flow system and IF production scheme for the time-resolved experiments. The excitation source was a Coherent CR-8 Ar⁺ laser which prepared the $(v', J') = (6, 72)$ ro-vibrational state in IF(B) at 476.5 nm. The laser was equipped with a temperature controlled, intracavity etalon which provided single frequency excitation with a linewidth of about 50 MHz (FWHM). Typical output power was 50 mW.

The dye laser output was steered by a series of prisms and mirrors into the fluorescence cell. The laser beam entered the cell through a Brewster angle window and passed through a series of light baffles to reduce scattered light from reaching the cell interior. (The design of the laser axis and the light baffles were the same as that used in the pulsed experiments.) The 0.75 mm diameter laser beam was focused onto the center of the fluorescence cell with a 1 m focal length lens. A 48 percent loss in laser power was measured as the beam entered the cell. These losses occurred on the surfaces of the mirrors and the Brewster angle windows. Minimal losses occurred on the prism surface and the lens since both elements had antireflection coatings.

4. Fluorescence Detection and Data Processing

Total fluorescence was captured by an aspheric lens (f/0.5) which was used to seal the cell in one arm in place of a window. The aspheric lens was positioned so that the focal plane (25 mm focal length) was approximately at the center of the cell. A schematic

diagram of the apparatus is shown in Fig.3-7. The fluorescence was focused onto the slits of a 0.3 m scanning monochromator (McPherson 218, 1200 lines mm^{-1} grating blazed at 600 nm) with a 30 cm focal length lens. The monochromator showed the best instrumental resolution of (0.25 nm (FWHM)) with optimum signal intensity using 80 μm slit widths when initially exciting $v' = 3$. A reduction in signal intensity occurred when populating $v' = 1$ from $v'' = 0$. This was attributed to lower laser power and a small Franck-Condon factor for absorption. Therefore, to increase the signal-to-noise ratio, 200 μm slit widths were used which resulted in a 0.6 nm instrumental resolution. For the $v' = 6$ experiments, good signal-to-noise ratios were obtained using 150 μm slit widths (0.45 nm instrumental resolution).

The dispersed fluorescence was detected with an end-on GaAs PMT (RCA C31034A-02) which was housed in a cooled chamber that was directly attached to the exit port of the monochromator. The chamber contained a 1.3 cm focal length lens to image the dispersed fluorescence onto the photocathode. The PMT was cooled to 253°K which resulted in a dark count of 13 s^{-1} using a 1400 volt photocathode bias.

The signals from the PMT were observed on a picoammeter and typically ranged between 10^{-8} and 10^{-9} amps. Since low incident radiation powers were detected, photon counting was necessary to observe the spectrally resolved fluorescence.

The output of the PMT drove an amplifier/discriminator (PAR 1121), and the signal was measured with a PAR 1112 photon counter. Typically, 0.5 to 1.0 s count times gave adequate signal-to-noise ratios which

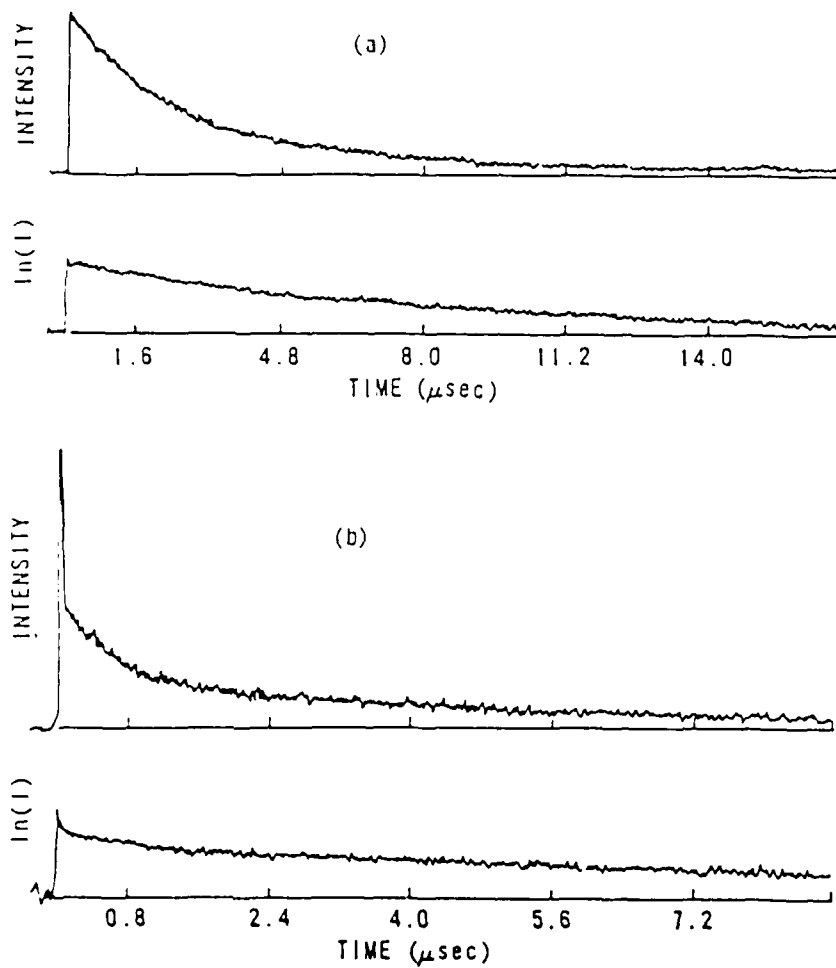


Figure 4-6. Total IF(B) fluorescence decay curves in the presence of O_2 : (a) $P(\text{O}_2) = 0.57$ Torr and (b) $P(\text{O}_2) = 2.2$ Torr.

increased the relative IF(B \rightarrow X) LIF signal.) The so called "negative" Stern-Volmer plots such as in Fig. 4-5b are thus indicative of I₂ quenching with I₂ being consumed as the bath gas pressure is increased. Therefore, Eq.(4-1) is rewritten as

$$\Gamma = \Gamma_R + Q_M[M] + Q_{I_2}[I_2] \quad (4-2)$$

Equation (4-2) can be used to estimate the I₂ quenching rate coefficient. At the previously defined baseline conditions, the Stern-Volmer plot intercepts ([M] = 0) typically yielded a decay rate, Γ_0 , of 1.7×10^5 s⁻¹ for $3 \leq v' \leq 7$. Subtracting the radiative rates from the Γ_0 rates for the respective initially pumped vibrational levels, the average residual intercept was 2.5×10^4 s⁻¹. An estimate of the I₂ quenching rate constant was obtained using $[I_2] = 6.0 \times 10^{13}$ molecules cm⁻³. (This is our best estimate of [I₂] in the chamber before any bath gas was added.) The estimated I₂ quenching rate coefficient, k_{I_2} , is thus 3.9×10^{-10} cm³ molecule⁻¹ s⁻¹.

2. Quenching by O₂

While quenching with the noble gases, N₂, and F₂ all revealed single exponential fluorescence decay curves, a difference was observed in the decay kinetics with O₂ as the bath gas. Figure 4-6 shows results for the decay of IF(B) fluorescence following excitation of $v' = 4$. A rapid initial decay was observed, followed after a few μ s by a slower decay. Analysis of these decay curves showed that the decay behavior can be approximated by the sum of two exponentials. Thus, a standard Stern-Volmer analysis was made by fitting a single exponential to the initial

In order to interpret these observations, we consider the following. According to Eq.(2-11c), the plot of Γ vs $[M]$ should extrapolate at zero added bath gas pressure to give the collision free radiative decay rate, Γ_R , of the initially prepared vibrational level. However, the observed Stern-Volmer plot intercepts, Γ_0 , were typically 30 percent faster than the known radiative decay rates (e.g., for $v'=6$, $\Gamma_R = 1.22 \times 10^5 \text{ s}^{-1}$ while we find $\Gamma_0 = 1.63 \times 10^5 \text{ s}^{-1}$). This result shows the quenching effects of residual I_2 and F_2 and, possibly, self-quenching by $IF(X)$.

In order to assess these additional quenching terms, we modified Eq.(2-11c) to give Eq.(4-1).

$$\Gamma = \Gamma_R + Q_{F_2}[F_2] + Q_{I_2}[I_2] + Q_{IF}[IF] + Q_m[M] \quad (4-1)$$

where Γ is the decay rate, Γ_R is the radiative rate of the initially pumped level, and the rates on the right side of Eq.(4-1) are quenching rates by the respective gases.

At "baseline" conditions, before the addition of a bath gas, the concentrations of F_2 and $IF(X)$ were estimated as $4 \times 10^{14} \text{ molecules cm}^{-3}$ and $3.3 \times 10^{13} \text{ molecules cm}^{-3}$, respectively. Using the measured F_2 quenching rate constant and assuming a self-quenching rate coefficient as large as gas kinetic ($Q_{IF} = 1.8 \times 10^{-10} \text{ cm}^3 \text{ molecule}^{-1} \text{ s}^{-1}$), we find that $Q_{F_2}[F_2] = 1.8 \times 10^3 \text{ s}^{-1}$ and $Q_{IF}[IF(X)] < 5.9 \times 10^3 \text{ s}^{-1}$. The respective first order F_2 and $IF(X)$ quenching rates at these base pressure conditions are two orders of magnitude less than the radiative decay rate and are, therefore, negligible. (Figure 4-5a specifically shows that $IF(X)$ is a negligible quencher of $IF(B)$ because enhanced $IF(X)$ production

indicated that the reaction could be explained as a bimolecular encounter between I_2 and F_2 . Furthermore, they concluded that the reaction can proceed via two branches with the major branch forming I_2F and the minor branch, electronically excited IF . Our results, in a relatively high pressure flow, imply that a third body may enhance the reaction. In a similar flow experiment, Birks et al.⁷ also reported IF enhancement with increased Ar pressures. They concluded that the added Ar choked the flow and, consequently, the residence time of the I_2 and F_2 in the cell was increased which led to a more complete reaction. We checked for such gas dynamic effects in our flow system but found none, and we must discard this as the explanation for our enhanced IF production. Kahler and Lee also suggested that, in high pressure $I_2 + F_2$ experiments, secondary reactions (i.e., $F + I_2$) may play an important role in forming IF . However, the mechanism of how a third body enhances IF production in a high pressure flow system is uncertain. At present, we have no definitive explanation for our enhanced IF production, but we can use the data in Fig. 4-5a to infer an important consequence of this phenomenon.

In Fig. 4-5a, we see that the production of $IF(X)$ first increases then levels off above 375 mTorr of added Ar. Figure 4-5b shows a Stern-Volmer plot for $IF(B)$ decay rates with Ar over the same pressure range as in Fig. 4-5a. These data imply that as the reactants are consumed (or, equivalently, as $IF(X)$ production increases) the observed $IF(B)$ decay rate is reduced. At added bath gas pressures exceeding one Torr, the observed decay rates became essentially constant and only an upper limit to the quenching rate coefficients could be obtained.

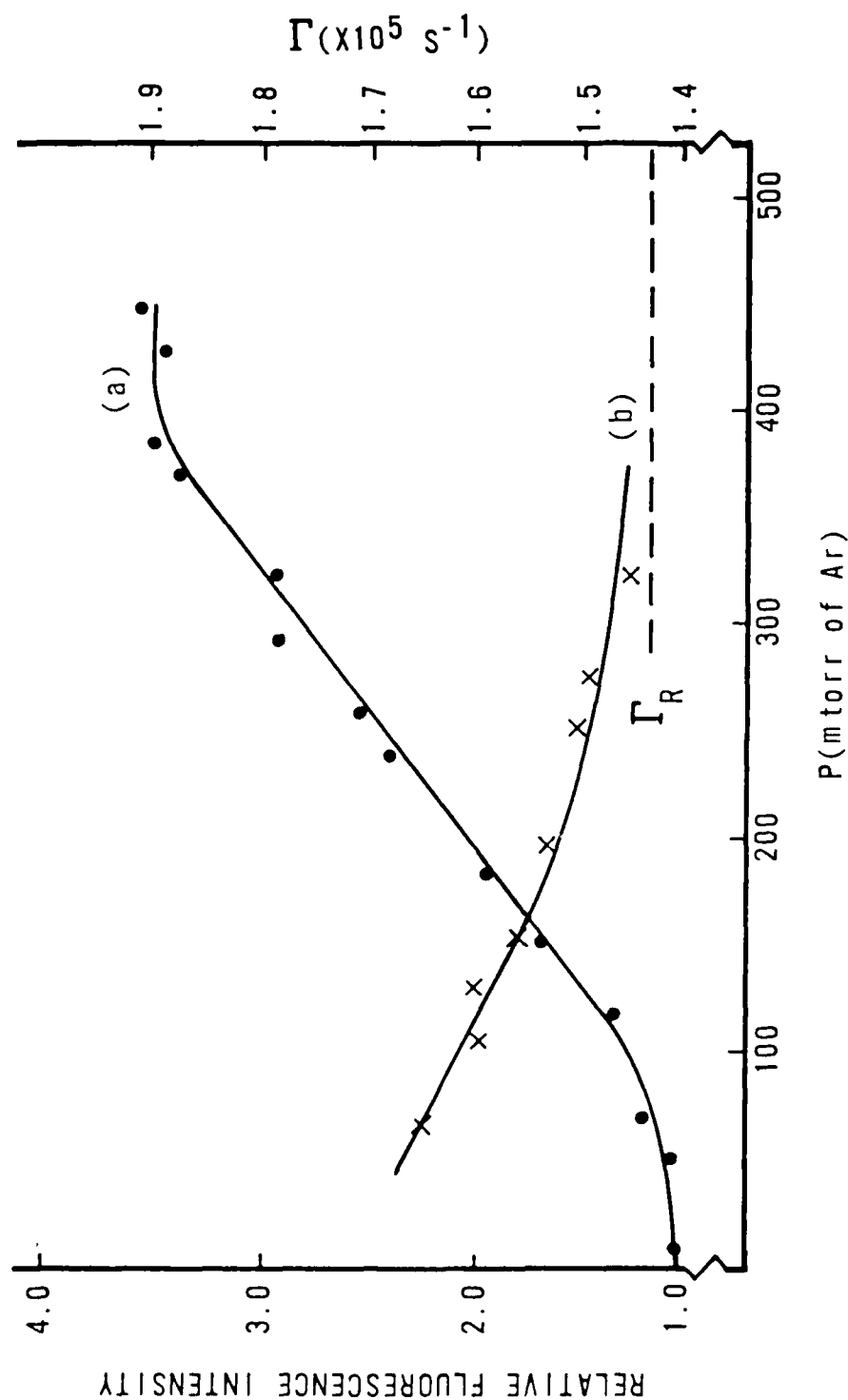


Figure 4-5. (a) Relative $IF(B \rightarrow X)$ fluorescence intensity as a function of Ar bath gas pressure. The intensity points were obtained by exciting IF with an Ar laser at 476.5 nm and were normalized to the value obtained at zero added Ar. (b) Stern-Volmer plot for $IF(B)$ decay with increasing Ar pressures. The initially prepared state was $(v', J')_1 = (3, 22)$. The asymptote of the curve approaches a value equal to $1.45 \times 10^5 \text{ s}^{-1}$ which agrees with the known radiative decay rate, Γ_R , of $1.44 \times 10^5 \text{ s}^{-1}$.

was added, $\text{IF(B)} + \text{M}$ collision frequencies increased and reduced the diffusional displacement of IF(B) molecules. Thus, a decrease in wall quenching would be detected as an increase in the radiative rate or, equivalently, an increase in the fluorescence intensity in cw experiments. (This effect would only be observed if the bath gas was an inefficient quencher.) However, the diffusion displacement that was calculated in Appendix F under these base pressure conditions (0.16 cm) was too small to account for this effect. Typically, diffusional effects become significant for lifetimes greater than $100 \mu\text{s}$.³⁷

Because of the reaction we chose for IF production, I_2 and F_2 were present in the reaction chamber, and both species were potential quenchers of IF(B) . As indicated below, the addition of a bath gas into the flow chamber enhanced IF production via the $\text{I}_2 + \text{F}_2$ reaction. As the I_2 and F_2 reacted away, there was less quenching caused by these species.

We monitored the relative IF(X) production as a function of bath gas pressure using cw LIF from an Ar^+ laser. (The 476.5 nm line excites the $\text{R}(71)$ line of the (6,0) band.) A typical plot is shown in Fig. 4-5a. It is clear that the LIF signal increased as Ar bath gas was added. The functional dependence of $\text{IF(B} \rightarrow \text{X)}$ chemiluminescence from the $\text{I}_2 + \text{F}_2$ reaction displayed a similar behavior. Both of these results indicate an enhanced production of IF as the bath gas pressure was increased. However, the mechanism for the increase in the IF concentration is unclear. It is important to emphasize that the reaction of I_2 with F_2 is a complicated process that has received considerable attention in the literature. In recent molecular beam experiments, Kahler and Lee³³

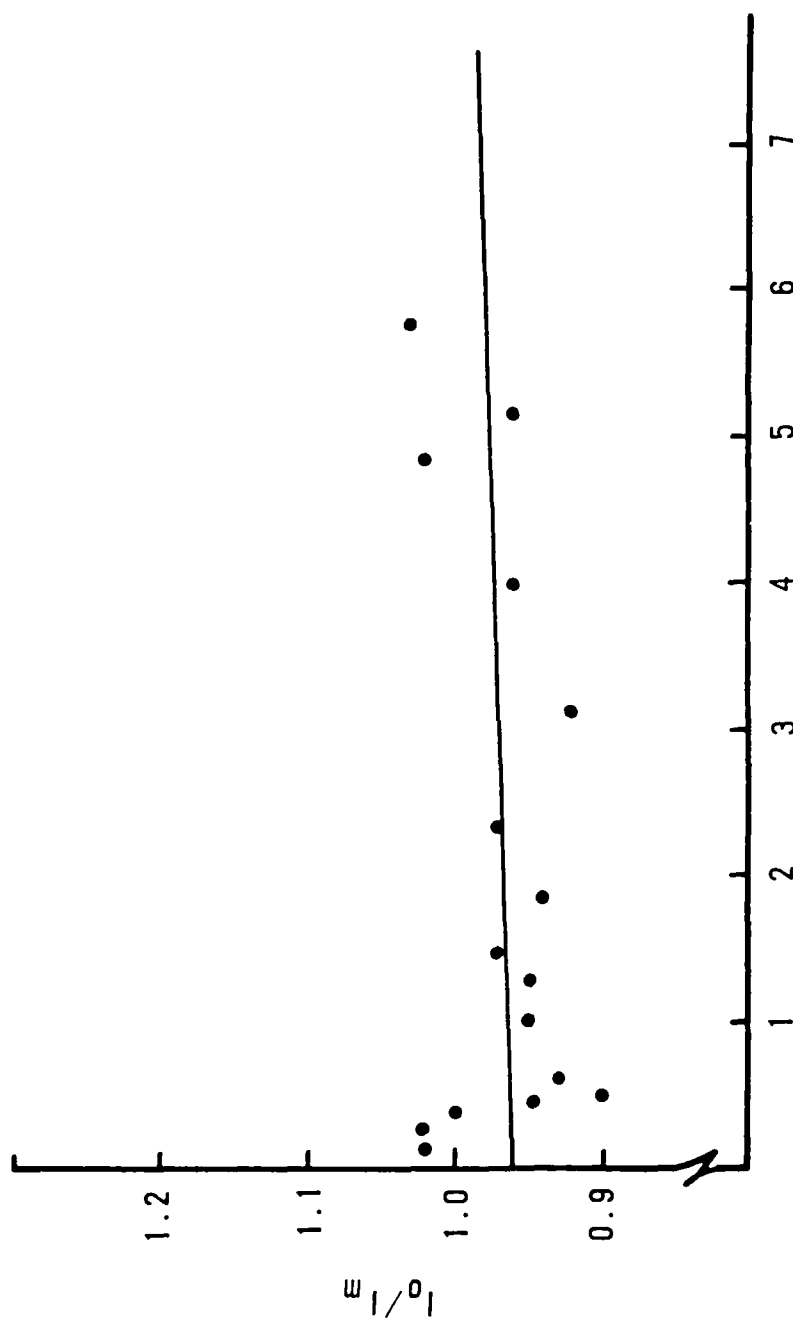


Figure 4-4. CW electronic quenching data for He. Note the increase in the fluorescence intensity at pressures below one Torr.

TABLE 4-1. IF(B) quenching rate constants by F₂.

v_i'	$Q_{F_2}(10^{-12} \text{ cm}^3 \text{ molecule}^{-1} \text{ s}^{-1})$
3	3.4 ± 0.5
6	4.5 ± 0.6
7	5.2 ± 0.4

Stern-Volmer plot assumed the typical behavior described by Eq.(2-11c). Similar trends were observed in the Stern-Volmer plots for the other noble gases and N₂. The quenching rate constants were, therefore, extracted in the high pressure limit of these plots. An upper limit for the IF(B) quenching rate constant by the noble gases and N₂ was determined as $1 \times 10^{-14} \text{ cm}^3 \text{ molecule}^{-1} \text{ s}^{-1}$. These quenching rate constants were independent of vibrational quantum level for $3 \leq v' \leq 8$.

The cw quenching data showed analogous behavior as seen in Fig. 4-4. An increase in the fluorescence intensity was observed as one Torr He was added which indicated an increase in the number of fluorescing IF(B) molecules. At He pressures greater than one Torr, the relative intensities assumed the typical quenching behavior. The rate constants were extracted in the high pressure limit of such plots; and the upper limit for the noble gas quenching coefficients were determined as $2 \times 10^{-14} \text{ cm}^3 \text{ molecule}^{-1} \text{ s}^{-1}$.

It may be argued that diffusional migration of IF(B) from the observation region resulted in the detection of shortened lifetimes through collisional quenching with the containment vessel.^{37,38} As the bath gas

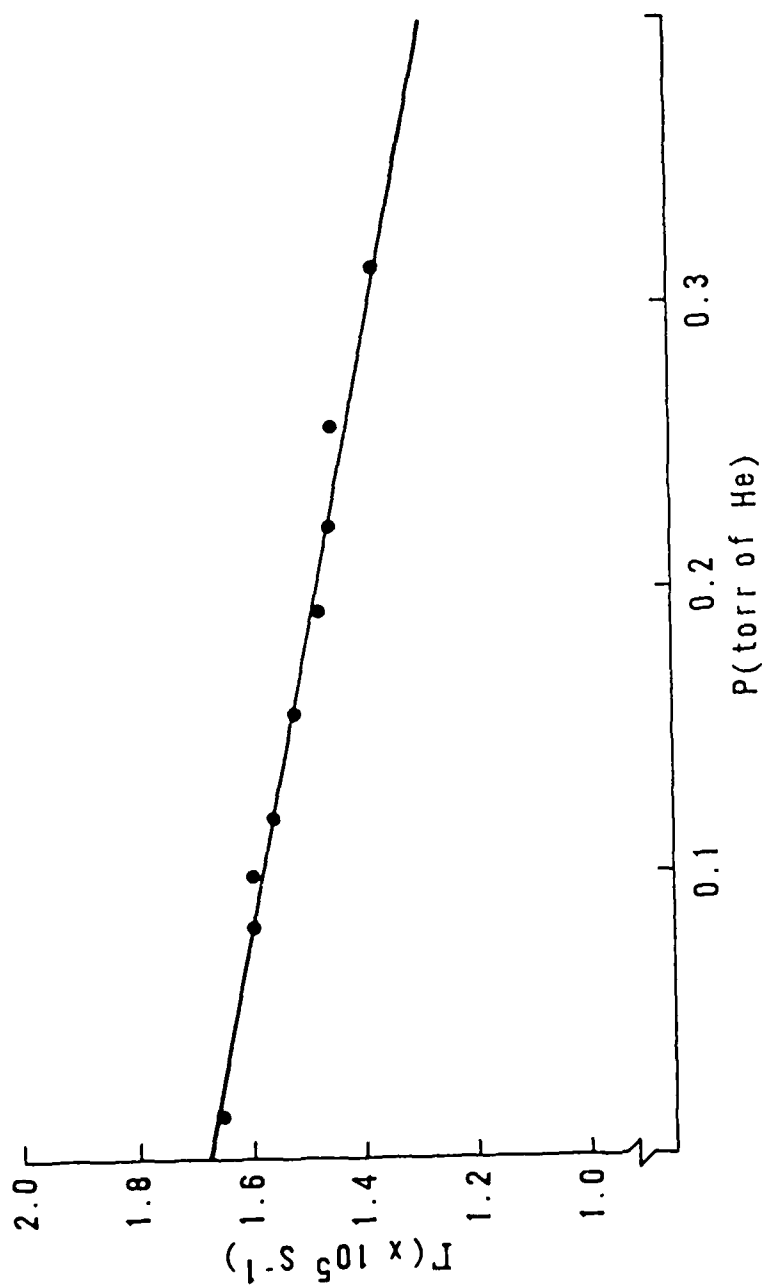


Figure 4-3. Stern-Volmer for quenching of IF(B) by He.

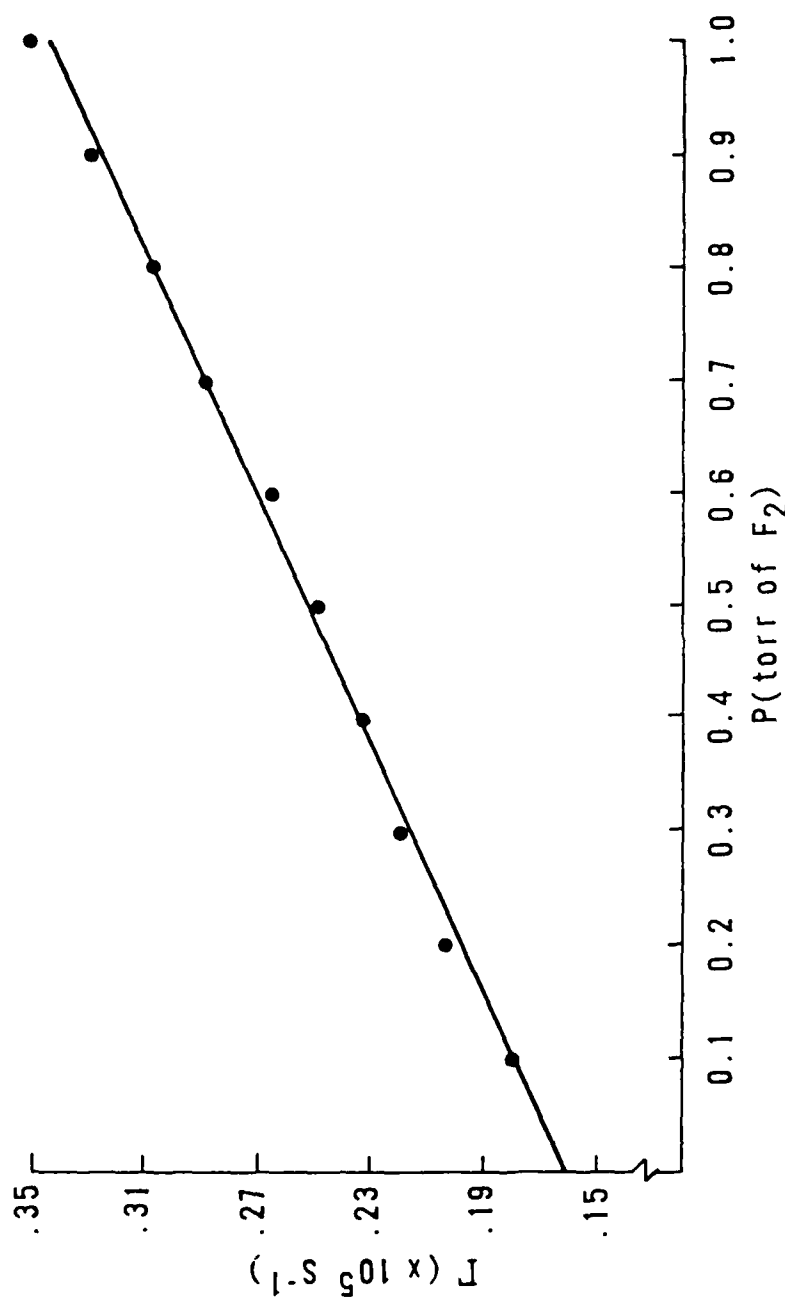


Figure 4-2. Stern-Volmer plot for quenching of IF(B) by F₂.

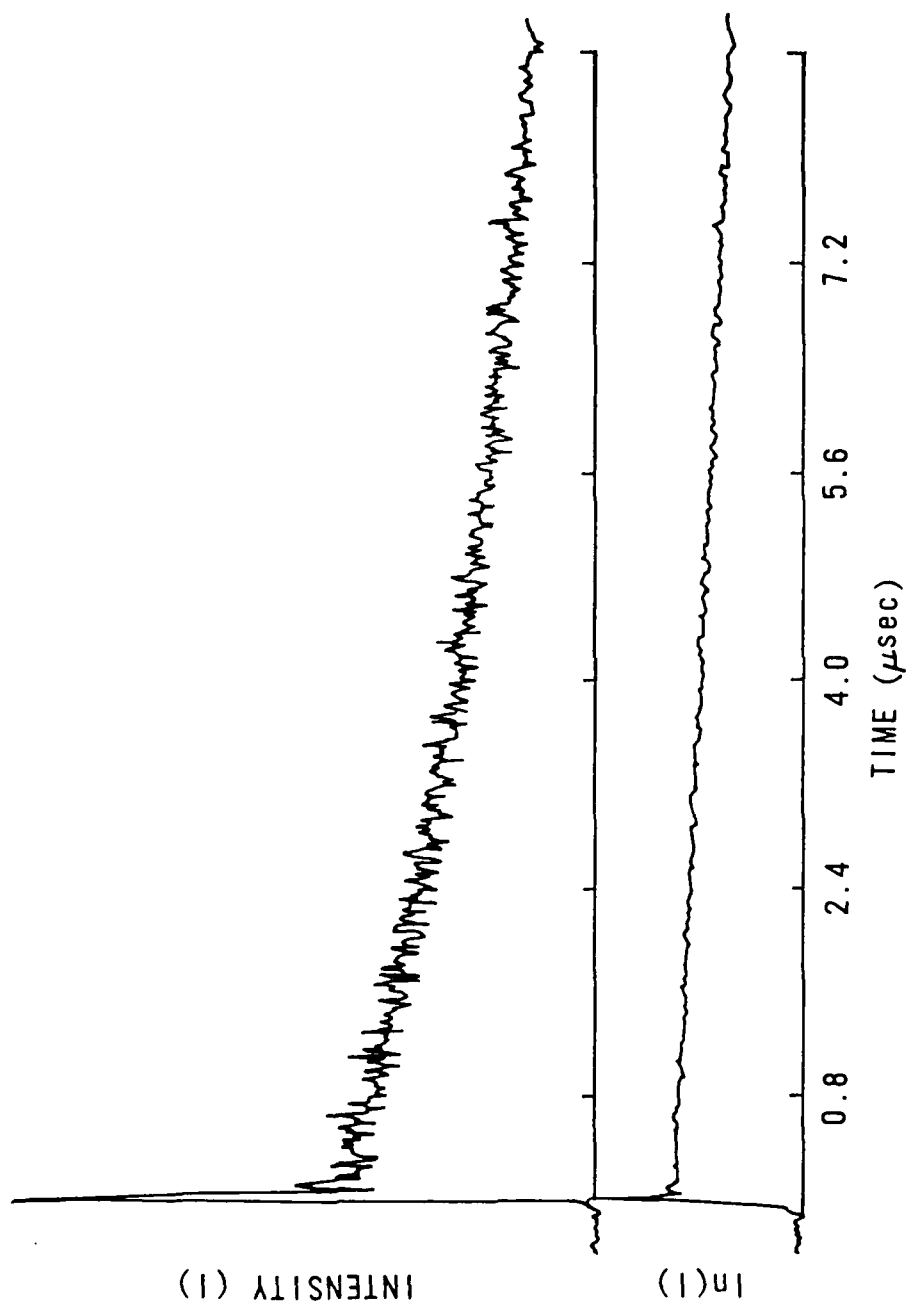


Figure 4-1. IF(B) total fluorescence decay curve and the corresponding logarithmic plot with 0.161 Torr of He. The initially prepared state was $v'=3$.

IV. RESULTS

A. Electronic Quenching

1. Quenching by Noble Gases, N_2 , I_2 , and F_2

Figure 4-1 shows an example of an IF(B) total fluorescence decay curve subsequent to excitation of $v'=3$ with 0.161 Torr of added He. The lower curve in this figure is the corresponding logarithmic plot. The logarithmic decays were linear over the 10 μs time scale for all the bath gases. The correlation coefficients for the single exponential fits were typically greater than 0.98.

The decay rates, Γ , for a series of 10 to 15 pressures were determined from the logarithmic plots and inserted into Eq.(2-11c) to extract the quenching rate constants. A sample Stern-Volmer plot is depicted in Fig. 4-2 for excitation of $(v', J') = (7, 24)$. The bath gas was F_2 . A summary of the F_2 quenching coefficients for initial excitation of $v'=3, 6$, and 7 is listed in Table 4-1. As seen in this table, the values showed a slight dependence on IF(B) vibrational quantum number. However, there was no deviation as a function of rotational quantum number upon exciting $J'=5, 24$, and 55 in both $v'=6$ and 7.

An unusual effect was observed in the Stern-Volmer plots for the noble gases and N_2 . Figure 4-3 shows an example of the IF(B) fluorescence decay behavior for He bath gas. As seen in this figure, the observed decay rate decreased with increasing He pressures. This trend was not characteristic of a traditional quenching behavior where an increase in the observed decay rate was expected with increasing bath gas pressures. As the partial pressure of He was increased to greater than one Torr, the

ranged from 4:1 for extremely weak signals to 150:1 for the most intense signals. The photon counter was interfaced to a PDP 11/V03 computer which stored the raw data on floppy disk for subsequent data analysis. A hard copy of the fluorescence spectra was also obtained by recording the analog signal from the photon counter on a strip-chart recorder (HP 7100 BM). (The raw data were amplified (PAR 113 preamplifier) and conditioned (PAR 189 selective amplifier) before being displayed on the strip-chart recorder.)

A second PMT (RCA 4832) was attached directly to the observation window of the fluorescence cell to monitor the stability of the fluorescence intensity. The PMT detected total, spectrally unresolved fluorescence through various long pass filters which were used to eliminate detection of the pump wavelengths. The output was measured on a picoammeter (Keithly 480) and displayed on the strip-chart recorder. Frequency shifts in dye laser due to drift or mode-hopping were easily noticed as a drastic diminution in fluorescence intensity.

The determination of the energy transfer rate constants required accurate relative intensity measurements of vibrational or rotational bands. Therefore, the light collection efficiency of the fluorescence detection system was measured to provide a wavelength dependent correction factor. This procedure is discussed in Appendix H.

and late sections of the decay curves, and plotting these rates against bath gas pressure to obtain the rate constants, Q_f and Q_s , respectively. Examples of the Stern-Volmer plots are shown in Fig. 4-7.

The rate constant, Q_f , for IF(B) depletion at short times was determined as $(8.27 \pm 1.4) \times 10^{-12} \text{ cm}^3 \text{ molecule}^{-1} \text{ s}^{-1}$. A weak dependence of Q_f on v_i' was observed but experimental uncertainties prohibited an accurate determination of this dependence. (For example, the quenching rate coefficient at short times was measured as $1.0 \times 10^{-11} \text{ cm}^3 \text{ molecule}^{-1} \text{ s}^{-1}$ in $v' = 4$, while $Q_f = 7.0 \times 10^{-12} \text{ cm}^3 \text{ molecule}^{-1} \text{ s}^{-1}$ in $v' = 3$.) The rate constant, Q_s , determined at long times was $(1.41 \pm 0.15) \times 10^{-12} \text{ cm}^3 \text{ molecule}^{-1} \text{ s}^{-1}$. This rate coefficient was independent of the vibrational energy level.

There are several possible explanations for the kinetic behavior observed in the O_2 quenching studies. Clyne et.al. observed analogous behavior in the time resolved B state fluorescence of BrF^{39} and $BrCl^{40}$. In their work, initial fast decays were followed by a slower decay. They attributed this behavior to B state thermalization which red shifted the fluorescence. This fluorescence red shift was due to emission originating from the lower vibrational levels which were being collisionally populated. Clyne et.al. used various color filters and a PMT whose response curve became weak in the red end of the visible spectrum. Thus, the sensitivity was much greater for fluorescence originating from the initially excited levels than for the thermalized levels. Thermalization was observed as a rapid reduction in the fluorescence from the initially pumped level. As thermalization became more complete, the observed decay

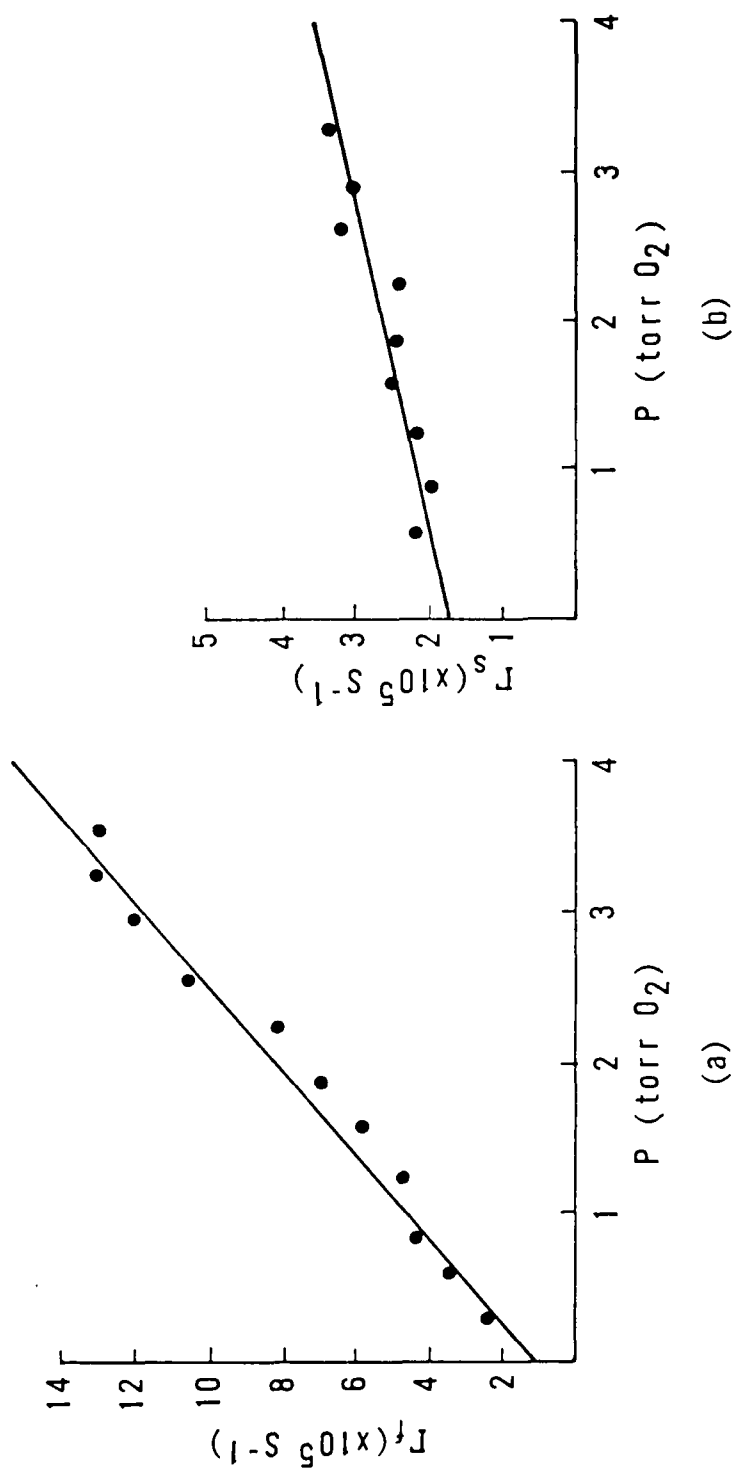
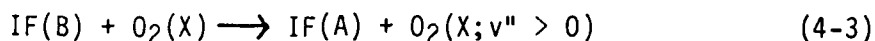


Figure 4-7. Stern-Volmer plots for determining IF(B) depletion rate constants at (a) short times and (b) long times.

rate slowed because of the shift toward the red part of the visible spectrum where the PMT was less efficient. The initial decay at short times was attributed to vibrational relaxation, while the decay at long times was due to electronic quenching.

This interpretation is not valid in the present work since the PMT had a flat response over the entire emission range of any v' level in IF(B). In addition, Clyne et.al. observed this behavior for rare gases while no such behavior was seen for any rare gases in this study.

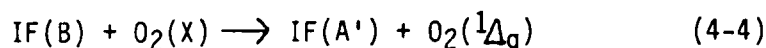
A second possible explanation is the energetically allowed process



Chemiluminescence from the IF ($A \rightarrow X$) system has been reported⁷ from 500 to 800 nm which is in the range of the PMT used in this work. Time resolved emission from two electronic states of IF, each having two different lifetimes, would display a double exponential behavior. One would expect the Stern-Volmer plots to yield purely radiative decay rates for the two states at the zero pressure intercepts. As seen in Fig. 4-7, however, the intercepts at long and short times are comparable. The problem with this explanation is that the $A^3\pi(1)$ state should be much more metastable than the $B^3\pi(0^+)$ state. This is indeed what is observed in the analogous Br_2 and ICl systems where A state lifetimes were found to be on the order of hundreds of microseconds.^{41,42} The present results strongly suggest that the observed emission at both short and long times is due solely to B state decay.

The most plausible explanation is, in a sense, a combination of the

two given above. The O_2 quenching mechanism could proceed via an $E \rightarrow E$ process where $O_2(^1\Delta_g)$ molecules are formed via reaction (4-4).



The reverse process has been suggested as being important in the chemical pumping of $IF(B)$ by $O_2(^1\Delta_g)$.⁴³ The $A'^3\Pi(2)$ state is estimated to have a potential minimum as low as 13500 cm^{-1} .⁴³ If this were the case, $IF(B)-O_2(X)$ collisions could result in a near resonant process following excitation of $v' > 3$ in $IF(B)$. The energy difference involved in a $B \rightarrow A'$ transition is estimated to be about 7800 cm^{-1} which is adequate for forming $O_2(^1\Delta_g)$. Therefore, the rate constant, Q_f , determined at short times may be due to $E \rightarrow E$ energy transfer between $IF(B)$ and $O_2(X)$. The slower rate constant, Q_s , determined at longer times may then be attributed to "true" electronic quenching of $IF(B)$.

It may also be argued that $IF(B) - O_2(X)$ collisions could populate high vibrational levels ($v'' > 20$) in $IF(X)$. But, by the Franck-Condon principle, these transitions would most probably be disallowed due to extremely small vibrational band overlaps.

This proposed mechanism satisfactorily accounts for the similarities in the zero-pressure intercepts that were obtained in both the noble gas and N_2 quenching studies, and those obtained from an analysis of O_2 quenching at long and short times. This process may also explain the weak dependence of Q_f on v_i' . As lower vibrational levels in $IF(B)$ are collisionally populated, subsequent O_2 collisions would be less effective in producing $O_2(^1\Delta_g)$ since the energy difference between $IF(B; v')$ and $IF(A')$ would be insufficient to provide the required energy.

3. Quenching by H₂O

Figure 4-8 shows examples of total IF(B) fluorescence decays with H₂O as the bath gas subsequent to laser excitation of $v'=4$. The IF(B) decays were well approximated by a double exponential. The quenching data were recorded on both a 5 μ s and 20 μ s time scale to determine the decay rates Γ_i and Γ_d at short and long times, respectively. The decay rates were determined by fitting a single exponential to each portion of the fluorescence decay curve. The respective rate constants, Q_i and Q_d , were then obtained using the standard Stern-Volmer analysis.

An analysis of the initial, fast decay gave an average quenching rate constant, Q_i , of $(2.4 \pm .7) \times 10^{-10} \text{ cm}^3 \text{ molecule}^{-1} \text{ s}^{-1}$. This rate constant had a weak dependence on the vibrational quantum number, ranging from $1.9 \times 10^{-10} \text{ cm}^3 \text{ molecule}^{-1} \text{ s}^{-1}$ for $v'=3$ and 4 to $3 \times 10^{-10} \text{ cm}^3 \text{ molecule}^{-1} \text{ s}^{-1}$ for $v'=5$ and 6. In contrast, Q_d showed a stronger dependence on the vibrational quantum number. The respective quenching rate constants for $v'=4, 5$, and 6 were $(1.8 \pm 0.4) \times 10^{-12} \text{ cm}^3 \text{ molecule}^{-1} \text{ s}^{-1}$, $(3.9 \pm .9) \times 10^{-12} \text{ cm}^3 \text{ molecule}^{-1} \text{ s}^{-1}$, and $(7.6 \pm 1.6) \times 10^{-12} \text{ cm}^3 \text{ molecule}^{-1} \text{ s}^{-1}$.

A qualitative examination of H₂O quenching was made by spectrally resolving the IF(B) fluorescence to possibly interpret the quenching mechanism. These studies began at high base pressures, typically 0.30-0.40 Torr with no added H₂O. Figure 4-9a shows the temporal history of both the initially populated, $v'=4$ state and the collisionally populated vibrational level, $v'=3$, both in the absence of H₂O. Figure 4-9b shows the temporal histories of the same vibrational levels with 15 mTorr

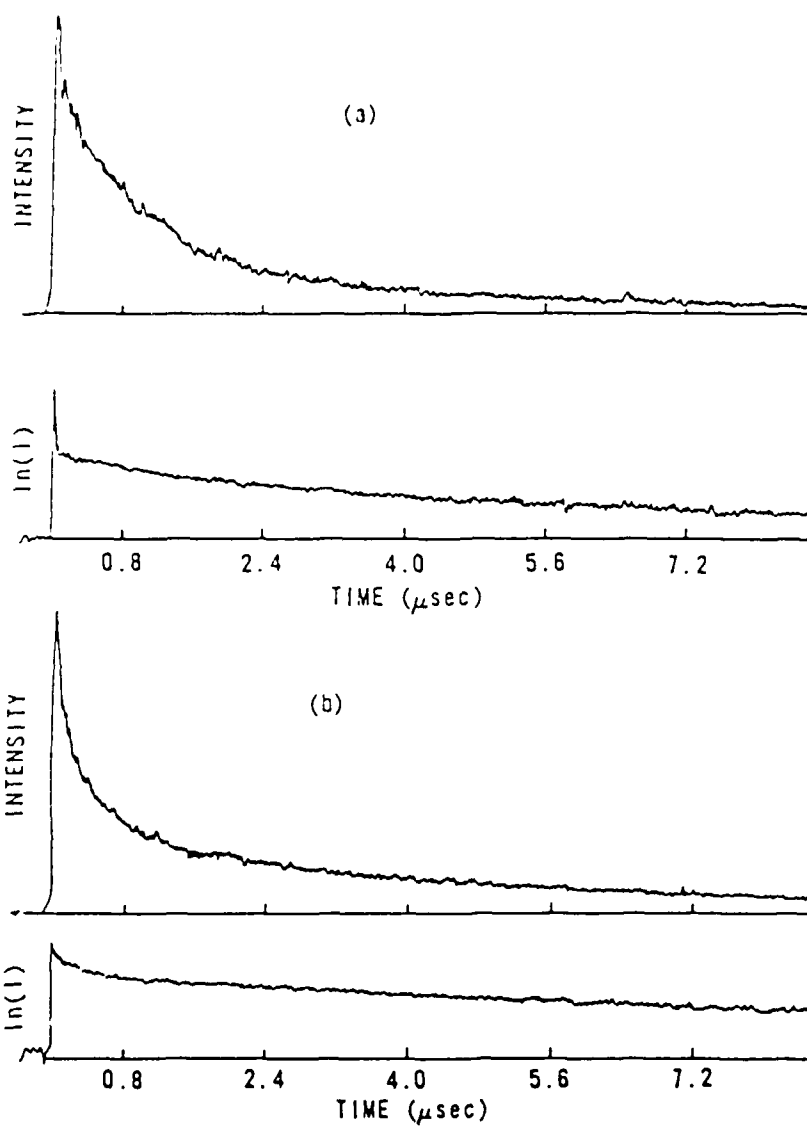


Figure 4-8. Total IF(B) fluorescence decays with H_2O :
(a) $P(\text{H}_2\text{O}) = 24$ mTorr and (b) $P(\text{H}_2\text{O}) = 300$ mTorr.

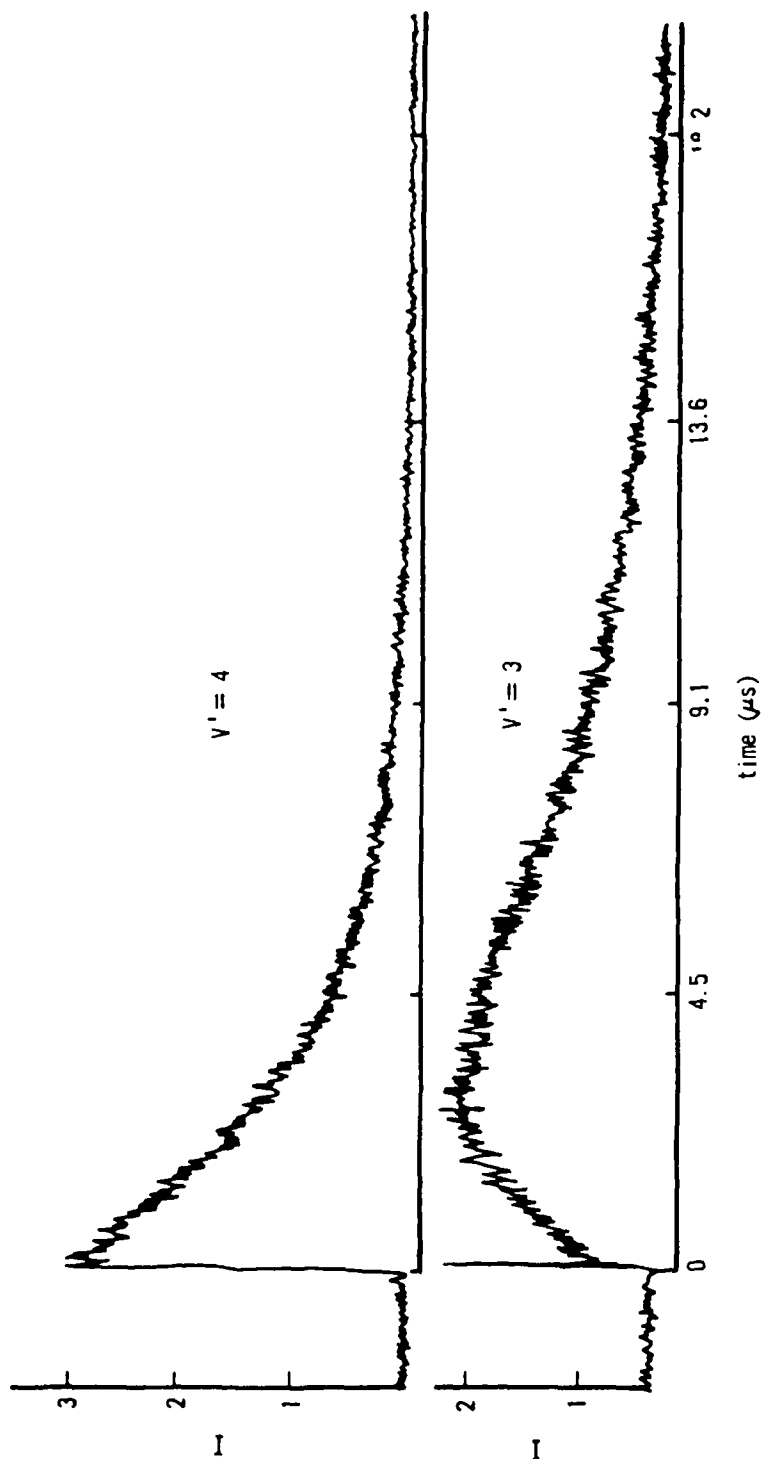
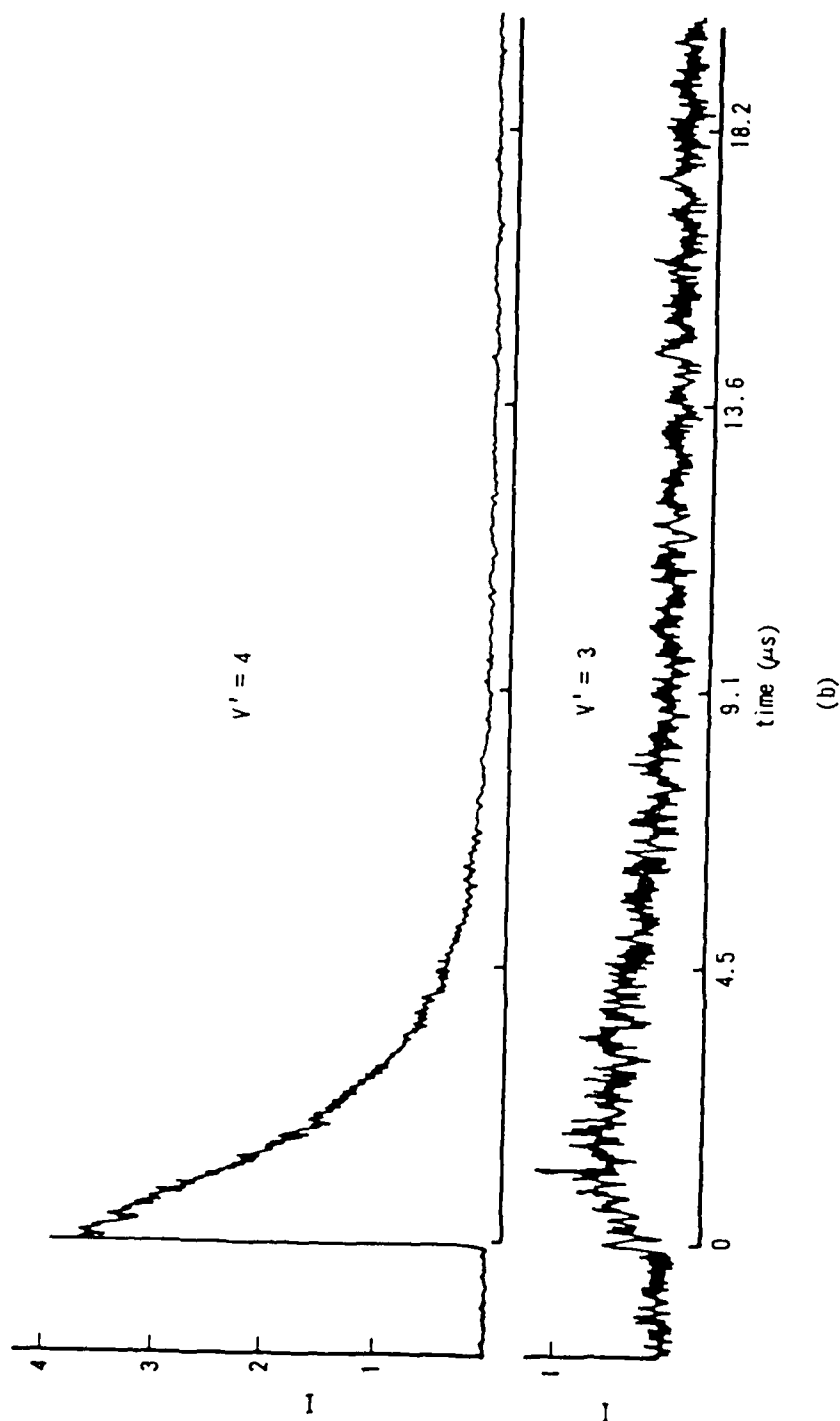


Figure 4-9a. Temporally and spectrally resolved IF(B) fluorescence emission with no added H_2O . The initially prepared state was $v' = 4$. The initial spike in the lower figure was caused by stray laser light.



(b)

Figure 4-9b. Temporally and spectrally resolved $IF(B)$ fluorescence emission with 15 mTorr of added H_2O .

of added H₂O. The initial, $v'=4$ state exhibited an increase in the decay rate which was characteristic of electronic quenching. In contrast, fluorescence emission from $v'=3$ decreased by a factor of two as seen in Fig. 4-9b. Emission from $v'=2, 1$, and 0 was also negligible, being indistinguishable from the baseline noise. These results suggested that the population loss occurred in either $v'=3$ or $v'=2$ through non-radiative decay. A near resonant energy exchange between IF(B; $v'=2$ or 3) and H₂O may provide the depletion pathway. Similar results were also obtained after exciting $v'=3, 5$, and 6.

These results may possibly be interpreted as follows. The ground electronic state of H₂O contains numerous vibrational transitions which may be resonant with the energy released in the decay of IF(B) to an unspecified, lower electronic state. Thus, IF(B) depletion at short times may be due to an $E \rightarrow V$ energy exchange at short times. This process is expected to be rapid if the transfer process is resonant. The slower kinetic process would subsequently be detected at long times, and may possibly be attributed to "true" IF(B) quenching by H₂O.

C. Vibrational Relaxation: Time-Resolved Results

Figure 4-10 shows decay curves that were obtained in the time resolved vibrational relaxation experiments. Figure 4-10a shows the decay from the initially prepared $v'=3$ state, while Fig. 4-10b shows the time histories of the collisionally populated levels, $v'=2$ and 4.

The first order vibrational transfer rates, $K(m,n)$, were extracted from the spectra using the Montroll-Shuler model described in Chapter II. The numerical routine required an initial value for the relaxation rate.

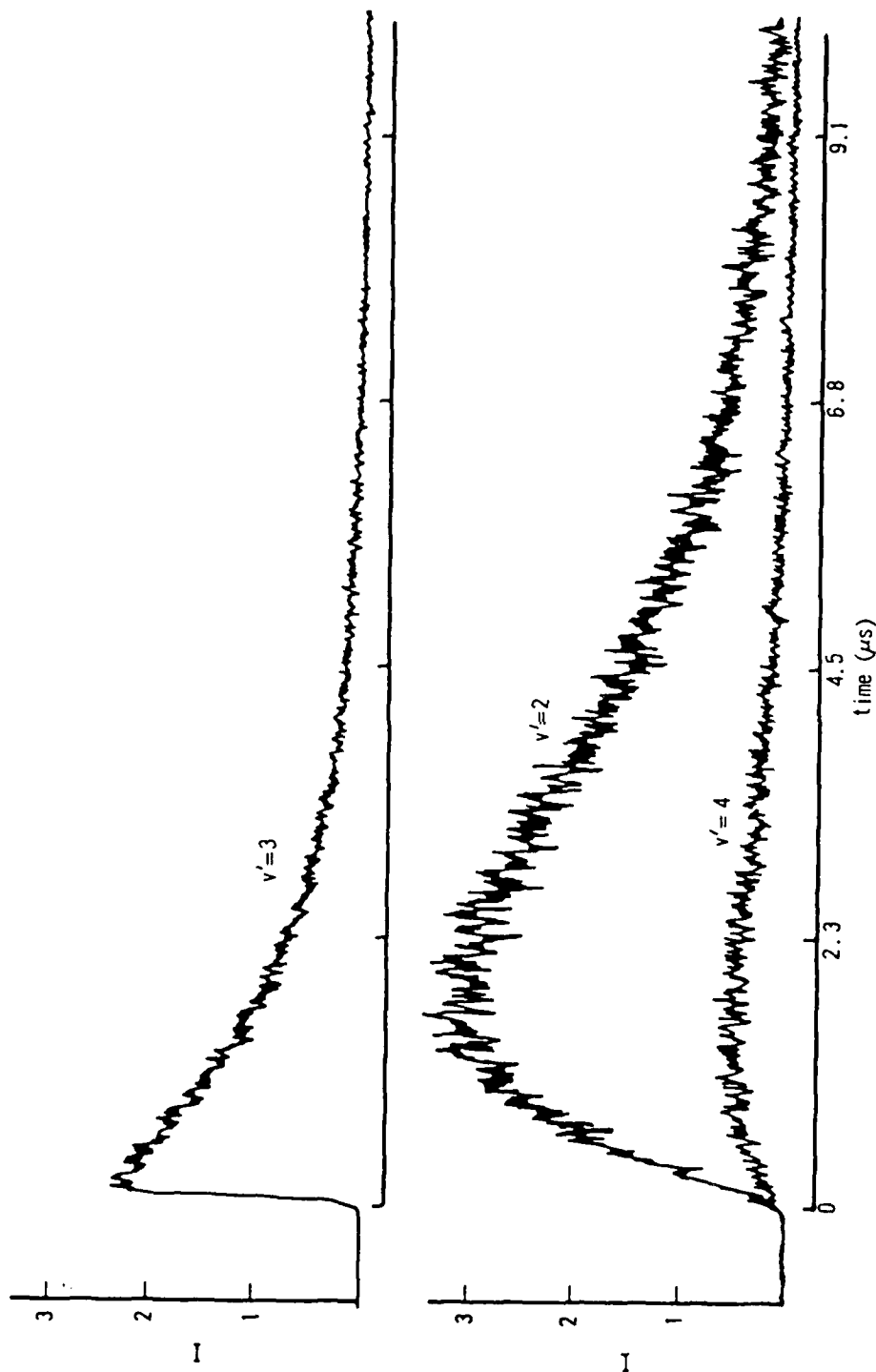


Figure 4-10. Time evolutions of $v' = 2$, 3, and 4 subsequent to excitation of $v' = 3$ with 0.65 Torr of He.

A nonlinear regression fit to the data was made with the rate constant being internally adjusted until a reasonable fit was found.⁴⁴ The fitting routine was not very sensitive to the choice of the initial guess. Problems may occur if the initial rate differed by an order of magnitude from the actual rate, but no support of this situation has yet been observed. Figure 4-11 shows two examples of the results of this numerical procedure.

The validity of Eq.(E-5) for analyzing vibrational relaxation in IF was examined by generating some synthetic data, fitting the equation to the data, and extracting the rate constants.⁴⁴ Doing this, it was found that the rates obtained from the fit were within one percent of those that were used to generate the data. If we generate data which is consistent with the assumptions used to derive Eq.(E-5), then the error drops to 1 part in 10^6 , and represents the accuracy of the numerical procedure. The one percent error obtained in the above model is, therefore, a real effect and represents the error inherent in the model.

As shown in the development of the Montroll-Shuler solution, concurrent radiative effects were included by multiplying the analytic solution by a factor of $\exp(-\Gamma t)$, where Γ is the sum of the radiative and quenching rates. This average lifetime introduced negligible error in the the rate constants for the $\Delta v = \pm 1$ transitions since the lifetimes did not vary by more than five percent from the initially populated level.

Tests were made on the goodness of the fits by varying the decay rate Γ through an alteration in the quenching rate constant. The test case was for an F_2 bath gas where the quenching rate constant was changed

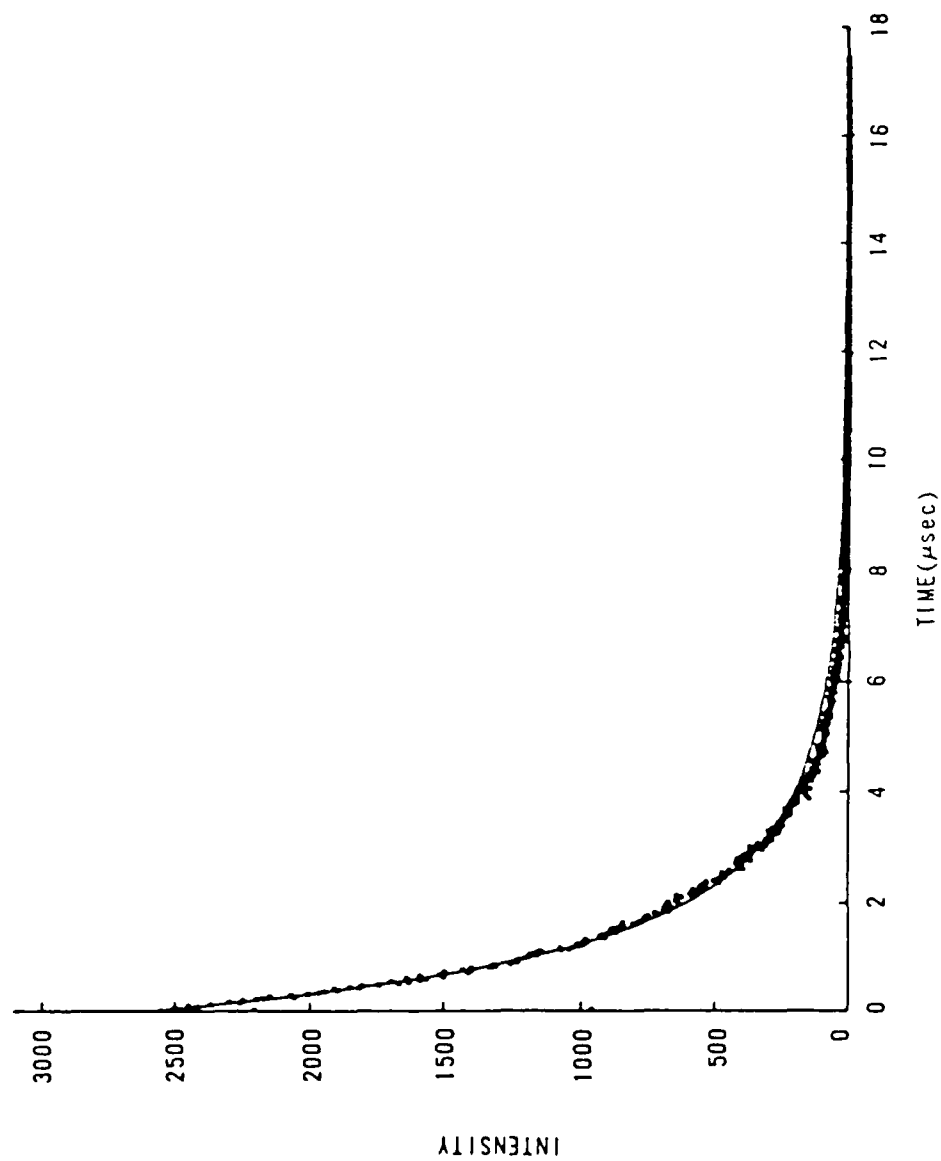


Figure 4-11a. Comparison of data and fit using the Montroll-Shuler model with 1.7 Torr of He. This figure shows the decay of the initially populated, $v' = 3$ level.

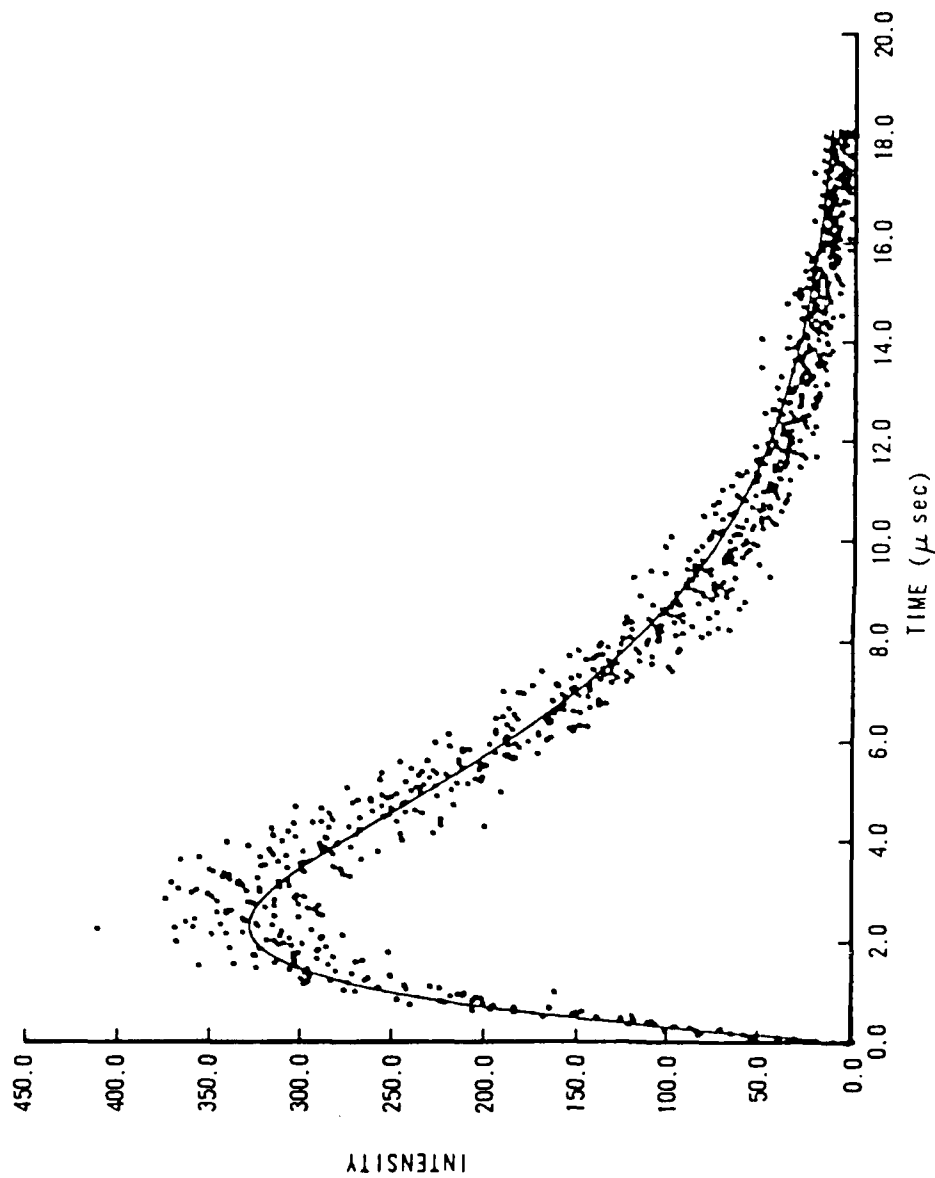


Figure 4-11b. Comparison of data and fit using the Montroll-Shuler model with 1.7 Torr of He. This figure shows the time history of the collisionally populated, $v' = 2$ level.

from $4 \times 10^{-12} \text{ cm}^3 \text{ molecule}^{-1} \text{ s}^{-1}$ to $1 \times 10^{-14} \text{ cm}^3 \text{ molecule}^{-1} \text{ s}^{-1}$ at a pressure of 1.0 Torr (i.e., Γ was changed from $2.7 \times 10^5 \text{ s}^{-1}$ to $1.4 \times 10^5 \text{ s}^{-1}$). The results showed that the rate constants differed by less than 15 percent for a two order of magnitude change in the quenching rate constant. Therefore, systematic errors in the measurement of the quenching rate constants did not affect the accuracy of the fitting routine used to extract the relaxation rate coefficients.

The first order vibrational relaxation rates, $K(m, n)$ that were obtained by fitting the data as shown in Fig. 4-10 are of two types. The fluorescence decay curve shown in Fig. 4-10a gives the rate of total removal from the initially prepared state to all other vibrational levels. The time history of the collisionally populated "satellite" band is displayed in Fig. 4-10b. As discussed in Appendix D, the rising exponential corresponds to the rate at which the level is populated from the "parent" state, while the decreasing exponential gives the rate of population removal from the observed "satellite" band. Thus, two rate constants are extracted from spectra such as in Fig. 4-10b: the state-to-state transfer rate into the level, and the total removal rate coefficient out of the collisionally populated state.

The second order rate constant, $k(m, n)$, is obtained by plotting $K(m, n)$ as a function of bath gas pressure. Figure 4-12 shows an example of such a plot for the collisionally populated, $v' = 2$ state. Thermally averaged cross sections were also calculated using Eq.(4-5).

$$\sigma = k(\pi\mu/8kT)^{1/2} \quad (4-5)$$

AD-A159 242

COLLISIONAL DYNAMICS OF THE $B3PI(0+)$ STATE OF IODINE
MONOFLUORIDE(U) AIR FORCE INST OF TECH WRIGHT-PATTERSON
AFB OH SCHOOL OF ENGINEERING P J WOLF MAR 85

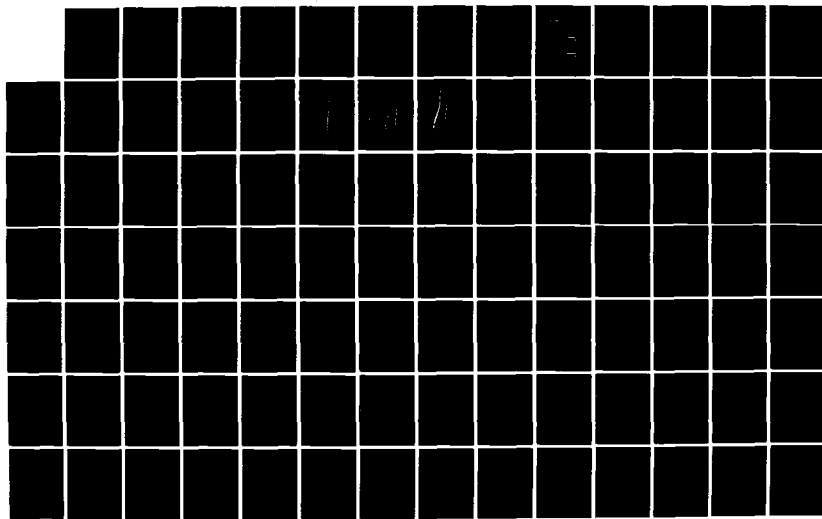
2/3

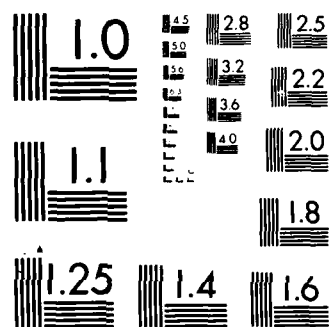
UNCLASSIFIED

AFIT/DS/PH/85-1

F/G 7/4

NL





MICROCOPY RESOLUTION TEST CHART
NATIONAL BUREAU OF STANDARDS 1963-A

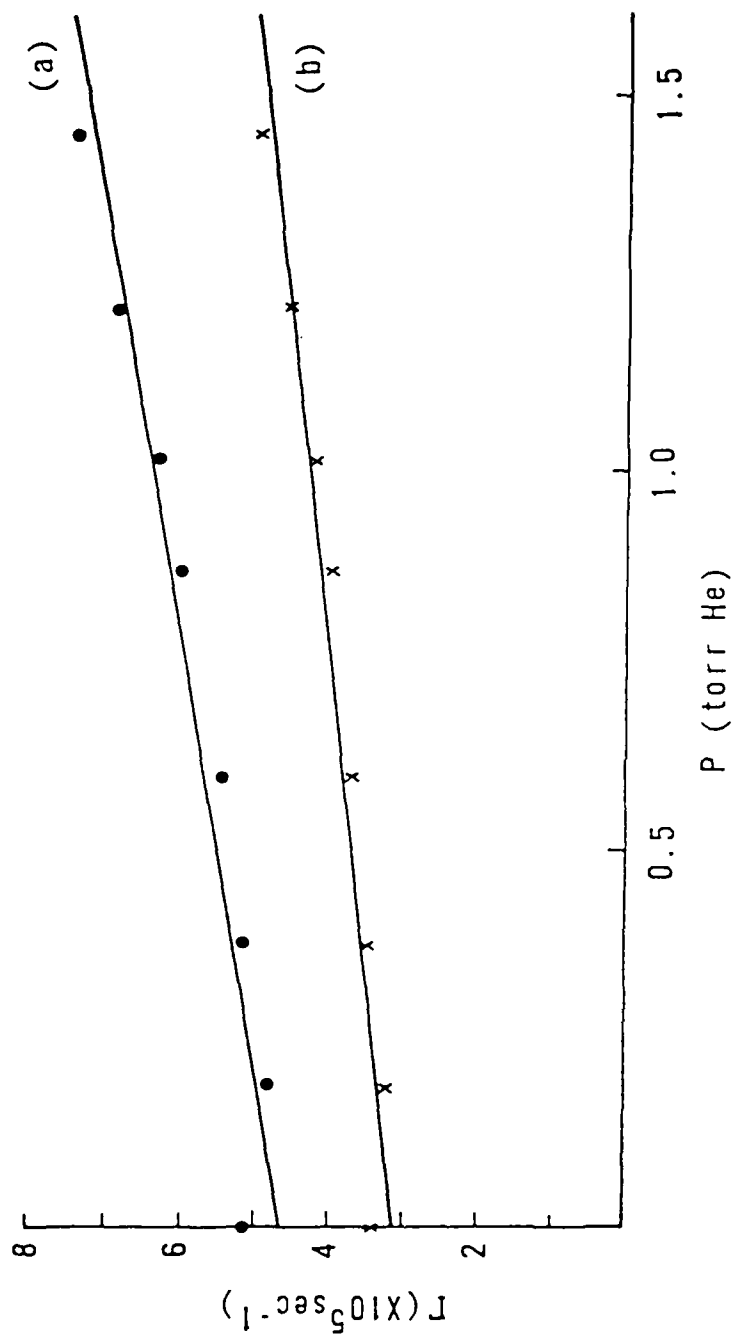


Figure 4-12. Stern-Volmer plot for extracting the vibrational relaxation rate constants: (a) data for determining $k(3,2)$ and (b) data for determining the total removal rate constant from $v'=2$.

where μ is the reduced mass of the IF and bath gas system, k is Boltzmann's constant, and T is the gas temperature. The total removal rate constants and the corresponding cross-sections are summarized in Table 4-2. The state-to-state values are listed in Table 4-3. The errors quoted in these tables are (1σ) from the mean and represent the inherent statistical uncertainties in the data.

Note that the zero bath gas intercepts in Fig. 4-12 are unusually large. At $M = 0$, the intercepts in this figure should extrapolate to zero since no relaxation from $v' = 3$ occurs at these bath gas pressures. Typically, the zero-pressure intercepts ranged from $1.5 \times 10^4 \text{ s}^{-1}$ to $5.5 \times 10^4 \text{ s}^{-1}$. (These values were obtained after subtracting off both the radiative decay rate and the average IF(B) quenching rate by I_2 .) These values showed a possible dependence on vibrational quantum number from $v' = 3$ to $v' = 8$, and indicated the rapidity of vibrational relaxation by residual I_2 . (The contributions from F_2 and IF(X) were previously shown to be unimportant in the quenching studies. Using the estimated I_2 concentration defined previously, the approximate vibrational energy transfer rate constant due to I_2 was estimated as $1.7 \times 10^{-10} \text{ cm}^3 \text{ molecule}^{-1} \text{ s}^{-1}$.)

C. Vibrational Transfer: CW Results

Figure 4-13 shows a portion of a cw fluorescence spectrum to illustrate the population evolution of the initial IF(B; $v' = 3$) distribution in the presence of He. At zero added He pressure (Fig. 4-13a), the spectrum primarily consists of emission from the initially prepared state, $(v', J') = (3, 22)$. Emission from the collisionally populated,

TABLE 4-2. Total vibrational removal rate constants and the corresponding cross sections obtained in the pulsed experiments. The rate constants and cross sections have units of $\text{cm}^3 \text{ molecule}^{-1} \text{ s}^{-1}$ and cm^2 , respectively. The errors are 1σ from the mean.

Bath	Vibrational Level	k_v	σ_v
He	2	$(3.9 \pm 0.5) \times 10^{-12}$	$(3.1 \pm 0.4) \times 10^{-17}$
	3	$(6.6 \pm 0.9) \times 10^{-12}$	$(5.2 \pm 0.7) \times 10^{-17}$
	4	$(9.0 \pm 1.3) \times 10^{-12}$	$(7.0 \pm 1.0) \times 10^{-17}$
	5	$(1.2 \pm 0.2) \times 10^{-11}$	$(9.3 \pm 1.6) \times 10^{-17}$
	6	$(1.4 \pm 0.2) \times 10^{-11}$	$(1.1 \pm 0.2) \times 10^{-16}$
	7	$(1.6 \pm 0.2) \times 10^{-11}$	$(1.2 \pm 0.2) \times 10^{-16}$
	8	$(2.3 \pm 0.4) \times 10^{-11}$	$(1.7 \pm 0.3) \times 10^{-16}$
Ne	2	$(1.1 \pm 0.1) \times 10^{-12}$	$(1.8 \pm 0.2) \times 10^{-17}$
	3	$(2.2 \pm 0.2) \times 10^{-12}$	$(3.7 \pm 0.4) \times 10^{-17}$
	4	$(3.3 \pm 0.5) \times 10^{-12}$	$(5.5 \pm 0.8) \times 10^{-17}$
N ₂	2	$(1.9 \pm 0.4) \times 10^{-12}$	$(3.6 \pm 0.8) \times 10^{-17}$
	3	$(2.8 \pm 0.3) \times 10^{-12}$	$(5.5 \pm 0.6) \times 10^{-17}$
	4	$(4.0 \pm 0.7) \times 10^{-12}$	$(7.7 \pm 1.4) \times 10^{-17}$
F ₂	2	$(3.7 \pm 0.7) \times 10^{-12}$	$(8.2 \pm 1.5) \times 10^{-17}$
	3	$(4.7 \pm 0.6) \times 10^{-12}$	$(1.0 \pm 0.1) \times 10^{-16}$

TABLE 4-3. State-to-state vibrational transfer rate constants and corresponding cross sections obtained in the pulsed experiments. The rate constants and cross sections have units of $\text{cm}^3 \text{ molecule}^{-1} \text{ s}^{-1}$ and cm^2 , respectively. The errors are 1σ from the mean.

Bath	v_i	v_f	$k(v_i, v_f)$	$\sigma(v_i, v_f)$
He	3	2	$(5.9 \pm 0.6) \times 10^{-12}$	$(4.6 \pm 0.5) \times 10^{-17}$
		4	$(1.0 \pm 0.1) \times 10^{-12}$	$(8.1 \pm 1.1) \times 10^{-18}$
	4	3	$(8.4 \pm 0.8) \times 10^{-12}$	$(6.6 \pm 0.6) \times 10^{-17}$
		5	$(1.7 \pm 0.2) \times 10^{-12}$	$(1.3 \pm 0.2) \times 10^{-17}$
	5	4	$(1.1 \pm 0.2) \times 10^{-11}$	$(8.8 \pm 1.4) \times 10^{-17}$
		6	$(1.9 \pm 0.3) \times 10^{-12}$	$(1.5 \pm 0.2) \times 10^{-17}$
	6	5	$(1.3 \pm 0.2) \times 10^{-11}$	$(1.1 \pm 0.2) \times 10^{-16}$
		7	$(2.2 \pm 0.3) \times 10^{-12}$	$(1.7 \pm 0.3) \times 10^{-17}$
	7	6	$(1.4 \pm 0.2) \times 10^{-11}$	$(1.1 \pm 0.2) \times 10^{-16}$
		8	$(2.5 \pm 0.4) \times 10^{-12}$	$(2.0 \pm 0.3) \times 10^{-17}$
Ne	3	2	$(1.4 \pm 0.2) \times 10^{-12}$	$(2.4 \pm 0.4) \times 10^{-17}$
		4	$(5.5 \pm 0.8) \times 10^{-13}$	$(9.2 \pm 0.1) \times 10^{-18}$
N_2	3	2	$(2.8 \pm 0.6) \times 10^{-12}$	$(5.4 \pm 1.2) \times 10^{-17}$
	4	3	$(4.2 \pm 0.5) \times 10^{-12}$	$(8.0 \pm 1.0) \times 10^{-17}$
F_2	3	2	$(5.8 \pm 0.5) \times 10^{-12}$	$(1.3 \pm 0.1) \times 10^{-16}$

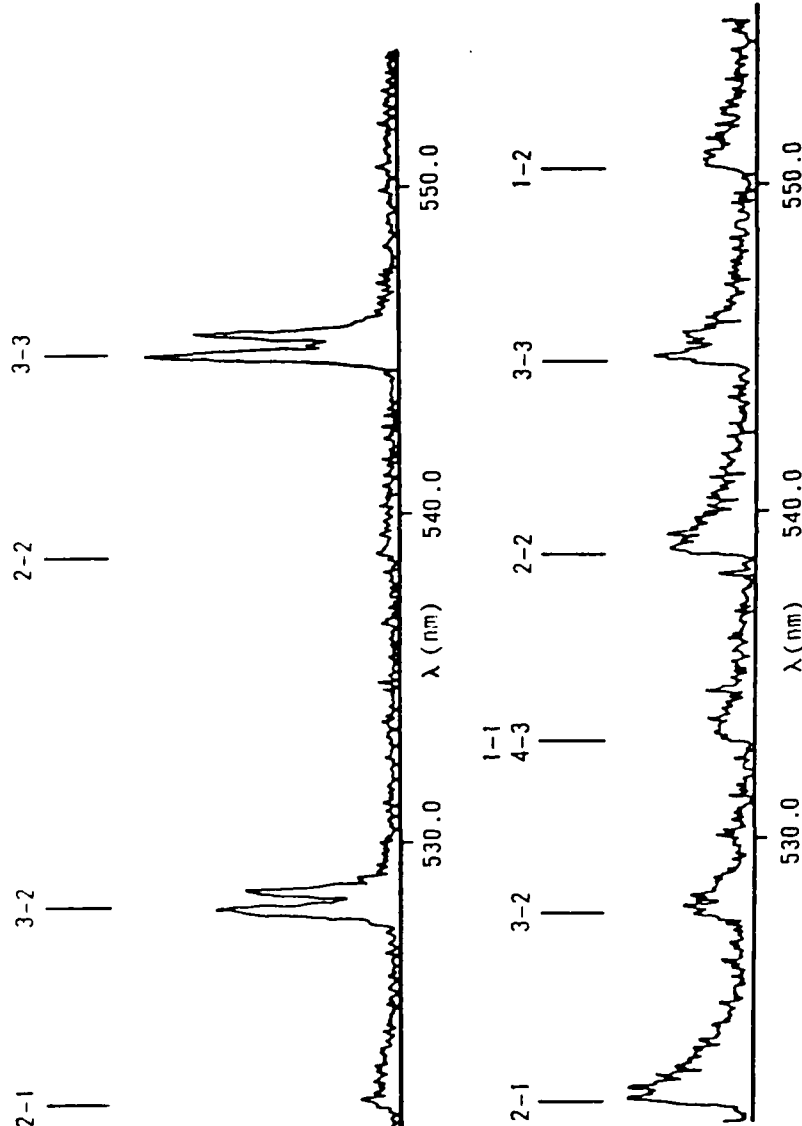


Figure 4-13. Spectrally resolved IF(B) fluorescence emission showing the development of vibrational satellite bands by energy transfer with He: upper spectra, $P(\text{He}) = 0.0$ Torr; lower spectra, $P(\text{He}) = 400$ mTorr.

$v'=2$ state is also noticable. The residual He in the cell was previously estimated as 6×10^{13} atoms cm^{-3} and may be responsible for this initial population redistribution. However, residual I_2 was also observed in the chamber prior to the addition of the bath gas as discussed in Chapter III. As shown in the time resolved experiments, the presence of residual I_2 forms a kinetically active background which may affect the B state population distribution. Therefore, it is unclear whether this redistribution is due to residual He or residual I_2 . We can only conclude that this initial redistribution is due to both species. Typically, the population in $v'=2$ was less than one percent of the total B state population at base pressure conditions, and represented a negligible perturbation in the initial B state population. The emission from the $v'=3$ level also shows the characteristic P-R doublet structure originating from the initial J' level.

As the He pressure is increased to 400 mTorr (Fig. 4-13b), a substantial number of molecules have been transferred to other vibrational levels, even though there remains a noticable emission from $v'=3$. Also, the characteristic P-R doublet structure from the initial J' level has disappeared resulting in the formation of a well defined band head. This indicates a significant rotational redistribution in $v'=3$.

The fluorescence emission spectra, such as in Fig. 4-13, were used to extract the relative vibrational population distributions by determining the area under each vibrational band. This procedure is detailed in Appendix I. Vibrational bands used in this analysis were chosen based on their large Franck-Condon factors and isolated positions which pre-

vented band overlap. Typically, three to four spectra were obtained for each v' level which allowed us to make consistency checks on the relative population determinations.

The area, $A_{v',v''}$ of an isolated band (v',v'') is related to the population of the v' level, $N_{v'}$, through the equation

$$A_{v',v''} = C N_{v'} q_{v',v''} \nu^3 \alpha(\nu) \quad (4-6)$$

where $q_{v',v''}$ is the Franck-Condon factor, ν is the transition frequency, C is a constant, and $\alpha(\nu)$ is the relative efficiency of the detection system (see Appendix H). The transition frequencies were taken at the band heads of the vibrational transitions while the values of $q_{v',v''}$ were obtained from the RKR potential calculations of Clyne and Mc Dermid.⁹

Using Eq.(4-6), we calculated the relative vibrational populations at various bath gas pressures. Figure 4-14 shows an example of this analysis where the relative populations were calculated from the transfer spectra like those shown in Fig. 4-13 by determining the ratios $N(v')/N$. The frame with no added He shows only emission from the initially prepared, $v'=3$ level. (The relative population of vibrational levels collisionally populated due to $\text{IF(B)}-\text{I}_2/\text{He}$ collisions are not shown since these populations were less than one percent of the total B state number density.) As He is added, the $v'=3$ population is redistributed forming collisionally populated satellite bands. The redistribution favors the population of the lower vibrational levels with the population in $v'=4$ never exceeding five percent of the total B state number density at the highest pressure.

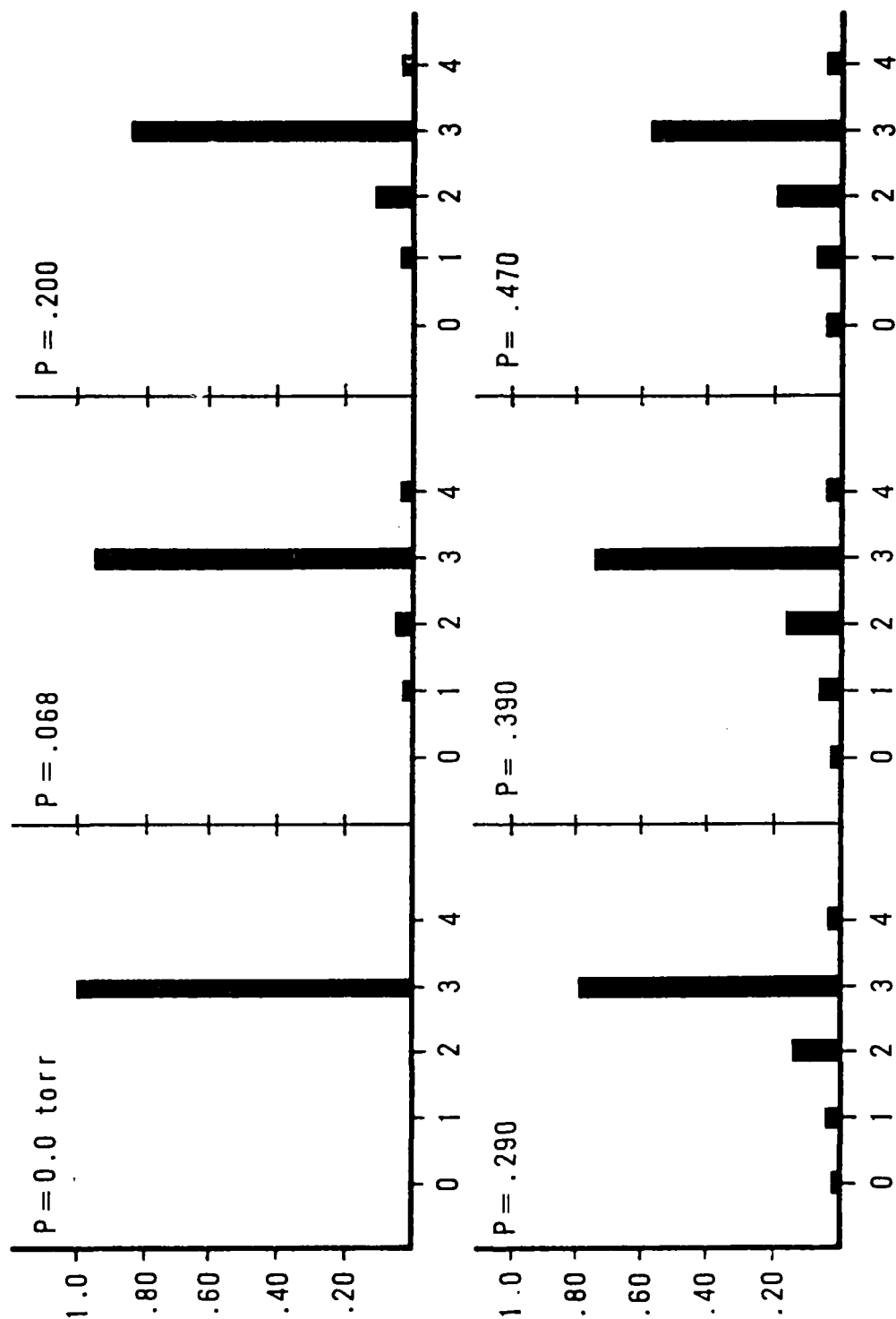


Figure 4-14. Relative steady-state IF(B) vibrational population distributions as a function of He pressure.

The values of the relative populations, $N(v')/N$ and $N(v')/N(v_1')$, were inserted into Eqs.(2-7b) and (2-8b) to extract the rate constants. As discussed in Chapter II, Eqs.(2-7b) and (2-8b) were developed by including a rate describing electronic quenching and vibrational transfer by background gases. The best estimates for these rate constants (obtained from the zero pressure intercepts in the pulsed experiments) for insertion into these equations were:

$$v' = 1 \quad R_B N_B \sim 1.0 \times 10^4 \text{ s}^{-1}$$

$$v' = 3 \quad R_B N_B \sim 3.6 \times 10^4 \text{ s}^{-1}$$

$$v' = 6 \quad R_B N_B \sim 1.8 \times 10^5 \text{ s}^{-1}$$

Figure 4-15 shows the plots of Eqs.(2-7b) and (2-8b) for extracting the vibrational transfer rate constants with He as the bath gas. The rate constants are obtained from the slope of these plots, and the error bars shown in this figure are due to systematic uncertainties. (See Appendix J for a discussion of the errors.)

The correlation coefficients for the plots which showed linear behavior were greater than 0.96. Back-transfer correction calculations to these rate constants showed a negligible deviation ($\leq 7\%$) from the rate constants originally extracted from these plots. The lack of curvature in the plots was another indication that vibrational back transfer was absent. This result is rather surprising since multiple collisions (i.e., radiative rate is less than the collision frequency) are dominant at the pressures used in this study. (For example, with $P_{\text{He}} = .100$ Torr, $IF(R) - \text{He}$ collisions occur at a rate of $1.3 \times 10^6 \text{ s}^{-1}$.) The values of the

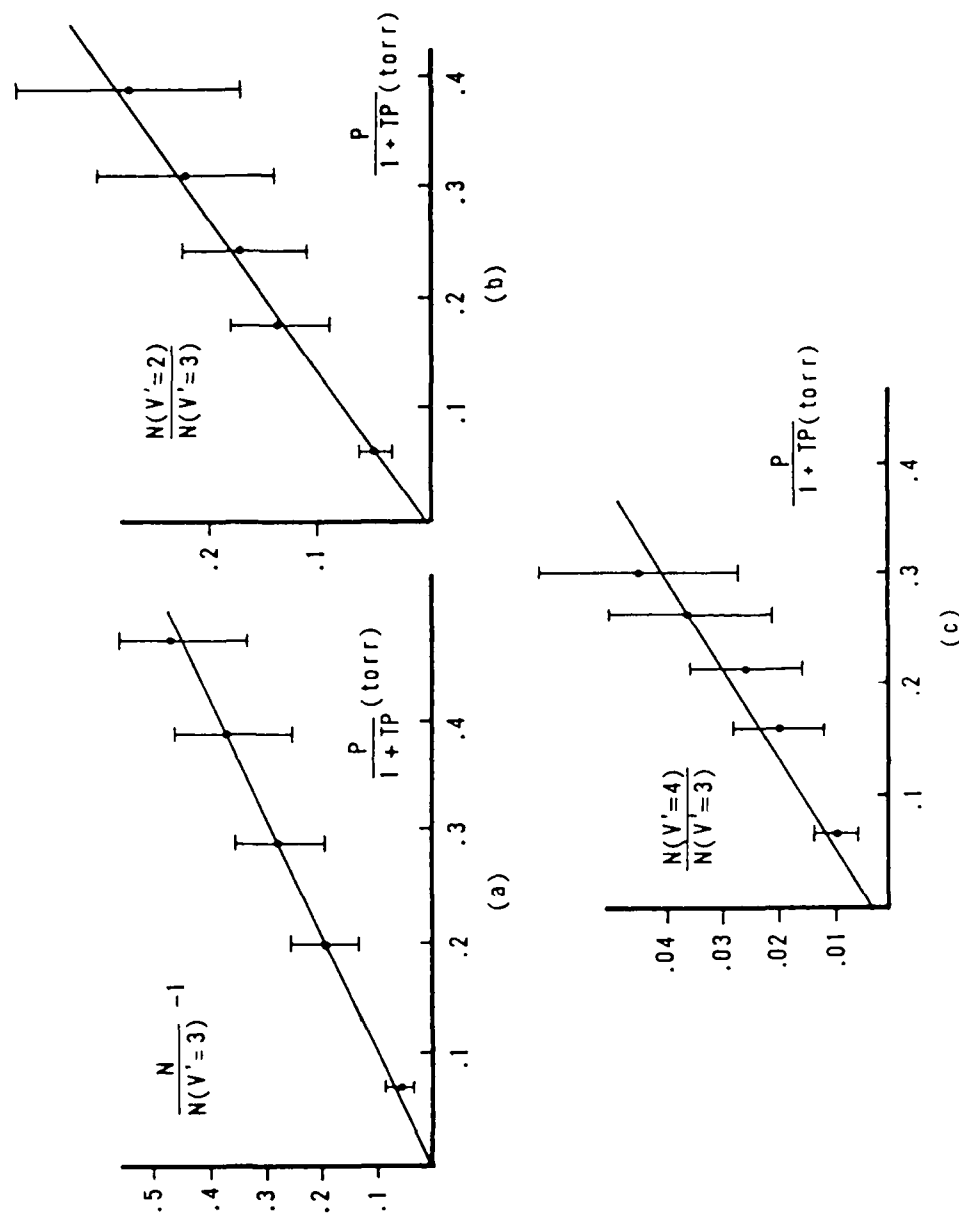


Figure 4-15. CW vibrational relaxation data for He. The slopes of the lines in (a), (b), and (c) are k' , $k(3,2)'$, and $k(3,4)'$, respectively. The error bars represent the estimated systematic uncertainties in the data.

vibrational relaxation rate constants along with the corresponding cross sections calculated from Eq.(4-5) are collected in Table 4-4. The errors quoted in this table are due to systematic uncertainties in the data.

D. Multiple Quantum Vibrational Transfer

For the following discussion, multiple quantum vibrational transfer is defined as an exchange of two or more IF(B) vibrational quanta with translational energy of the bath gas in a single V-T collision. As shown below, the cw vibrational relaxation data indicate that, to within experimental error, the magnitude of the $\Delta v = -2$ rate constants are less than 11 percent of the respective total removal rate constants for each bath gas. However, the time resolved data indicate that multiple quantum transfer may not be important.

In the cw studies, the possible presence of multiquantum transfer is examined using Eq.(2-8b) which is reproduced below.

$$N(v_f)/N(v_i) = k(v_i, v_f)'M/[1+(Q_m'+k_v')M+R_B'N_B] \quad (2-8b)$$

where $v_f = v_i \pm n$ ($n = 2, 3, 4, \dots$). Figure 4-16 shows an example of a plot of Eq.(2-8b) corresponding to a $\Delta v' = -2$ change in v_i' . The bath gas is Ar and the initially prepared state is $v' = 3$. The best fit to the data was obtained using a linear regression analysis. Similar plots were obtained with the other bath gases. The rate constants, $k(3,1)$, which were obtained from the slopes of such plots are collected in Table 4-5.

Analyses of the $v' = 0$ data were also made using Eq.(2-8b) in the $v' = 3$ excitation studies. However, we could not make meaningful conclusions from the Stern-Volmer plots because erratic behavior was observed

TABLE 4-4. CW vibrational transfer rate constants and corresponding cross sections.

BATH	v_i'	v_f	$k(v_i', v_f)$ (cm^3 molecule $^{-1}$ sec $^{-1}$)	$\sigma(v_i', v_f)$ (cm^2)
He	6	A11	$(1.4 \pm 0.5) \times 10^{-11}$	$(1.1 \pm 0.4) \times 10^{-16}$
		5	$(9.8 \pm 4.0) \times 10^{-12}$	$(7.7 \pm 3.1) \times 10^{-17}$
		7	$(1.8 \pm 0.8) \times 10^{-12}$	$(1.4 \pm 0.6) \times 10^{-17}$
	3	A11	$(5.6 \pm 2.0) \times 10^{-12}$	$(4.4 \pm 1.6) \times 10^{-17}$
		2	$(4.9 \pm 1.8) \times 10^{-12}$	$(3.8 \pm 1.4) \times 10^{-17}$
		4	$(7.2 \pm 3.2) \times 10^{-13}$	$(5.7 \pm 2.5) \times 10^{-18}$
	1	A11	$(2.1 \pm 0.8) \times 10^{-12}$	$(1.7 \pm 0.6) \times 10^{-17}$
		0	$(1.7 \pm 0.7) \times 10^{-12}$	$(1.4 \pm 0.5) \times 10^{-17}$
		2	$(4.7 \pm 2.1) \times 10^{-13}$	$(3.9 \pm 1.7) \times 10^{-18}$
Ne	3	A11	$(1.7 \pm 0.7) \times 10^{-12}$	$(2.8 \pm 1.2) \times 10^{-17}$
		2	$(1.3 \pm 0.5) \times 10^{-12}$	$(2.2 \pm 0.9) \times 10^{-17}$
		4	$(3.7 \pm 1.6) \times 10^{-13}$	$(6.1 \pm 2.6) \times 10^{-18}$
	1	A11	$(5.0 \pm 1.8) \times 10^{-13}$	$(8.5 \pm 3.0) \times 10^{-18}$
		0	$(3.8 \pm 1.5) \times 10^{-13}$	$(6.3 \pm 2.5) \times 10^{-18}$
		2	$(1.0 \pm 0.4) \times 10^{-13}$	$(1.8 \pm 0.7) \times 10^{-18}$
Ar	3	A11	$(1.2 \pm 0.4) \times 10^{-12}$	$(2.6 \pm 0.9) \times 10^{-17}$
		2	$(8.8 \pm 0.4) \times 10^{-13}$	$(2.0 \pm 0.1) \times 10^{-17}$
		4	$(1.4 \pm 0.6) \times 10^{-13}$	$(3.2 \pm 1.4) \times 10^{-18}$

TABLE 4-7. Total rotational relaxation rate constants and corresponding cross sections. The errors are (1σ) from the mean.

GAS	k_r (10^{-11} cm ³ molecule ⁻¹ s ⁻¹)	σ_r (10^{-15} cm ²)
He	9.67 \pm 1.30	0.76 \pm .10
Ne	9.80 \pm 2.00	1.64 \pm .33
Ar	10.80 \pm 1.65	2.41 \pm .36
Kr	12.50 \pm 1.43	3.63 \pm .42
Xe	11.20 \pm 1.30	3.69 \pm .43
N ₂	11.00 \pm 1.95	2.13 \pm .38

method for determining this ratio is detailed in Appendix I. Vibrational backtransfer corrections were not applied to the data since this effect was negligible in the cw vibrational transfer experiments. The plot of Eq.(2-9b) is shown in Fig. 4-20, where $P' = P/[1 + (Q_m' + k_v')P + R_B'N_B]$ with P , the bath gas pressure in Torr. All of these plots show a curvature at $P' > 0.08$ Torr ($P(\text{bath}) \geq 0.15$ Torr). The initial linear section of these plots at low pressures is due to rotational relaxation while the nearly flat portion at high pressures indicates that rotational thermalization has been achieved as demonstrated below. Therefore, the rotational relaxation rate constants were obtained in the low pressure limit (linear portion) of these plots. The rate coefficients extracted from the initial slopes represent lower limits for R-T energy transfer. The results are listed in Table 4-7.

The vibrational band envelope shown in Fig. 4-19c is composed of P and R lines which represent transitions from rotational states that have

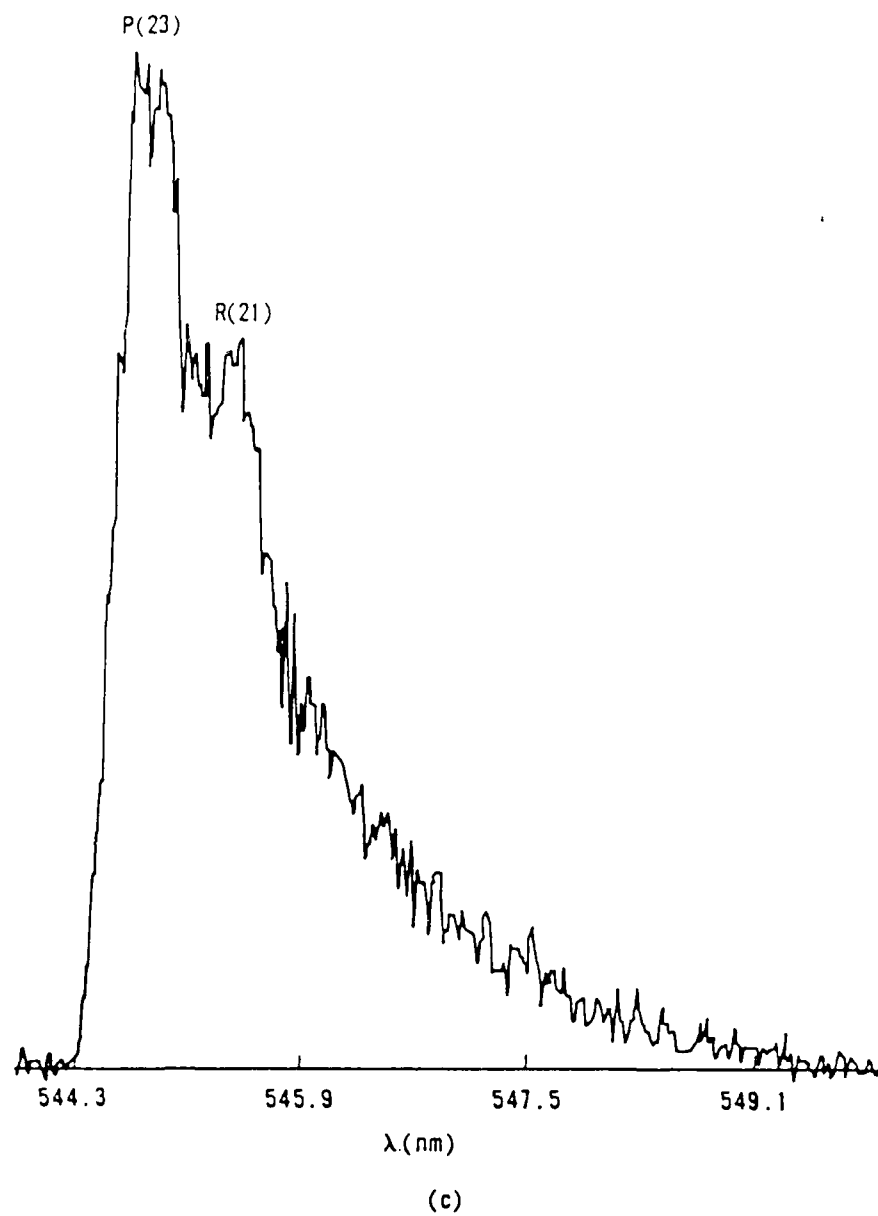


Figure 4-19c. IF(B; $v'=3$) rotational population re-distribution with 200 mTorr of added He.

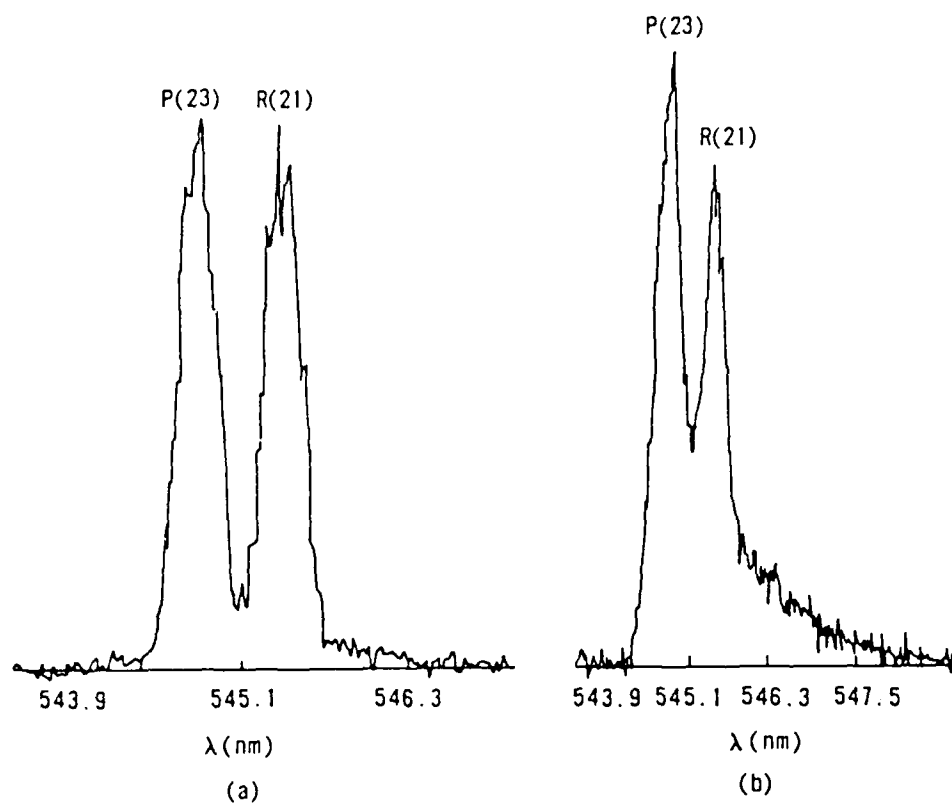


Figure 4-19. IF(B; $v' = 3$) fluorescence emission showing the rotational population redistribution from $J' = 22$ with He bath gas: (a) $P(\text{He}) = 0$ mTorr and (b) $P(\text{He}) = 30$ mTorr.

further complicated by the presence of residual I_2 since V-V effects with this gas will also contribute to the short time dependence of the decay curve.

E. Rotational Relaxation

1. Rate Constants

Figure 4-19 shows the rotational redistribution of the initial $J' = 22$ population in $v' = 3$ as He is added to the system. In Fig. 4-19a, the fluorescence emission originates from the initially prepared J' level. The width of the P-R doublet emission lines in this figure is due to the monochromator's instrumental resolution (0.25 nm). The addition of He forces a redistribution of rotational population from $J' = 22$ to neighboring rotational states resulting in a broadening of the original P-R doublet emission as seen in Fig. 4-19b. This population redistribution occurs about equally on both sides of the initial rotational level with the blue end forming a bandhead corresponding to a $\Delta J' \sim 20$. A tail is formed toward the red end of the spectrum which corresponds to a J' change of about 23. At higher bath gas pressures, the tail becomes less extensive due to multiple collisions which seek to establish an equilibrium distribution as seen in Fig. 4-19c. Thus, an additional redistribution occurs in the collisionally populated states which forces the population toward the Boltzmann maximum.

The total rate of removal from $J' = 22$ was obtained by applying Eq.(2-9b) using the $k_{v'}$ values from the cw experiments and the $R_B N_B$ values determined previously. The ratio of $N(J' = 22)/N(v' = 3)$ was obtained from an analysis of the spectra such as shown in Fig. 4-19. The

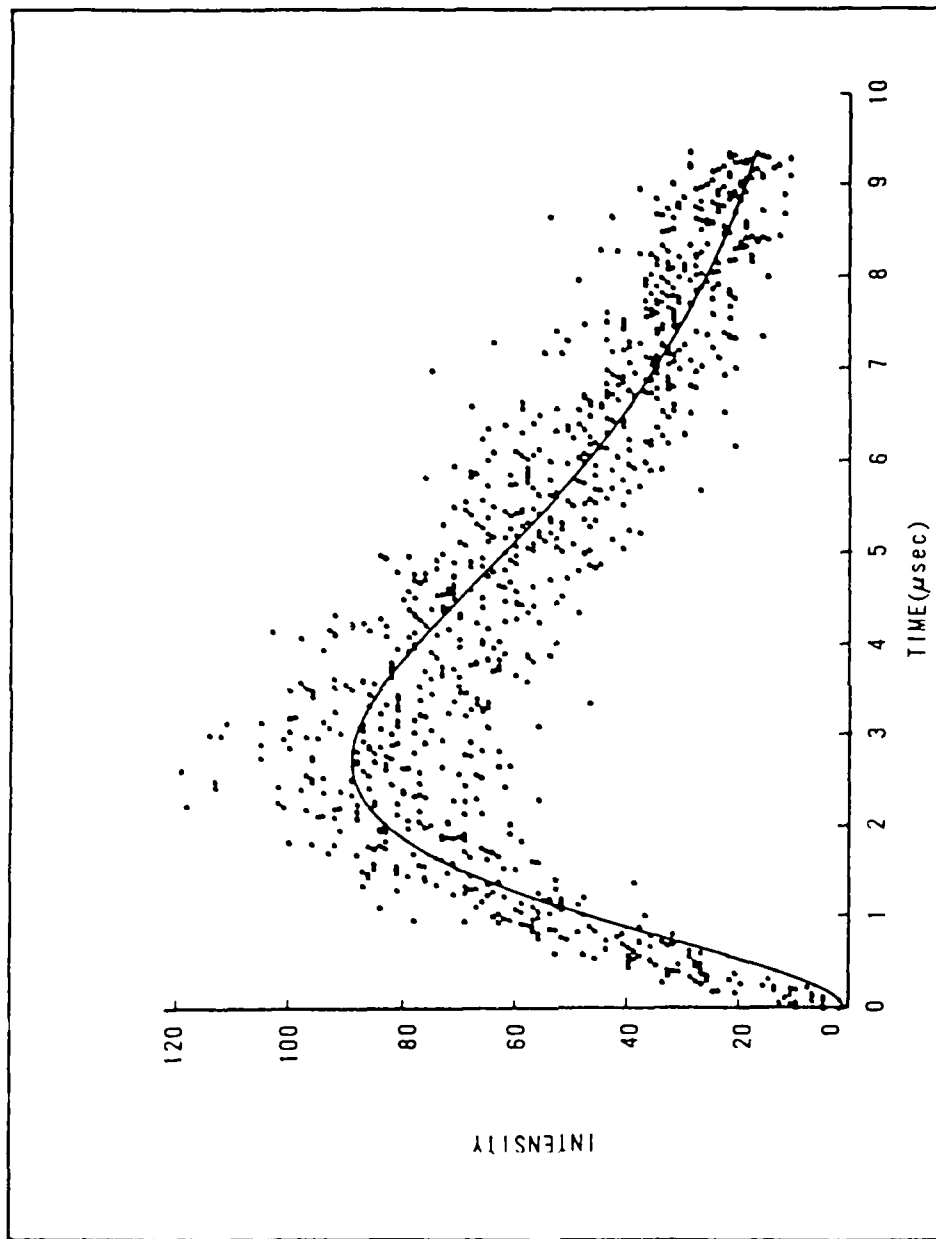


Figure 4-18. Comparison of data and fit using the Montroll-Shuler model for the decay of a $\Delta v = -2$ transfer band. The initially prepared state was $v' = 6$ with 60 mTorr of Ne bath gas.

population is observed until ~ 220 mTorr of He is added to the system. To within our ability to read these spectra which is limited by noise, essentially no relaxation is observed at He pressures below 200 mTorr. From these spectra, it appears that population of $v'=2$ occurs through single quantum transitions since there is a pressure induction region where $v'=2$ population becomes observable only after a significant population accumulates in $v'=3$.

As shown in Appendix K, single quantum transitions are recognized in fluorescence decay curves by a t^2 dependence at short times in a $\Delta v = -2$ transfer band. To determine what short times are, it must be remembered that $\Gamma t \ll 1$, where $\Gamma = kM$, so we can series expand the exponential in Eq.(K-7). For this discussion, we use a rate constant, $k(3,2)$, which has a value of $5 \times 10^{-12} \text{ cm}^3 \text{ molecule}^{-1} \text{ s}^{-1}$ as measured with He. Thus, at 220 mTorr of He, Γ is $3.5 \times 10^4 \text{ s}^{-1}$. To satisfy the inequality, $\Gamma t \ll 1$, we must have $t < 2.8 \mu\text{s}$. This time scale is easily observed in Fig. 4-17. However, it is quite difficult to accurately determine the short time dependence of these decay curves since there is relatively little population in $v'=2$. The background noise simply inhibits one from drawing any conclusions from this figure. Figure 4-18 emphasizes this point. In this figure, we see a computer fit to the data using the Montroll-Shuler model (assuming a two step cascade) for a $v'=6 \rightarrow v'=4$ transfer with 60 mTorr of Ne. At short times, the fitted curve may show some indication of a t^2 dependence. The fit to the data is quite good and notice that it is nearly impossible to, at least qualitatively, determine the time dependence of the experimental decay curve at short times. The problem is

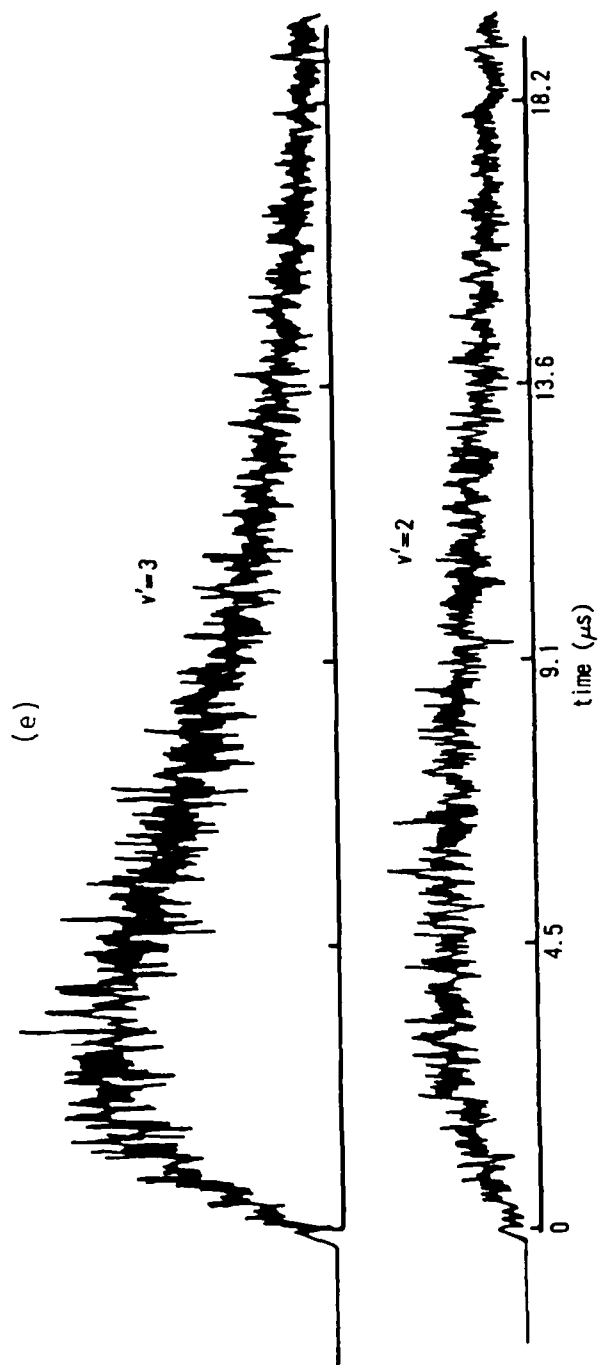


Figure 4-17e. Temporal history of the collisionally populated $v'=3$ and $v'=2$ states subsequent to initial population of $v'=4$ with 275 mTorr of He bath gas.

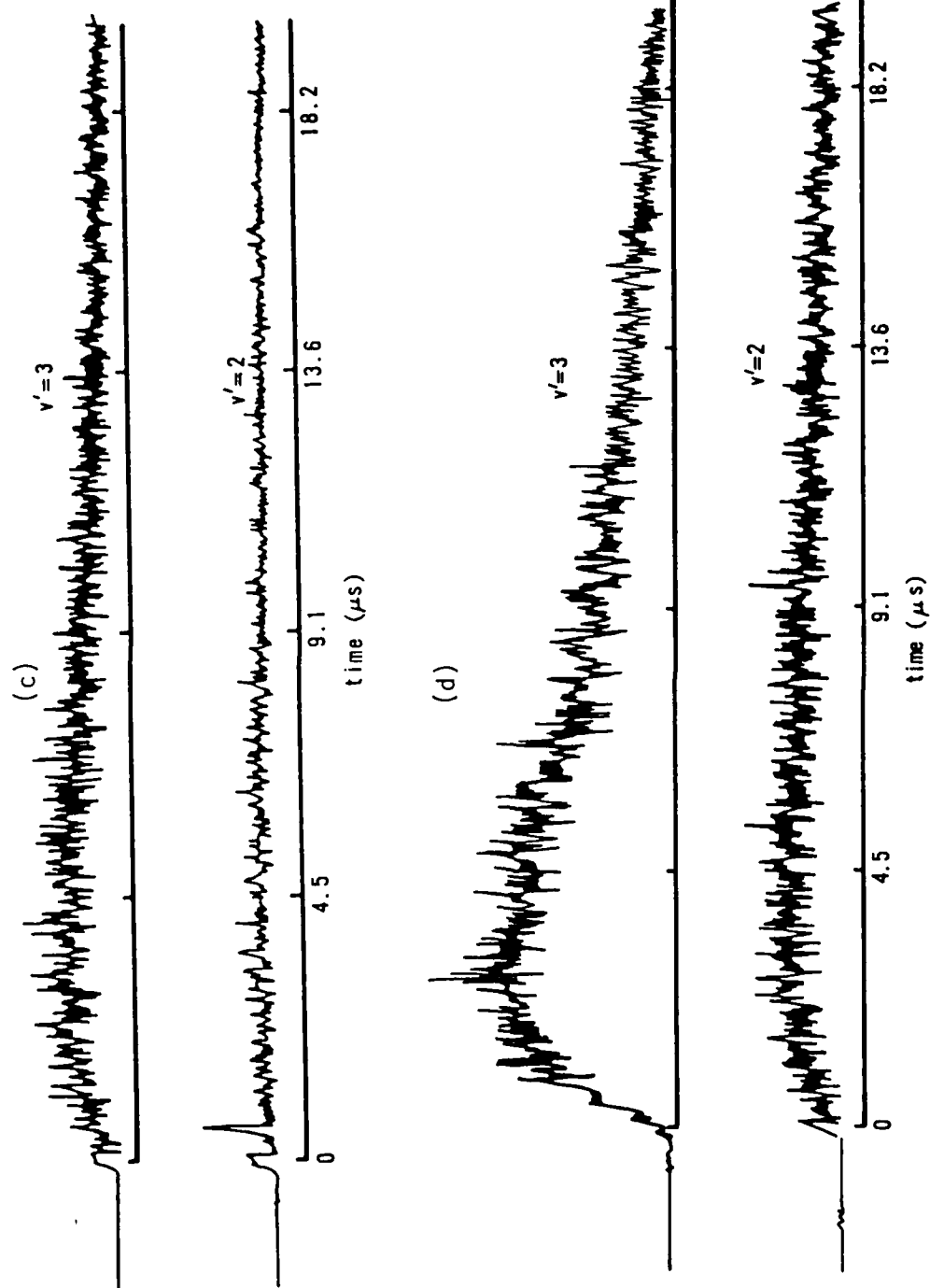


Figure 4-17. Temporal histogram of the collisionally populated $v'=3$ and $v'=2$ states subsequent to initial population of $v'=4$ with He bath gas: (c) $P(\text{He}) = 80 \text{ mTorr}$ and (d) $P(\text{He}) = 200 \text{ mTorr}$.

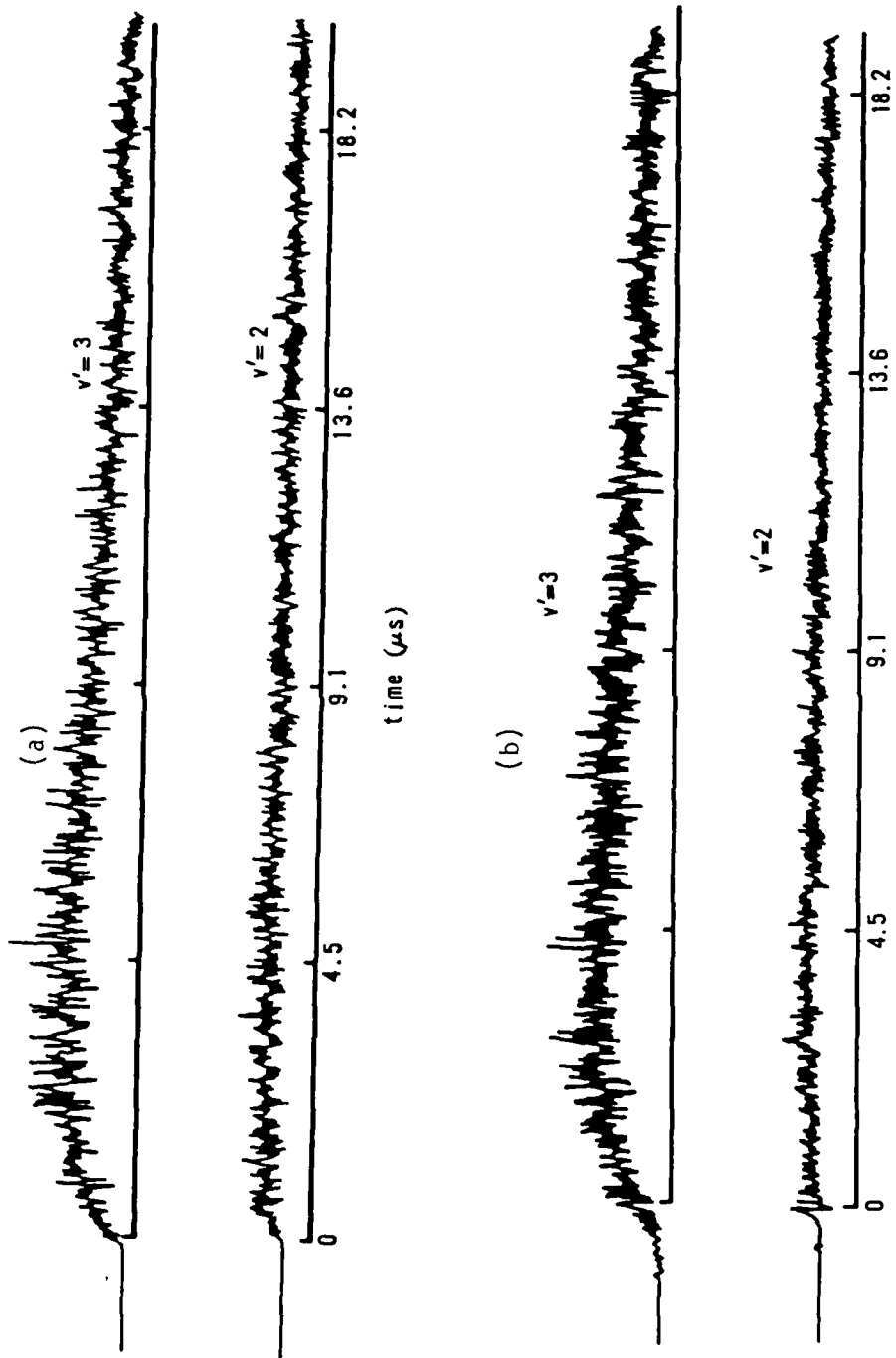


Figure 4-17. Temporal history of the collisionally populated $v' = 3$ and $v' = 2$ states subsequent to initial population of $v' = 4$ with He bath gas: (a) $P(\text{He}) = 0$ mTorr and (b) $P(\text{He}) = 12$ mTorr.

TABLE 4-6. Vibrational relaxation rate constant ratios for the initial excitation of $v'=3$ in the cw experiments.

BATH	$k(3,2)/k_v$	$k(3,4)/k_v$	$k(3,1)/k_v$	$[k(3,2)+k(3,4)]/k_v$
He	.88	.13	.11	1.01
Ne	.76	.11	.12	.87
Ar	.73	.15	.11	.88
Kr	.70	.17	.12	.87
Xe	.94	.22	.17	1.06
N ₂	.80	.16	.05	.96
Avg	$(.80 \pm .09)$	$(.16 \pm .04)$	$(.11 \pm .04)$	$(.96 \pm .08)$

maximum rate at which $\Delta v = -2$ transfer bands are populated in a single collision from the initially populated level is 15 percent of the total removal rate.

A series of temporally and spectrally resolved fluorescence experiments were also conducted to examine the possibility of multiple vibrational transitions. These experiments were performed by first reducing the base pressures (i.e., no added bath gas) to about 19 mTorr which minimized vibrational relaxation by residual I₂. The temporal histories of both $v'=3$ and $v'=2$ were then monitored subsequent to $v'=4$ excitation while increasing the He bath gas pressures from 0 mTorr to 300 mTorr. Figure 4-17a shows the temporal history of $v'=3$ and $v'=2$ with no added He. In successive frames of this figure, we see that the population in $v'=3$ continually increases with increasing He pressures, but no $v'=2$

in the $N(v'=0)/N(v'=3)$ ratios as the bath gas pressure was increased. The erratic behavior was attributed to difficulty in determining the $v'=0$ populations due to extremely small signal-to-noise ratios. Typically, the population in $v'=0$ was less than two percent of the total B state number density at the highest bath gas pressures used in these experiments.

The absolute values of the rate constants listed in Table 4-5 are subject to large uncertainty. At low bath gas pressures, the population in a $\Delta v = -2$ transfer band was typically less than three percent of the total B state population at $P < 100$ mTorr of added bath gas. This resulted in small signal-to-noise ratios and, therefore, large errors. Appreciable population (i.e., $N(v' = -2) \sim 0.1N$) in a $\Delta v = -2$ transfer band was only observed after adding 300 mTorr of an efficient relaxer such as He or N_2 as shown in Fig. 4-14. Thus, the rate constants listed in Table 4-5 are considered, at best, upper limits for $\Delta v = -2$ multiple quantum transitions.

Table 4-6 shows the ratios of the $k(\Delta v = \pm 1)$ and $k(\Delta v = -2)$ rate constants to the total removal rate constants, k_v , that were obtained in the $v'=3$ cw experiments. (The estimated errors for these values are ± 40 percent.) As seen in this table, the sums of $k(\Delta v = -1)$ and $k(\Delta v = +1)$ are equal to k_v to within experimental error. This result may indicate that multiquantum transfer is not important in these studies. However, the $k(\Delta v = -2)/k_v$ ratios fall within the error bounds, and this additional information may indicate the possible presence of multiquantum vibrational transfer. Therefore, based on the experimental data, the

Table 4-5 Estimated multiple quantum vibrational transition rate constants. The values are upper limits. The units are $\text{cm}^3 \text{ molecule}^{-1} \text{ s}^{-1}$.

Bath	v_i	v_f	$k(v_i, v_f)$
He	6	4	1.5×10^{-12}
	3	1	6.2×10^{-13}
Ne	3	1	2.0×10^{-13}
Ar	3	1	1.3×10^{-13}
Kr	3	1	9.9×10^{-14}
Xe	3	1	8.6×10^{-14}
N ₂	3	1	7.9×10^{-13}
O ₂	6	4	2.6×10^{-12}
	3	1	8.7×10^{-13}

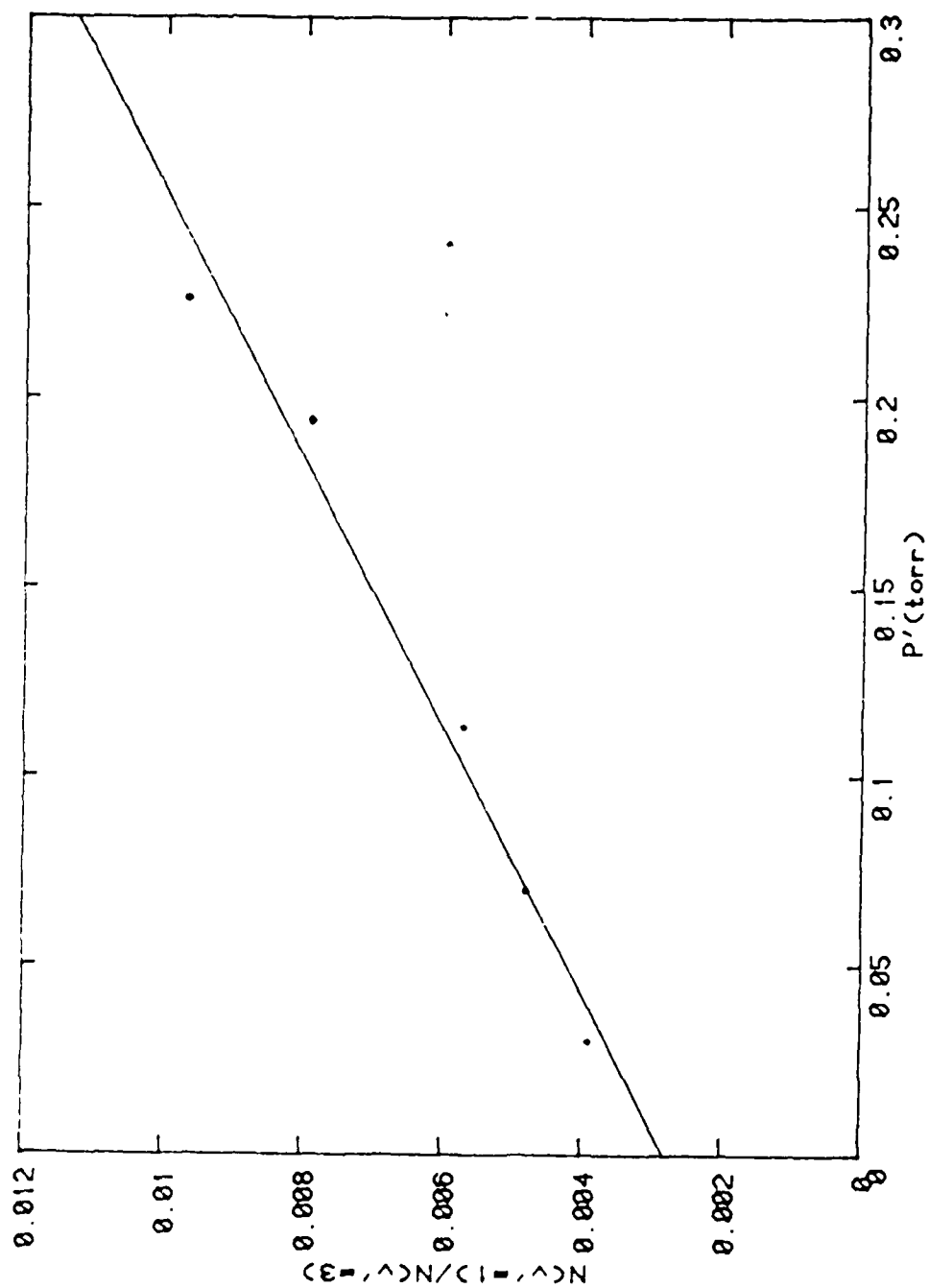


Figure 4-16. CW Stern-Volmer plot for determining the $\Delta v = -2$, multiquantum rate constant $k(3,1)$. P' is the reduced pressure which is defined as $P/(1 + (Q_m' + k_v')P + R_B' P_B)$ with P in Torr.

TABLE 4-4. (Continued)

BATH	v_i	v_f	$k(v_i, v_f)$ (cm^3 $\text{molecule}^{-1} \text{ s}^{-1}$)	$\sigma(v_i, v_f)$ (cm^2)
Kr	3	A11	$(8.3 \pm 2.9) \times 10^{-13}$	$(2.4 \pm 0.8) \times 10^{-17}$
		2	$(5.8 \pm 2.3) \times 10^{-13}$	$(1.7 \pm 0.7) \times 10^{-17}$
		4	$(1.4 \pm 0.6) \times 10^{-13}$	$(4.0 \pm 1.7) \times 10^{-18}$
Xe	3	A11	$(5.1 \pm 1.9) \times 10^{-13}$	$(1.6 \pm 0.6) \times 10^{-17}$
		2	$(4.8 \pm 1.5) \times 10^{-13}$	$(1.6 \pm 0.5) \times 10^{-17}$
		4	$(1.1 \pm 0.5) \times 10^{-13}$	$(3.8 \pm 1.6) \times 10^{-18}$
N ₂	3	A11	$(4.0 \pm 1.4) \times 10^{-12}$	$(7.7 \pm 2.7) \times 10^{-17}$
		2	$(3.2 \pm 1.3) \times 10^{-12}$	$(6.2 \pm 2.4) \times 10^{-17}$
		4	$(6.5 \pm 2.8) \times 10^{-13}$	$(1.2 \pm 0.5) \times 10^{-17}$
	1	A11	$(2.2 \pm 0.8) \times 10^{-12}$	$(4.3 \pm 1.5) \times 10^{-17}$
		0	$(1.8 \pm 0.7) \times 10^{-12}$	$(3.6 \pm 1.4) \times 10^{-17}$
		2	$(4.8 \pm 2.1) \times 10^{-13}$	$(9.2 \pm 4.0) \times 10^{-18}$
O ₂	6	A11	$(2.4 \pm 0.8) \times 10^{-11}$	$(4.7 \pm 0.7) \times 10^{-16}$
		5	$(2.2 \pm 8.8) \times 10^{-11}$	$(4.5 \pm 1.8) \times 10^{-16}$
		7	$(2.9 \pm 1.2) \times 10^{-12}$	$(5.9 \pm 2.5) \times 10^{-17}$
	3	A11	$(7.9 \pm 2.8) \times 10^{-12}$	$(1.6 \pm 0.6) \times 10^{-17}$
		2	$(5.9 \pm 2.4) \times 10^{-12}$	$(1.2 \pm 0.4) \times 10^{-17}$
		4	$(7.4 \pm 3.2) \times 10^{-13}$	$(1.5 \pm 0.6) \times 10^{-18}$

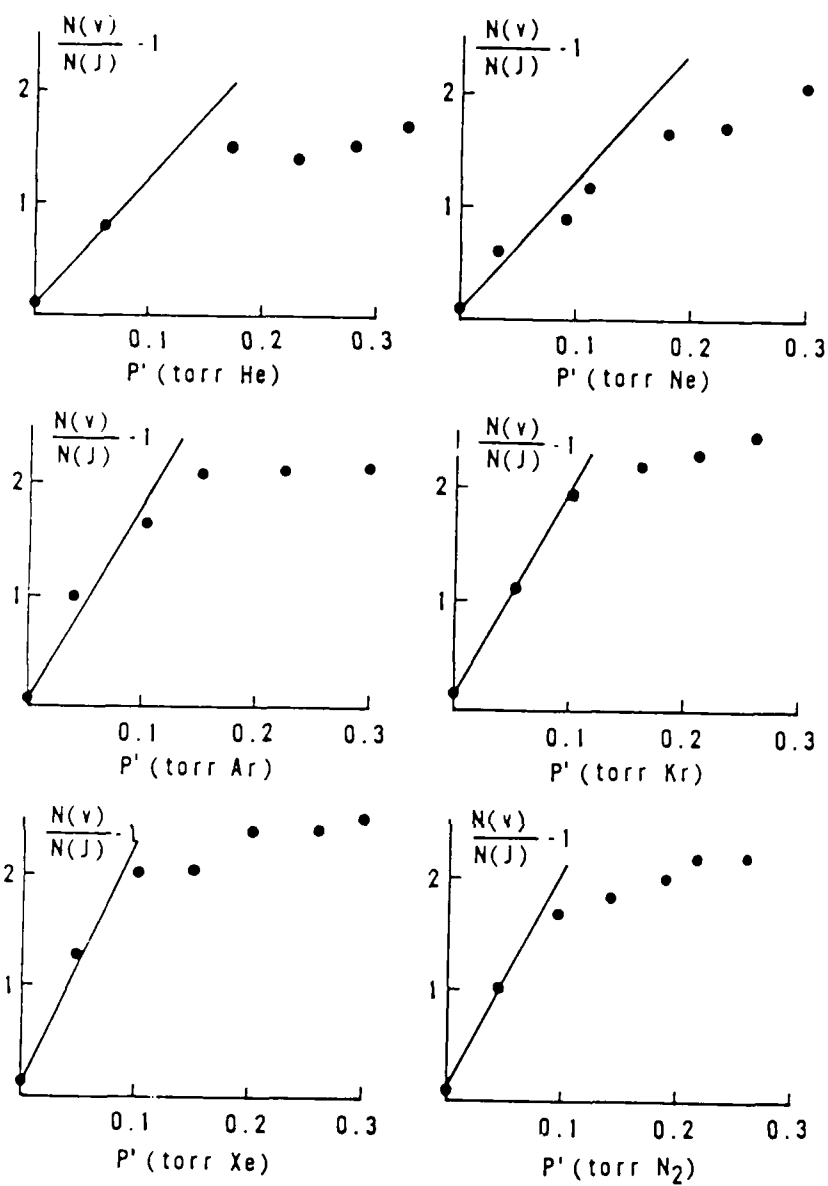


Figure 4-20. IF(B; $v'=3$) rotational relaxation data with various collision partners.

appreciable population. An estimate of the rotational temperature was obtained by first selecting two points along this curve and determining the approximate rotational level corresponding to the P(J) or R(J) line at the appropriate wavelength. Typically, the rotational level can be estimated to within $\pm(3-4)J$ levels using this method. The intensities corresponding to emission from the rotational states J_1 and J_2 were inserted into Eq.(4-7) to obtain the approximate rotational temperature, T_R .

$$\ln[I_1(J_2' + J_2'' + 1)/I_2(J_1' + J_1'' + 1)] = B_{v'} \Delta Jhc/kT_R \quad (4-7)$$

where $J = J_1'(J_1'' + 1) - J_2'(J_2'' + 1)$ and $B_{v'} = B_e - \alpha_e(v' + 1/2)$. This method was applied to several high pressure vibrational spectra for all the collision partners, and the analysis yielded an estimated rotational temperature of (312 ± 80) K. Thus, the curvature in the Stern-Volmer plots was attributed to rapid rotational thermalization resulting in a 300 K Boltzmann distribution of rotational energy levels.

2. Band Contours: Rotational Memory

An examination of the contours of transferred vibrational states may contain information about the possibility of the degree of conservation of $J' = 22$ or rotational memory. As shown in Fig. 4-19a, the initially populated rotational level is easily observed in these experiments. Thus, if complete preservation of the initially populated level occurred, one would expect to see definite P-R doublet features atop the overall contour of the vibrationally transferred bands. Furthermore, if only partial retention occurred, definite features are expected to be observed due to the sensitivity of the detection system. This structure

would then be attributed to emission from a few rotational levels having a J' value close to that of the initially pumped rotational level.

A search was made for total rotational memory in a strong $v'=2$ band since vibrational relaxation favored the population of lower vibrational levels. The preserved rotational states were also expected to be partially relaxed since, even at low bath gas densities, the degree of rotational relaxation in the initial vibrational state would be inherited by the transferred vibrational state, followed by collisional relaxation in $v'=2$ itself. Of all the $v'=2$ bands examined, no features of complete rotational memory were observed for any collision partner.

At low bath densities, the $v'=2$ bands revealed a somewhat rounded shape which may be indicative of partial rotational retention. As the collision partner density increased, the rounded band structure disappeared with the band forming a well defined head. Although partial memory could exist, the instrumental resolution was determined as the primary cause of this low pressure band structure. Furthermore, the excitation of a rotational state lying near the Boltzmann maximum (i.e. $J'=22$ in IF(B)) makes the search for partial memory more difficult since rotational memory and a collisionally relaxed distribution are indistinguishable. However, a set of runs was made in which $v'=4$ was pumped to $J'=45$. There was no discernable evidence of any rotational memory in $v'=3$.

3. Band Contours: Multiquantum Transfer

A qualitative evaluation of multiquantum rotational transfer was made by comparing band shapes produced by different gases at pressures

TABLE 4-8. Estimated J changes per collision for various collision partners. The pressures correspond to similar degrees of rotational relaxation for each bath gas.

BATH	P(torr)	$\Delta J/\text{collision}$
He	0.069	4
Ne	0.051	9
Ar	0.043	11
Kr	0.048	11
Xe	0.049	11
N ₂	0.053	8

which caused nearly identical degrees of rotational relaxation. Figure 4-21 shows a comparison of two rotationally relaxed $v'=3$ bands with He and Xe. The degree of relaxation is comparable, being 43 percent with He and 52 percent for Xe.

Both spectra reveal emission on the red side of the spectrum, terminating at about 547.9 nm. This corresponds to emission from $J' \sim 45-50$ as determined using Durie's tabulated values.⁵ At $P_{\text{He}} = 0.069$ Torr, IF(B)-He collisions occur at ~ 8 per lifetime while IF(B)-Xe collisions occur at ~ 1.8 per lifetime with $P_{\text{Xe}} = 0.049$ Torr. Thus, the change in J per collision is greater for Xe (~ 11) than for He (~ 4) at comparable degrees of rotational relaxation. Table 4-8 summarizes the estimated J changes per IF(B)-M collision for all the bath gases at similar degrees of rotational relaxation.

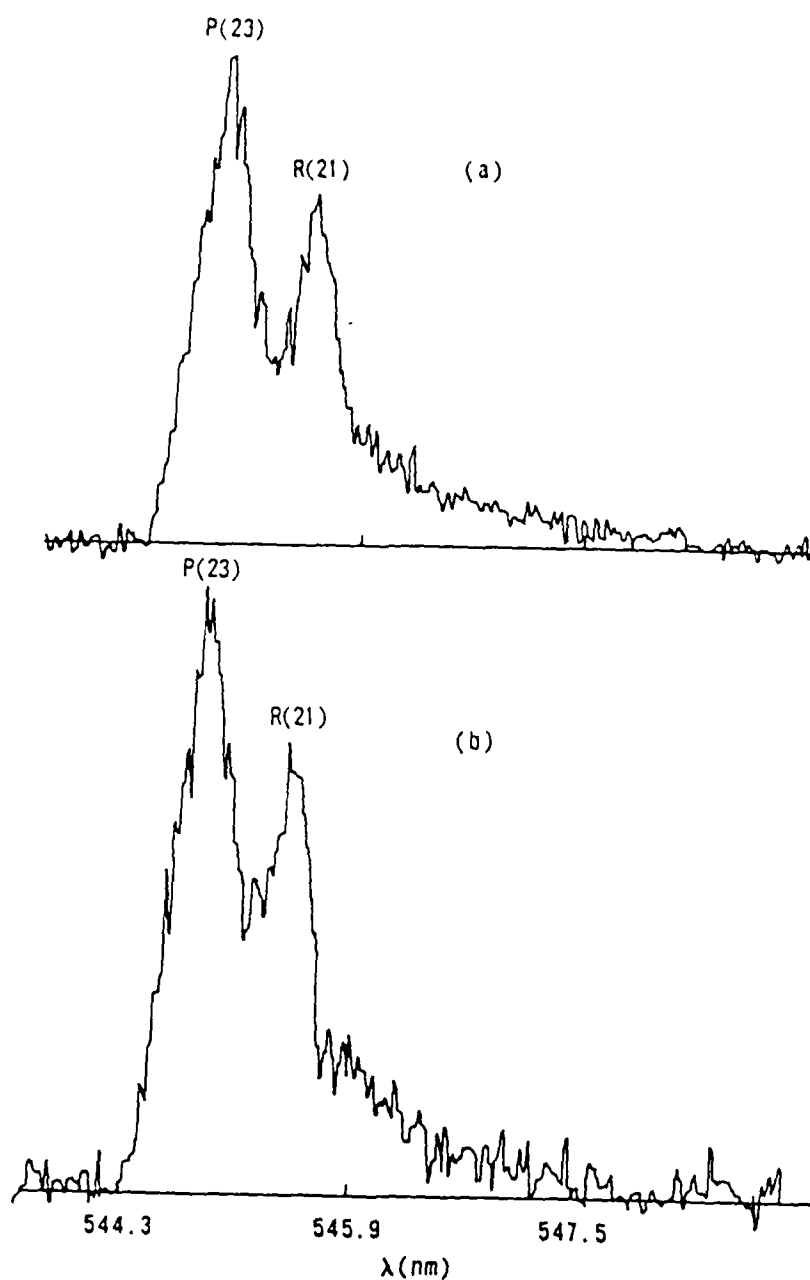


Figure 4-21. Comparison of $v' = 3$ rotational distributions with He and Xe: (a) $P(\text{He}) = 0.069$ Torr and (b) $P(\text{Xe}) = 0.049$ Torr.

These results qualitatively suggest that the lighter collision partners lead to more emission in the neighborhood of the initial J level, while the heavier gases lead to a spreading of emission over a wider range of wavelengths at comparable collision frequencies. Thus, collisional rotational redistribution seems to occur via multiquantum jumps in a single collision.

V. DISCUSSION

A. Electronic Quenching

1. Cross Sections

Tables 5-1 and 5-2 summarize the IF(B) electronic quenching cross sections, σ_q , which were calculated using Eq.(4-6). As a measure of comparison, the respective gas kinetic cross sections for IF(B) + M collisions are also listed. These gas kinetic cross sections, which were calculated using Eq.(5-1), represent the largest possible cross section value that can be obtained in the classical, hard sphere approximation.

$$\sigma_g = \pi(d_{IF} + d_M)^2/4 \quad (5-1)$$

where d_{IF} is the hard sphere diameter of IF ($\sim 4.4 \times 10^{-8}$ cm) and d_M is the molecular or atomic diameter of the collision partners. Approximate values for the collision partners, d_M , were taken from the listing compiled by Hirshfelder, Curtiss, and Bird.⁴⁵ The ratio of σ_q to σ_g (labeled P_q) is listed in the last column of Tables 5-1 and 5-2 and represents quenching probabilities (or efficiencies) based on the classical approximation.

As seen in Tables 5-1 and 5-2, collisions between IF(B) molecules and both the noble gases and N_2 were uniformly inefficient in quenching B state fluorescence. The only appreciable quenchers were O_2 , F_2 , H_2O , and I_2 . The quenching cross sections for O_2 and F_2 were a factor of 10^2 to 10^3 greater than those for the noble gases and N_2 . Iodine was the most efficient quencher with a cross section 10^5 times greater than those for

TABLE 5-1. Summary of electronic quenching cross sections, gas kinetic cross sections, and quenching probabilities. The cross sections are in units of cm^2 . See text for explanation.

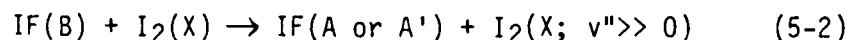
Collision Partner (initially prepared state)	σ_q	σ_g	P_q
He ($3 \leq v' \leq 8$)	$\leq 7.9 \times 10^{-20}$	3.8×10^{-15}	2.1×10^{-5}
Ne ($3 \leq v' \leq 8$)	$\leq 1.6 \times 10^{-19}$	4.1×10^{-15}	3.9×10^{-5}
Ar ($3 \leq v' \leq 8$)	$\leq 2.2 \times 10^{-19}$	4.8×10^{-15}	4.6×10^{-5}
Kr ($3 \leq v' \leq 8$)	$\leq 2.9 \times 10^{-19}$	5.0×10^{-15}	5.7×10^{-5}
Xe ($3 \leq v' \leq 8$)	$\leq 3.1 \times 10^{-19}$	5.5×10^{-15}	5.6×10^{-5}
F ₂ ($v' = 3$)	$(7.4 \pm 1.1) \times 10^{-17}$	5.0×10^{-15}	1.5×10^{-2}
($v' = 6$)	$(9.9 \pm 1.2) \times 10^{-17}$		2.0×10^{-2}
($v' = 7$)	$(1.1 \pm 0.1) \times 10^{-17}$		2.2×10^{-2}
I ₂ ($3 \leq v' \leq 6$)	9.2×10^{-15}	6.9×10^{-15}	1.30
N ₂ ($3 \leq v' \leq 8$)	$\leq 1.9 \times 10^{-19}$	5.2×10^{-15}	3.7×10^{-5}

TABLE 5-2. IF(B) deactivation cross sections and relative efficiencies for O_2 and H_2O . The cross sections are in units of cm^2 . See text for explanation.

Collision Partner (initially pre- pared state)	σ_q	σ_g	P_q
a. short time values			
H_2O ($3 \leq v' \leq 6$)	$(3.8 \pm 1.1) \times 10^{-15}$	4.0×10^{-15}	0.94
O_2 ($3 \leq v' \leq 8$)	$(1.2 \pm 0.2) \times 10^{-16}$	4.8×10^{-15}	2.5×10^{-2}
b. long time values			
H_2O ($v' = 4$)	$(2.8 \pm 0.5) \times 10^{-17}$	4.0×10^{-15}	6.9×10^{-3}
($v' = 5$)	$(6.2 \pm 1.4) \times 10^{-17}$		1.5×10^{-3}
($v' = 6$)	$(1.2 \pm 0.3) \times 10^{-16}$		3.0×10^{-2}
O_2 ($3 \leq v' \leq 8$)	$(2.1 \pm 0.3) \times 10^{-17}$	4.8×10^{-15}	4.4×10^{-3}

the noble gases and N₂. Water vapor was also very efficient in removing IF(B) population at short times. At longer times, the cross sections for H₂O were comparable to those determined for O₂ and F₂.

As discussed previously, IF(B) + O₂ collisions may induce a rapid E → E energy exchange. A similar mechanism may be responsible for the rapid IF(B) quenching by I₂(X). A potential process is described in Eq.(5-2).



The decay of IF(B; v' = 3), for example, to either of these electronic states might populate I₂(X) vibrational levels in the range from v'' = 30 to v'' = 40.

2. Comparisons to Previous Studies

The quenching efficiencies for He, N₂, and O₂ determined in the present studies agreed with the qualitative observations of Davis, Hanco, and Shea¹⁷ when lasing was observed from collisionally populated states in IF(B). The output of the optically pumped IF laser showed no degradation from 4 to 200 Torr of added He or 40 Torr of added N₂. The laser typically supported 1.9×10^4 IF(B)-He collisions per lifetime and 2.9×10^4 IF(B) - N₂ collisions per lifetime which demonstrated that the two collision partners were extremely inefficient quenchers. However, the IF laser became very unstable for O₂ pressures greater than five Torr. Under the lasing conditions, IF(B) - O₂ collisions occurred at a rate of 250 per lifetime. Furthermore, the IF(B) quenching rate constant measured in the present study due to O₂ showed that 10 collisions per lifetime were sufficient to alter the total B state population under

TABLE 5-3. Comparison of B state quenching cross sections (units of cm^2) given as the first number, and quenching efficiencies given in parenthesis for IF, BrF, and BrCl.

BATH	BrF	BrCl	IF
Ar	$\leq 2.1 \times 10^{-18}$ (4.9×10^{-4})	2.8×10^{-17} (6.2×10^{-3})	$\leq 2.2 \times 10^{-19}$ (4.6×10^{-5})
O ₂	4.0×10^{-17} (3.3×10^{-2})	1.1×10^{-16} (7.9×10^{-2})	2.13×10^{-17} (4.5×10^{-3})

these lasing conditions. For example, IF(B) fluorescence was quenched at a rate of $1.3 \times 10^6 \text{ s}^{-1}$ at $P(\text{O}_2) = 5 \text{ Torr}$. This first order quenching rate was a factor of 10 greater than either the spontaneous ($1.3 \times 10^5 \text{ s}^{-1}$) or estimated stimulated ($3.4 \times 10^5 \text{ s}^{-1}$) emission rates.¹⁷ Therefore, the dominance of O₂ quenching over these radiative processes resulted in a 90 percent reduction in the IF(B) population that was available for lasing.

The results of this quenching study are directly comparable to similar studies performed in BrF(B)³⁹ and BrCl(B).⁴⁰ Table 5-3 shows a comparison of the quenching cross sections and quenching efficiencies (given in parenthesis). In Table 5-3, we see that the B state of these molecules are relatively immune to electronic quenching. In general, the results of this study agree with those obtained in the B states of the halogen species where collisional electronic quenching by various atomic and molecular collision partners was inefficient.²⁶

When electronic quenching in BrF(B)⁴⁶ with both BrF(X) and Br₂ and

BrCl(B)⁴⁷ with Cl₂ was examined in the upper vibrational manifold (vibrational levels lying near the predissociation limit), it was discovered that the cross sections approached the gas kinetic value (10⁻¹⁵ cm²). Clyne et al. postulated that collision induced predissociation through rapid V-V energy transfer provided the depletion pathway. This process, which is kinetically equivalent to electronic deactivation, was suspected to occur via collisional ladder climbing, usually in multiquantum jumps, which made electronic quenching extremely efficient.

Since IF(B) predissociates¹² at $v' = 8, J' \geq 52$ and $v' = 9, J' \geq 7$, one might expect the IF(B) depletion rate constants to show a strong dependence upon v' subsequent to the initial excitation of high lying vibrational levels. Clyne et al. indeed find this to be the case in both BrF(B)⁴⁶ and BrCl(B)⁴⁷. However, the results of the present study show that the quenching cross sections for the noble gases, N₂, I₂, and O₂ do not depend on vibrational quantum number for $3 \leq v' \leq 8 (J' < 30)$. Thus, collision induced predissociation is not important in IF(B) at the pressures used in these studies. (The dependence of the F₂ and H₂O quenching cross sections on v_i' are also too weak to account for such a process since the respective values for F₂ and H₂O change by no more than a factor of two and five from $v' = 3$ to $v' = 7$.)

This observation can be explained on the basis of the IF(B) vibrational transfer results discussed in the next section. Vibrational relaxation via $\Delta v = -1$ jumps was determined as the dominant relaxation pathway. In fact, the probability for $\Delta v = +1$ collisions was only 18 percent of that for $\Delta v = -1$ which was in agreement with detailed balance.

Therefore, the relatively large vibrational spacings ($\sim 400 \text{ cm}^{-1}$), which essentially forces relaxation to occur down the vibrational manifold, precludes upward collisional ladder climbing to predissociated vibrational levels. Further studies at even much lower pressures are required to examine the possibility of collision-induced predissociation in IF(B).

B. Vibrational Energy Transfer

1. Cross Sections

A comparison of the vibrational energy transfer cross sections listed in Tables 4-2, 4-3, and 4-4 show that the values obtained in both the cw and time resolved experiments are in good agreement to within experimental error. The cw state-to-state values were about 20 to 30 percent lower than the corresponding time resolved values. The cw total removal rate constants showed better agreement, being within $\pm(15-20)$ percent of the time resolved rate constants.

Computer modeling was performed to better gauge how well the vibrational transfer rate constants obtained in both the cw and time resolved experiments agreed. The first model simulated the steady-state experiments using the rate constants determined in the pulsed experiments. The model calculation solved for the relative steady-state population distribution of nine vibrational levels. It was constrained to the initial condition that when all the transfer rates were zero (i.e., at zero bath gas pressure), all of the population resided in $v'=3$. The inputs to the model were the rates of transfer between any two levels. While there are only nine stable vibrational levels in IF(B) and population data for only five of the levels, the calculation involved a large number of levels for phy-

sical reasons. This prevented any pileup of population in the highest level by accounting for predissociative losses in $v'=9$. (All population transferred from $v'=8$ to $v'=9$ is assumed to be lost.) The calculation solved nine linearly independent equations in nine unknowns by matrix inversion. An outline of the development of this model is discussed in Appendix L.

Since the only known rate constants that were input to the model were $k(3,2)$ and $k(3,4)$, allowances were made for determining other vibrational transition rates by linearly scaling the $k(3,2)$ and $k(3,4)$ rate constants with vibrational quantum number. This assumption is not unreasonable since the rate constants listed in Tables 4-3 and 4-4 show some indication of such a scaling relationship. The rate constants, $k(3,2)$ and $k(3,4)$, inserted into the model had values of 5.9×10^{-12} and $1.0 \times 10^{-12} \text{ cm}^3 \text{ molecule}^{-1} \text{ s}^{-1}$, respectively. Figure 5-1 shows the results of this model which imitated the relative population distributions with He as the bath gas. For simplicity, only the relative populations in $v'=2, 3$ and 4 are shown. As seen in consecutive frames of this figure, the calculated vibrational state distributions mirrored the experimental values quite well. The calculated relative populations in $v'=2$ and $v'=3$ were typically 30 percent greater than the experimental values which was within the cw error estimates. Figure 5-2 shows a Stern-Volmer plot for determining the total vibrational transfer removal rate constant from $v'=3$ using the calculated distributions. The rate constant, obtained from the slope of this plot, is $6.1 \times 10^{-12} \text{ cm}^3 \text{ molecule}^{-1} \text{ s}^{-1}$. This value compares favorably with the cw experimental

energy transfer is not dominant. For $N_2 + IF(B)$ and $O_2 + IF(B)$ collisions, a V-(R,T) process may occur in which vibrational quanta in $IF(B)$ are given up to both rotation and translation in N_2 and O_2 . Similarly, V-V energy transfer may be the dominant relaxation mechanism in $IF(B) + F_2$ collisions. The vibrational constant, ω_e , for $F_2(X)$ is about 800 cm^{-1} which indicates that a $\Delta v = \pm 2$ jump in $IF(B)$ could result in a $\Delta v = \pm 1$ transition in $F_2(X)$.

Perhaps a better method to clarify the quantitative trends seen in Fig. 5-5 for the noble gases is to use the SSH theory of vibrational relaxation. From Eq.(B-10), the vibrational transfer probability should obey $\ln(P) = A - B\mu^{1/3}$ if the exponential term, $\exp[-3/2 (\Theta'/T)^{1/3}]$, dominates the behavior. Figure 5-6 shows a plot of the relative vibrational transfer cross sections, $\sigma(3,2)/\sigma_g$, vs $\mu^{1/3}$ for the noble gases. (The data were obtained from the $v'=3$, cw excitation experiments.) As seen in Fig. 5-6, the vibrational transfer probabilities monotonically decrease with increasing collision reduced mass. The qualitative agreement between the data and the predicted behavior from the SSH theory is satisfactory since changing the collision reduced mass also changes the interaction potential. This result may be thought of simply: a lower collision reduced mass involves higher velocity collisions on the average which are relatively more efficient in producing an exchange of energy.

An important trend in $IF(B)$ vibrational energy transfer was obtained when observing the dependence of the cross sections measured for a given bath gas on the initially excited vibrational level. Figure 5-7 shows a

cross sections subsequent to excitation of $v'=3$. The relative state-to-state values show the same behavior. The error bars indicate the uncertainties in the values.

In Fig. 5-5, the relative cross sections for the noble gases show a smooth, decreasing dependence on $\mu^{1/2}$ with the maximum in the transfer efficiency occurring for the lightest collision partner, He. The decreasing dependence of σ_v/σ_g vs $\mu^{1/2}$ indicates that the heavier collision partners, which have smaller average velocities, are less likely to induce collisional transitions in IF(B). Furthermore, this figure shows that the probability for vibrational energy transfer for the noble gases is very small with σ_v/σ_g being unity representing the most efficient transfer process possible on a classical basis. As discussed in Appendix B, the most effective encounter will occur when the mean collision frequency, $1/\tau_c$, is greater than the period of vibration, ν . For IF(B; $v'=3$) where $\nu = 1.2 \times 10^{13} \text{ s}^{-1}$, the product $\tau_c \nu$ will be less than unity when $\mu^{1/2}$ has a value of $1.0 (\text{amu})^{1/2}$ (assuming an interaction distance of $2.2 \times 10^{-8} \text{ cm}$ which is the approximate radius of the IF molecule). The results discussed above indicate that the translational energy of the bath gas ($E_{tr} = 200 \text{ cm}^{-1}$ at $T = 300 \text{ K}$) is not sufficient to produce a unit probability for energy transfer since the energy required for such a process must be about 400 cm^{-1} .

Figure 5-5 also shows that the diatomic collision partners do not follow the trend in $\mu^{1/2}$ as do the noble gases. In fact, no particular trend is recognizable for these gases. The anomalies in the relative efficiencies for the diatomics N_2 , F_2 , and O_2 may indicate that V-T

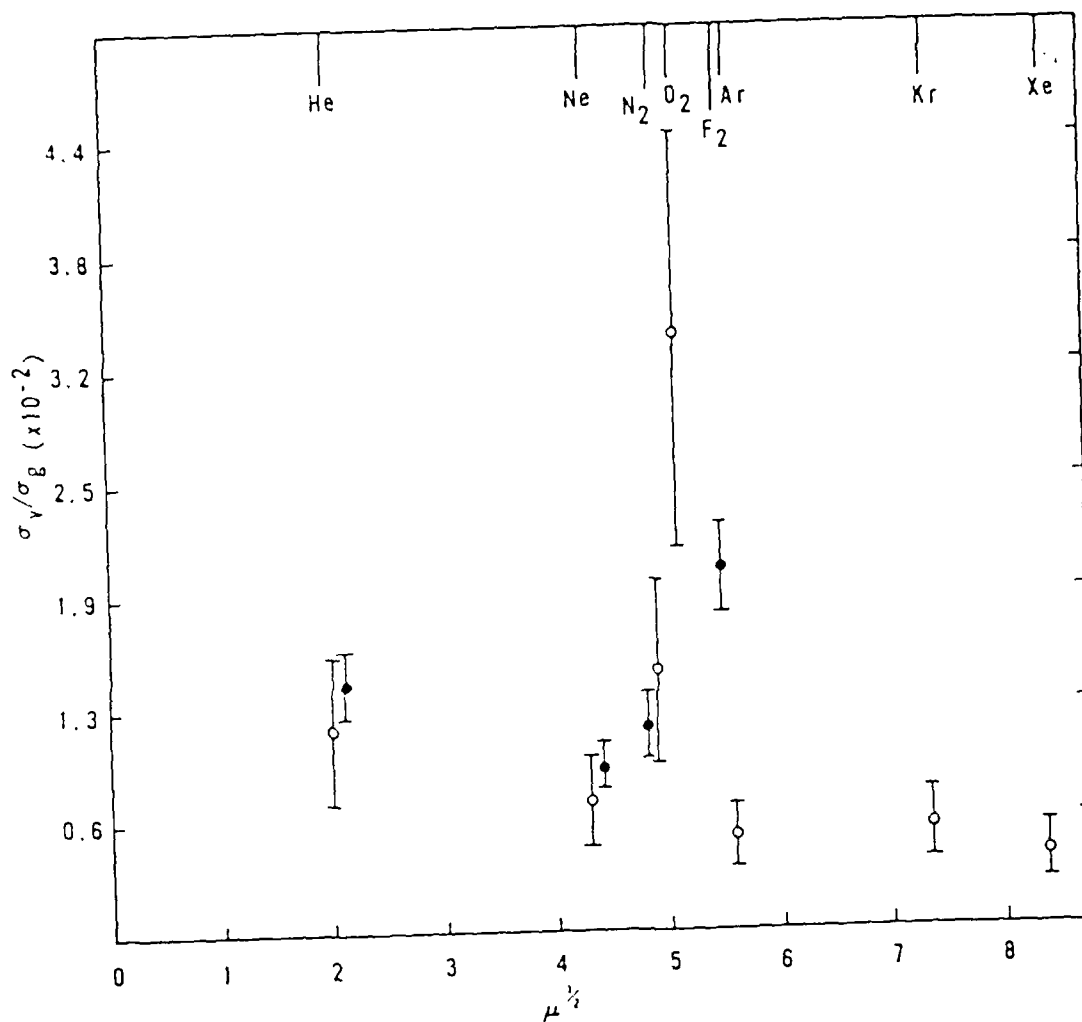


Figure 5-5. Plot of the vibrational transfer efficiencies vs. the square root of the collision reduced mass. Notation: o = steady-state values; • = time resolved values.

energy ($\sim 400 \text{ cm}^{-1}$) equal to the difference between the vibrational levels v and $v-1$ to the bath gas, than it is for the bath gas to sacrifice energy for causing an upward vibrational transition in IF(B) . Physically, the translational energy of a bath gas at room temperature is about 200 cm^{-1} . This energy is not sufficient to make upward IF(B,v) transitions highly probable since such a transition requires the bath gas to expend about 400 cm^{-1} of energy.

2. Cross Section Trends

Classically, a collisional V-T interaction between a diatomic molecule (assumed to be a harmonic oscillator) and a bath gas, M , has the highest probability for producing a change in the oscillator state when the interaction occurs along the internuclear axis of the diatomic molecule. The effectiveness of this interaction depends on both the relative velocity, v , of the collision partners and the interaction distance, ℓ . As discussed in Ref. 3, vibrational transfer is qualitatively most efficient when the period of oscillation, ν , of the molecule is comparable to the duration of the interaction (mean collision time), τ_c , where $\tau_c = \ell/v$ and $v = (8kT/\pi\mu)^{1/2}$. Therefore, a plot of the vibrational transfer cross section, σ_v , vs $\mu^{1/2}$ should give physical information on the cross section dependence on both the relative velocity of the collision partner and the mean collision time.

Figure 5-5 shows a plot of σ_v/σ_g vs $\mu^{1/2}$ where the cross sections taken from Tables 4-2, 4-3, and 4-4 were converted into estimated efficiencies or transition probabilities using Eq.(5-1). The relative cross sections shown in this figure were obtained using the total vibrational

TABLE 5-4. Ratios of $k(3,2)$ to $k(3,4)$ rate constants obtained from the cw experiments.

GAS	$k(3,4)/k(3,2)$
He	0.15
Ne	0.14
Ar	0.21
Kr	0.24
Xe	0.23
N ₂	0.20
O ₂	0.13
AVG	0.18 ± 0.04

In this equation, $V(r)$ is the perturbation Hamiltonian which leads to vibrational transitions and ΔG_v is the energy level spacing between $v'=4$ and $v'=3$. For a harmonic oscillator, the ratio of the matrix elements in Eq.(5-6) is $4/3$ using the Landau Teller scaling relationship. Then, with $\Delta G_v = 386.6 \text{ cm}^{-1}$ and $T = 300 \text{ K}$, the ratio of $k(3,4)/k(3,1)$ is 0.21. The ratios actually measured are listed in Table 5-4. The average measured value is (0.18 ± 0.04) which is in excellent agreement with the theoretical value. The principle of detailed balancing also holds for the other vibrational levels using the values obtained in both the pulsed and cw experiments.

As shown in Table 5-4, the probability for downward vibrational relaxation is greater than that for upward transfer. This result means that, in a V-T process, it is easier for IF(B) to give up an amount of

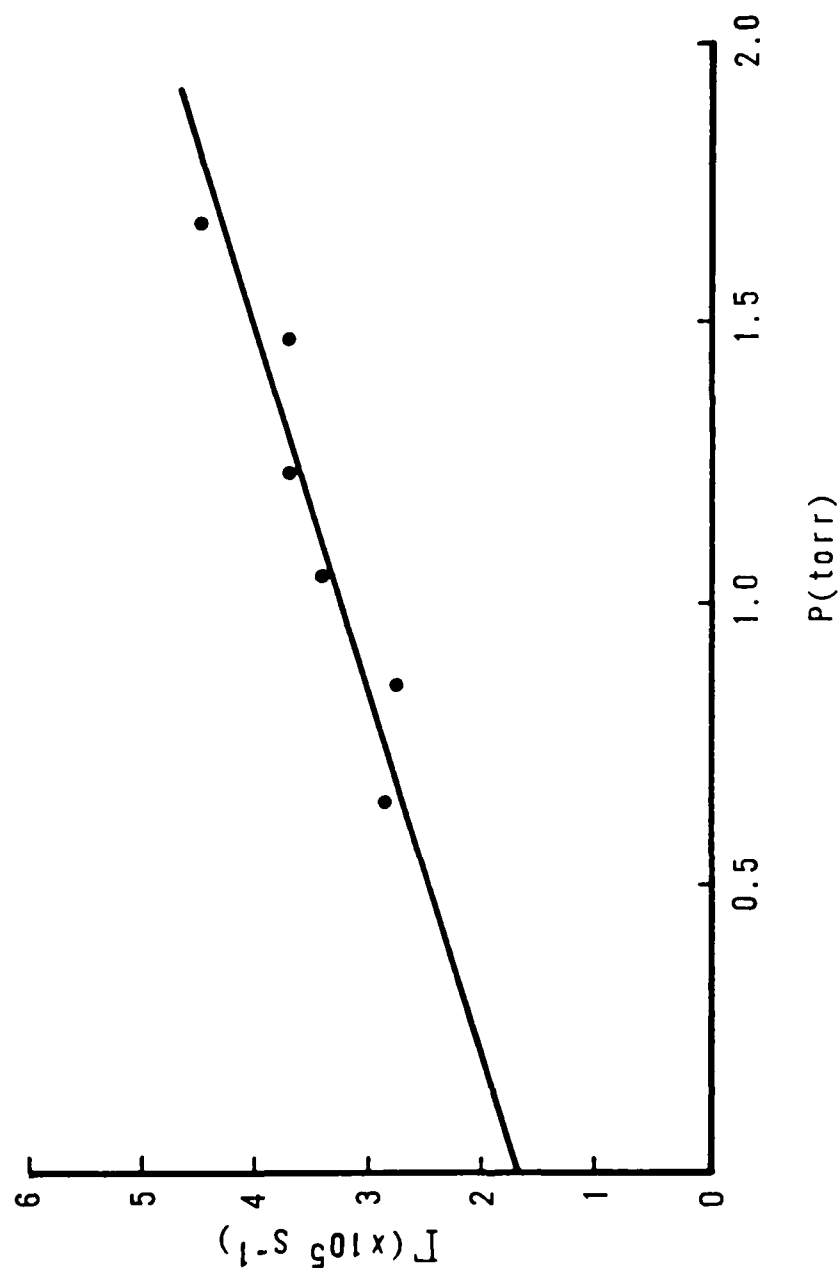


Figure 5-4. Stern-Volmer plot for determining the rate constant $k(3,2)$ from the data of Fig. 5-3b.

ere obtained from the raw data. The comparison between the two curves in Fig. 5-3c is quite good considering the simplicity of the model. The initial slope of the upper curve in Fig. 5-3b gives the rate of total removal from $v'=3$ while the long time slope gives the rate of transfer from $v'=2$ to $v'=3$. The rate constants, k_v and $k(2,3)$, were determined by plotting the decay rates at short and long times, respectively, against the bath gas pressure. Figure 5-4 shows a sample Stern-Volmer plot for determining the k_v rate constant. The value of the slope is $4.9 \times 10^{-12} \text{ cm}^3 \text{ molecule}^{-1} \text{ s}^{-1}$ which is within 25 percent of the measured rate constant obtained in the pulsed experiments. The rate constant $k(3,2)$ was determined as $1.1 \times 10^{-12} \text{ cm}^3 \text{ molecule}^{-1} \text{ s}^{-1}$. This value agrees to within 25 percent of the value obtained from detailed balance.

The measurement of the state-to-state vibrational transfer rate constants affords an opportunity to verify the principle of microscopic reversibility. This principle states that, at equilibrium, the transition rate from microscopic state i to state j is related to the rate of the reverse transition ($j \rightarrow i$) by

$$k(i,j)/k(j,i) = \exp(-\Delta G_v/kT) \quad (5-5)$$

where ΔG_v is the vibrational spacing between the vibrational states i and j . The ratio for the levels $v'=3$ and $v'=4$ in Eq.(5-5) was not directly measured, but the ratio of $k(3,4)/k(3,2)$ is known. The relation between these rate constants is

$$\frac{k(3,4)}{k(3,2)} = \frac{k(3,4)}{k(4,3)} \times \frac{k(4,3)}{k(3,2)} = \frac{\exp -\Delta G_v}{kT} \left| \frac{\langle 4 | V(r) | 3 \rangle}{\langle 3 | V(r) | 2 \rangle} \right|^2 \quad (5-6)$$

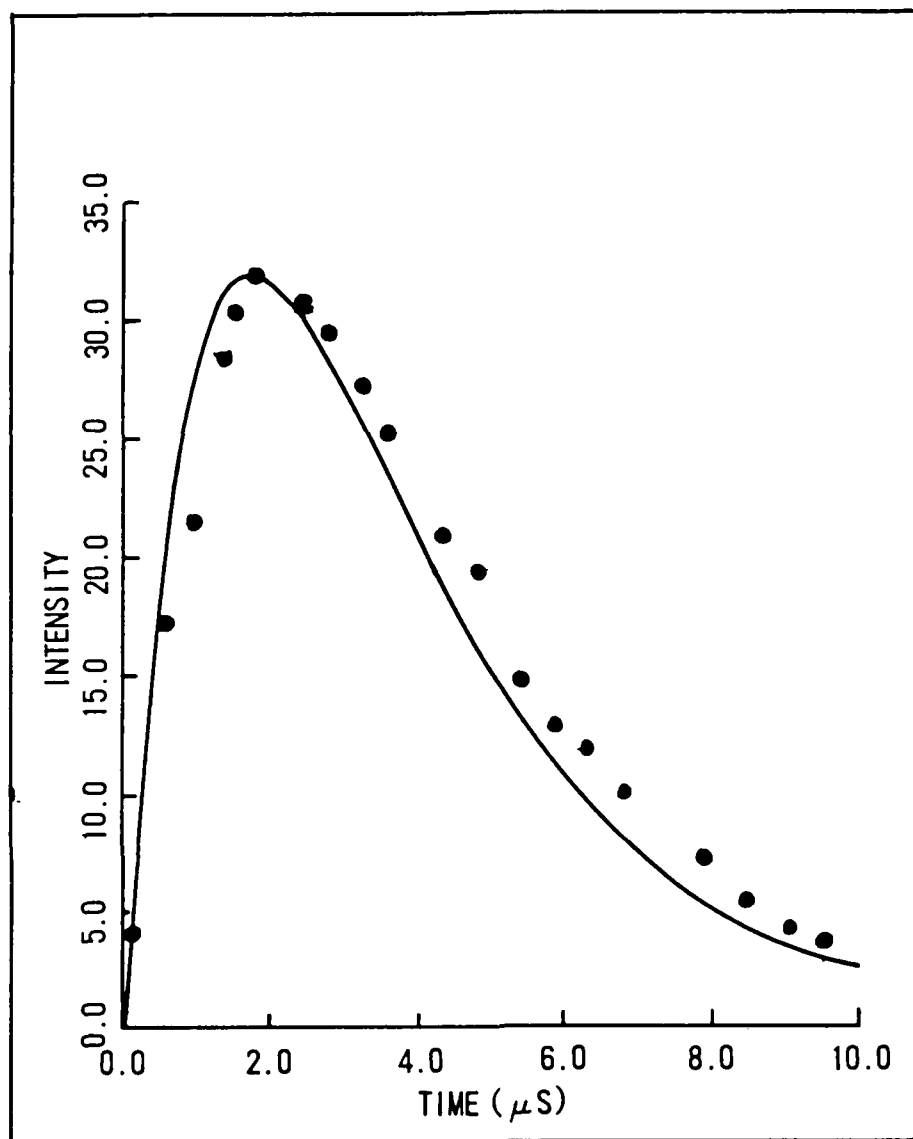


Figure 5-3c. Temporal history of $v'=2$ following excitation of $v'=3$ with 1.25 Torr of He. The solid curve represents the simulated $v'=2$ decay curve (solution to Eq. (5-4)). The solid circles are actual data points taken from the recorded decay curves. The data points were normalized to the maximum intensity of the simulated decay curves.

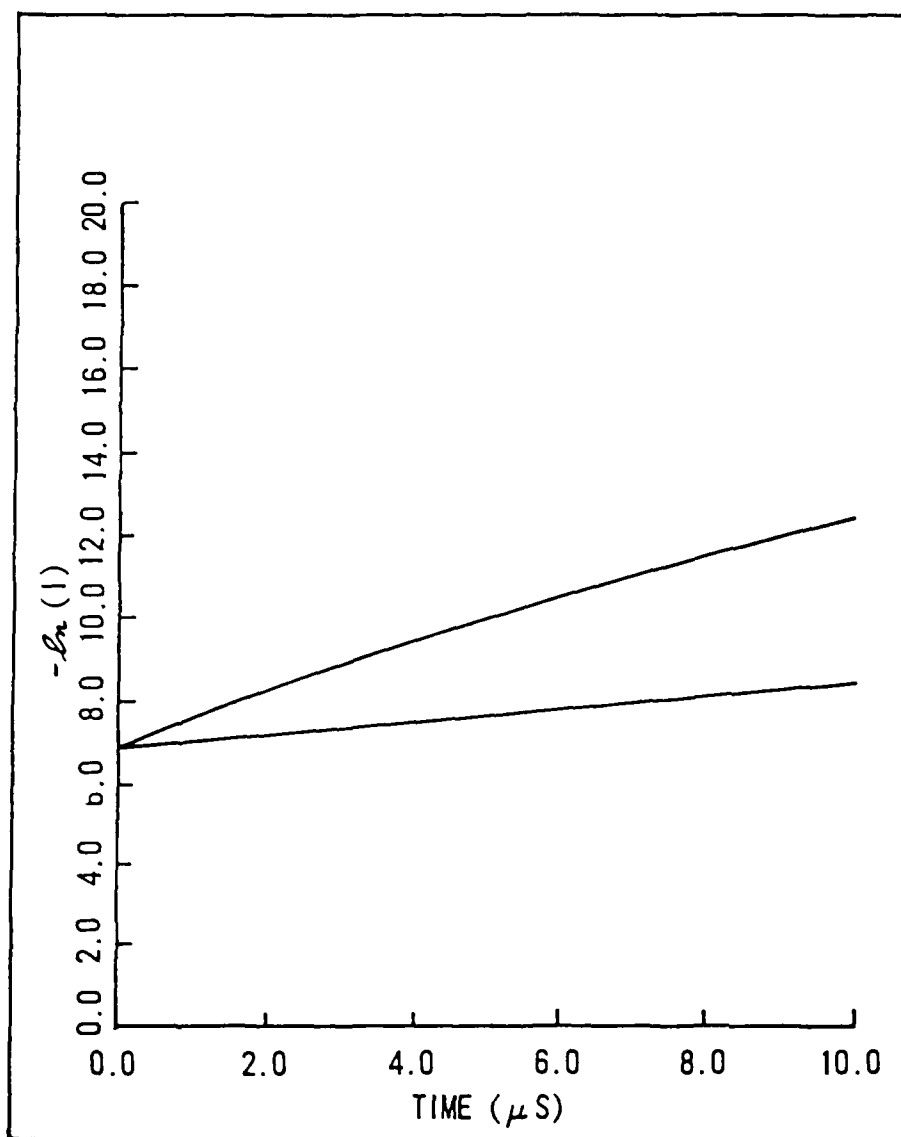


Figure 5-3b. Upper curve: natural logarithm of the decay curve in Fig 5-3a; the lower curve represents purely radiative decay from $v'=3$. See text for explanation.

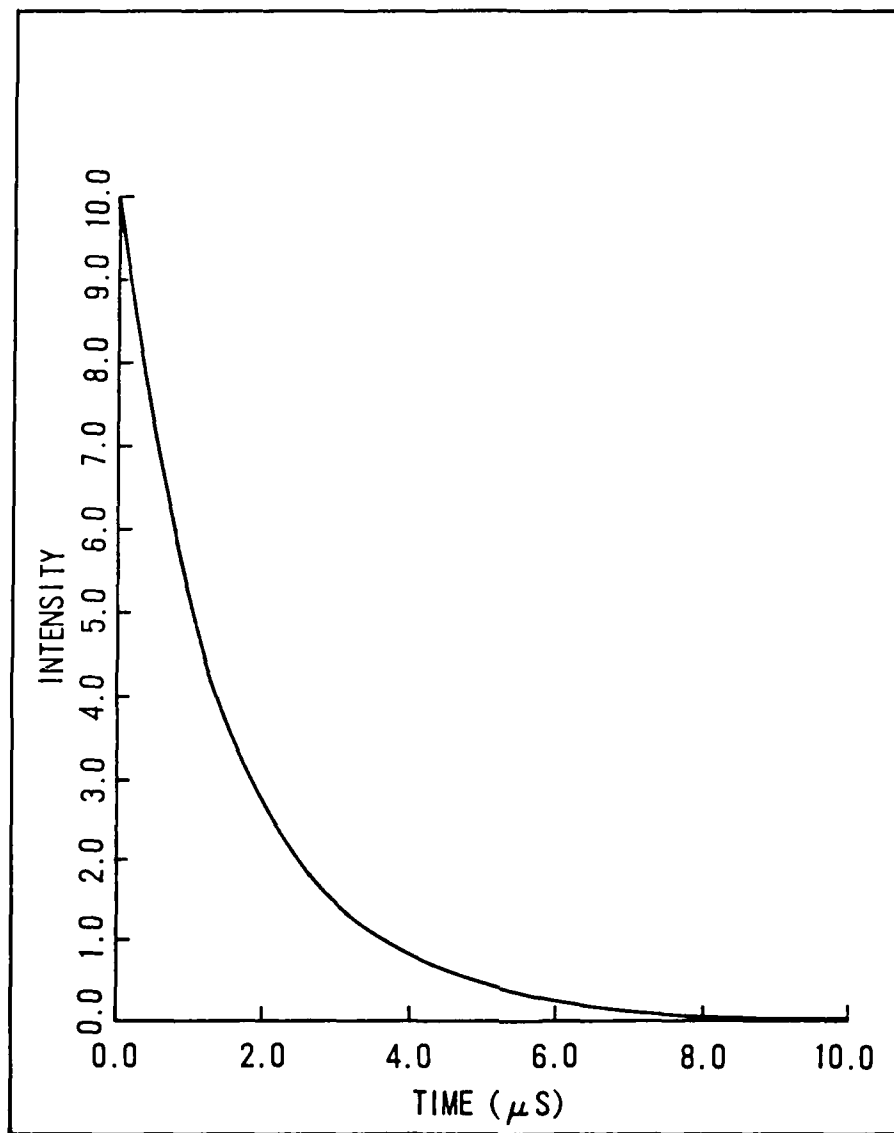


Figure 5-3a. Computer simulated fluorescence decay curve from the initially prepared $v'=3$ level using the rate constants measured in the cw experiments. The bath gas was He at 1.25 Torr.

value of $5.6 \times 10^{-12} \text{ cm}^3 \text{ molecule}^{-1} \text{ s}^{-1}$.

A second model was employed to reproduce the time resolved fluorescence decay curves using the measured cw vibrational transfer rate constants. The decay curves were predicted by directly integrating a set of rate equations for a five level system in which $v'=3$ was initially populated.⁴⁴ (For simplicity, we only consider single quantum transitions.) The equations for the initially prepared and collisionally populated states are given in Eqs.(5-3) and (5-4), respectively.

$$\begin{aligned} \frac{dN(3)}{dt} = & -k(3,2)M N(3) - k(3,4)M N(3) - AN(3) - Q_m M N(3) - R_B N_B \\ & + k(2,3)M N(2) \end{aligned} \quad (5-3)$$

$$\begin{aligned} \frac{dN(v)}{dt} = & k(v+1,v)M N(v+1) - k(v,v+1)M N(v) - k(v,v-1)M N(v) - \\ & Q_m M N(v) - AN(v) - R_B N_B \end{aligned} \quad (5-4)$$

where $R_B N_B$ accounts for electronic quenching and vibrational transfer by residual I_2 . A gas kinetic value ($3 \times 10^5 \text{ s}^{-1}$) was used for $R_B N_B$; and the respective values of $k(3,2)$ and $k(3,4)$ were 4.9×10^{-12} and $7.2 \times 10^{-13} \text{ cm}^3 \text{ molecule}^{-1} \text{ s}^{-1}$. The transfer rates for the other vibrational levels were obtained by linearly scaling the measured $k(3,2)$ and $k(3,4)$ rate constants. Figure 5-3 shows samples of the predicted decay curves for $v'=3$ and $v'=2$ at 1.25 Torr of He. Figure 5-3b shows the natural logarithm of the decay curve in Fig. 5-3a. The linear line in Fig. 5-3b (lower curve) represents radiative decay from $v'=3$ while the upper curve represents the solution to Eq.(5-3). Figure 5-3c illustrates the time history of $v'=2$, and the solid circles represent actual data points that

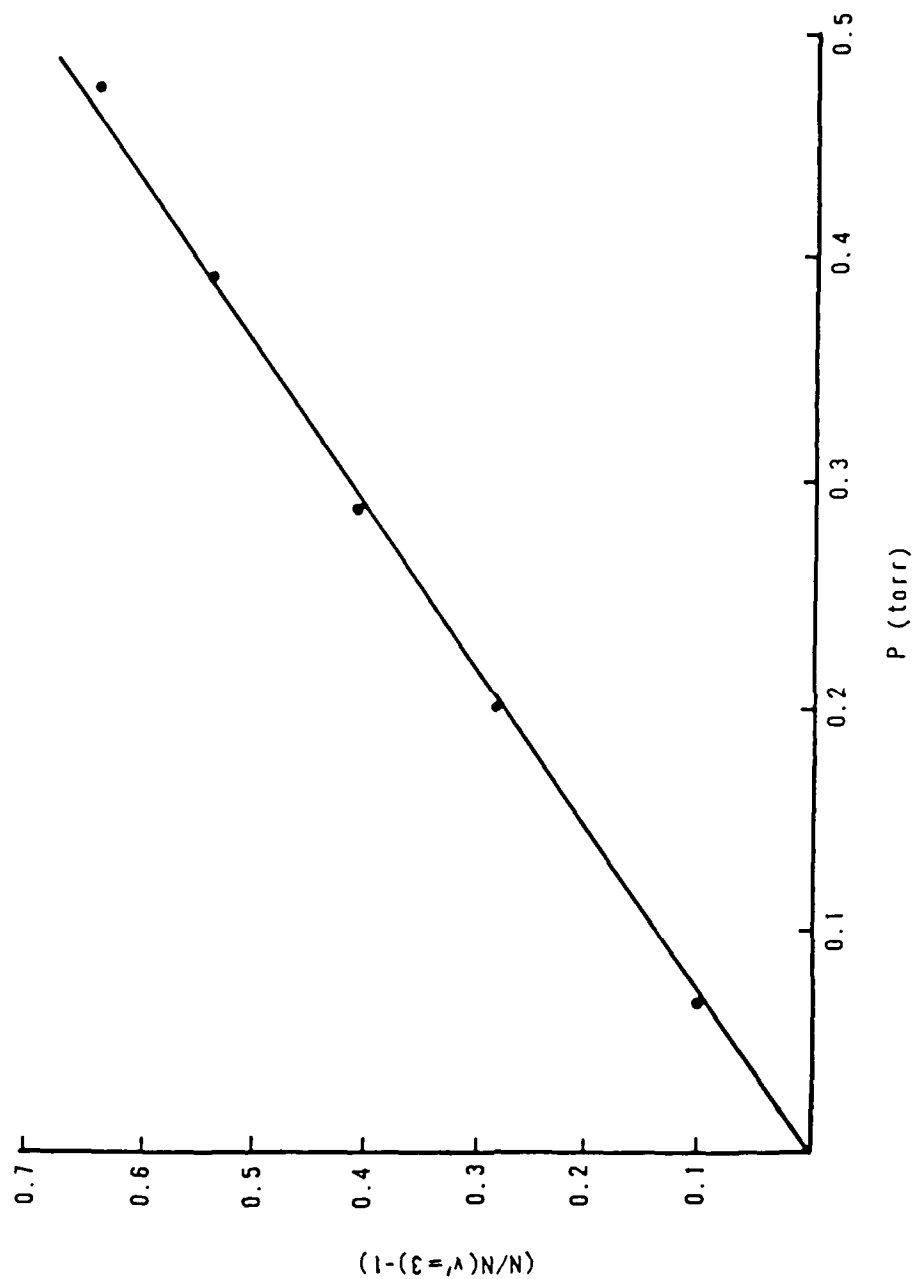


Figure 5-2. Stern-Volmer plot for determining the total removal rate constant - from $v'=3$ using the synthetic data of Fig. 5-1.

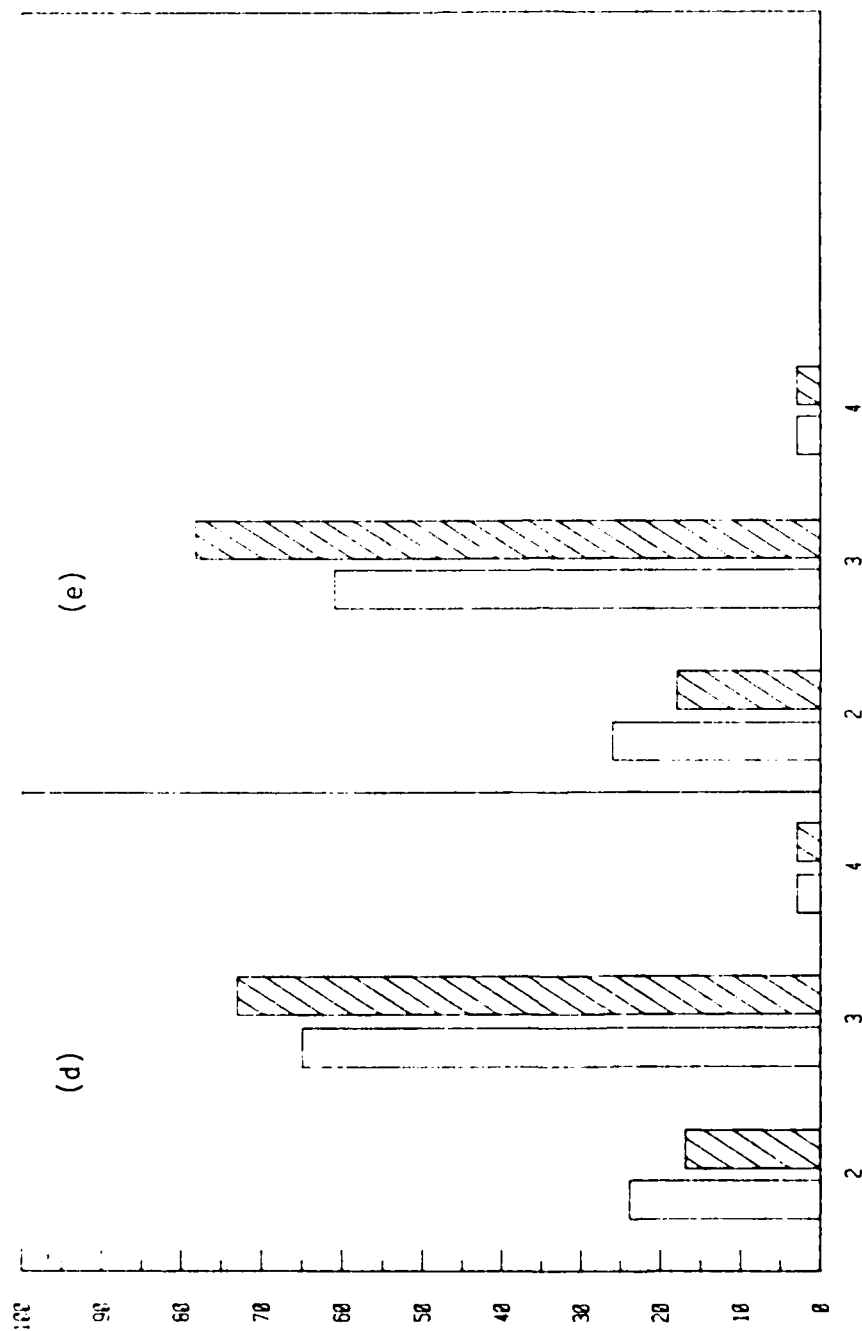


Figure 5-1. Steady-state model predictions of the IF(B) relative populations in $v'=2, 3$ and 4 using the rate constants measured in the time resolved experiments. The bath gas is He at: (d) 0.390 Torr and (e) 0.470 Torr.

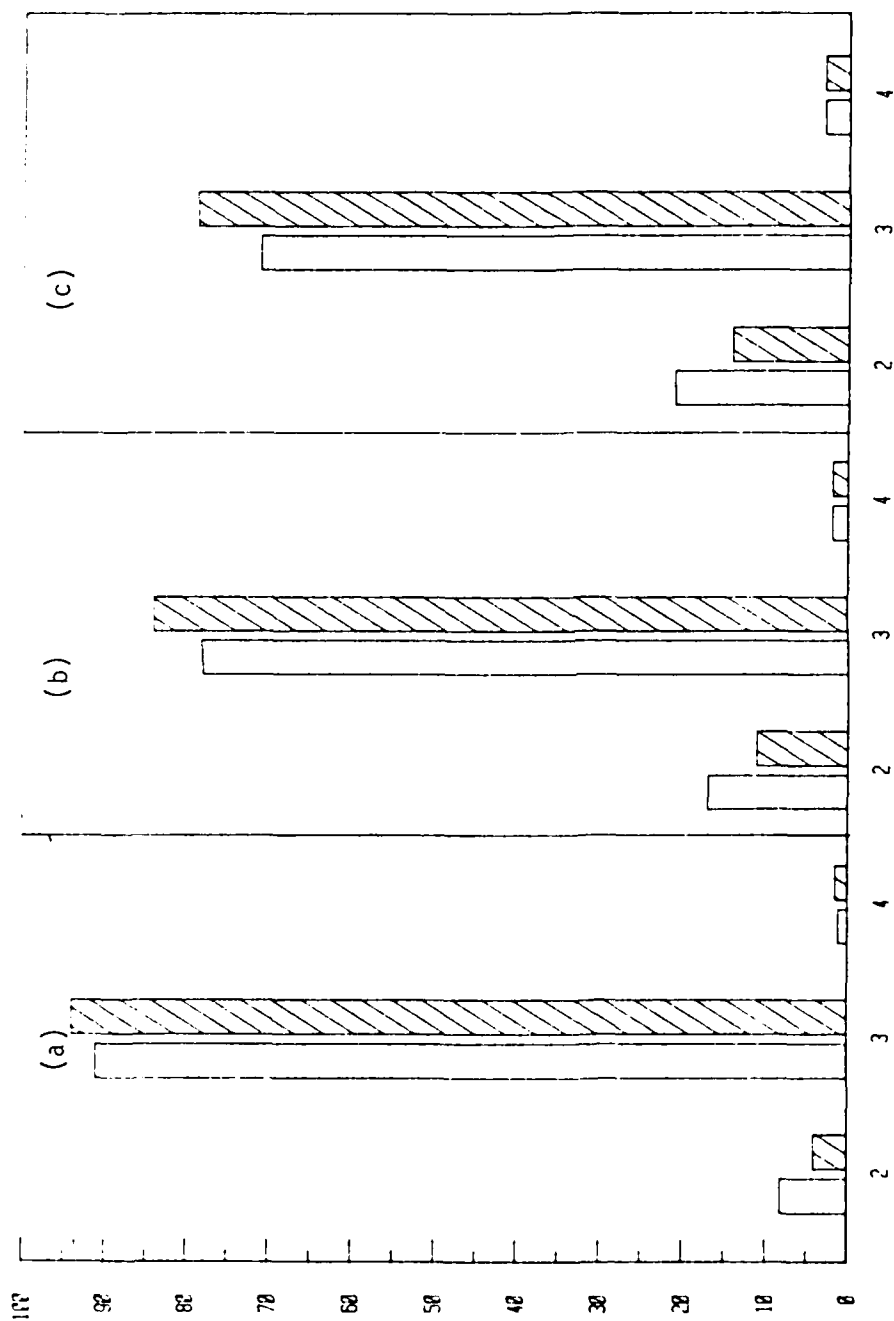


Figure 5-1 Steady-state model predictions of the IF(B) relative populations in $v' = 2, 3$, and 4 using rate constants measured in the time resolved experiments. The bath gas is He at : (a) 0.068 Torr, (b) .200 Torr, and (c) .290 Torr. Notation: = cw experimental data; = predicted data.

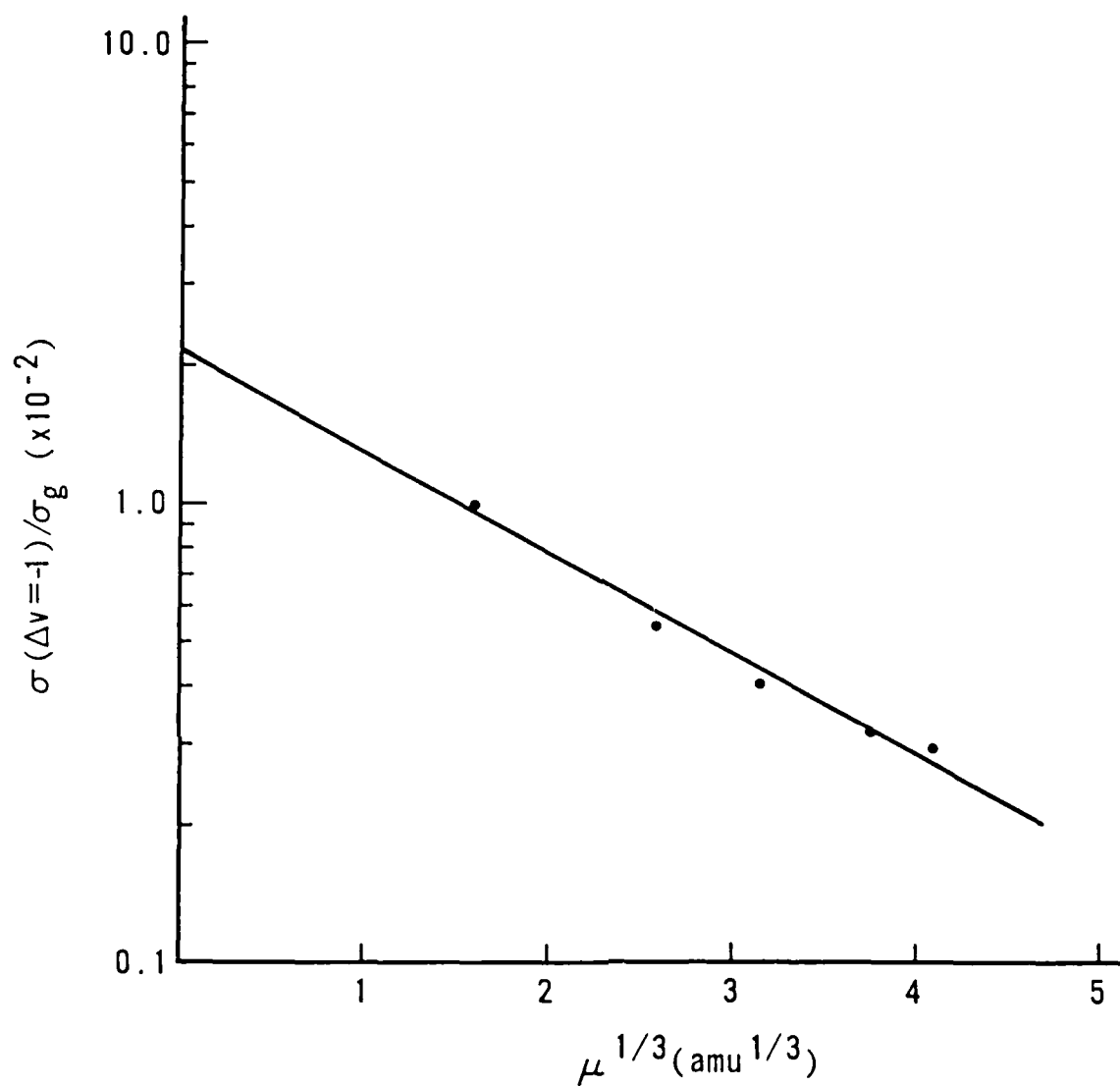


Figure 5-6. Vibrational relaxation probabilities for IF(B; $v'=3$) with the noble gases plotted logarithmically against reduced mass to the 1/3 power.

plot of the $\Delta v = -1$ cross sections vs vibrational quantum number that were obtained in the pulsed experiments (indicated by open circles). The bath gas in this scaling study was He. The error bars in Fig. 5-7 represent the statistical uncertainties in the data. As seen in this figure, the vibrational transfer cross sections linearly depend on the vibrational quantum number.

Similar trends were observed in the cw excitation studies with He, Ne, and N_2 as bath gases. The cross sections that were calculated from the cw data provide positive evidence for this linear scaling relationship since no assumptions about atom-diatom interactions were made in the kinetic analysis. In these experiments, the fundamental vibrational relaxation rate constant, $k(1,0)$, was directly measured and converted into a cross section, $\sigma(1,0)$, using Eq.(4-5). Upon comparing $\sigma(1,0)$ with the $\Delta v = -1$ cross sections determined in $v' = 3$ and $v' = 6$, we see that the $\sigma(v,v-1)$ cross sections linearly scale as v' as shown by the solid circles in Fig. 5-7. (The error bars in this figure represent the systematic uncertainties in that data.) Furthermore, the extrapolated value of $\sigma(1,0)$ for the time resolved data agrees very well with the experimentally determined cw value. Similar trends were also observed in the $\sigma(v,v+1)$ cross sections obtained in both the cw and pulsed excitation experiments.

The trends observed in Figs. 5-5, 5-6, and 5-7 strongly indicate that IF(B) + M vibrational energy transfer collisions are highly adiabatic; and these trends can be explained by the standard vibrational relaxation theories discussed in Appendix B. Several conclusions drawn from this

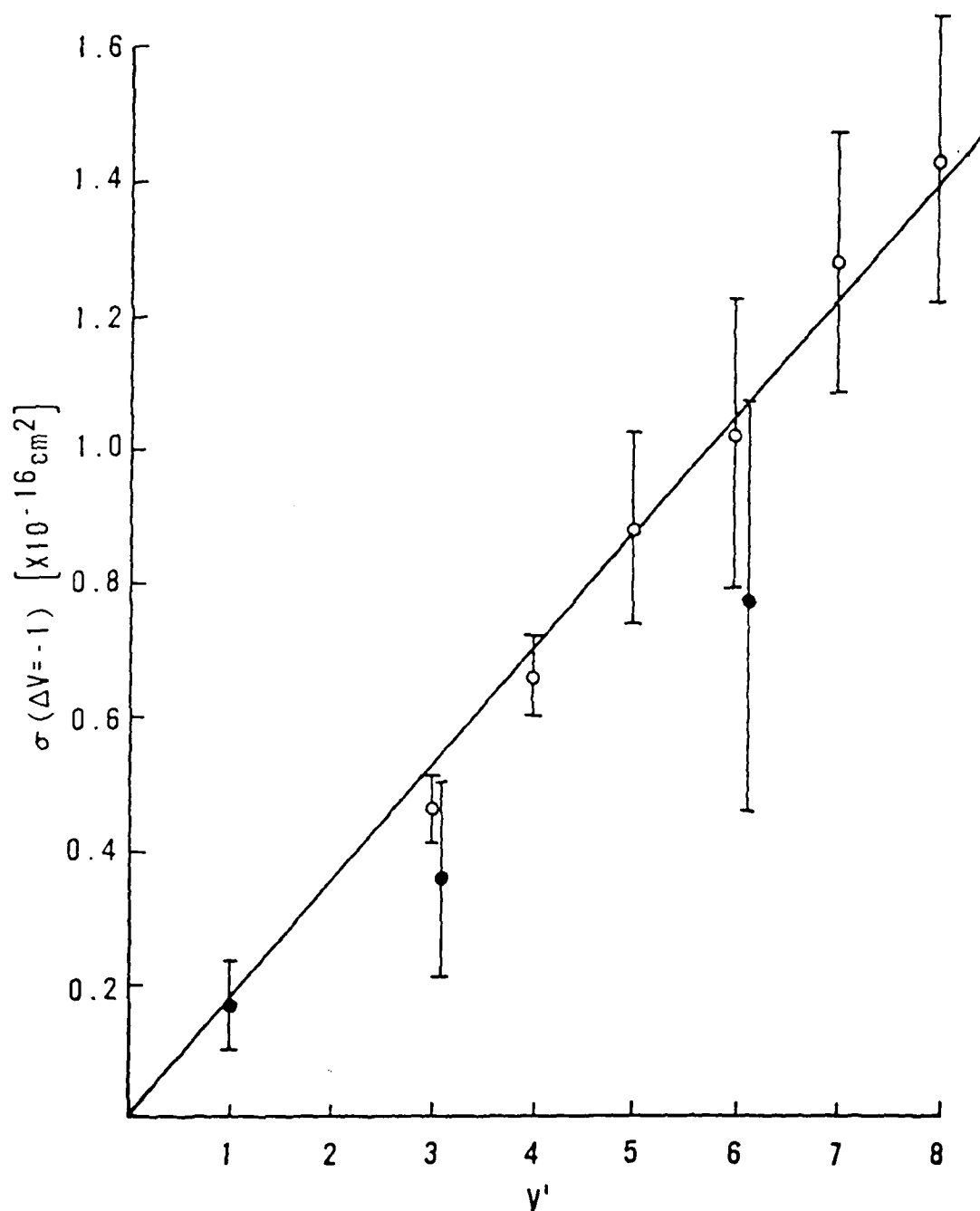


Figure 5-7. Vibrational level scaling of the $v = -1$ energy transfer cross sections. The time resolved data (o) was slightly offset from the cw data (●) for clarity.

discussion support this collision picture. First, IF(B) + M encounters, resulting in an energy exchange through IF(B) vibration, can be realized only if the collision occurs along the repulsive part of the interaction potential as indicated by σ_v/σ_g being much less than one. That is, no long range forces such as dipole-induced dipole effects contribute to the collision process. Secondly, the linearly decreasing dependence of $\sigma(v, v-1)/\sigma_g$ on $\mu^{1/3}$ for the rare gases shows that the lighter collision partners are more effective in transferring energy than the heavier gases. This means that the average velocity of the lighter collision reduced mass system more closely matches the IF(B;v') vibrational frequency relative to that for the more massive system. Therefore, larger relative vibrational transition probabilities are expected for the lighter collision partners. Finally, the linear scaling of the state-to-state vibrational transfer cross sections with vibrational level agrees with the predicted behavior from the adiabatic V-T theories of Landau and Teller⁴⁸ and Schwartz, Slawsky, and Hertzfeld⁴⁹. Since the energy difference between any two vibrational levels is essentially constant in IF(B), the probability for a collisional vibrational transition will only depend on the quantum number of the initially excited state in a simple V-T process.

3. Multiple Quantum Vibrational Transfer

As discussed in the results section, multiquantum vibrational transfer may not be observable in these experiments. Based on this discussion, we stated that the upper limit for the multiquantum transfer rate constants were approximately 11 percent of the total vibrational

relaxation rate constants for a given bath gas.

Computer modeling was performed to test this conclusion. The model simulated the steady-state experiments in which $v'=3$ was initially prepared. (The model was described previously.) The multiquantum rate constants, $k(3,1)$ and $k(3,5)$ were added to the existing code. The value of these rate constants were chosen as 0.1, 0.2, 0.3, 0.4, and 0.5 times the $k(3,2)$ and $k(3,4)$ rate constants. Figure 5-8 shows sample results. As seen in this figure, the predicted populations in $v'=1$ using $k(3,1) = 0.5k(3,2)$ are about 60 percent greater than the experimental values. This difference is larger than the upper limit for the error estimates made in the experimentally determined ratios, $N(v'=1)/N$ (~ 40 percent). Similar results were obtained with $k(3,1)$ being 0.3 and 0.4 times the $k(3,2)$ rate constant. Thus, these rate constants did not accurately predict the experimental findings. However, the vibrational population distributions predicted using the remaining rate constants were within the error limits of the experimental data. Therefore, this model predicted that multiquantum transfer can occur with a rate constant of $\sim 9.2 \times 10^{-13} \text{ cm}^3 \text{ molecule}^{-1} \text{ s}^{-1}$ using He as the bath gas. This value is 19 percent of the measured $v'=3$ to $v'=2$ rate constant and agrees with the previous estimate made from the cw experimental data.

Continuing this analysis with the other noble gases, we found similar results for the population distributions. That is, the model predicted rate constants that agreed reasonably well with the estimated multiquantum rate constants determined previously. At bath gas pressures of one Torr, the first order multiquantum rate for He is $2.0 \times 10^4 \text{ s}^{-1}$. This value is an order of magnitude less than both the radiative decay rate

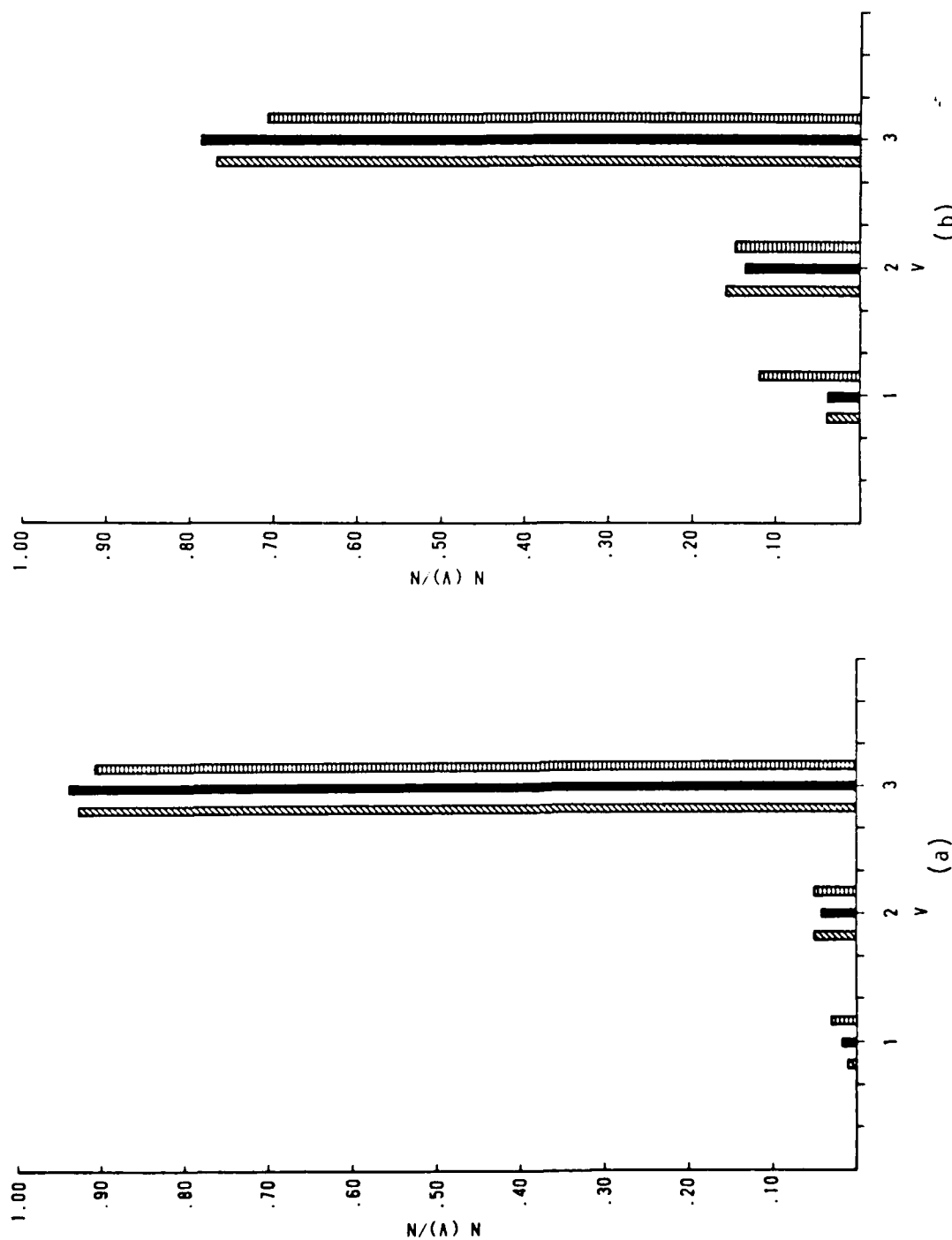


Figure 5-8. Predicted population distributions due to multiquantum vibrational transfer. The He pressures are: (a) 0.068 Torr and (b) .290 Torr. Notation: \blacksquare : $k(3,1)=0.5k(3,2)$; \hatchedbox : $k(3,1)=0.7k(3,2)$; and \blacksquare = experimental values.

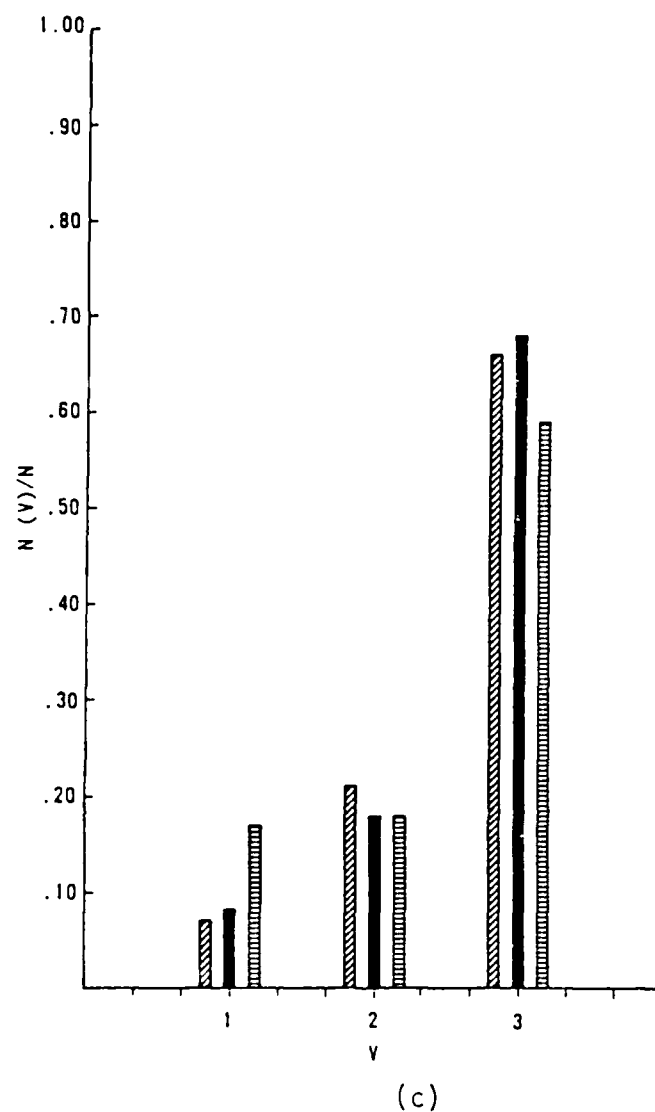


Figure 5-8c. Predicted population distributions due to multiquantum vibrational transfer. The bath gas is He at 0.475 Torr.

and the single quantum vibrational transfer rate (assuming $v' = 3$ is initially prepared). These calculations lend support to the conclusions made in the pulsed experiments that multiquantum transfer may not be important.

Since we have shown that $IF(B) + M$ collisions are adiabatic in nature, the small probability for a v greater than one change in a single collision is not unreasonable. According to Ehrenfest's adiabatic principle (Appendix B), the vibrational energy ($\sim 800 \text{ cm}^{-1}$) that must be transferred in the collision to accommodate such a process is four times the amount of energy contained in the bath gas at room temperature. More accurate experiments under single collision conditions are required to absolutely determine the importance of multiple vibrational transitions in $IF(B)$.

4. Comparisons with Other Studies

Kinetically, vibrational energy transfer dominated electronic quenching in $IF(B)$ with the noble gases and N_2 as the bath gases. However, electronic quenching by O_2 , F_2 , and H_2O effectively competed with vibrational relaxation in the lower B state manifold while vibrational transfer dominated in the upper part of the manifold. This was because the vibrational transfer cross sections increased linearly with v' while the electronic quenching rate coefficients remained relatively unchanged.

The results of this study compare favorably with those reported in $I_2(B)$ ^{27,50-52} and $Br_2(B)$.⁵³ (Comparisons with other halogen and interhalogen diatomics are not made because state-resolved vibrational transfer data are not available.) In general, these studies showed

that "true" electronic quenching is slow when compared to vibrational energy transfer. Even when collision induced predissociation was postulated as the dominant depletion mechanism, the rapidity of this process may indicate the effectiveness of V-T or R-T energy transfer and not electronic quenching.

A comparison of the $I_2(B)$, $Br_2(B)$ and $IF(B)$ data shows that, for a given initially populated vibrational state and collision partner, the vibrational transfer rate constants measured in $IF(B)$ are about a factor of 10 to 100 times smaller than those measured in I_2 or Br_2 . The relative efficiency of V-T transfer in $IF(B)$ is a consequence of an energy gap argument. For example, in $I_2(B) + M$ collisions,⁵⁰ $k(15,14)$ was reported as $6.2 \times 10^{-11} \text{ cm}^3 \text{ molecule}^{-1} \text{ s}^{-1}$ for initial excitation of $v' = 15$. This value is a factor of ten greater than $k(\Delta v = -1)$ involving $v' = 3$ in $IF(B)$. The spacing between $v' = 3$ and $v' = 2$ in $IF(B)$ is about 390 cm^{-1} (or $\sim 1.9 kT$ at $T = 300 \text{ K}$); while the spacing between $v' = 15$ and $v' = 14$ in $I_2(B)$ is only $\sim 100 \text{ cm}^{-1}$ ($\sim 0.5 kT$). Thus, the efficiency of vibrational transfer with the more widely spaced levels in $IF(B)$ is expected to be lower than in I_2 if V-T transfer is the dominant mechanism. Similar results are obtained when comparing $IF(B)$ V-T rate constants with those reported in both $Br_2(B; v' = 11)$ ⁵³ and $I_2(B; v' = 6, 25, 43)$.⁵⁴

Another comparison that can be made is that of the range of multi-quantum vibrational transfer. Multiquantum transfer occurred with a high probability in the upper vibrational manifold of $I_2(B)$. For example, a $\Delta v = +4$ and $\Delta v = +2$ transitions were observed in a single collision subsequent to the initial preparation of $v' = 43$ and $v' = 25$. A $\Delta v = +2$ change in a single collision was also observed in $Br_2 + N_2$ collisions.

TABLE 5-5. Relative energy transfer cross sections
determined in the $v'=3$ excitation studies.

Bath	σ_r/σ_v
He	17
Ne	57
Ar	92
Kr	150
Xe	231
N ₂	27

However, multiquantum transfer was exxestially absent in $I_2(B, v'=6) + M$ collisions.⁵⁴ Qualitatively, these studies indicated that multiquantum transfer occurred only between levels that were within kT (200 cm^{-1}) of the initially populated state. (For $I_2(B)$, ΔG_v between $v'=40$ and $v'=43$ and between $v'=23$ and $v'=25$ are 174 cm^{-1} and 175 cm^{-1} , respectively. But, a $\Delta v = -2$ change in $I_2(B, v'=6)$ requires 230 cm^{-1} .) Based on the results of these studies, multiquantum vibrational transfer in $IF(B)$ should also be small since 800 cm^{-1} of energy is required to make a $\Delta v' = -2$ change.

C. Rotational Energy Transfer

Rotational energy transfer in $IF(B)$ dominated all other kinetic processes as indicated in Table 5-5. In this table, we list the ratios of the cross sections for rotational transfer to those for vibrational transfer with the noble gases. As seen in this table, the rotational transfer cross sections are 20 to 200 times greater than the vibrational transfer values for a given bath gas.

The rotational energy transfer cross sections from Table 4-7 are sum-

marized in Fig. 5-9. In this figure, we plot the estimated efficiencies or transition probability for an R-T collision, σ_r/σ_g , against the square root of the collision reduced mass. (The error bars shown in Fig. 5-9 represent the accuracy with which these quantities can be determined in these experiments.) Several features contained in Fig. 5-9 reveal a possible interpretation of the rotational energy transfer mechanism. First, Fig. 5-9 shows that the rotational transfer cross sections for each collision partner are approximately equal to their respective gas kinetic values since these values may be in error by as much as a factor of two or three. This observation suggests a brief collision encounter which results in an efficient, impulsive energy transfer.

Secondly, the relative cross sections increase with collision reduced mass. This observation can best be understood on a classical basis. The average amount of angular momentum, L , available in a collision is

$$\bar{L} = \bar{r} \times \bar{p} \quad \text{or} \quad L = \mu \bar{v} b \quad (5-7)$$

where b is the impact parameter, μ is the collision reduced mass, and \bar{v} is the average relative velocity.⁵⁵ If it is assumed that the impact parameter, b , in Eq.(5-7) does not widely vary for different collision partners, it follows that $L \propto \mu^{1/2}$ with $\bar{v} = (8kT/\pi\mu)^{1/2}$. Therefore, the heavier collision partners, on the average, bring more orbital angular momentum into the collision which is available for exchange with rotational angular momentum. Therefore, the smooth variation of σ_r/σ_g may reflect the amount of rotational energy available in the collision.

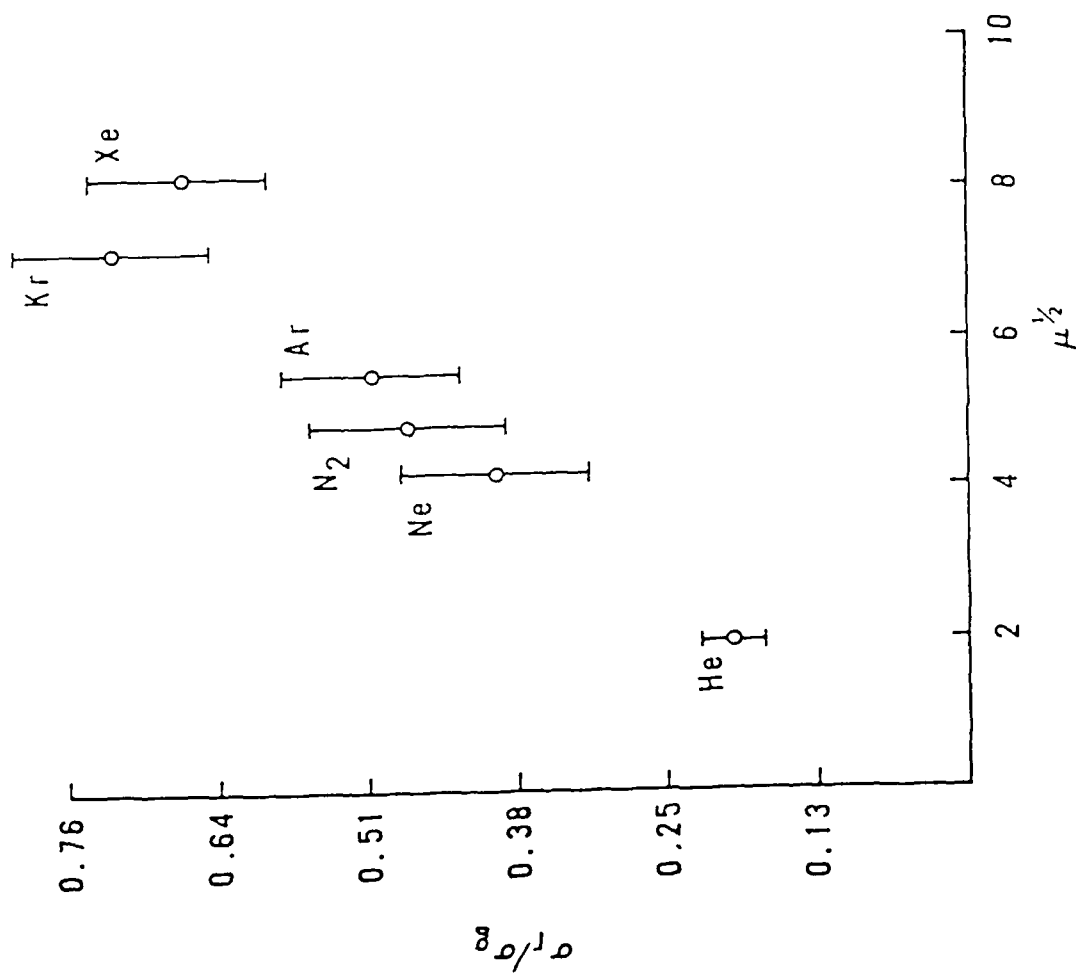


Figure 5-9. Plot of the rotational transfer efficiencies vs. the square root of the collision reduced mass.

A simple physical picture of this collision process can be described as follows. IF(B) + M collisions can occur in the following way: (a) M can interact with IF(B) perpendicular to the IF plane of rotation, (b) M can collide with IF(B) in the rotation plane but perpendicular to the internuclear axis, or (c) collisions can occur in the rotation plane along the internuclear axis. As discussed before, collisions along the internuclear axis adequately describe the vibrational transfer collision interaction. (On the average, this type of collision is less frequent than the other two types which accounts for the low vibrational transfer efficiencies.) In order for R-T collisions to be efficient, the bath gas must be able to alter the IF(B) rotational angular momentum. This can only occur if the bath gas approaches IF(B) in the planes perpendicular or parallel to IF(B) rotation. These types of collisions are about 2/3 more probable than head-on collisions which also increases the relative probability for R-T transfer over V-T energy transfer.

The large probabilities for R-T energy transfer suggest that the collision process occurs along the anisotropic part of the interaction potential (i.e. long range forces may influence the R-T collision probability). Since IF possesses a dipole moment an induced dipole in the noble gases may influence the collision process. (For IF(X, $v''=0$), the electric dipole moment was measured as 1.948 D.⁵⁶ The dipole moment for IF(B), however, may have a larger value.) The potential for a dipole-induced dipole interaction is proportional to α/r^6 , where α is the polarizability and r is the distance between atom A and the IF molecule. Using this potential in classical scattering theory⁵⁷, one finds that the scattering cross section, $\sigma(g)$, at an initial relative velocity, g , is

directly proportional to $(\alpha/\mu g^2)^{1/3}$. However, these experiments were conducted under non-molecular beam conditions at a temperature, T . Thus, the total cross section, σ , is obtained by integrating $\sigma(g)$ over the Maxwell-Boltzmann distribution of velocities, $f(g)$, where $f(g) \propto g^3 \exp(-\mu g^2/RT)$. Performing the integration, one finds that the total cross section, σ , is proportional to $(\alpha\mu^{1/2})^{1/3}$. Figure 5-10 shows a plot the rotational transfer cross sections, σ_r , against the quantity $(\alpha\mu^{1/2})^{1/3}$ for the noble gases. The values of α were obtained from the listing of Miller and Bederson.⁵⁸ This figure apparently shows that the cross sections for rotational transfer linearly increase with the product of the polarizability of the collision partner and the collision reduced mass. Polarization effects may, therefore, be important in rotational energy transfer in IF(B).

The qualitative features of the rotational distributions in the initially populated vibrational state revealed the possibility of multiquantum rotational transitions occurring in a single collision. Unlike the vibrational relaxation in which the optical selection rule is apparently obeyed ($\Delta v = \pm 1$), the probability for a change in J by $\Delta J > 1$ seems to be higher than for $\Delta J = \pm 1$. Even though a precise determination of the relaxation mechanism could not be made, the qualitative results do agree with the results of previous studies. For example, a change in J by more than one quantum in a single collision was observed in electronically excited states of I_2 ,^{27,59} Na_2 ,²¹ and Li_2 .²² Also, computer modeling of the rotational distribution in the $B^3\Pi(0^+)$ state of IF produced by $O_2(^1\Delta) + I_2 + F$ reaction agreed with the experimental data only when allowance was made for multiquantum transitions with $\Delta J = \pm 15$.⁴³ The

APPENDIX B: Elementary Vibrational Transfer Theories

This appendix presents a brief discussion of elementary vibrational energy transfer theories. Since the majority of the collision partners used in the present experiments are simple atoms, the discussion is limited to the exchange of IF(B) vibrational energy to translational energy of the heat bath. Also, no rotational-to-translation models are presented since state resolved rotational relaxation data were not obtained in the present studies.

1. Collision Geometry

The simplest vibration-to-translation (V-T) energy transfer model to consider is a collinear collision between a vibrating diatomic molecule, AB, and an atom C. The collision geometry is shown in Fig. B-1. AB is assumed to be a simple harmonic oscillator with an equilibrium internuclear distance, d . The distance between atom C and the AB center-of-mass is r , and X is the displacement of the oscillator AB from equilibrium. The intermolecular potential energy, $V(r)$, varies with r during the collision. Also, since molecule AB is vibrating, X will also vary with time. Thus, this system has a time-dependent perturbation (changing external force), represented by the change in r , acting on a quantized periodic motion, represented by the variation of X .

2. Adiabatic Approximation

Expressions describing transition probabilities for vibrational energy transfer can be derived using various collision theories.² A simple, although revealing interpretation of this collision process

TABLE A-1. IF(B) collision-free lifetimes and electric dipole moments.

<u>v'</u>	<u>τ_R</u>	<u>$R_e ^2$</u>
0	7.0 \pm .5	1.07 \pm .07
1	6.7 \pm .3	1.11 \pm .05
2	7.1 \pm .6	1.06 \pm .09
3	6.9 \pm .3	1.09 \pm .04
4	7.4 \pm .6	1.02 \pm .08
5	8.1 \pm .4	0.95 \pm .05
6	8.2 \pm .4	0.95 \pm .05
7	8.6 \pm .4	0.93 \pm .04
8	8.6 \pm .5	0.95 \pm .05

TABLE A-2. IF(B) spectroscopic constants.

<u>TERM</u>	<u>DUNHAM COEFFICIENT</u>	<u>X STATE VALUE</u>	<u>B STATE VALUE</u>
T_e	$Y_{0,0}$	0	19052.28285
ω_e	$Y_{1,0}$	610.22649	411.27590
$\omega_e x_e$	$-Y_{2,0}$	3.12534	2.85844
$\omega_e y_e$	$Y_{3,0}$	-2.6139×10^{-3}	-6.2411×10^{-2}
B_e	$Y_{0,1}$	0.27970959	0.22766136
α_e	$-Y_{1,1}$	1.87215×10^{-3}	1.74204×10^{-3}

APPENDIX A: Radiative and Spectroscopic Properties of the IF(B X) System

Table A-1 lists the average radiative lifetimes, τ_R , and the corresponding dipole moments, $|\mu_e|^2$, for each stable vibrational level as determined by Clyne and McDermid.¹² The radiative lifetimes and dipole moments have units of μs and (Debye)², respectively. The lowest order spectroscopic constants for both the B and X states of IF are collected in Table A-2. These constants are routinely used in low to medium resolution spectroscopic studies. Higher order terms are found in Ref.13, and should be used for calculating line positions in high resolution experiments. All of the spectroscopic constants are in units of cm^{-1} .

52. J. I. Steinfeld and A. N. Schweid, J. Chem. Phys., 53, 3304 (1970).
53. M. A. A. Clyne, M. C. Heaven, and S. J. Davis, J. Chem. Soc., Faraday Trans. 2, 76, 961 (1980).
54. R.B. Kurzel, E.O. Degenkold, and J.I. Steinfeld, J. Chem. Phys., 56, 1784 (1972).
55. R. E. Weston and H. A. Schwartz, Chemical Kinetics, (Printice-Hall, NY, 1972).
56. K.P.R. Nair, J. Hoeft, and E. Tiemann, Chem. Phys. Lett., 60, 253 (1979).
57. R.E. Johnson, Introduction to Atomic and Molecular Collisions (Plenum Press, NY, 1982).
58. T.M. Miller and B. Bederson, Adv At Mol Phys, 13, 1 (1977).
59. R. B. Kurzel, J. I. Steinfeld, D. A. Hatzenbuehler, and G. E. Leroy, J. Chem. Phys., 55, 4822 (1971).
60. R. J. Rubin and K. E. Shuler, J. Chem. Phys., 26, 137 (1957).
61. N. W. Bazley, E. W. Montroll, R. S. Rubin, and K. E. Shuler, J. Chem. Phys., 28, 700 (1958).
62. S. Chapman and T. G. Cowling The Mathematical Theory of Nonuniform Gases, (Cambridge Univ. Press, NY, 1970).
63. P. R. Bevington, Data Reduction and Error Analysis for the Physical Sciences, (McGraw-Hill, NY, 1969).
64. R. D. Evans, The Atomic Nucleus (McGraw-Hill, NY, 1955), pp.470-502.

34. P. D. Whitefield and S. J. Davis, Chem. Phys. Lett., 83, 44 (1981).
35. E. H. Appelman and M. A. A. Clyne, J. Chem. Soc., Faraday Trans. 1, 71, 2072 (1975).
36. D. E. Rosner and H. D. Allendorf, J. Phys. Chem., 75, 308 (1971).
37. P. H. Sackett and J. T. Yardley, J. Chem. Phys., 57, 152 (1972).
38. S. E. Schwartz and H. S. Johnston, J. Chem. Phys., 31, 1286 (1969).
39. M. A. A. Clyne and J. P. Liddy, J. Chem. Soc., Faraday Trans. 2, 76, 1569 (1980).
40. M. A. A. Clyne and L. C. Zai, J. Chem. Soc., Faraday Trans. 2, 78, 1221 (1982).
41. M.A.A. Clyne, M.C. Heaven, and E. Martinez, J. Chem. Soc., Faraday Trans. 2, 76, 177 (1980).
42. S.J. Harris, W.C. Natzle, and C.B. Moore, J. Chem. Phys., 70, 4215, (1979).
43. P. D. Whitefield, R. F. Shea, and S. J. Davis, J. Chem. Phys. 78, 6793 (1983).
44. The computer code for the Montroll-Shuler solution, tests of the applicability of this solution for IF(8), and the computer model for simulating IF(8) time resolved vibrational relaxation data were developed by R. F. Shea, Air Force Weapons Laboratory, Kirtland AFB, NM, 1982-1983.
45. J. O. Hirschfelder, C. F. Curtiss, and R. B. Bird, Molecular Theory of Gases and Liquids, (Wiley, NY, 1954).
46. M.A.A. Clyne and I.S. McDermid, J. Chem. Soc., Faraday Trans. 2, 73, 1094 (1977).
47. M.A.A. Clyne and I.S. McDermid, Faraday Discuss. Chem. Soc., 67, 316 (1979).
48. L. Landau and E. Teller, Phys. Z. Sowj. Un., 10, 34 (1936).
49. R. M. Schwartz, Z. I. Slawsky, and K. F. Herzfeld, J. Chem. Phys., 20, 1591 (1952).
50. R. L. Brown and W. Klemperer, J. Chem. Phys., 41, 3072, (1964).
51. R. B. Kurzel and J. I. Steinfeld, J. Chem. Phys., 53, 3293 (1970).

16. S. J. Davis and L. Hanco, Appl. Phys. Lett., 37, 692 (1980).
17. S. J. Davis, L. Hanco, and R. F. Shea, J. Chem. Phys., 78, 172 (1983).
18. S. J. Davis, L. Hanco, and P. J. Wolf, J. Chem. Phys. (in press, 1985).
19. J. Franck and R. W. Wood, Phil. Mag., 21, 314 (1911).
20. a. W. Demtroder, Laser Spectroscopy, Springer Series in Chemical Physics, Vol. 5, (Springer-Verlag, Berlin, 1981).
b. J. L. Kinsey, Ann. Rev. Phys. Chem., 28, 399 (1977).
c. M. Broyer, G. Gouedard, J. C. Lehmann, and J. Vigue, Adv. At. Mol. Phys., 12, 165 (1976).
21. see K. Bergmann, W. Demtroder, M. Stock, and G. Vogl, J. Phys. B., 7, 2036 (1974); T. A. Brunner, N. Smith, A. W. Karp, and D. F. Pritchard, J. Chem. Phys., 74, 3324 (1981) and associated references.
22. see Ch. Ottinger and M. Schroder, J. Phys. B., 13, 4163 (1980) and associated references.
23. H. P. Broida and T. Carrington, J. Chem. Phys., 38, 136 (1963).
24. E. H. Fink, D. L. Akins, and C. B. Moore, J. Chem. Phys., 69, 3379 (1978).
25. T. A. Caughey and D. R. Crosley, J. Chem. Phys., 69, 3376 (1978); J. Chem. Phys., 71, 736 (1979).
26. J. I. Steinfeld, J. Phys. Chem. Ref. Data, 13, 445 (1984).
27. J. I. Steinfeld and W. Klemperer, J. Chem. Phys., 42, 3475 (1965).
28. G. M. Jurisich and F. F. Crim, J. Chem. Phys., 74, 4455 (1981).
29. R.F. Shea, Private Communication, Air Force Weapons Laboratory, 1983.
30. E. W. Montroll and K. E. Shuler, J. Chem. Phys., 26, 137 (1957).
31. For a review of this solution, see J. F. Clarke and M. McChesney, The Dynamics of Real Gases, (Butterworths, Washington, 1964).
32. J. Valentini, M. J. Coggiola, and Y. T. Lee, Int. J. Chem. Kinetics, 8, 605 (1976).
33. C. C. Kahler and Y. T. Lee, J. Chem. Phys., 73, 5122 (1980).

REFERENCES

1. R. B. Bernstein, ed., Atom-Molecule Collision Theory, A Guide for the Experimentalist (Plenum Press, NY, 1979).
2. a. M. S. Child, Molecular Collision Theory, (Academic Press, NY, 1974).
b. J. D. Lambert, Vibrational and Rotational Relaxation in Gases, (Oxford Univ. Press, Oxford, UK, 1977).
c. J. T. Yardley, Introduction to Molecular Energy Transfer, (Academic Press, NY, 1980).
d. K. F. Hertzfeld and T. A. Litovitz, Absorption and Dispersion of Ultrasonic Waves, (Academic Press, NY, 1959).
3. J. I. Steinfeld, J. Chim. Phys., 64, 17 (1967).
4. R. A. Durie, Proc. Roy. Soc. (London), A207, 388 (1951).
5. R. A. Durie, Can. J. Phys., 44, 337 (1966).
6. M. A. A. Clyne, J. A. Coxon, and L. W. Townsend, J. Chem. Soc., Faraday Trans. 2, 68, 2134 (1972).
7. J. W. Birks, S. D. Gabelnick, and R. S. Johnston, J. Mol. Spectrosc., 57, 23 (1976).
8. J. A. Coxon, Chem. Phys. Lett., 33, 136 (1975).
9. M. A. A. Clyne and I. S. McDermid, J. Chem. Soc., Faraday Trans. 2, 72, 2242 (1976).
10. G. Herzberg, Molecular Spectra and Molecular Structure, I. Spectra of Diatomic Molecules, (Van Nostrand Reinhold Co., NY, 1950).
11. M. A. A. Clyne and I. S. McDermid, J. Chem. Soc., Faraday Trans. 2, 72, 2252 (1976).
12. M. A. A. Clyne and I. S. McDermid, J. Chem. Soc., Faraday Trans. 2, 74, 1644 (1978).
13. T. Trickl and J. Wanner, J. Mol. Spectrosc., 104, 174 (1984).
14. M. Trautmann, T. Trickl, and J. Wanner, Ber. Bunsenges Phys. Chem., 86, 842 (1982).
15. S. J. Davis, Laser Digest, AFWL-TR-79-104, 167 (Spring 1977).

assumptions that were made in this work. For example, more precise experiments are needed to quantitatively determine the quenching mechanism by O_2 and H_2O . Furthermore, low pressure IF(B) quenching and vibrational transfer experiments are needed to determine the collisional effects of I_2 and IF(X) on IF(B). Single collision experiments are also needed to absolutely determine the importance of multiple vibrational transitions.

Finally, the most important study that should be attempted is a low pressure (single collision), state-resolved rotational transfer investigation. Such a study would be the first for an interhalogen diatomic and would be one of the few performed in an electronically excited state of a heteronuclear diatomic molecule. These studies are necessary for several reasons. First, rotational energy transfer data provide information on the angular dependence of the intermolecular interaction potential. This information can then be used to determine selection rules for the energy transfer process. For example, inversion symmetry considerations in homonuclear molecules such as I_2 restrict ΔJ transitions to $+2J$. This selection rule should be relaxed in IF since there exists no inversion symmetry, and a more extensive rotational redistribution may be observed. Finally, the effects of polar collision partners on the rotational transfer process should be more dramatically evident since IF possesses a permanent dipole moment.

method for analyzing the experimental data.

Rotational energy transfer in $\text{IF}(\text{B}; v')$ with the noble gases and N_2 was the most efficient collisional process in $\text{IF}(\text{B})$. Rotational energy transfer was typically 200 times more efficient than vibrational transfer. The efficiencies for R-T energy transfer showed a strong dependence on both the collision reduced mass and the polarizability of the collision partner with the largest rate constants being measured for the heavier collision partners such as Kr. An examination of the vibrational band envelopes indicated that multiquantum rotational jumps may be highly probable within the B state vibrational levels.

B. Further Studies

The vibrational transfer data that was presented in this text should be adequate to make meaningful comparisons with a number of scattering models which have been proposed to explain energy transfer in gases. Since the B state of IF behaves as a classical harmonic oscillator as indicated by the observed trends in the cross sections, the more traditional theories such as Landau-Teller and SSH should first be employed to predict both the absolute rates and the observed trends in the cross sections. More sophisticated quantum mechanical models may then follow this analysis. These calculations are important since they not only test the model and its limitations, but also provide physically important intermolecular potential parameters. These parameters can then be used in numerical trajectory calculations to obtain a physical picture of the collision process.

Additional experiments should be performed to evaluate certain

The vibrational transfer rate constants were typically two orders of magnitude greater than the corresponding quenching rate constants for the noble gases and N_2 . For O_2 and F_2 , however, electronic quenching effectively competed with vibrational transfer in the lower vibrational manifold. The vibrational transfer cross sections for the noble gases, N_2 , and O_2 scaled linearly with vibrational quantum number (i.e., $\sigma(v, v-1)$ monotonically increased with v .) The lightest collision partners were the most efficient vibrational transfer agents; and the vibrational transfer efficiency for the noble gases appeared to monotonically decrease with the collision reduced mass as predicted by the SSH vibrational transfer theory. These results showed that the elementary vibrational transfer theories accurately predicted the observed trends in $IF(B)$. Finally, vibrational relaxation predominately occurred via a $\Delta v = -1$ cascade with multiquantum vibrational transfer not being important.

An important result of these vibrational transfer experiments was that the numerical value of the rate constants determined in the two experimental methods agreed to within experimental error. The results showed that both methods were needed to completely characterize the vibrational transfer process. Temporally and spectrally resolved LIF was the most accurate method for determining the absolute magnitudes of the rate constants since the events are observed in real time. The cw method provided a quantitative evaluation of the population redistribution and multiquantum transfer processes. The cw method also provided an unambiguous determination of vibrational rate scaling since no a priori assumptions were made about the collision process in developing the

VI. CONCLUSIONS

A. Summary

Detailed collisional energy transfer was studied in the $B^3\Pi(0^+)$ state of iodine monofluoride (IF) using laser induced fluorescence (LIF) in a chemically reactive flow system. Electronic quenching and vibrational energy transfer were studied as a function of both initially populated vibrational level and collision partner using both steady-state and time resolved LIF methods. Rotational energy transfer was studied as a function of collision partner by measuring the total removal rate from an initially populated rotational level under cw excitation conditions.

The B state of IF was relatively immune to electronic quenching by the noble gases and N_2 ; and an upper limit for the quenching rate constant by these gases was assigned as $1 \times 10^{-14} \text{ cm}^3 \text{ molecule}^{-1} \text{ s}^{-1}$. These rate constants were also independent of vibrational quantum number. Quenching by F_2 and O_2 was more efficient but displayed relatively slow rate coefficients. Electronic quenching by I_2 efficiently depleted the IF(B) population with a rate constant estimated as 1.3 times greater than the gas kinetic value. The rapid quenching of IF(B) by I_2 is striking and may indicate a process in which $I_2(X; v'' \gg 0)$ is formed. Quenching by O_2 may be a two-fold process where, at short times, $E \rightarrow E$ energy transfer may provide the initial loss of IF(B) population. IF(B) depletion rate constants were also measured for H_2O . At short times, H_2O efficiently removed IF(B) population with a thermally averaged cross section approaching the hard sphere value.

Vibrational energy transfer dominated electronic quenching in IF(B).

these kinetic processes may not be immediately evident.

These experiments also show that the two experimental methods are complementary to each other, and both methods are needed to fully characterize detailed energy transfer processes. The time resolved experiments provide the most natural method for determining rate constants since the events are observed in real time. The accuracy in determining these rate coefficients depends only on the method which is used to extract the values from the data. However, this experimental method has two drawbacks. First, time resolved LIF methods do not allow one to determine how the population is redistributed among the available energy levels since the method involves observing the time history of a single quantum state. Secondly, the analysis of the data becomes very complex when V-T or R-T transfer is studied among energy levels which are very closely spaced (i.e. when $\Delta G_v < kT$).

These two problems are overcome by performing the cw experiments. The steady-state experiments provide an unambiguous determination as to how the population is redistributed among the various energy levels, and an uncumbersome evaluation of multiquantum transfer processes which become important for closely spaced energy levels. Since the relative population distributions are known, providing that one accounts for additional kinetic effects due to background gases, the steady-state analysis lends itself to a straightforward determination of the rate constants for situations when the energy levels are closely spaced. However, systematic errors can plague the accuracy of the absolute value of the rate constants. This problem is absent in the pulsed experiments with the errors being due to statistical uncertainties in the data.

results of these previous studies coupled with the qualitative conclusions in this work strongly suggest that multiple quantum rotational transitions occur in IF(B). However, conclusive evidence of this mechanism can only be obtained in low pressure (single collision), rotationally state resolved experiments.

D. General Observations Concerning Steady-State and Time-Resolved Experiments

The results of these energy transfer studies show that problems may occur in determining energy transfer rate constants using cw LIF in a chemically reactive flow system. The problem originates from the chemically reactive nature of the flow system. As we have seen in the present experiments, chemically reactive systems (i.e., the $I_2 + F_2$ reaction) are very sensitive to changes in the flow conditions as indicated by the increase in the IF(X) number density with increased bath gas pressures. The effect of changes in both flow conditions and the concentration of unreacted species must be accounted for in the cw data analysis if they affect the kinetics of the collision process being studied.

This problem is surmounted by performing the experiments using temporally and spectrally resolved LIF. Here, the time history of molecules rather than the relative number density in a vibrational or electronic state is important. Small changes in the flow conditions will not affect the determination of the rate constants. In fact, as seen in the quenching studies, anomalous behaviors will surface in the data analysis providing additional kinetic information which will be masked in the cw experiments. This additional information can only be obtained in cw experiments by performing separate studies, usually with foresight, since

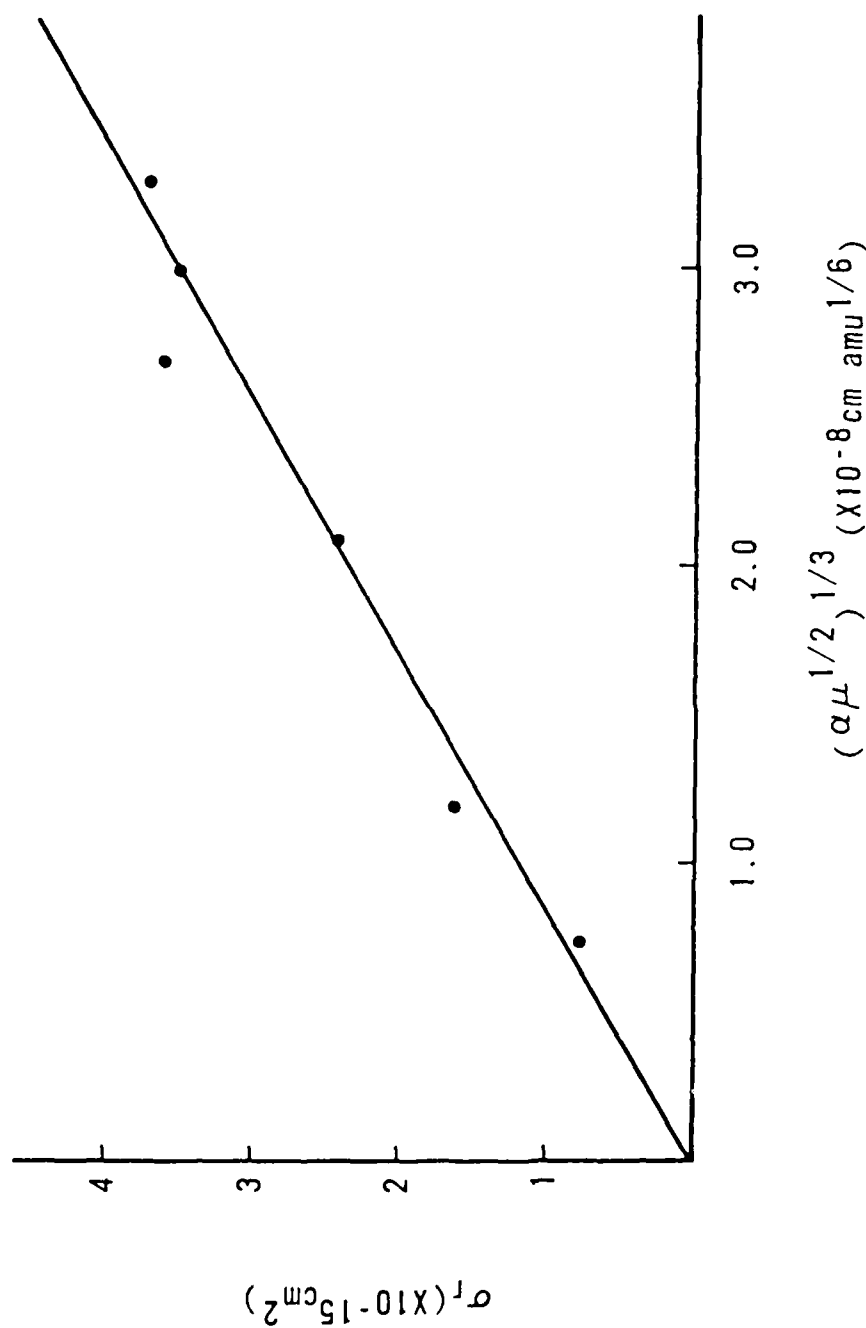


Figure 5-10. Plot of the rotational transfer cross sections vs. the polarizability parameter, $(\alpha \mu^{1/2})^{1/3}$, for the noble gases.

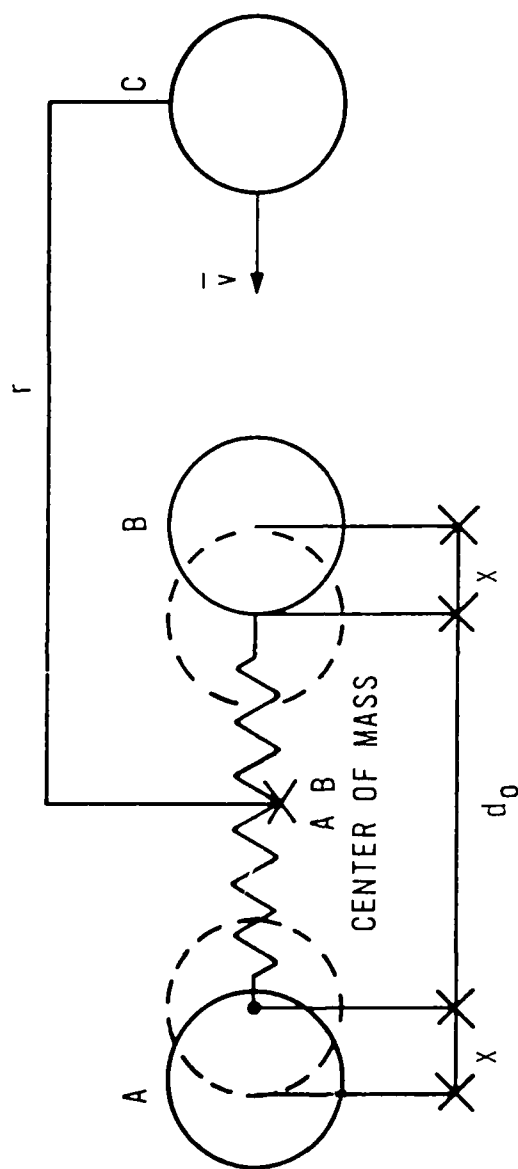


Figure B-1. Collision geometry for an atom-diatom encounter.

describing the efficiency of vibrational energy transfer is obtained using Ehrenfest's adiabatic principle.^{2d} This principle is based on the effect of an external force on a quantized periodic motion. In particular, if the relative change in the strength of the external force is small during the period of motion, then the process is called adiabatic. In classical collision theory (i.e., when one deals with collisions involving a molecule and an atom which are both treated as elastic hard spheres), adiabatic collisions describe encounters which involve "soft" forces. Since these forces change slowly with distance, there is usually no net transfer of energy between the collision partners. In contrast if the change of force is strong during the period of motion, quantum transitions can occur in which case the process is called non-adiabatic or impulsive.

These two processes are usually expressed in terms of an adiabaticity parameter, ξ , which is defined below.

$$\xi = \tau_c / t \quad (B-1)$$

where τ_c is the duration of the collision, and t is the period of motion. Therefore, adiabatic collisions correspond to large values of ξ while the criterion for a non-adiabatic process is

$$\xi < 1 \text{ or } \tau_c < t \quad (B-2)$$

The collision time can be expressed as

$$\tau_c = \ell / v \quad (B-3)$$

where ℓ is the effective range of the intermolecular force and v is the average thermal velocity of the collision pair, given by

$$\bar{v} = (8kT/\pi\mu)^{1/2} \quad (B-4)$$

Thus, the criterion for efficient energy transfer becomes

$$(8kT/\pi\mu)^{1/2} > \ell \Delta E/h \quad (B-5)$$

where $\Delta E = h\nu = h/t$ and ν is the frequency of the periodic motion. So, qualitatively, energy transfer will be favored for collisions involving partners with small masses, small energy level spacings, a steep intermolecular potential (small value of ℓ), and high temperatures.

3. Landau-Teller Model

Landau and Teller⁴⁸ developed an elementary theory of vibrational relaxation based on Ehrenfest's adiabatic principle. The Landau-Teller theory assumes that perturbations which induce transitions are linear in the normal coordinate, which is the internuclear separation for a harmonic oscillator. It is also assumed that this perturbation is small so that first order perturbation calculations can be made. With these assumptions, Landau and Teller found that the probability, P_{10} , for a collisional transition from $v = 1$ to $v = 0$ was represented by the Fourier component of the time dependent perturbation at the oscillator frequency:

$$C_0 \propto |X_{10}|^2 \left[\int_{-\infty}^{+\infty} F(t) \exp[2\pi i \nu t] dt \right]^2 \quad (B-6)$$

where $X_{10} = \langle v = 1 | X | v = 0 \rangle$, X is the displacement of the oscillator, $F(t)$ is the force, and ν is the oscillator frequency. If the time depen-

dent force, $F(t)$, experienced by the molecule rapidly changes as the atom approaches, the force will have many Fourier components. It is, therefore, likely that some of these Fourier components will occur at the oscillator frequency, ν , making a transition highly probable.

Landau and Teller also concluded that the probability of energy transfer depends on the ratio of the period of vibration to the interaction time. They assumed an interaction potential of the form $V(r) = V_0 \exp(-\alpha r)$ where $\alpha = 2\pi\nu/v$.

Averaging over the Maxwell distribution of velocities for the relative motion, the average probability of deactivation per collision is

$$P_{10} \propto \exp[-3(2\pi^4\mu\nu^2/\alpha^2 kT)^{1/3}] \quad (B-7)$$

In general, the average probability of deactivation per collision for any transition from vibrational level n to $n-1$ was determined as

$$P_{n,n-1} = n P_{10} \quad (B-8)$$

where P_{10} is given in Eq.(B-7). Equation (B-8) indicates that the matrix elements for collisional transitions are identical, to within a constant, with those for radiative transitions. Therefore, the same selection rules hold for collisional transitions as for radiative ones: transitions can occur only between adjacent vibrational levels.

Equation (B-7) shows the same qualitative features for the efficiency of vibrational transfer as in Ehrenfest's adiabatic principle. That is, efficient transfer is favored for small masses, small vibrational frequencies, short interaction distances, and high temperatures.

4. SSH Theory

The Landau-Teller theory assumes an adiabatic collision which leads to small transition probabilities. The intermolecular potential describes a weak interaction in which colliding molecules are turned around at a large separation and thus, any perturbation will be weak. Such an interaction is not realistic because it ignores the attractive component of the intermolecular potential. This attractive part causes an acceleration of the colliding partners and aids in the energy transfer process.

Schwartz, Slawsky, and Herzfeld⁴⁹ developed a quantum mechanical theory which incorporated the attractive part of the potential. The form of the potential was

$$V(r) = V_0 \exp(-\alpha r) - \epsilon \quad (\text{B-9})$$

Equation (B-9) essentially describes a repulsive potential; and the attractive forces, represented by $(-\epsilon)$, are regarded as simply increasing the velocity of relative motion, thus favoring a higher transition probability. Using this potential, the SSH V-T relaxation probability is

$$P_{n,n-1} \propto [V_{n,n-1}]^2 \frac{\theta'}{\theta} \left(\frac{\theta'}{\theta}\right)^{1/6} \exp[-3/2(\theta'/\theta)^{1/3} + \theta/2T + \epsilon/kT] \quad (\text{B-10})$$

where $\theta' = 4\pi^2\omega^2/k\alpha^2$ and $\theta = \hbar\omega/k$.^{2b}

The term, $[V_{n,n-1}]^2$, is the square of the matrix element for the transition between states n and $n-1$. It represents the coupling of the initial and final states of the oscillator under the influence of the perturbation produced by the collision. This term also corresponds to the

square of the Fourier component of the varying force at the oscillator frequency which as described in the Landau-Teller theory. This matrix element is given by Eq.(B-11) for single quantum vibrational transitions.

$$[V_{n,n-1}]^2 = \alpha^2 (\bar{A})^2 n/2 \gamma \quad (B-11)$$

where α is the repulsion parameter, $\gamma = 4\pi^2\nu/h$ and $(\bar{A})^2$ is a mass dependent term.

The results of the SSH theory qualitatively give the same mass, temperature, and vibrational frequency dependence on the transition probability as was found in the Landau-Teller theory. The major difference between the two theories, though, is the exponential term which includes the attractive part of the potential, $-\epsilon$. For cases where the attractive potential is large, the term $\exp(\epsilon/kT)$ becomes dominant. This gives rise to a higher transition probability which will vary inversely with temperature.

More complicated vibrational energy transfer theories can be found in the literature. But, qualitative comparisons are usually made between experimental data and the three theories discussed in this section. For quantitative comparisons, the SSH theory is most widely used. In past studies, the SSH theory accounted semi-quantitatively for most of the principal features of vibrational energy transfer, and give fair quantitative predictions for simple molecules.²

APPENDIX C: Steady-State Backtransfer Corrections

The correction for vibrational backtransfer in Eq.(2-8b) due to multiple collisions is obtained by adding an input term from all other vibrational levels to Eq.(2-7a). From the master equation, the appropriate expression is

$$N(v_i) = \frac{S_{0i}'N_0 + k(v_{i+1}, v_i)'M N(v_{i+1}) + k(v_{i-1}, v_i)'M N(v_{i-1})}{1 + R_B'N_B + (Q_m' + k_v')M} \quad (C-1a)$$

where $\sum_j k_{ji} N_j = k(v_{i+1}, v_i)N(v_{i+1}) + k(v_{i-1}, v_i)N(v_{i-1})$ and only $\Delta v = \pm 1$ transitions are considered (i.e., $v_f = v_{i \pm 1}$). Combining Eqs.(C-1a) and (2-4a), one obtains after rearrangement

$$\begin{aligned} [1 + Q_m'M + R_B'N_B] [N/N(v_i)] + [k(v_{i+1}, v_i) N(v_{i+1})/N(v_i) \\ + k(v_{i-1}, v_i)'N(v_{i-1})/N(v_i)] M = k_v'M \end{aligned} \quad (C-1b)$$

Equation (C-1b) provides a very convenient method for obtaining a backtransfer correction to the vibrational relaxation rate constants. After obtaining the state-to-state rate constants from the experimental data, the reverse rates, $k(v_{i+1}, v_i)$, are calculated using detailed balance. These values are then inserted into Eq.(C-1b) to obtain the "corrected" value for the total removal rate constant, k_v' . This procedure is continued by cycling the results through Eqs.(2-8) and (C-1b) until consistent values are obtained. Although these equations were developed for single quantum transitions, extensions for multiple quantum transitions can easily be made.

Specific trends in the Stern-Volmer plots which are used to extract the rate constants may indicate the presence of vibrational backtransfer. Assuming that the vibrational level, v_{i-1} , is solely responsible for collisional repopulation, Eq. (C-1b) is re-written as

$$(1 + Q_m'M + Q_B'N_B)[N/N(v_i)] = k_v'M - k(v_{i-1}, v_i)'M N(v_{i-1})/N(v_i) \quad (C-2)$$

Since the ratio $N(v_{i-1})/N(v_i)$ is also proportional to the bath gas density, M , via Eq.(2-8b), we have

$$N/N(v_i) \propto C_1M + C_2M^2 \quad (C-3)$$

Therefore, relative number densities which have a quadratic dependence on the bath gas density in a Stern-Volmer plot is evidence for multiple collision, backtransfer effects.

In the R-T studies, rotational backtransfer need not be considered since only a small fraction of molecules transferred out of J_i return to it.²⁵ This is a consequence of the fact that $\Delta E_r \ll kT$ at room temperature for IF(B) which results in a large probability for multiquantum transfer. For example, the rotational level spacings are typically less than 20 cm^{-1} around the Boltzmann maximum in the B state of IF($J_m \sim 21$). According to Ehrenfest's principle, this means that multiquantum transitions are highly probable with as much as 10 rotational quanta being exchanged in a single collision. Therefore, secondary collisions which deplete J_f result in the population of a wide range of rotational energy levels.

However, vibrational backtransfer must be considered since vibrational

transfer from v_i affects all rotational levels equally. But, vibrational transfer into v_i from other collisionally populated vibrational levels will most likely populate a rotational level other than the initially excited one. So, by simply combining Eqs.(C-1a) and (2-9), one obtains after rearrangement:

$$P[N(v_i)/N(J) - 1] - TM = k_r'M \quad (C-4a)$$

where

$$P = 1 + (Q_m' + k_v')M + R_B'N_B \quad (C-4b)$$

and

$$T = k(v_{i+1}, v_i)' N(v_{i+1})/N(v_i) + k(v_{i-1}, v_i)' N(v_{i-1})/N(v_i) \quad (C-4c)$$

APPENDIX D: Qualitative Features of Temporally Resolved Vibrational Relaxation Data.

Although a unique interpretation of the simple vibrational relaxation problem presented in Chapter II cannot be made, some general features of spectrally and temporally resolved vibrational relaxation can be described. For simplicity, assume that all of the upward rates are negligible. Thus, Eqs.(2-13) reduce to:

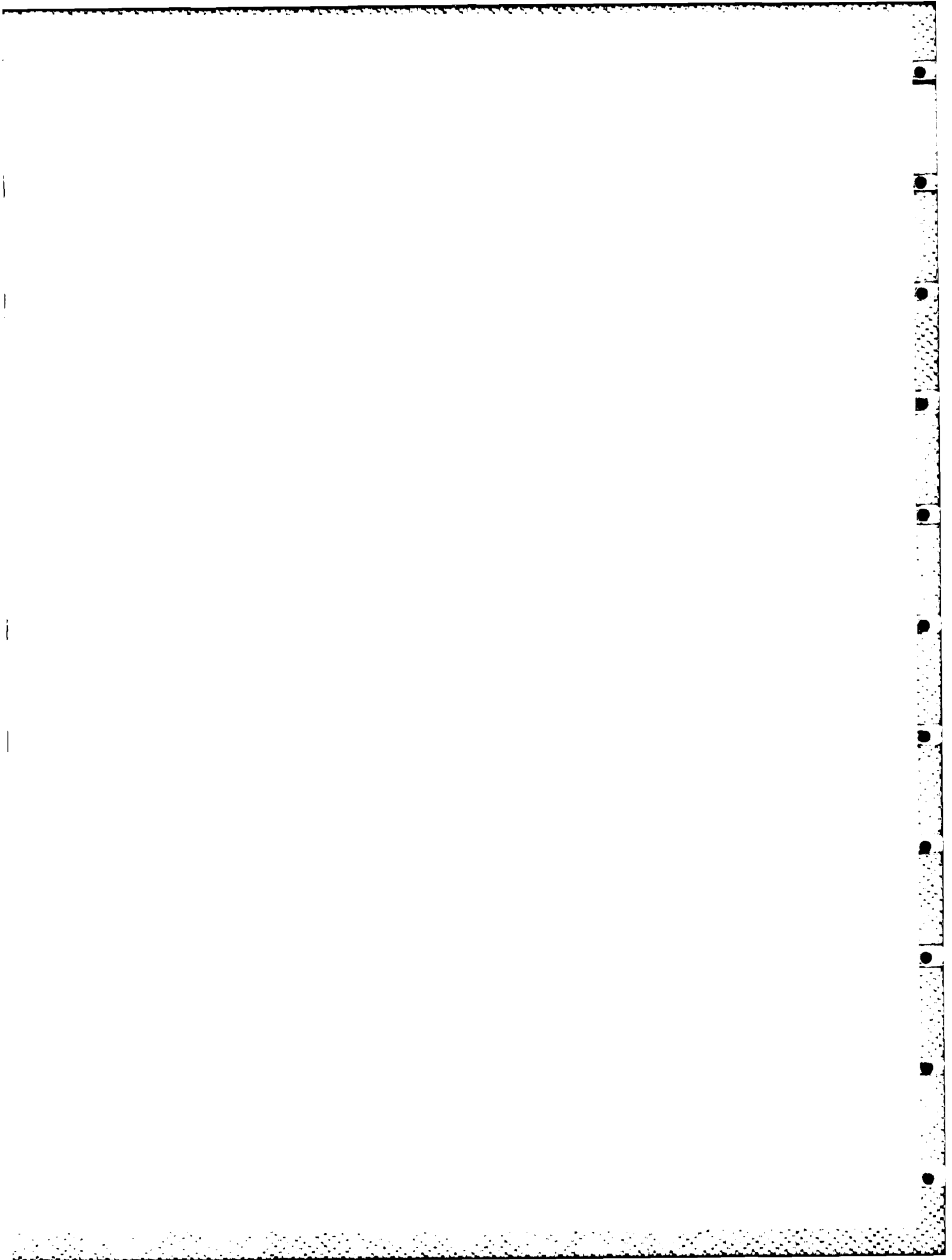
$$N(v)_t = N(v)_{t=0} e^{-\alpha' t} \quad (D-1a)$$

$$N(v-1)_t = \frac{\beta}{\gamma' - \alpha'} [e^{-\alpha' t} - e^{-\gamma' t}] \quad (D-1b)$$

where $\alpha' = k(v, v-1)M + \Gamma(v)$, $\beta = k(v, v-1)M N(v)_{t=0}$, and $\gamma' = k(v-1, v-2)M + \Gamma(v-1)$

Equation (D-1a) shows that the population in the initially excited state decays exponentially in time with the decay rate being much faster than the decay observed for total fluorescence. This effect is graphically demonstrated in Fig. D-1. (These spectra were obtained in the presence of 1.3 Torr of He subsequent to excitation of $v' = 3$ in IF(B).) Spectrally unresolved fluorescence is pictured in Fig. D-1a in which the decay results from the removal of population from the entire B state manifold. Figure D-1b represents the time evolution of the spectrally resolved $v' = 3$ state. The decay of $v' = 3$ combined with the data in Fig. D-1a is direct evidence that the population in $v' = 3$ is being redistributed among the vibrational levels in IF(B).

Equation (C-1b) shows that the time evolution of the population in the



"satellite" bands is described by a difference in two exponentials as depicted in Fig. D-2. The characteristic rising and falling exponential corresponds to: (1) the time required to populate $v-1$ from v , and (2) the subsequent collisional decay of the state to $v-2$ coupled with quenching and radiative effects. The maximum in the decay curve occurs when $dN(v-1)/dt = 0$ or at $t = C/M$, where C is a constant and with $\bar{\Gamma}(v) = \bar{\Gamma}(v-1)$. Thus, this maximum decreases towards shorter times as the bath gas pressure is increased. This means that, at higher bath gas pressures, it takes less time to populate $v-1$ from v . Of course, at these higher pressures, enough population has built up in $v-1$ that relaxation to $v-2$ must now be included in the analysis. The high pressures also increase the probability of backtransfer due to multiple collisions thereby forcing the inclusion of reverse rates (i.e., $k(v-1, v)$) to account for this process.

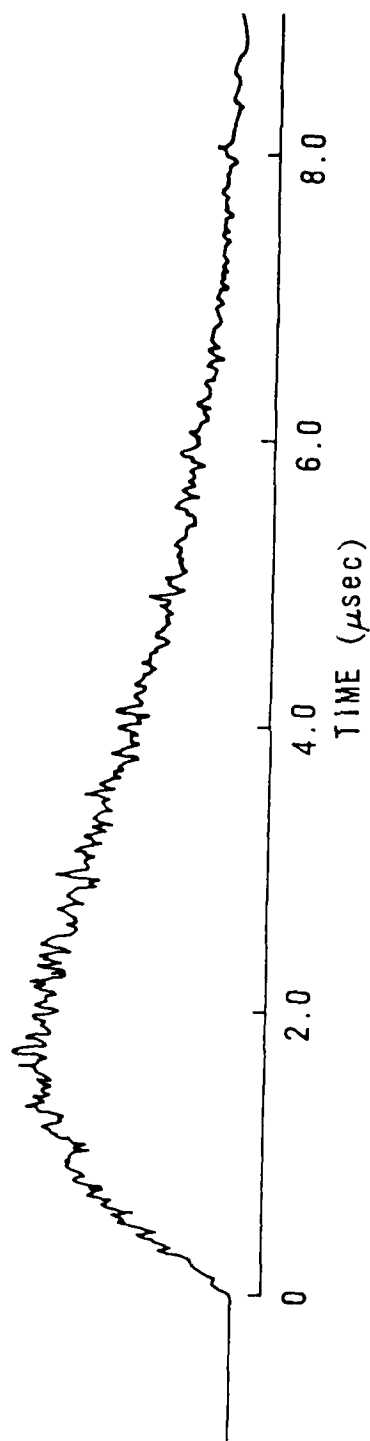


Figure D-2. Time history of $v' = 2$ in IF(B) subsequent to $v' = 3$ excitation.

APPENDIX E: Montroll and Shuler Solution to Time Resolved Vibrational Relaxation

The Montroll and Shuler (MS)³⁰ kinetic equation describing the time evolution of a system of harmonic oscillators immersed in an inert heat bath (omitting quenching and radiative effects) is given below.

$$\frac{dX_n(t)}{dt} = -K(n,n+1)X_n(t) - K(n,n-1)X_n(t) + K(n+1,n)X_{n+1}(t) + K(n-1,n)X_{n-1}(t) \quad (E-1)$$

where $n = 0, 1, 2, \dots$, $X_n(t)$ is the population of level n , and $K(n,m)$ is the first order vibrational relaxation rate constant from level n to level m . The general relaxation equation was further simplified using the Landau-Teller prescription for the collisional transition probabilities.^{2d} These rates have the form

$$\begin{aligned} K(n,n-1) &= k(n, n-1)M = nk(1,0)M \\ K(n-1,n) &= n \exp(-\Theta)k(1,0)M \end{aligned} \quad (E-2)$$

where $\Theta = h\nu/kT$ and ν denotes the fundamental frequency of the oscillators. The quantity M is the bath gas concentration and $k(1,0)$ is the basic parameter in the analysis. The equation solved by Montroll and Shuler is

$$dX_n(t)/dt = k(1,0) \left[ne^{-\Theta} X_{n-1} - [n + (n+1)e^{-\Theta}] X_n + (n+1)X_{n+1} \right] \quad (E-3)$$

For an initial δ -function distribution in which

$$X_n(0) = \begin{cases} 1 & \text{if } n = m \\ 0 & \text{otherwise} \end{cases} \quad (E-4)$$

the equation describing the time development of the population of any

AD-A159 242

COLLISIONAL DYNAMICS OF THE B3PI(0+) STATE OF IODINE
MONOFLUORIDE(U) AIR FORCE INST OF TECH WRIGHT-PATTERSON
AFB OH SCHOOL OF ENGINEERING P J WOLF MAR 85

3/3

UNCLASSIFIED

AFIT/DS/PH/85-1

F/G 7/4

NL

END

FILED

ETC

vibrational level is

$$x_n(t) = \frac{(1 - e^{\Theta})}{(e^{-\tau} - e^{\Theta})} e^{m\Theta} \left(\frac{e^{-\tau} - 1}{e^{-\tau} - e^{\Theta}} \right)^{m+n} F(-n, -m, 1; U^2) \quad (E-5)$$

where

$$U = \frac{\text{SINH}(\Theta/2)}{\text{SINH}(\tau/2)}$$

$$\tau = Kt(1 - e^{-\Theta})$$

F = hypergeometric function

The solution to the master equation presented above does not consider concurrent collisional (i.e., quenching) or radiative transitions. However, when a study involves vibrational relaxation in an electronically excited state, one must account for these kinetic events to properly describe the full relaxation process. Rubin and Shuler,⁶⁰ in studying this effect, found that concurrent transitions do not change the relaxation behavior of the system of harmonic oscillators. The only change is in the time scale of the relaxation in that Eq.(E-5) must be multiplied by $\exp(-\Gamma t)$ where Γ is given by Eq.(2-11c). Therefore, time resolved vibrational relaxation data were analyzed by fitting the data to the corrected form of Eq.(E-5), in which there exists only one adjustable parameter: the vibrational relaxation rate constant, $K(1,0)$.

The unique feature of the MS solution is that it takes into account not only the initial decay from various vibrational levels, but also the reverse pathways which become important at the higher bath gas pressures

(i.e., multiple collisions repopulating the initial level). Corrections for anharmonicity can also be included in the analysis. This correction is more difficult since it would involve numerical integration of the general relaxation equation. But, the relaxation behavior of a system of anharmonic oscillators can be represented, quite accurately, by a system of harmonic oscillators provided the anharmonic constants are not very large.⁶¹ For example, Bazley et al.⁶¹ showed that the difference in the relaxation behavior between the harmonic and anharmonic oscillators was quite small, amounting at most to 0.1 or about $5x_e$ for OH ($x_e = 2.217 \times 10^{-2}$) where $x_e = \omega_e x_e / \omega_e$. In the case of O_2 , the difference amounted to less than 0.01 or $\sim 1x_e$ ($x_e = 7.639 \times 10^{-3}$). Based on these results, the difference between an harmonic and an anharmonic oscillator analysis in the B state of IF ($x_e = 3.2 \times 10^{-3}$) should be less than one percent. Therefore, the harmonic oscillator analysis should quite accurately describe vibrational relaxation in IF(B).

APPENDIX F: Number Density Estimates for the Time Resolved Experiments

Precise measurements of IF(X) number densities could not be made due to the kinetically unstable nature of the molecule. However, an upper limit of the IF(X) concentration was estimated in the following way given typical starting conditions (i.e. no bath gases and a choked flow). First, the I₂/He flow was established, resulting in a cell pressure of 0.07 Torr, with a 15 Torr helium back pressure in the I₂ reservoir. Since the iodine vapor pressure is 0.3 Torr at room temperature, the ratio of P(He) to P(I₂) was ~50:1 in the cell assuming a saturated flow. This gives an estimated iodine cell pressure of 2×10^{-3} Torr. Next, the F₂/He flow was established. This flow raised the total cell pressure from 0.07 Torr to 0.2 torr with 1.3×10^{-2} Torr of the total being F₂. Therefore, the maximum IF(X) concentration was 6.4×10^{13} molecules cm⁻³ assuming that all the I₂ has reacted. The remainder of the gas mixture was estimated as 6.0×10^{15} atoms cm⁻³ of He and 3.9×10^{14} molecules cm⁻³ of unreacted fluorine.

In practice, the IF(X) number density was less than the above estimated value since fluorescence from unreacted I₂ was observed using 514.5 nm radiation with both reactants in the cell. Therefore, it is desirable to calculate a lower limit for the IF(X) concentration and then average the two values to obtain reasonable number density estimates.

An estimate for the lower limit of the IF(X) concentration was obtained by solving the kinetic expressions describing reactions (3-1) and (3-2). The kinetic equation describing reaction (3-2) is

$$\frac{d[IF(X)]}{dt} = k_2 [I_2F] [F] \quad (F-1)$$

where k_2 is the rate constant for reaction (3-2). Assuming that $[I_2F]$ is small, we can solve for $[I_2F]$ in the steady-state approximation. The result is given in Eq.(F-2).

$$[I_2F] = k_1[I_2] [F_2]/k_2[F] \quad (F-2)$$

Inserting Eq.(F-2) into Eq.(F-1), we obtain

$$\frac{d[IF(X)]}{dt} = k_1[I_2][F_2] = \frac{-d[I_2]}{dt} = \frac{-d[F_2]}{dt} \quad (F-3)$$

Integrating Eq.(F-3), the expression for $[IF(X)]$ is given below.

$$[IF(X)] = k_1[I_2][F_2]t \quad (F-4)$$

Letting $t = 40$ ms, which is the estimated transit time between the reactant mixing point and the laser excitation region, the lower limit for $[IF(X)]$ is 2.0×10^{12} molecules cm^{-3} . Solving Eq. (F-3) for $[I_2]$ and $[F_2]$, the remaining reactant concentrations were estimated as follows: $[F_2] = 4.1 \times 10^{14}$ molecules cm^{-3} and $[I_2] = 6.2 \times 10^{13}$ molecules cm^{-3} . Thus, the average gas densities were: $[IF(X)] = 3.3 \times 10^{13}$ molecules cm^{-3} , $[F_2] = 4.0 \times 10^{14}$ molecules cm^{-3} , $[I_2] = 3.1 \times 10^{13}$ molecules cm^{-3} , and $[\text{He}] = 6.0 \times 10^{15}$ atoms cm^{-3} .

Using these estimated number densities, the $IF(B)$ concentration was determined by assuming linear absorption.^{20a} Thus, we have

$$[IF(B)]/[IF(X)] \sim 1 - I/I_0 = 1 - \exp(-\ell[IF(X)]\alpha) \quad (F-5)$$

where I/I_0 is the fraction of the incident laser intensity absorbed in a medium of length ℓ , and α is the absorption cross section. The fraction $[IF(B)]/[IF(X)]$ was estimated as 0.03 using $\ell = 10.16$ cm and $\alpha = 8.5 \times 10^{-17}$ cm² as determined by Clyne and McDermid.¹² Therefore, $[IF(B)]$ was approximately 1×10^{12} molecules cm⁻³.

The $IF(B) + M$ collision frequencies at 300 K can now be calculated via Eq.(F-6).

$$Z = \sigma v N_A \quad (F-6)$$

where $\sigma = .25\pi(d_A + d_{IF})^2$, v is the mean relative velocity, and N_A and d_A are respectively the number density and diameter of the target molecules. Assuming an IF collision diameter of 4.4×10^{-8} cm, where $d_{IF} = 0.5(d_{F_2} + d_{I_2})$, the estimated collision frequencies for baseline conditions are listed in Table F-1. Also listed in this table is the quantity $(Z\tau_R)^{-1}$ which gives the number of $IF(B)$ radiative lifetimes per collision.

There are three conclusions that can be drawn from this table. First, the $IF(B)$ - $IF(X)$ encounters are in the collision free regime with approximately 25 $IF(B)$ radiative lifetimes per collision. Therefore, collisional interactions between these molecules are not important. Secondly, since the $I_2 + F_2$ reaction produces a rich visible chemiluminescence spectrum⁷ which populates a large number of $IF(X)$ vibrational and rotational levels, the high frequency of $IF(X)$ -He collisions assures vibrational and rotational thermalization in $IF(X)$ before $IF(X)$ molecules

TABLE F-1. IF(B) + M collision frequencies, Z, and, correspondely, the number of IF(B) lifetimes per collision, $(Z\tau_R)^{-1}$. The average IF(B) lifetime was taken as $7 \mu s$.

Collision Partner(M)	Z (collisions s^{-1})	$(Z\tau_R)^{-1}$
IF(X)	5.7×10^3	25
He	2.9×10^6	.05
F ₂	9.2×10^4	2
I ₂	7.3×10^4	2

reach the laser excitation region. Finally, Table F-1 indicates that a premature population redistribution will occur from the initially prepared IF(B; v') state before adding a bath gas. That is, there are 28 IF(B)-He collisions before IF(B) radiatively decays. This results in the collisional population of other IF(B) quantum states from (v_f' , J_f'). Collisional encounters between IF(B) and both I₂ and F₂ are also likely to occur further relaxing the initial IF(B; v') distribution through, possibly, V-V energy transfer. This population distribution presents a constant background, and the collisional effects of the added bath gas are examined by monitoring the change in the temporal history of these levels while altering the bath gas concentration.

In time resolved experiments, care must be taken to ensure that there is no net flow of excited molecules out of the observation region. Since IF molecules were heavily diluted in helium, the coefficient of mutual diffusion was estimated using Eq.(F-7).⁶¹

TABLE F-1. IF(B) + M collision frequencies, Z, and the corresponding number of IF(B) lifetimes per collision, $(Z\tau_R)^{-1}$. The average IF(B) lifetime was taken as $7\mu s$.

Collision Partner(M)	Z (collisions s ⁻¹)	$(Z\tau_R)^{-1}$
IF(X)	5.7×10^3	25
He	2.9×10^6	.05
F ₂	9.2×10^4	2
I ₂	7.3×10^4	2

reach the laser excitation region. Finally, Table F-1 indicates that a premature population redistribution will occur from the initially prepared IF(B;v') state before adding a bath gas. That is, there are 28 IF(B)-He collisions before IF(B) radiatively decays. This results in the collisional population of other IF(B) quantum states from (v_i',J_i'). Collisional encounters between IF(B) and both I₂ and F₂ are also likely to occur further relaxing the initial IF(B;v') distribution through, possibly, V-V energy transfer. This population distribution presents a constant background, and the collisional effects of the added bath gas are examined by monitoring the change in the temporal history of these levels while altering the bath gas concentration.

In time resolved experiments, care must be taken to ensure that there is no net flow of excited molecules out of the observation region. Since IF molecules were heavily diluted in helium, the coefficient of mutual diffusion was estimated using Eq.(F-7).⁶²

$$D_{12} = \frac{3}{8} \sqrt{\pi/2} \frac{1}{N S_d} (kT/\mu)^{1/2} \quad (F-7)$$

where $N = N_{IF} + N_{He}$, $S_d = .25 (d_{IF} + d_{He})^2$, and μ the reduced mass. Using the number densities estimated previously, the coefficient of mutual diffusion is $1.2 \times 10^3 \text{ cm}^2 \text{ s}^{-1}$. This large coefficient means that a uniform distribution of particles is achieved quickly in the cell. This interpretation was experimentally verified by measuring cell pressures in two widely separated locations.

The root mean square displacement of excited IF molecules was calculated using

$$(\bar{x}^2)^{1/2} = (2 D_{12} t)^{1/2} \quad (F-8)$$

where D_{12} is the coefficient of mutual diffusion.⁶² In $7 \mu\text{s}$, which is the average lifetime of IF(B), this distance is 0.16 cm or one laser beam diameter. Therefore, a 0.16 cm displacement toward or away from the detector would have no effect on temporal measurements since the emitting species is still within the observation region defined by the focal plane of the aspheric lens.

APPENDIX G: Laser Excitation Spectra Results

Low resolution laser excitation spectra of the $v'' = 0$ bands for $3 \leq v' \leq 8$ were obtained by recording total IF(B) fluorescence intensity as a function of laser wavelength. The laser wavelength scans were made between 445 and 550 nm. These spectra were then used to identify the initially formed (v', J') states in the time resolved energy transfer studies. Table G-1 lists the band heads and the corresponding Franck-Condon factors for the observed vibrational transitions.

Figure G-1 shows a vibrational excitation spectrum recorded at 0.5 nm resolution between 450.0 and 506.0 nm. All of the vibrational bands were easily assigned using Durie's band head measurements.⁵ The vibrational structure in Fig. G-1 shows a dominance of the $v'' = 0$ progression with some possible evidence of some $v'' = 1$ bands. The intensity alteration in the vibrational structure is primarily due to the dye laser pumping efficiency as depicted by the dye power curve in Fig. G-1.

Fluorescence from residual I_2 is clearly visible which prevented $(2,0)$, $(1,0)$, and $(0,0)$ excitation spectra from being recorded at wavelengths longer than 497.0 nm. The I_2 fluorescence was actually much more intense than the IF fluorescence after normalizing the peak intensities with respect to both the dye power curve and the Franck-Condon factors. This indicated that the I_2 concentration was much greater than the IF concentration in the cell. One must, therefore account for the kinetic effect of this background gas.

Figure G-2 shows a selected region of the $(4,0)$ band recorded between 486.8 and 489.0 nm under higher resolution (0.4 cm^{-1}). Since there exist

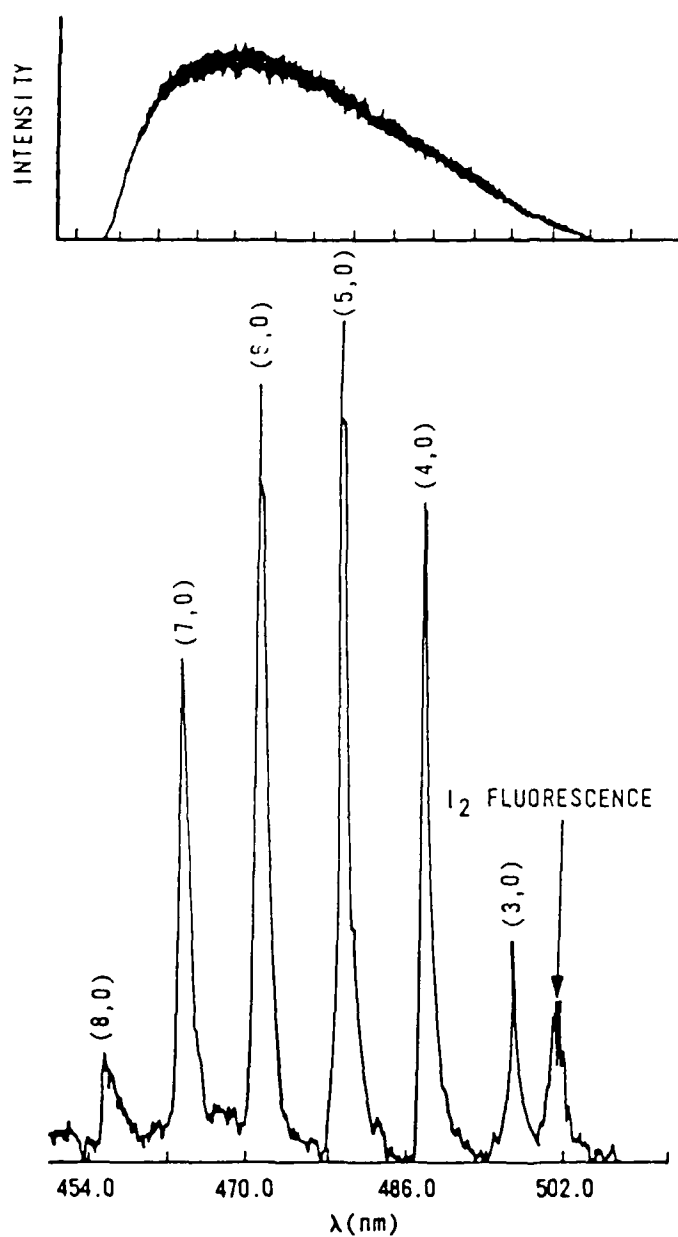


Figure G-1. Laser excitation spectrum recorded at 0.5 nm resolution showing the IF(B \rightarrow X) vibrational structure. The coumarin 102 dye curve is shown at the top of the figure.

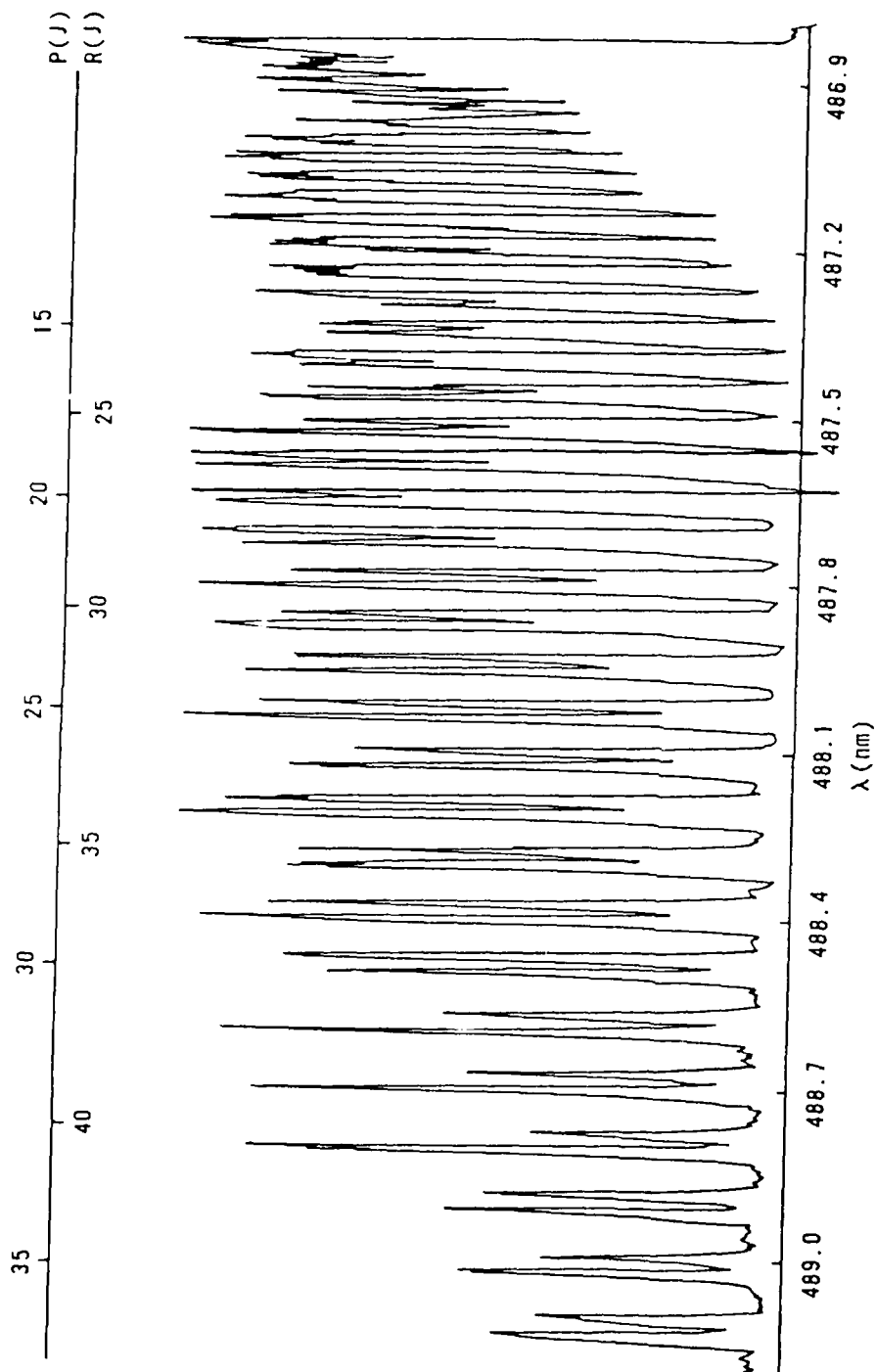


Figure G-2. Rotationally resolved excitation spectrum of the (4,0) band recorded at 0.4 cm^{-1} resolution.

Table G-1. Air wavelengths of band heads and Franck-Condon factors of the IF $B \rightarrow X$ system seen in laser induced fluorescence.

BAND	AIR/nm ^a	$q_v'v''^b$
(3,0)	496.125	0.09
(4,0)	486.817	0.119
(5,0)	478.028	0.133
(6,0)	469.736	0.131
(7,0)	461.931	0.117
(8,0)	454.600	0.096

a. Reference 5, b. Reference 9

only single, naturally occurring isotopes of I and F, the rotational structure appeared as a set of regular P-R doublets. The rotational structure was fairly well resolved for most bands except near the band head. Typically, rotational levels up to $J' = 60$ were observed in all the spectra.

The rotational assignments were made by the method of combination differences, i.e., using

$$R(J) - P(J) = 4B_v'(J + 1/2) \quad (G-1a)$$

$$R(J-1) - P(J+1) = 4B_v''(J + 1/2) \quad (G-1b)$$

where $B_v = B_e - \alpha_e(v + 1/2)$. Durie's values were used for the rotational

In contrast, consider the relaxation of vibrational levels through sequential cascade as shown in Fig. K-1b. The simplified rate expression for the same four level system is

$$\frac{d}{dt} \begin{bmatrix} N_v \\ N_{v-1} \\ N_{v-2} \\ N_{v-3} \end{bmatrix} = M \begin{bmatrix} -k(v,v-1) & 0 & 0 & 0 & N_v \\ k(v,v-1) & 0 & 0 & 0 & N_{v-1} \\ 0 & k(v-1,v-2) & 0 & 0 & N_{v-2} \\ 0 & 0 & k(v-2,v-3) & 0 & N_{v-3} \end{bmatrix} \quad (K-4)$$

The solutions to these equations are

$$N_v = N_v^0 \exp(-\Gamma t) \quad (K-5)$$

$$N_{v-1} = N_v^0 [1 - \exp(-\Gamma t)] \quad (K-6)$$

$$N_{v-2} = \frac{k(v-1,v-2)N_v^0}{k(v,v-1)} [\Gamma t - 1 - \exp(-\Gamma t)] \quad (K-7)$$

$$N_{v-3} = \frac{k(v-2,v-3)k(v-1,v-2)N_v^0}{[k(v,v-2)]^2} [1 + \Gamma t + (\Gamma t)^2/2 - \exp(-\Gamma t)] \quad (K-8)$$

where $\Gamma = k(v,v-1)M$ and $N_v^0 = (N_v)_{t=0}$. The approximate solutions for the population evolution of the collisionally populated states at short times are

$$N_{v-1} \sim \Gamma N_v^0 t = C_1 t \quad (K-9)$$

$$N_{v-2} \sim \frac{\Gamma^2 k(v-1,v-2)N_v^0}{k(v,v-1)} t^2 = C_2 t^2 \quad (K-10)$$

$$N_{v-3} \sim \frac{\Gamma^3}{6} \frac{k(v-2,v-3)k(v-1,v-2)}{[k(v,v-1)]^2} N_v^0 t^3 = C_3 t^3 \quad (K-11)$$

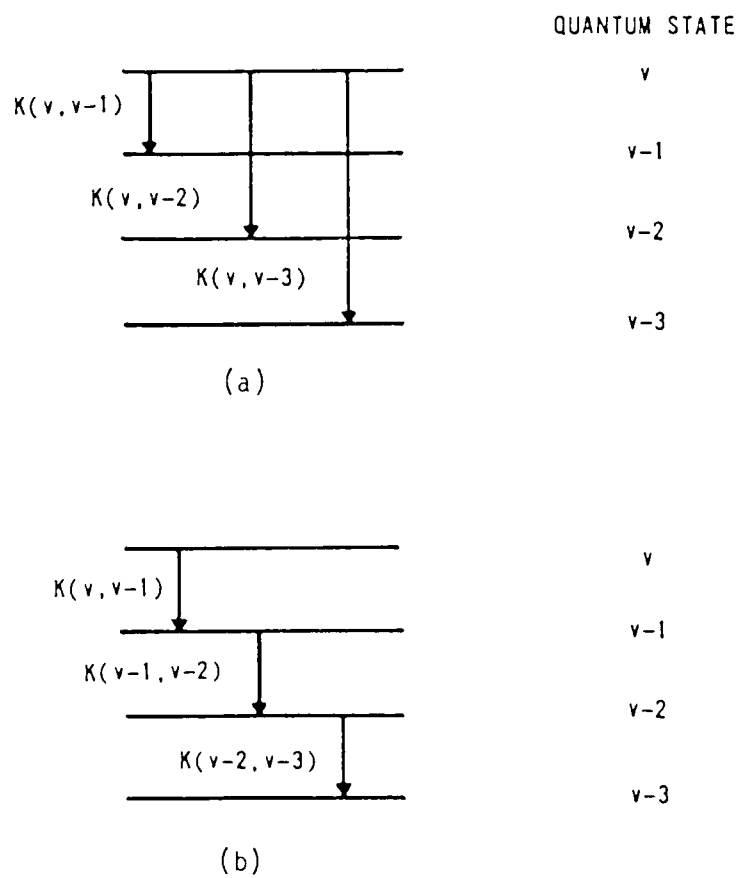


Figure K-1. Schematic energy level diagram comparing (a) multiple and (b) single quantum transitions.

APPENDIX K: Multiquantum Vibrational Transfer

The structure of the fluorescence decay curves from the collisionally populated levels provides information on multiple quantum vibrational transitions. Under single collision conditions, the differential equation describing multiquantum vibrational transfer, as depicted in Fig. K-1a, is expressed as:

$$\frac{d}{dt} \begin{bmatrix} N_v \\ N(v-1) \\ N(v-2) \\ N(v-3) \end{bmatrix} = M N_v \begin{bmatrix} -k_v \\ k(v,v-1) \\ k(v,v-2) \\ k(v,v-3) \end{bmatrix} \quad (K-1)$$

where we only consider a four level system and downward transitions. The subsequent decay from these states are omitted since the transfer process is being analyzed at short times. In Eq.(K-1), k_v is the total removal rate from state v , which is defined as the sum of the state-to-state vibrational transition rates, $k(v,v-\Delta v)$ with $\Delta v = 1,2,3$. The solution to this equation is

$$\bar{N} = \frac{(N_v)_{t=0}}{k_v} (1 - e^{-k_v t}) \begin{bmatrix} 1 \\ k(v,v-1) \\ k(v,v-2) \\ k(v,v-3) \end{bmatrix} \quad (K-2)$$

For small t , the exponential can be expanded and Eq.(K-2) approximated as

$$\bar{N} = \bar{C} k_v t \quad (K-3)$$

where \bar{C} is the column matrix of the ratio of rate constants. Therefore, at short times, multiquantum vibrational transfer is recognized by the linear rise in the fluorescence decay curve of the satellite bands.

lute magnitude of the rate constants are of little importance. Rather, for the present purposes, a comparison of the relative efficiencies are the most meaningful.

B. Time-Resolved Error Estimates

The systematic errors inherent in the determination of the cw rate constants are not present in the pulsed values since the time resolved experiments directly yield first order rates from the data. The accuracy of the rate constants is strictly due to the errors associated with the fitting routine which is used to extract the first order rates and the model assumed. However, these sources of error are insignificant when compared to the errors quoted in Tables 4-2 and 4-3.

All of the energy transfer rate constants were calculated from the slope of a linear least squares fit to the data. The scatter in the data points reflect the uncertainties associated with statistical fluctuations. Using the error analysis for statistical uncertainties in Ref. 63, the following estimates were made. The average uncertainty in the quenching rates is ± 15 percent. These values ranged from ± 10 percent for F_2 quenching to ± 20 percent for O_2 . The determination of both the total vibrational transfer and the state-to-state rate constants are good to within ± 15 percent. The uncertainties in these rates showed very little variation between collision partners or initially populated vibrational level.

between the uncertainties, the accuracy in the total removal rate constant was estimated as ± 38 percent. Since the evaluation of the state-to-state rate constants depended on prior knowledge of the total removal rate coefficient, any error in the determination of the quantity will be amplified. This source of error combined with the errors in the relative number densities resulted in an upper limit of ± 40 percent for the error in the $\Delta v = \pm 1$ rate constants involving efficient relaxers. This error limit increased to about ± 45 percent in the determination of $k(\Delta v = \pm 1)$ for Kr and Xe.

The errors in determining the lower limits of the total rotational relaxation rates came from three sources. First, the method of measuring intensities was changed from an integration of band areas to the measurement of peak heights. This method introduced large discrepancies since complete spectral resolution of the initially pumped rotational level was not possible above the starting gas pressures. Secondly, a prior determination of the vibrational relaxation rate constants was needed to evaluate the rotational transfer data. Any errors in this quantity will be amplified in obtaining the rotational transfer rate coefficient. Finally, as mentioned previously, an error in τ_R was introduced in converting k_r' to k_r . All of these factors indicate that the values of the total rotational transfer rate constants for all the collision partners may be in error by as much as a factor of two or three. Even though the error limits for k_r are large, meaningful comparisons can be made among the various collision partners to obtain information on the physical processes involved in the relaxation process. That is, the abso-

APPENDIX J: Error Analysis

A. CW Error Estimates

CW photometry experiments inherently have many sources of systematic errors which affect the accuracy and, therefore, the overall precision of the rate constants. In these studies, the systematic errors are derived from four sources: (1) uncertainties in the Franck-Condon factors, (2) errors in measuring the relative response of the detection system, (3) uncertainties in the area measurements, and (4) errors in the radiative lifetimes which were used to convert $k(\Delta v)'$ to $k(\Delta v)$.

The uncertainties in the Franck-Condon factors, $q_v'v''$, were obtained from the estimates of Clyne and McDermid,⁹ since no experimental verification of these values have yet been made. Since all the bands used in this study possess strong Franck-Condon factors, a constant error of ± 10 percent was assumed. The error in the relative detection efficiency term, $\alpha(\lambda)$, was more difficult to estimate. This error was determined by comparing $\alpha(\lambda)$ curves that were obtained in the pulsed and cw experimental systems. These uncertainties typically ranged between ± 10 percent for $\lambda \leq 500$ nm or $\lambda \geq 650$ nm to ± 20 percent for $500 < \lambda < 650$ nm. The error in the relative vibrational state densities were obtained from the relative areas error estimates. Typically, the uncertainties in the areas ranged from ± 5 -10 percent for the intense transitions to ± 15 -20 percent for the weak bands. Also, a ± 10 percent mean deviation was used for the radiative lifetimes as determined by Clyne and McDermid.¹²

Using the standard techniques of error propagation,⁶³ where the estimated uncertainties are added in quadrature assuming no correlation

lines without a bath gas. Statistically, the relative areas of the P and R lines are equal to the ratio of the Honl-London factors, S_J . For $J' = 22$, the ratio $S_P(J)/S_R(J) = (J + 1)/J = 1.05$. The measured areas at the base pressures, which are proportional to the peak heights, gave ratios that were in good agreement with the theoretical value. The experimental ratios typically varied by ± 10 percent of the ratio of the Honl-London factors. Finally, the total area representing the population in $J' = 22$ that was inserted into Eq.(2-9b) was obtained by summing the contributions of the P and R lines.

latter was determined by measuring the area bounded by the photon count record and the baseline using a planimeter. The area measurements of the $v'=3$ bands were made simpler since band overlap was absent.

Rotational transfer was manifested as a broadening of the emission from the initial rotational level upon addition of a bath gas as seen in Fig. 4-21. Thus, a measurement of the peak heights of the rotational lines, $H(J)$, was more indicative of the true population in that level. In order to minimize the error in measuring heights which may be due to a convolution from nearby rotationally transferred states, it was assumed that the FWHM points of the initial P and R lines were conserved in each spectra for all the bath gas pressures. After locating the FWHM points in each spectra, the height of the R(21) line was measured from the baseline of the spectra to the center of the FWHM points. In all the spectra, only the R(21) line was used to determine the rotational population since instrumental resolution prohibited the P(23) line from being distinguished from the bandhead at higher pressures. The height of the R(21) line was converted to an area using Eq.(I-1).

$$A(R) = [H(R)/H(R)_0] A(R)_0 \quad (I-1)$$

where $H(R)$ is the peak height at a bath gas pressure, P , and $H(R)_0$ and $A(R)_0$ are the height and area of the R(21) line in the absence of a bath gas. The area of the P(23) line was then computed using

$$A(P) = [H(P)_0/H(R)_0] A(R) \quad (I-2)$$

where $H(P)_0/H(R)_0$ is the ratio of the heights of the R(21) and P(23)

APPENDIX I: Spectral Band Area Calculations in the CW Experiments

1. Vibrational Transfer Experiments

The area under each vibrational band was analytically computed by summing the total photon counts under each band. Typically, 200 to 300 counts were summed over the wavelength range of a vibrational transition. The baseline was determined by subtracting the average background noise from each photon count in a given set of runs. The source of the background noise was primarily PMT dark count and ranged between 8 and 17 counts s^{-1} depending on the amplifier/discriminator selection. At high bath gas pressures, the summing began at the band head and continued until the baseline was reached. At low bath gas pressures, many bands did not reveal a well-defined head. Thus, the photon counts were summed between points where baseline deviations first occurred.

The spectra for three bath gases (He, Ne, and N_2) were also analyzed by measuring the area bounded by the photon count record and the baseline using a Lasico Model 9314 electronic planimeter. This method for determining areas was used to check the precision of the summation code. The two methods agreed to within five percent for obtaining the relative areas of two vibrational bands (i.e., $A(v' = 3 \rightarrow v'' = 1)/A(v' = 2 \rightarrow v'' = 1) = .05$).

2. Rotational Transfer Experiments

The ratio of the population in the initially populated rotational state, $N(J)$, to the total population in $v' = 3$, $N(v)$, was required to calculate the total rotational relaxation rate from Eq.(2-9b). The

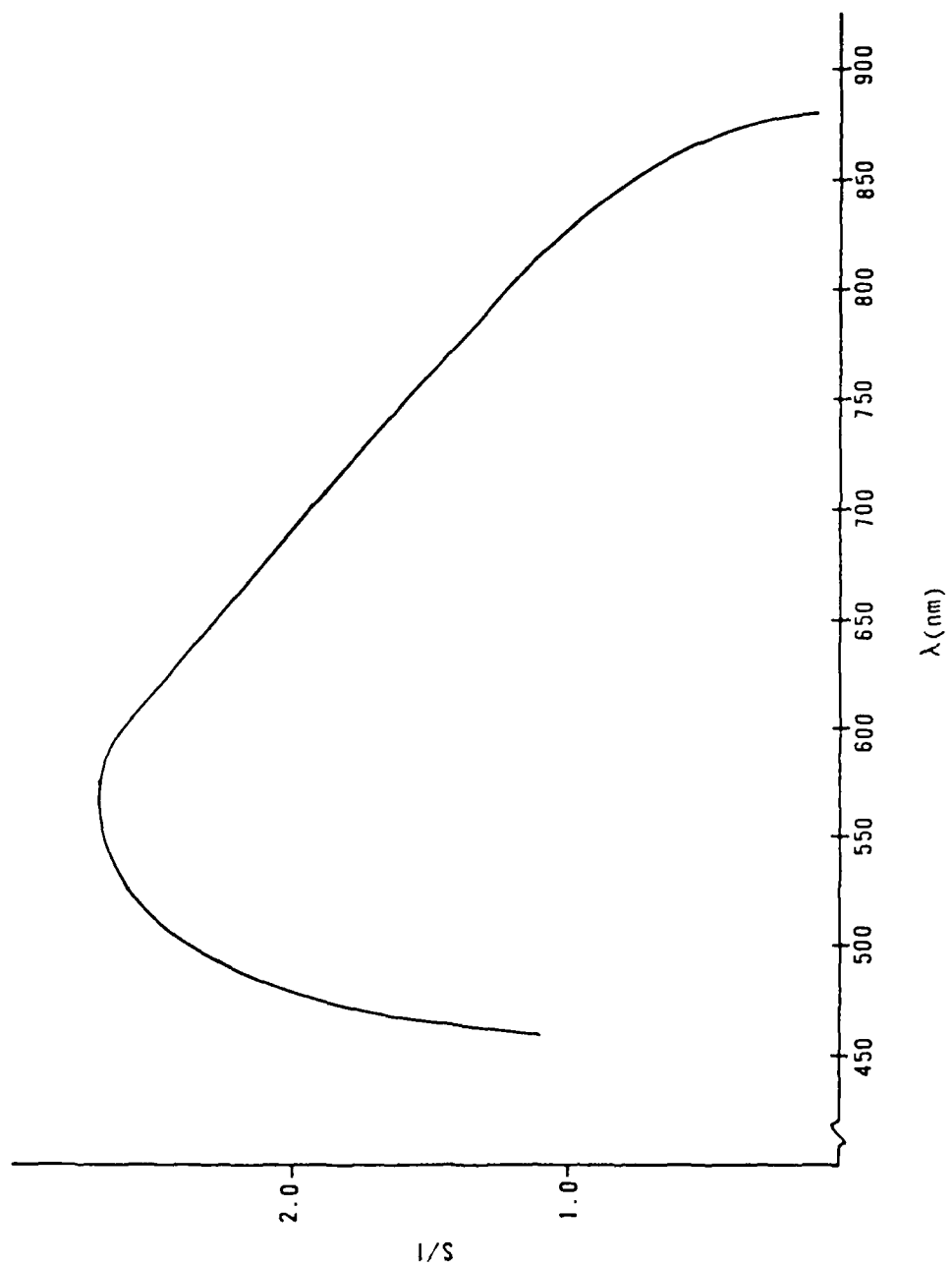


Figure H-2. A plot of the relative balckbody response (experimental to theoretical) as a function of wavelength.

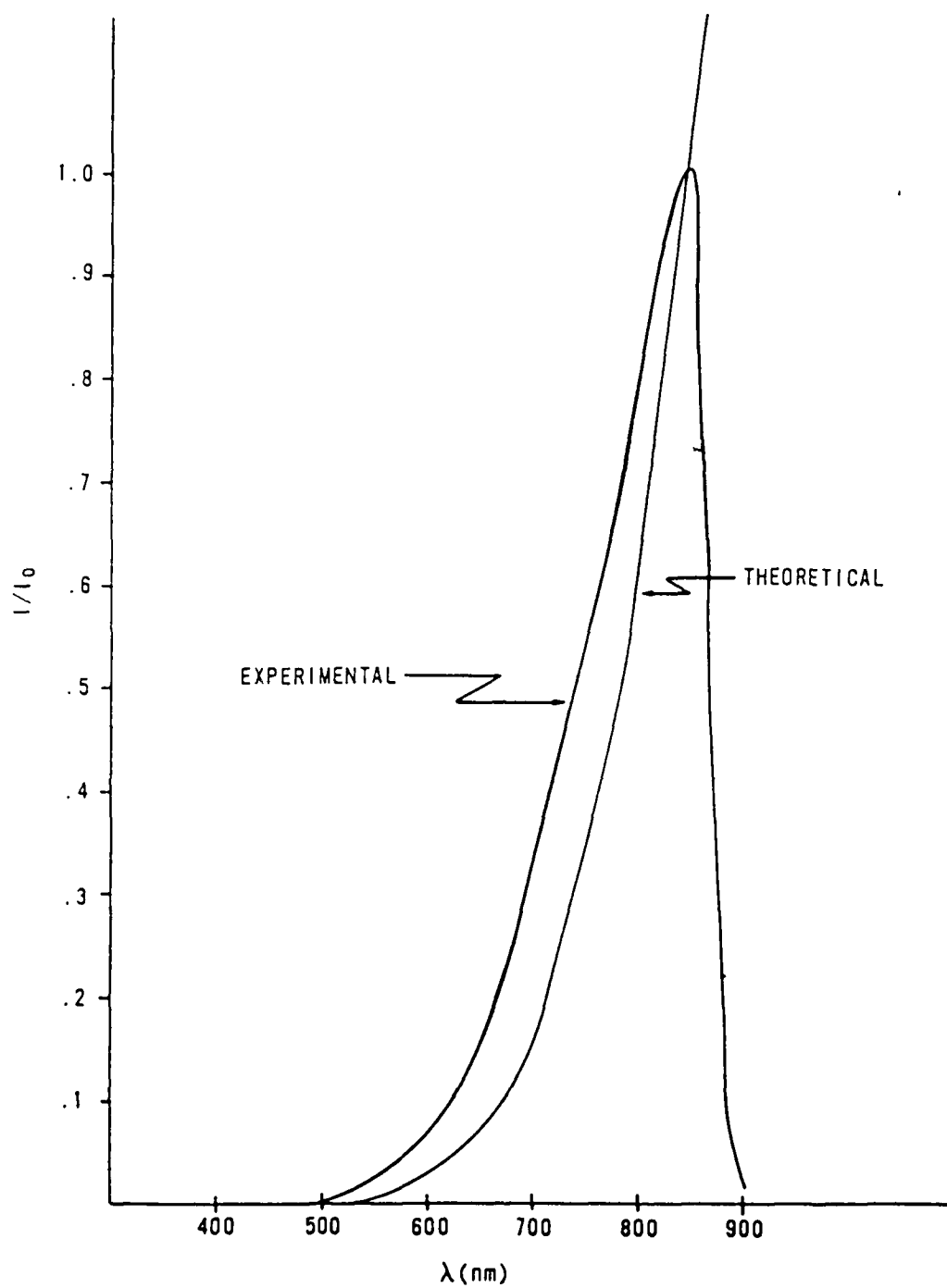


Figure H-1. A comparison of the experimental to theoretical blackbody spectra. The curves were normalized at the wavelength corresponding to the maximum response of the detection system.

APPENDIX H: Calibration of the Fluorescence Detection System.

The wavelength dependent response of the fluorescence detection system to an applied signal was determined by comparing experimental and theoretical blackbody spectra. A standard blackbody source was placed at the observation window of the cell and was left to equilibrate at 1385°K for 24 hours. A blackbody spectrum was recorded between 450 and 900 nm using a Keithly 414S picoammeter which measured the photocurrent from the RCA C31034A-02, cooled photomultiplier tube. A hard copy of the blackbody spectrum was displayed on a strip-chart recorder. The PMT signal, S , was subsequently compared to the theoretical intensity, I , using

$$S = \alpha(\lambda) I \quad (H-1)$$

where $\alpha(\lambda)$ is a calibration factor which depends on the response characteristics of the grating, photomultiplier tube, and also on the geometry of the system. The theoretical intensity was calculated using Planck's blackbody distribution

$$N(\lambda) = \frac{2c^2h}{\lambda^5} (\exp[hc/\lambda kT] - 1) \quad (H-2)$$

A comparison of the two blackbody curves is shown in Fig H-1. The two curves were normalized at the maximum response of the detection system which occurred at 847.5 nm. Figure H-2 displays the plot of S/I versus wavelength to determine the appropriate corrections for the signal response of the detection system.

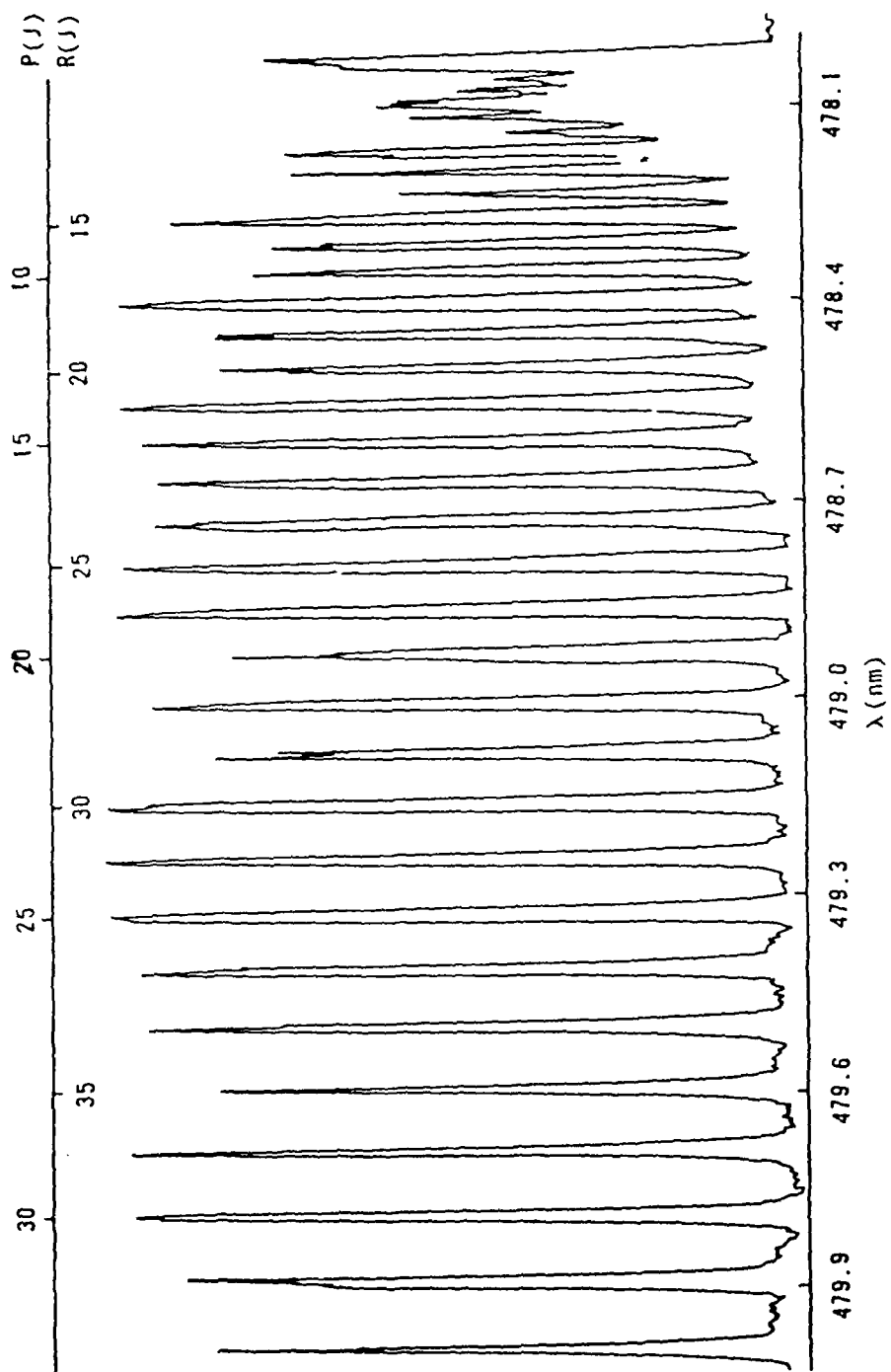


Figure G-3. Laser excitation spectrum of the (5,0) band. Note the lack of rotational resolution as compared to Fig. G-2.

constants B_e and α_e .⁵ Centrifugal distortion was neglected in making the assignments. The application of Trickl and Wanner's molecular constants¹³ did not alter the rotational assignment since these spectra were obtained at relatively low resolution.

Since nuclear interchange symmetry does not apply for heteronuclear diatomics, the nuclear spin statistical weight is the same for each rotational level. Therefore, the intensity alterations of the rotational branches are governed solely by the Boltzmann distribution with the appropriate statistical weight given by $S_J/(2J + 1)$. The Honl-London factor, S_J , has a value of J and $J + 1$ for the R and P branch, respectively.¹⁰ For a typical P-R doublet in the IF excitation spectra, the R line correlates with a ground state rotational level J'' which is some 7 levels above the J'' value for the P line. Thus, at high J values above the Boltzmann maximum, the R line, which corresponds to the higher J level, has a lower intensity than the P line in the doublet.

Not all the vibrational bands showed a well resolved rotational structure. As seen in Fig. G-3, the (5,0) band was a particularly simple one because the $P(J)$ and $R(J + 7)$ lines are overlapped throughout much of the band.

Comparing Eqs. (K-3) and (K-11) shows that the functional form of the population growth in the satellite bands is drastically different depending on whether or not multiquantum vibrational transfer is present. The form of Eq. (K-11) for sequential cascade shows that the population in the $\Delta v > -1$ states has a higher order dependence on time, indicating that the population in these states grows only when significant population is present in the next highest level. The basic principles of analysis for collisional relaxation via sequential cascade are the same as the methods used to analyze radioactive-series decay.⁶⁴

APPENDIX L: Steady-State Vibrational Transfer Modeling

The general relaxation equation governing both collisional redistribution and radiative decay is given by

$$dY_i/dt = Y_i(0)/\tau - Y_i/\tau + \sum_j [k(j,i)M Y_j - k(i,j)M Y_i] = 0 \quad (L-1)$$

In Eq.(L-1), Y_i is the relative population, N_i/N , of a vibrational state i , τ is the effective lifetime [$\tau = (1/\tau_R + Q_m M)^{-1}$], and $k(i,j)$ is the collisional rate from state i to state j . In this equation, the input is divided among the available energy levels according to $Y(0)$ which is a statement of the initial conditions, and the output according to \bar{Y} .

Solving this equation in steady-state, one obtains

$$Y_i = Y_i(0) + \sum_j \tau [k(j,i)M Y_j - k(i,j)M Y_i] \quad (L-2)$$

or, in matrix form

$$\bar{Y}(0) = \bar{Y} (\bar{I} - \bar{\tau} \bar{A}) \quad (L-3)$$

The effective lifetime term, $\bar{\tau}$, was written in matrix form to explicitly account for the variation in the radiative lifetimes for each vibrational level. The term \bar{A} is the matrix of relaxation rates with the elements described in Eq.(L-2). Rewriting Eq.(L-3) as

$$\bar{Y} = (\bar{I} - \bar{\tau} \bar{A})^{-1} \bar{Y}(0) \quad (L-4)$$

the relative populations, Y_i , were determined as a function of bath gas pressure, M , by specifying both an initial δ -function distribution in a given vibrational level and the rates $k(i,j)$ and $k(j,i)$. By assuming

only $\Delta v = \pm 1$ transitions, the matrix A becomes a simple tri-diagonal matrix. The main diagonal terms represent the total removal from a vibrational level while the off-diagonal terms describe the state-to-state transitions. The relative populations, Y_i , can then be obtained by solving Eq.(L-4) by matrix inversion.

The form of Eq.(L-4) also allows one to determine the effects of multiquantum transfer in the initial vibrational distribution. Simply, one only needs to insert additional off-diagonal elements to describe this process. The scaling of the vibrational transfer rates can also be examined if high bath gas pressures are used so one achieves nearly complete relaxation of the initial distribution. This relaxation is needed to avoid dominance of the $k(i,j)$ rates out of the initially populated vibrational level at low pressures. To analyze the vibrational scaling of the rates, one needs to input rates out of a particular level (preferably, the $k(1,0)$ rate should be used) and use various scaling parameters to obtain a population distribution which can then be compared to the experimental data.

VITA

Paul James Wolf was born on 31 May 1956 at Ashyia AFB on the Japanese island of Kyushu. He graduated from St. Peter's Preparatory High School in 1974 and, continuing in the Jesuit tradition of academic excellence and social liberalism, he attended Regis College in Denver, Colorado. In 1978, he graduated, summa cum laude, from Regis College and received a Bachelor of Science degree in Physics. That year, Paul Wolf was also commissioned a Second Lieutenant in the United States Air Force through the AFROTC program at the University of Colorado, Boulder, Colorado. He then entered the Air Force Institute of Technology, Dayton, Ohio from which he received a Master of Science degree in Engineering Physics in 1979. Selected by the Air Force to continue his education, he was enrolled in the Ph.D program at AFIT where he completed the course work for a Doctor of Philosophy degree in physics. He was reassigned to the Advanced Laser Technology Division of the Air Force Weapons Laboratory in Albuquerque, New Mexico to complete his dissertation.

Permanent Address: 770 2nd Street
Secaucus, NJ 07094

UNCLASSIFIED

SECURITY CLASSIFICATION OF THIS PAGE

REPORT DOCUMENTATION PAGE

1a. REPORT SECURITY CLASSIFICATION Unclassified			1b. RESTRICTIVE MARKINGS	
2a. SECURITY CLASSIFICATION AUTHORITY			3. DISTRIBUTION/AVAILABILITY OF REPORT Approved for public release; distribution unlimited	
2b. DECLASSIFICATION/DOWNGRADING SCHEDULE				
4. PERFORMING ORGANIZATION REPORT NUMBER(S) AFIT/DS/PH/85-1			5. MONITORING ORGANIZATION REPORT NUMBER(S)	
6a. NAME OF PERFORMING ORGANIZATION Air Force Institute of Technology		6b. OFFICE SYMBOL (If applicable) AFIT/EN	7a. NAME OF MONITORING ORGANIZATION Air Force Weapons Laboratory Short Wavelength Laser Branch	
6c. ADDRESS (City, State and ZIP Code) Wright-Patterson AFB, Ohio 45433			7b. ADDRESS (City, State and ZIP Code) Kirtland AFB, New Mexico 87117-6008	
8a. NAME OF FUNDING/SPONSORING ORGANIZATION Air Force Office of Scientific Research		8b. OFFICE SYMBOL (If applicable)	9. PROCUREMENT INSTRUMENT IDENTIFICATION NUMBER	
8c. ADDRESS (City, State and ZIP Code) Bolling AFB, Washington DC			10. SOURCE OF FUNDING NOS.	
			PROGRAM ELEMENT NO. PROJECT NO. TASK NO. WORK UNIT NO.	
11. TITLE (Include Security Classification) Collisional Dynamics of the B ³ -(0 ¹) State of Iodine Monofluoride (U)			61102F -- -- 23037202	
12. PERSONAL AUTHOR(S) Wolf, Paul James				
13a. TYPE OF REPORT PhD Dissertation		13b. TIME COVERED FROM J: 1 1981 TO Dec 1984	14. DATE OF REPORT (Yr., Mo., Day) 1985 March	15. PAGE COUNT 222
16. SUPPLEMENTARY NOTATION <div style="text-align: right;">Approved for public release: RAW AFB 150-1. <i>John E. Wolaver</i> 19 AUG 85 John E. WOLAVER Dean for Research and Professional Development Air Force Institute of Technology (AFIT) Wright-Patterson AFB, Ohio 45433</div>				
17. COSATI CODES			18. SUBJECT TERMS (Continue on reverse if necessary)	
FIELD	GROUP	SUB GR	Laser induced fluorescence, Iodine monofluoride, electronic quenching, vibrational energy transfer, rotational energy transfer.	
07	04	0		
20	05	0		
19. ABSTRACT (Continue on reverse if necessary and identify by block number) Electronic quenching and vibrational and rotational energy transfer rate constants in IF(B) were determined in a chemically reactive flow system using both steady-state and time-resolved laser induced fluorescence. IF(B) deactivation by the noble gases and nitrogen was extremely slow for all the stable B state vibrational levels. The only appreciable quenchers were fluorine, oxygen, water vapor, and iodine. Double exponential IF(B) fluorescence decays were observed with both oxygen and water vapor indicating two depletion processes occurring over the lifetime of IF(B). Vibrational transfer was 100 to 1000 times more efficient than electronic quenching; and the vibrational transfer process was adequately described as an adiabatic encounter. The relative V-T cross sections for the noble gases showed a smooth dependence on the collision reduced mass. The cross sections for nitrogen, oxygen, and fluorine showed no clear dependence on the collision reduced mass signifying that a V-T process may not be the dominant mechanism. The IF(B) vibrational transfer cross sections for the noble gases, nitrogen, and oxygen scaled linearly (Con't)				
20. DISTRIBUTION/AVAILABILITY OF ABSTRACT UNCLASSIFIED/UNLIMITED <input checked="" type="checkbox"/> SAME AS RPT. <input type="checkbox"/> DTIC USERS <input type="checkbox"/>			21. ABSTRACT SECURITY CLASSIFICATION Unclassified	
22a. NAME OF RESPONSIBLE INDIVIDUAL PAUL J. WOLF			22b. TELEPHONE NUMBER (Include Area Code) (505) 844-1871	22c. OFFICE SYMBOL A FWL/ARDD

Block 18. Collision dynamics

Block 19. with vibrational quantum number, and downward, single quantum jumps dominated the transfer pathway. Rotational energy transfer with the noble gases and nitrogen was the most efficient kinetic process in IF(B). The estimated efficiencies for the total population removal from a single J level were typically 100 times greater than that for vibrational transfer. The rotational transfer cross sections displayed a smooth dependence on both the collision reduced mass and the polarizability of the collision partner.

END

FILMED

10-85

DTIC